DEPARTAMENT OF
MATERIALS SCIENCE & DEPARTMENT
OF LIFE SCIENCES

DIGITAL MICROFLUIDICS FOR ISO-THERMAL NUCLEIC ACID AMPLIFICATION

EXPLORING SENSING METHODOLOGIES

BEATRIZ JORGE COELHO

Master in Micro and Nanotechnology Engineering

DOCTORATE IN NANOTECHNOLOGIES AND NANOSCIENCES

NOVA University Lisbon

May, 2023

NOVA SCHOOL OF SCIENCE & TECHNOLOGY

DEPARTAMENT OF MATERIALS SCIENCE & DEPARTMENT OF LIFE SCIENCES

DIGITAL MICROFLUIDICS FOR ISO-THERMAL NUCLEIC ACID AMPLIFICATION

EXPLORING SENSING METHODOLOGIES

BEATRIZ JORGE COELHO

Master in Micro and Nanotechnology Engineering

DOCTORATE IN NANOTECHNOLOGIES AND NANOSCIENCES

NOVA University Lisbon

May, 2023

DEPARTAMENT OF
MATERIALS SCIENCE & DEPARTMENT OF
LIFE SCIENCES

DIGITAL MICROFLUIDICS FOR ISOTHERMAL NUCLEIC ACID AMPLIFICATION

EXPLORING SENSING METHODOLOGIES

BEATRIZ JORGE COELHO

Master in Micro and Nanotechnology Engineering

Adviser: Rodrigo Ferrão de Paiva Martins
Full Professor, NOVA University Lisbon

Co-advisers: Pedro Miguel Ribeiro Viana Baptista
Full Professor, NOVA University Lisbon

Rui Alberto Garção Barreira do Nascimento Igreja
Associate Professor, NOVA University Lisbon

Examination Committee:

Chair: João Paulo Borges,
Full Professor, NOVA University Lisbon

Rapporteurs: Duarte Miguel de França Teixeira dos Prazeres,
Full Professor, Instituto Superior Técnico

Lorena Diéguez,
Head of the Medical Devices research group, International Iberian Nanotechnology Laboratory

Co-adviser: Rui Alberto Garção Barreira do Nascimento Igreja,
Associate Professor, NOVA University Lisbon

Members: Maria Goreti Ferreira Sales,
Associate Professor with Habilitation, University of Coimbra

Henrique Leonel Gomes,
Associate Professor with Habilitation, University of Coimbra

José Ricardo Ramos Franco Tavares,
Associate Professor with Habilitation, NOVA University Lisbon

DOCTORATE IN NANOTECHNOLOGIES AND NANOSCIENCES

NOVA University Lisbon
May, 2023

Digital Microfluidics for Isothermal Nucleic Acid Amplification: Exploring Sensing Methodologies

To my pets, parents and friends.

To my nephew Duarte, who passed away too soon.

ACKNOWLEDGMENTS

At the end of such a long journey, I must acknowledge everyone who enriched it and contributed to its finalization.

First of all, I would like to thank my supervisors, Professor Pedro Baptista, Professor Rodrigo Martins and Professor Rui Igreja, for all their support. Thank you, Professor Pedro, for your never-ending wit and extremely valuable insights in all fields, within your expertise or not. I assure you that an outsider would not doubt you to be an expert in Materials Science and Molecular Biology equally. Thank you so much for all your lessons, which I will apply to my future in- and outside the lab. Thank you, Professor Rodrigo Martins, for trusting me and giving me the opportunity to work on this PhD project - I would certainly not be here without you. Thank you for answering any of my questions within minutes and solving any issue in the exact same day. To Professor Rui Igreja, thank you for your supervision and for all the opportunities you provided me to evolve. Thank you for always being available to discuss and improve any of my ideas.

Secondly, I must acknowledge my host institutions, CENIMAT, CEMOP and UCIBIO, for giving me access to any equipment, reagent and expertise in all the fields I studied during this PhD work. Also, a broader acknowledgement should go to the NOVA School of Science and Technology, for all the training given to me thus far.

Thirdly, I will acknowledge my pets. Not only Aquiles and Ema who live in my house, but also to all my pets at *Quintinha ABC*, where I volunteer. There is nothing more rewarding than the joy you show me just by realizing I've arrived, whether you're feeling OK or sick, whether it is sunny or rainy. Dear reader: how many humans do this for you? I'll guess not many…

Finally, a very special thanks to my family and friends. To my parents, Lígia and Fernando, thank you for your eternal care, love and patience. Thank you for being there during the good times and the absurdly more frequent bad times. To my all-time friends, Eunice, Priscila and

Cláudio - thank you for being my lighthouse and providing me with so many moments of laughter.

And of course, thank you to all the researchers of CENIMAT, CEMOP and UCIBIO. Without your moral and technical support, I'm sure I would have never finished this endeavor. From CENIMAT, thank you Andreia dos Santos, Maria João, Joana Neto, Joana Pinto, Alexandra Gonçalves, André Moura, Emanuel Carlos, Carolina Marques, João Coelho, Raquel Barrulas, Rita Branquinho, Adriana Costa, Fernanda Carvalho, Daniela Gomes, Sara Silvestre, Maria Morais, Sofia Ferreira, Tomáses and Leonor Matias. From CEMOP, thank you Jenny Boane, Joana Figueira, Ana Rovisto, Jorge Martins, Inês Cunha, Deneb Menda, Ana Santa, Maria Pereira, Ricardo Ferreira, Tiago Carvalho, Raquel Barras, Tiago Mateus, Cátia Figueiredo, Cristina & Diana Gaspar. And from UCIBIO, thank you Beatriz Oliveira, Daniela Ferreira, Margarida Silva, Cinthia Barroco, Catarina Rodrigues and Luís Raposo. And everyone I unfortunately forgot. My brain is not what it used to be…

“It's dark because you are trying too hard. Lightly child, lightly. Learn to do everything lightly. Yes, feel lightly even though you're feeling deeply. Just lightly let things happen and lightly cope with them. So throw away your baggage and go forward. There are quicksands all about you, sucking at your feet, trying to suck you down into fear and self-pity and despair. That's why you must walk so lightly. Lightly my darling." (Aldous Huxley)

ABSTRACT

Digital Microfluidics (DMF) has recently emerged as a promising candidate for nucleic acid amplification for molecular diagnostics, by virtue of its precise control over unit droplets without the need of any propulsion devices, ease of integration with chemical/biological reactions and multiplex assay capabilities. Nevertheless, current scientific research is still far from accomplishing the full potential of the technique, so new, innovative nanotechnology/biotechnology hybrid approaches are necessary. As such, the purpose of this work is to contribute for the paradigm shift of nucleic acid amplification from central laboratories to point-of-care (POC) by designing and fabricating DMF devices compatible with isothermal nucleic acid amplification (loop-mediated isothermal amplification - LAMP). For biological validation of the devices, detection of cancer biomarker *c-Myc* is performed, and further real-time amplification monitoring is attempted through several methodologies, namely fluorescence, impedance and electrochemical measurements. The DMF devices produced herein enable optimal temperature control, crucial for LAMP reactions, and further allow for a novel methodology of reagent mixing, based on dual actuation with back-and-forth motion and actuation frequency tuning. Such innovations lead to successful amplification of 0.5 ng/μL or 90 pg of *c-Myc* in one hour, in line with the range reported in the literature, and further monitoring of the LAMP reaction profile by microscopy-based fluorescence measurements. Impedimetric and electrochemical methodologies did not meet the tight criteria required for biomarker detection, yet the developments achieved herein open the path for other applications. Lastly, the dielectric layer (key element of a DMF device) was optimized to assure long reactions (up to two hours) without device degradation.

Keywords: Digital microfluidics, loop-mediated isothermal amplification, real-time nucleic acid amplification monitoring

RESUMO

A microfluídica digital (MFD) surgiu como uma tecnologia promissora para amplificação de ácidos nucleicos em diagnóstico molecular, permitindo controlo sobre gotas unitárias sem necessidade de dispositivos de propulsão, facilidade de integração com reações químicas/biológicas e capacidade de realização de ensaios simultâneos. Contudo, a investigação científica atual ainda está longe de atingir o máximo potencial da técnica, pelo que são necessárias abordagens novas, inovadoras e híbridas de nanotecnologia e biotecnologia. Como tal, o propósito deste trabalho é contribuir para a mudança de paradigma da amplificação de ácidos nucleicos de laboratórios centralizados para ponto-de-atendimento (PDA) através do desenho e fabricação de dispositivos de MFD compatíveis com amplificação isotérmica de ácidos nucleicos (*loop-mediated istothermal amplification* - LAMP). Para validação biológica dos dispositivos, será detetado o biomarcador de cancro *c-Myc*, e testada a monitorização da amplificação em tempo real através de várias metodologias, nomeadamente medidas de fluorescência, impedância ou medidas eletroquímicas. Os dispositivos MFD produzidos permitem um controlo ótimo da temperatura, crucial para reações LAMP, e introduzem uma metodologia para mistura de reagentes, com movimentos em vaivém e ajuste da frequência de atuação. Tais inovações conduziram à amplificação de 0.5 ng/µL ou 90 pg de *c-Myc* em uma hora, em linha com o intervalo relatado na literatura, permitindo ainda monitorização do perfil da reação LAMP através de medidas de fluorescência mediadas por microscopia. As metodologias impedimétricas e eletroquímicas não cumpriram os exigentes critérios requeridos para deteção de biomarcadores, no entanto, os desenvolvimentos alcançados abrem caminho para outras aplicações. Por último, a camada dielétrica (elemento-chave de um dispositivo MFD) foi otimizada para assegurar reações mais longas (até duas horas) sem degradação do dispositivo.

Palavras-chave: Microfluídica digital, *loop-mediated istohermal amplification*, monitorização da amplificação de ácidos nucleicos em tempo real

CONTENTS

LIST OF FIGURES

Appendices

List of Tables

Appendices

List of acronyms

2D	Two dimensional
3D	Three dimensional
A	Area
ABS	Acrylonitrile butadiene styrene
AC	Alternating current
ALD	Atomic layer deposition
ANOVA	Analysis of variance
B3	Backward outer primer
BIP	Backward inner primer
bp	Base-pairs
BST	Barium Strontium Titanate
C2CA	Circle-to-circle amplification
cDNA	Complementary DNA
CMF	Continuous-flow microfluidics
CNT	Carbon nanotubes
COVID-19	Coronavirus disease 2019
CVD	Chemical vapor deposition
DC	Direct current

DMF	Digital microfluidics
DNA	Deoxyribonucleic acid
dNTP	Deoxynucleotide triphosphate
DrMF	Droplet microfluidics
dsDNA	Double-stranded DNA
e-beam	Electron beam
EBT	Eriochrome black T
EICE	Electrowetting on insulator coated electrodes
EIS	Electrochemical impedance spectroscopy
EISm	Electrolyte-insulator-semiconductor
ELISA	Enzyme-linked immunosorbent assay
EWOD	Electrowetting-on-dielectric
F3	Forward outer primer
FDA	Food and Drug Administration
FET	Field effect transistor
FIP	Forward inner primer
FITC	Fluorescein isothiocyanate
FWHM	Full width at half maximum
GPIB	General Purpose Interface Bus
GUI	Graphical User Interface
HNB	Hydroxy naphthol blue
HSA	Human serum albumin
IDE	Inter-digitated electrode
IGZO	Indium-Gallium-Zinc-Oxide
ITO	Indium-Tin-Oxide
LAMP	Loop-mediated isothermal amplification

LFA	Lateral flow assay
LOD	Limit of detection
MALDI-MS	Matrix-assisted laser desorption/ionization mass spectrometry
MIM	Metal-insulator-metal
MIS	Metal-insulator-semiconductor
MOCVD	Metal organic chemical vapor deposition
MOSFET	Metal-oxide-semiconductor field effect transistor
NAA	Nucleic acid amplification
OEW	Optoelectrowetting
ParC	Parylene C
PCB	Printed circuit board
PCR	Polymerase chain reaction
PDMS	Polydimethylsiloxane
PECVD	Plasma enhanced chemical vapor deposition
PEN	Polyethylene naphthalate
PET	Polyethylene terephthalate
PID	Proportional–integral–derivative
PLA	Polylactic acid
PMF	Paper microfluidics
PMT	Photomultiplier tube
POC	Point-of-care
PTC	Positive temperature coefficients
PTFE	Polytetrafluoroethylene
RF	Radio frequency
RNA	Ribonucleic acid
RPA	Recombinase polymerase amplification

RT	Room temperature
SARS-CoV-2	Severe acute respiratory syndrome coronavirus 2
SAW	Surface acoustic wave
SD	Standard deviation
SE	Secondary electrons
SEM	Scanning electron microscopy
ssDNA	Single-stranded DNA
TAE	Tris-Acetate-Ethylenediaminetetraacetic acid
TSH	Thyroid stimulating hormone
UV	Ultraviolet
XRD	X-ray diffraction

LIST OF SYMBOLS

π	The ratio of the circumference of a circle to its diameter, having a value rounded to eight decimal places of 3.14159265 (symbol: π).
A_{vo}	Loop gain of an operational amplifier
B_o	Bond number
C	Capacitance
Cp	Heat capacity at constant pressure
d	Thickness or distance
E_{BD}	Critical electric field
E_{OC}	Open circuit potential
f	Frequency
g	Gravitational constant
I	Current
R	Resistance
t	Time
V	Voltage
v_-	Inverting output voltage
v_+	Non-inverting output voltage
V_{BD}	Dielectric breakdown voltage
v_{in}	Input voltage

V_{out}	Output voltage
V_{RMS}	Root mean square voltage
Z	Impedance
γ	Surface tension
γ_{LG}	Liquid-gas surface tension
γ_{SG}	Solid-gas surface tension
γ_{SL}	Solid-liquid surface tension
ε_0	Vacuum permittivity
ε_R	Relative permittivity
θ	Contact angle
κ	Thermal conductivity
λ	Wavelength
ρ	Density

1

Motivation

Cancer is currently one of the leading causes of death worldwide according to the World Health Organization[1], with over 19 million new cases and almost 10 million deaths in 2020, as estimated by the International Agency for Research on Cancer[2]. In the same year, the COVID-19 (Coronavirus disease 2019) pandemic caused nearly 1.9 million deaths worldwide[3], approximately five times less deaths than cancer. It is therefore imperative to grant cancer the same or even a higher health emergency status than COVID, not only to prevent this infirmity, but also to improve patient outcome. Early cancer detection is one of the main (if not the main) instruments for success in treatment as well as long-term survival rates[4], and has been considered a key intervention area in healthcare policy[5]. Point-of-care (POC) devices are relevant agents in early cancer detection[6], performing specific tests near the patient, with a much smaller delay between testing and receiving the final result[7,8] in comparison to centralized facilities - either private/public laboratories, hospitals and other healthcare facilities – where tests are executed and further interpreted by experts[9,10]. Such devices support cancer detection through the identification of cancer biomarkers, biomolecules that indicate the presence of cancer, produced either as a response to cancer or by cancerous cells[11,12]. Accordingly, it is of utter relevance to invest in research and development of POC devices capable of performing specific and sensitive detection of appropriate cancer biomarkers. Digital microfluidics (DMF) arises as a promising base technology for POC devices, namely in the field of cancer biomarker detection, allowing for precise control of individual droplets of a wide volume range (nano- to micro-liters) over an electrode array[13–15]. Having such a high degree of freedom, droplets can perform any routine assigned by the user, according to electrode disposition[14,16–21]. Particularly, in the most common DMF configuration (closed configuration), droplets are sandwiched between two plates, thus enabling all possible fluidic operations: dispensing, mixing, merging or splitting. In this configuration, droplet motion is typically achieved through the electrowetting-on-dielectric phenomenon, whereby an electric field is applied between operating electrodes and the ground electrode (usually the top plate), forcing charge redistribution within the droplet and enabling droplets to move from a non-actuated (OFF) to an actuated (ON) electrode[22].

The purpose of this PhD project is to design and produce a DMF platform able to perform loop-mediated isothermal amplification (LAMP) of cancer biomarker DNA and further detect said DNA. LAMP was the chosen amplification methodology, considering its outstanding robustness, specificity and sensibility[23–26]. Moreover, as an isothermal strategy, LAMP eliminates intricate thermal cycling procedures and subsequently allows for lower energy consumption. To test and validate the DMF platform for cancer biomarker detection, the *c-Myc* proto-oncogene was chosen. This promising cancer biomarker oncogene is known as a "master

regulator"[27], due to its involvement in cell growth, proliferation and metabolism, which cumulatively intervene in tumorigenesis initiation and expansion[27–31]. In addition, *c-Myc* targets about 15% of the human genome[32] and the overexpression of such oncogene has been associated to a large percentage (40%) of tumors[27,28], which further increases clinical relevance of this oncogene as a biomarker, as well as its early detection. Finally, several DNA detection methodologies compatible with DMF are explored in this work, as to determine which provides the more promising capability of cancer biomarker detection for POC. Among such methodologies are fluorescence detection, electrochemical detection and impedimetric detection.

2

INTRODUCTION

Disclaimer

Some excerpts of this section have been published in the following publication:

Coelho, B. J.; Pinheiro, T.; Marques, A. C.; Baptista, P. V.; Águas, H.; Igreja, R.; Martins, R.; Fortunato, E. Biossensores Com Incorporação de Microfluídica: Uma Mais-Valia No Diagnóstico Clínico. In *Novas Tecnologias da Saúde*; Fundação Amélia de Mello, Ed.; 2021.

B. J. Coelho investigated the literature and wrote the full length of this section. Some excerpts of the introduction presented below were further adapted to the reference above.

2.1 Digital Microfluidics as a promoter of automated POC

As can be deduced from the previous chapter, there is currently a great need for portable, low-cost point-of-care devices capable of automatically performing diagnostic tests and further providing the test results, and digital microfluidics (DMF) devices present an enormous potential to fill this gap. Digital microfluidics allows for discrete manipulation (hence "digital") of individual micro- to nano-liter droplets (hence "microfluidics") over an electrode array. As part of the microfluidics conception, DMF shares all of its predecessor's advantages, namely low volume consumption, portability and decreased toxic reagent handling. Nevertheless, digital microfluidics is the only concept that enables precise control over unit droplets, that is, unit micro-vessels or micro-reactors. Several fluidic operations are possible in such technology, namely reagent dispensing, merging and mixing with samples, and further integration with various readout techniques can provide a final result – all of which may be pre-programmed. Moreover, a myriad of liquid solutions and biological entities (including proteins) are compatible with this technology, meaning that several chemical and biological reactions may be carried out within DMF devices, inside micro-vessel droplets, thus enabling a number of low-volume, programmable applications, that may even be performed in a multiplex context: chemical synthesis, enzymatic reactions, nucleic acid amplification, proteomics, immunoassays, just to name a few[14,18,33]. Table 2.1 lists some of the most fascinating chemical and biological protocols automated via DMF. Nucleic acid-related protocols are extensively reviewed in section 2.6. Having such advantages in mind, one may easily envision DMF devices for portable, automated, user-friendly and easy-to-interpret POC healthcare.

Table 2.1: Brief record of laboratory procedures automated by means of DMF devices.

Scientific field	Innovation brought by DMF	Year
Proteomics	Automated purification of peptide-containing solutions for matrix-assisted laser desorption/ionization mass spectrometry (MALDI-MS)[34].	2005
	Simultaneous solution purification of several MALDI-MS samples[35].	2006
	Multiple, simultaneous, hydrogel-mediated proteolytic digestion[36].	2012
Immunoassays	Insulin and interleukin-6 detection by sandwich immunoassays mediated by magnetic beads[37]. The device automatically performed analyte and reagent mixing, allowed for antibody-analyte binding, followed by washing and finally, detection was possible via integration with a PMT (photomultiplier tube) module.	2008
	DMF platform for POC testing, featuring immunoassays from whole blood (including sample preparation), as well as DNA extraction and amplification by PCR (polymerase chain reaction)[38].	2008
	Immunoassay for detection of thyroid stimulating hormone (TSH) and 17β-estradiol (E2)[39], in an oil-free medium.	2012
	Screening of patient response to aromatase inhibitor therapy in breast cancer[40].	2017
	MR-BOX: a light, low-cost, fully integrated platform which uses flexible, inkjet-printed DMF devices for sample-to-result automated detection of measles and rubella immunoglobulin G in remote settings[41].	2018
	DMF platform for multiple bacteria detection, namely *E.coli* (*Escherichia coli*), BG (*Bacillus atrophaeus*), MS2 bacteriophage and HSA (human serum albumin)[42].	2019
	A DMF platform for sample-to-result newborn testing approved by the FDA (Food and Drug Administration)[43].	2020
Cell-related applications	First DMF chip to study cell manipulation under electrowetting-on-dielectric actuation[44].	2007
	Complete cell study DMF device, enabling 2D cell culture, namely cell seeding, growth and passaging to new sites[45]. Cell culture was successfully achieved for multiple cell lines: CHO-K1, NIH-3T3, HeLa, and INS-1[45].	2010
	3D cell culture of NIH-3T3 cells on hydrogels, performed in a DMF device[46].	2012
	Automated, multiplex cell assays (apoptosis studies)[47].	2012

Note: Extensive literature regarding all DMF applications can be consulted on references [14,18,33,48].

2.2 Paving the way for digital microfluidics: some historical contributions

The term "digital microfluidics" was first coined by the group of Prof. Richard Fair in 2002[49], yet the first studies regarding the effects of electricity applied to liquids were performed as early as 1875, by Dr. Gabriel Lippmann[50] (doctoral supervisor of Madam Marie Curie and Nobel Prize awardee). In his study, Dr. Lippmann described in detail the motion of the meniscus formed between a water-sulfuric acid solution and mercury placed within a glass capillary, while applying a potential difference between the two liquids. This was the basis of what was later defined by Dr. Beni and Dr. Hackwood as the electrowetting phenomenon, in 1981[51]. They proposed a passive display established through the application of voltage between a chromium/gold electrode and an electrolyte liquid, thus shifting from a transparent state to a white state due to the resulting movement of the electrolyte. Since the electrolyte moved along the electrode, "wetting" it, as a response to an electric field, this display was called an electrowetting display. Nevertheless, individual droplet movement over electrodes was only achieved in 1983, when Jean Pesant, Michael Hareng, Bruno Mourey and Jean Perbet submitted a patent describing a device "by means of which it is possible to cause fluid globules to circulate within a capillary space by means of pairs of electrodes establishing capture sites"[52]. The fore-mentioned discoveries are illustrated in Figure 2.1, exactly as depicted by the respective authors.

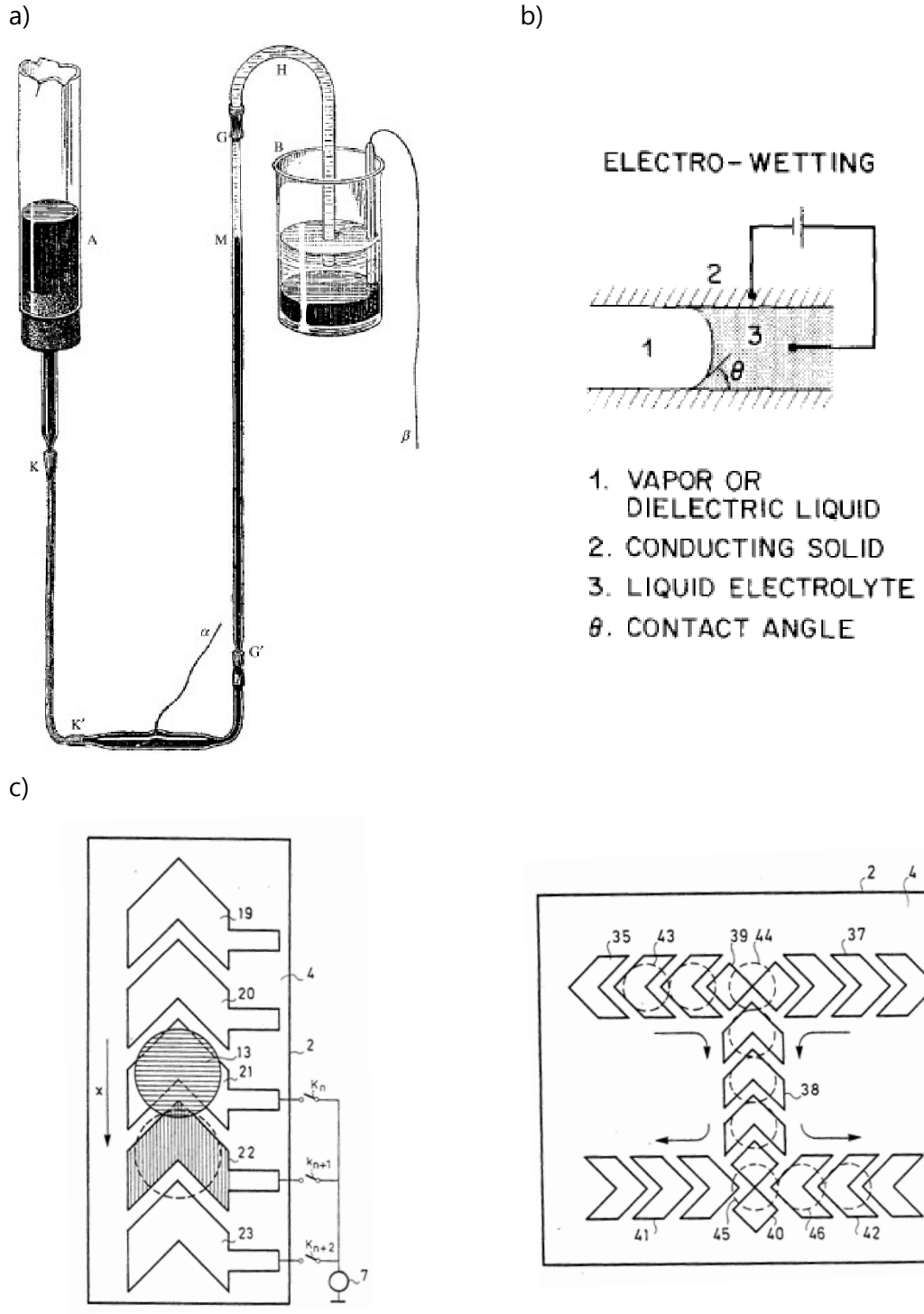

Figure 2.1: a) Initial experimental setup used by Dr. Lippmann to study the electrocapillarity phenomenon. Briefly, by applying a potential difference between wires α and β, a height variation was verified at the meniscus M formed at the interface of mercury (stored in receptacle A) and an acidic solution (stored in receptacle B). Adapted from [50] under law number 78-753 of the 17th July 1978 - source gallica.bnf.fr, hosted by *Bibliothèque nationale de France*. b) Schematic representing the electrowetting phenomenon described by Dr. Beni and Dr. Hackwood, where the dielectric liquid 1 would move in response to the voltage applied between the conducting solid 2 and the electrolyte liquid 3. Reprinted from [51] with the permission of AIP Publishing. c) Illustration of the electrode array developed by Jean Pesant and co-workers for moving fluid globules. Adapted from [52].

Later, in early 1990, Dr. Colgate and Dr. Matsumoto[53] disclosed moving liquids inside an array of capillaries connected to a liquid storage reservoir, by applying an electric potential between the capillaries and an electrode above the reservoir, which was separated from the liquid solution by an insulator (even though no practical application was reported). This strategy remains today the base for the most widely used method for moving droplets in DMF devices (see section 2.3). Finally, the greatest contribution to droplet movement in response to a potential difference was provided by Dr. Bruno Berge in 1993[54], who found a method for mitigating one of the most significant issues in electrowetting: electrochemical reactions on the metal-liquid interface (including liquid electrolysis), which would cause irreversible modification on said interface and consequently eliminate the electrowetting effect. In this work, a dielectric layer was added between the electrodes and the moveable liquid, thus allowing liquid actuation through the inert dielectric, while preventing contact with the metallic electrode (Figure 2.2).

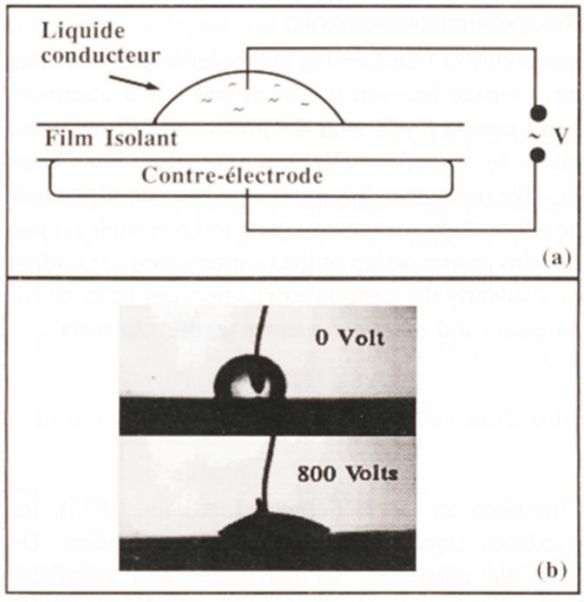

Figure 2.2: Demonstration of Dr. Berge's work in electrowetting-on-dielectric. Briefly, the contact angle of a conductive liquid with a dielectric film varies in response to the application of voltage between said liquid and an electrode placed beneath the dielectric film. Adapted from [54] under law number 78-753 of the 17th July 1978 - source gallica.bnf.fr, hosted by *Bibliothèque nationale de France*.

Such methodology was then called electrowetting on insulator coated electrodes (EICE), however, the contemporary nomenclature was changed to electrowetting-on-dielectric (EWOD). This and following works by Dr. Berge and co-workers are considered to have paved the way for modern electrowetting[55,56], and consequently, electrowetting-based DMF devices.

A few years later, in the 2000s, EWOD devices were rediscovered almost simultaneously by Professor Richard Fair from Duke University[49,57] and Professor Chang-Jin Kim from the University of California, Los Angeles[58,59], who considerably contributed to create the modern concept of DMF devices, as well as to diffuse this technology worldwide.

2.3 Droplet moving strategies

2.3.1 EWOD: the most common strategy

Electrowetting-on-dielectric (EWOD) is by far the most widely used method for moving droplets in DMF devices, perhaps due to its simplicity and overall easiness to produce. Nevertheless, before proceeding to the physical explanation of the EWOD phenomenon, some key concepts must be clarified. First, let us take into consideration that in a typical DMF or EWOD device, droplet dimensions are sub-millimetric, and surface tension dominates over gravity. The Bond number is helpful to understand such implications, as it is a dimensionless number that measures the ratio between gravitational forces and surface tension forces[60,61] (Equation 2.1):

$$Bo = \frac{\Delta\rho g R^2}{\gamma} \tag{2.1}$$

where $\Delta\rho$ is the difference of the density of the liquid and the surrounding fluid, g is the gravitational constant, γ is the surface tension, and R is a typical dimension of the droplet (droplet radius, for example).

For a Bond number much smaller than 1 (i.e. very small droplets), surface tension forces dominate, whereas for a Bond number much higher than 1 (i.e. large droplets), gravity dominates. Dealing with small droplets therefore means that several usual, common conceptions will not apply, and a basic understanding of surface tension is required.

Let us consider a liquid droplet on top of a solid, surrounded by air. An interface delineates the liquid domain from the gaseous domain – a dynamic interface, which will depend on the interactions between gas and liquid molecules. Considering the liquid droplet, molecules within the bulk of the droplet are surrounded by neighboring molecules in all directions, thus being equally affected in all directions (the total force exerted on such molecules is zero). However, molecules located at the edge of the droplet are only affected by cohesive forces of neighboring liquid molecules, and are therefore attracted inwards (interactions between liquid

and gas molecules do exist, but are neglectable). Surface tension can then be described as a measure of said cohesive forces, and it is expressed in units of energy per unit area (J/m^2) or force per unit length (N/m)[55,60].

The shape acquired by the liquid placed on the solid depends on the properties of the solid, the liquid and the surrounding gas (or fluid). If the liquid spreads over the solid, total wetting occurred; if, however, the liquid forms a droplet, only partial wetting occurred, and it is possible to draw a line connecting all three forms (solid, liquid and gas): the triple contact line, as depicted in Figure 2.3. When all forces acting upon this line are balanced, the droplet is at equilibrium and does not move (Equation 2.2, known as Young's equation).

$$\gamma_{LG} \cos\theta + \gamma_{SL} - \gamma_{SG} = 0 \tag{2.2}$$

Where γ_{LG} is the liquid-gas surface tension, θ is the contact angle formed between the droplet and the solid, γ_{SL} is the solid-liquid surface tension and γ_{SG} is the solid-gas surface tension.

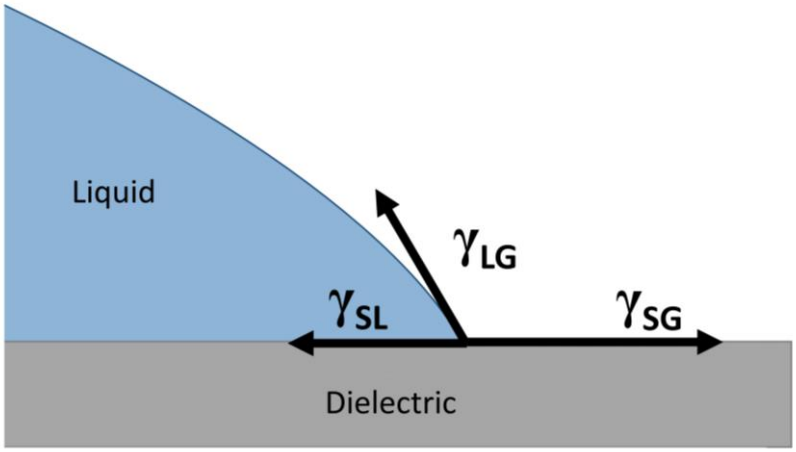

Figure 2.3: Schematic representation of the triple contact line and actuating surface tension forces, namely the solid-liquid surface tension (γ_{SL}), the liquid-gas surface tension (γ_{LG}) and the solid-gas surface tension (γ_{SG}).

Nevertheless, this balance may be disturbed by an electric field, giving rise to the EWOD phenomenon. As the name suggests, EWOD implies a change of the contact angle of a liquid droplet (i.e. wetting or de-wetting) over a dielectric layer as a response to an electric field applied between said droplet and a contact electrode directly beneath the dielectric film. In a microscopic view, as an electric field is applied to the liquid droplet, there is charge redistribution within the droplet (in accordance with the direction of the field), with like-charges accumulating at the droplet-dielectric interface. Since like-charges repel, a lateral force is generated at the triple contact line, resulting in droplet spreading over the dielectric layer. Thus, droplets

are moveable by subsequently applying and not applying voltage to the electrodes (ON/OFF states), with ON electrodes effectively attracting droplets standing on OFF electrodes. The Lippmann-Young equation accurately represents the change in contact angle resulting from the application of voltage:

$$\gamma_{LG}\cos\theta + \gamma_{SL} - \gamma_{SG} + \frac{CV^2}{2} = 0 \tag{2.3}$$

where C is the dielectric capacitance per unit area and V is the voltage applied.

The Lippmann-Young equation may also be re-written to relate the initial contact angle, θ_0 (no voltage applied) with the contact angle resulting from applying voltage, θ:

$$\cos\theta = \cos\theta_0 + \frac{C}{2\gamma_{LG}}V^2 \tag{2.4}$$

Or equivalently:

$$\cos\theta = \cos\theta_0 + \frac{\varepsilon_0\varepsilon_R}{2d\gamma_{LG}}V^2 \tag{2.5}$$

where ε_0 is the vacuum permittivity, ε_R is the relative permittivity of the dielectric material and d is the dielectric thickness.

It is noteworthy that the contact angle does not change infinitely as voltage increases, leading to the saturation effect, one of the most curious phenomena in EWOD theory. Several hypotheses have been put forward to explain such phenomenon, namely:

- Liquid electrical resistance[62]. Following this theory, the liquid droplet placed over the dielectric exhibits some electrical resistance, and as the droplet spreads, the distance between the triple contact line and the top electrode increases, therefore increasing the electrical resistance of the droplet.
- Zero surface-liquid energy limit[63]. This hypothesis, also known as PQRS model (in recognition of the hypothesis' authors - Peykov, Quinn, Ralston, and Sedev), reasons that the contact angle ceases to increase when thermodynamic stability is reached. In other words, saturation is achieved when the solid-liquid surface tension reaches zero, which is only possible if the liquid-gas surface tension projection is the exact opposite of the solid-gas surface tension.

- Charge trapping[64]. According to this theory, when the electric field is strong enough, charges are trapped within the dielectric, thus creating a permanent screening barrier which weakens the electrowetting effect.
- Dielectric breakdown[65]. It has been shown that at the vicinity of the triple contact line, the magnitude of the electric field may be up to ten times higher, due to material discontinuity. This increase in the electric field may lead to dielectric disruption and charge leakage (i.e. dielectric breakdown) as explained below.

The scientific discussion regarding the saturation effect is still not closed, and a multitude of other plausible explanations have been put forward[66–69]. Nevertheless, perhaps this phenomenon is due not only to one of the proposed solutions, but to a combination of said solutions, each one bearing different weights in the final result.

The last hypothesis is particularly interesting, as it is considered to be the most common cause for failure in EWOD-based DMF devices: dielectric breakdown. Dielectric breakdown occurs when the electric field is large enough to cause disruption of the dielectric, when bound electrons are freed from their respective atoms. These electrons can then be accelerated by the electric field and collide with other bound electrons, freeing them as well, creating an avalanche-like effect or avalanche breakdown. As a result of the avalanche, conductive paths are created between electrodes and liquid, leading to large current discharges that may even destroy the material[60]. The dielectric breakdown voltage is directly proportional to the dielectric thickness, as shown by Equation 2.6:

$$V_{DB} = dE_{DB} \tag{2.6}$$

where V_{DB} is the dielectric breakdown voltage, d is the dielectric thickness and E_{DB} is the critical electric field. Numerical simulations have further shown that the dielectric breakdown is closely related to the magnitude increase of the electric field in the vicinity of the triple contact line[70], and studies demonstrate current leakage resulting from dielectric breakdown[69].

Thus, the choice of dielectric material and respective thickness is of utmost importance in EWOD-based DMF devices (see Equations 2.5 and 2.6), and must balance a reasonable dielectric constant as well as dielectric thickness sufficiently large to prevent dielectric breakdown and simultaneously thin enough to enable actuation at relatively low voltages. In section 2.4.3, dielectric materials will be thoroughly discussed. Table 2.2 presents some of the most common dielectrics used in EWOD, and respective dielectric constants.

Table 2.2: Common dielectric materials for EWOD-based DMF devices, and respective dielectric properties.

Material	Dielectric constant	Dielectric strength	Reference
Al_2O_3 (Aluminum Oxide)	3-9	4-5 MV/cm	[71]
BST (Barium Strontium Titanate)	180	3 MV/cm	[72]
Parylene C	≈ 3	56 V/cm	[73]
Parylene HT	≈ 2.2	54 V/cm	[73]
PDMS (Polydimethylsiloxane)	2.3-2.8	2.50-6.35 MV/cm	[74,75]
Si_3N_4 (Silicon Nitride)	7.5	≈ 10 MV/cm	[76]
SiO_2 (Silicon Dioxide)	3.9	≈ 10 MV/cm	[76]
SU-8	≈ 4	4.4 MV/cm	[77]
Ta_2O_5 (Tantalum Pentoxide)	8-25	6 MV/cm	[78]

2.3.2 Alternatives to EWOD: droplet motion through acoustic, optic and magnetic methods

One of the most interesting alternatives to EWOD-driven droplet motion in DMF devices is motion through surface acoustic waves (SAWs). In a solid, elastic material, sound waves can propagate through the solid's atomic net, in a similar way to the propagation of the water waves that are produced when a pebble is thrown to a still lake. If said waves propagate on the surface of the solid, then they are considered SAWs. Traditionally, SAWs are generated by applying an electrical signal to interdigitated electrodes, and if these electrodes are deposited on a piezoelectric substrate, a mechanic wave will be produced at the surface (SAW), capable of producing a very effective, swift mixing motion within a droplet, or even propelling droplets towards the direction normal to the electrodes[79,80] (see Figure 2.4).

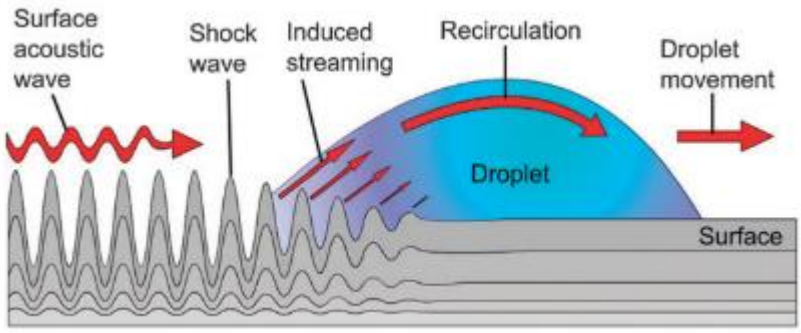

Figure 2.4: Schematic representation of the effect produced by a surface acoustic wave (SAW) on a single droplet. Reproduced from the work of Mark *et al.* [80] with permission from the Royal Society of Chemistry.

In the last twenty years, several SAW-based DMF devices have been developed, aiming for a multitude of applications ranging from particle collection[79] and mixing[79,81,82] within low-volume droplets, droplet motion and sensing[79,81,83,84] and localized heating[85]. Furthermore, it is worth mentioning that there is plenty of room for SAW and EWOD integration, since both technologies are compatible and may even achieve the same fluidic operations[82,84]. The SAW methodology enables a number of advantages, namely biocompatibility (extremely important for POC devices) and also fast, powerful droplet actuation[86].

Optically-induced electrowetting for droplet motion is also possible in DMF devices, a phenomenon first introduced by Chiou *et al.* in 2003[87], and known as optoelectrowetting (OEW). In this case, a photoconductive material (typically amorphous silicon) is placed between the substrate and metallic electrodes, and classic electrowetting states are generated by darkening or illuminating certain regions, over a superimposed AC signal. Thus, the conductivity of the photosensitive material varies by several orders of magnitude, and consequently, the dominant voltage drop shifts between the insulating layer and the photoconductive layer, therefore a pseudo-electrowetting effect is produced, which similarly enables droplet motion[86–88]. The requirements for achieving ON and OFF states are specific to each device, particularly when comparing single-sided actuation[89,90] (electrical signal applied between bottom electrodes) to double-sided actuation (electrical signal applied between bottom electrodes and the top plate)[88,91]. Moreover, the lighting operation scheme is opposite when using negative or positive photoconductors. Positive photoconductors (e.g. amorphous silicon) become more conductive when illuminated, whereas negative photoconductors (e.g. titanium oxide phthalocyanine) become less conductive when illuminated[92]. Figures 2.5 - 2.7 illustrate the major differences between the two actuation modes.

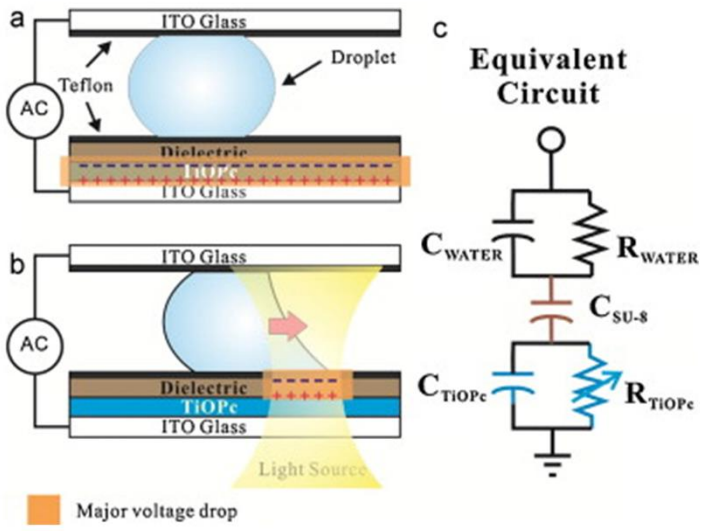

Figure 2.5: Schematic representation of double-side actuation OEW. a) OFF state, achieved by not applying a focused light source; b) ON state, achieved by applying a focused light source to the region where the droplet is intended to dislocate to; c) Equivalent electrical circuit of the structure. Reprinted from [91] with permission from Elsevier.

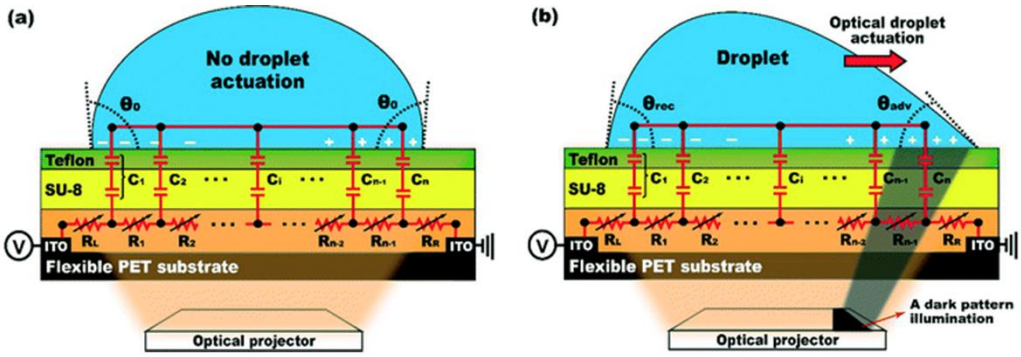

Figure 2.6: Schematic representation of single-side actuation OEW, with a negative photoconductor. a) OFF state, achieved by illuminating the entire substrate; b) ON state, achieved by darkening the region where the droplet is intended to dislocate to. Reproduced from [93] with permission from the Royal Society of Chemistry.

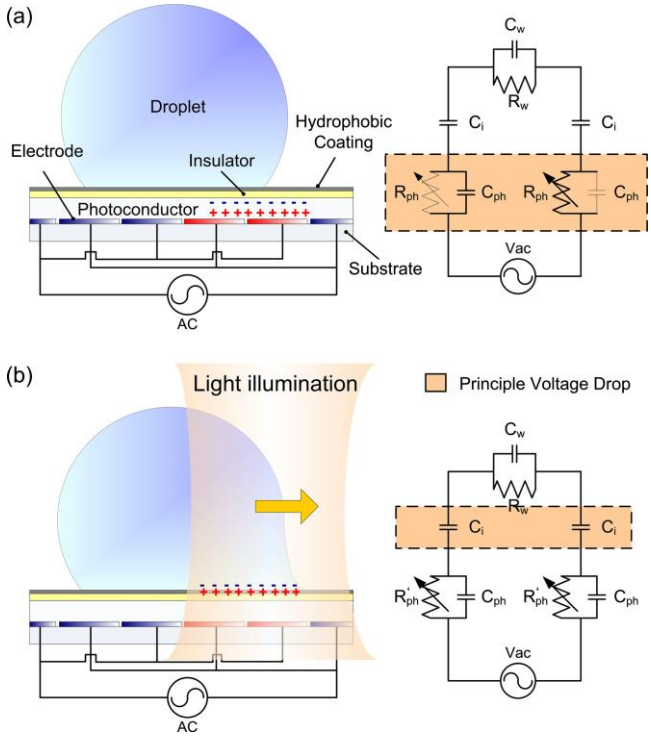

Figure 2.7: Another alternative for single-side actuation OEW (positive photoconductor). a) Right: OFF state, achieved by darkening the entire substrate; Left: equivalent electrical circuit, evidencing the major voltage drop for the OFF state. b) Right: ON state, achieved by illuminating the region where the droplet is intended to dislocate to; Left: equivalent electrical circuit, evidencing the major voltage drop for the ON state. Reprinted from [89] with the permission of AIP Publishing.

OEW allows for very low volume droplet control (down to 10 pL[88]) and even shares some of the fluidic operations enabled by EWOD, namely dispensing, splitting, multiple droplet transportation[94]. Moreover, it has been proven that micro-particles can also be transported by OEW, if embedded into the droplets[95,96]. Finally, in the last few years, OEW has been demonstrated to be highly compatible with increasingly popular modern technologies, such as 3D printing[97], flexible device fabrication techniques[93], plasmonics[98] or smartphones[97,99] (the latter have been used for very interesting studies of water quality monitoring). In comparison to EWOD, the major advantages of OEW are the elimination of complex electrode patterning and addressing, which frequently requires clean-room processing in EWOD, and an outstanding spatial addressing.

Magnetic fields are yet another viable alternative to the EWOD system for droplet motion, commonly referred to as digital magnetofluidics. Essentially, for this type of actuation, magnetic particles or fluids are embedded inside aqueous droplets, which are in turn placed on a hydrophobic substrate. A simple magnet can then be placed under said substrate, and

droplets are successfully driven by the magnetic field produced by the magnet, thus moving freely towards any desired region[100–106] (see Figure 2.8).

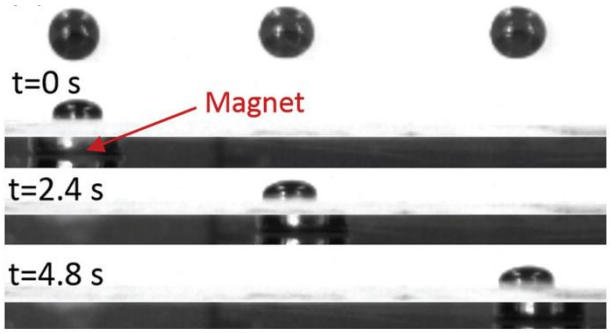

Figure 2.8: Classic setup for digital magnetofluidics, where a liquid droplet embedded with magnetic elements is placed onto a hydrophobic substrate, and can subsequently be moved by dislocating a magnet placed beneath the substrate. Reproduced from the work of Paul *et al.* [106] with permission from the Royal Society of Chemistry.

Magnetic actuation allows for controllable droplet shapes (ranging from almost perfect spheres to oblong droplets) and volumes, via combinations of substrate inclination and the strength of the applied magnetic field[106]. Furthermore, simple setups empower exceptional experimental outputs, namely the production and nanometer-precise motion of some of the smallest droplets ever reported, with volumes down to femto-liters[107]. Alternatively, the substrate itself can be modified to intervene in droplet actuation, either by enabling the coating of the droplet surface with ferrofluids and magnetic nanoparticles[108] (which are subsequently attracted towards a magnet) or by self-deforming in response to a magnetic field, forcing the droplet to move to the intended direction[109] (Figure 2.9).

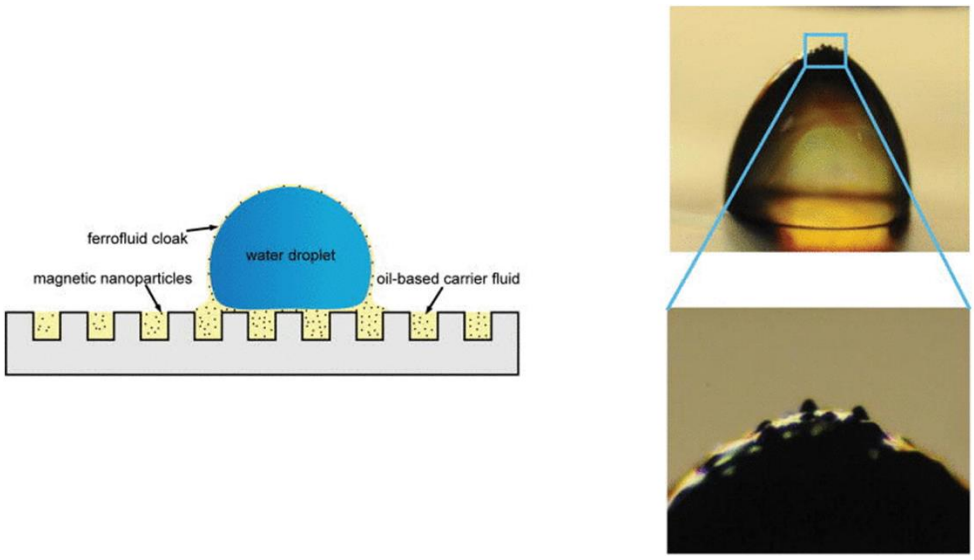

Figure 2.9: Schematic (left) and photograph (right) of water droplets coated with ferrofluid and magnetic nanopaticles present at the substrate for magnetofluidic motion. Reprinted from [108] with the permission of AIP Publishing.

Current applications of digital magnetofluidics include glucose electrochemical detection[100] and pH evaluation[103], nevertheless, droplets are able to carry magnetic elements[104–106], which may open the path for innovation in magnetic particle-dependent chemical and biological applications, such as the preparation of drug delivery or hyperthermia complexes at the micro- or nano-scale. Advantages of digital magnetofluidics include automation, low production cost, non-contact actuation, possibility of oil-free transportation, capability for moving droplets with high protein concentration and biocompatibility[102,104].

2.4 DMF devices: structure, materials and beyond

As can be deduced from the previous sections, the structure of a DMF device greatly varies according to the application intended or the droplet moving strategy. In this section, only EWOD-based DMF devices will be covered, as to avoid unnecessary and confusing arguments.

2.4.1 DMF formats: double- vs single-plate

DMF devices are broadly divided into two major categories: single-plate (or open format) and double-plate (or closed format) devices. As the names suggest, on single-plate devices, droplets move over a single substrate whereas on double-plate devices, droplets are sandwiched between two substrates. The choice of the most suited approach depends on the final

application, and each methodology has different (and relative) advantages and disadvantages (see Table 2.3).

Table 2.3: Comparison between single- and double-plate DMF approaches.

	Single-plate approach	Double-plate approach
Advantages	High droplet mixing efficiency	Prevents droplet evaporation
	Easy insertion and withdrawal of samples, on every region of the device	High-speed droplet transport
		Allows all fluidic operations: dispensing, splitting, merging, mixing and motion
Disadvantages	High evaporation rate	Lower droplet mixing efficiency; usually requires moving the resulting droplet back and forth to ensure mixing
	Lower-speed droplet transport	Harder to insert and recover samples; usually specific areas are required for this purpose
	Does not allow splitting and dispensing operations	
Suitability	Higher volume reactions (up to some micro-liters)	Low volume reactions (down to nano-liters or even pico-liters)

As mentioned before, according to the double-plate approach, droplets are sandwiched between two substrates: the top plate and the bottom plate. The bottom plate is composed of a substrate, either rigid (e.g. glass, printed circuit board) or flexible (e.g. paper, polyimide), where the electrode array is deposited. Covering the electrode array, a dielectric layer is deposited, to prevent current discharge, which in turn is coated by a hydrophobic layer, aiming to increase the contact angle of the droplet. The top plate is composed of a transparent substrate, so that droplets are visible, covered with a transparent, conductive layer to serve as the ground of the electric circuit (e.g. glass covered with Indium-Tin-Oxide). Finally, a spacer is used to separate top and bottom plates, as well as to define droplet height, and a filler medium (other than air) may be used to fill the gap between plates, such as silicone oil. The single-plate approach only includes the bottom plate, which presents the same composition as the double-plate bottom plate. However, for this second approach, the ground required for closing the circuit typically assumes one of two schemes: 1) the electrode array includes both grounded and non-grounded electrodes, sequentially or 2) the ground is assured by thin, conducting wires that pass through the droplets. Figure 2.10 represents the above-mentioned grounding techniques for both single- and double-plate DMF devices. Other methodologies have been

recently investigated[110,111], nevertheless, they surpass the scope of this work, which focuses on the double-plate configuration. Additional schemes have been reviewed elsewhere[112].

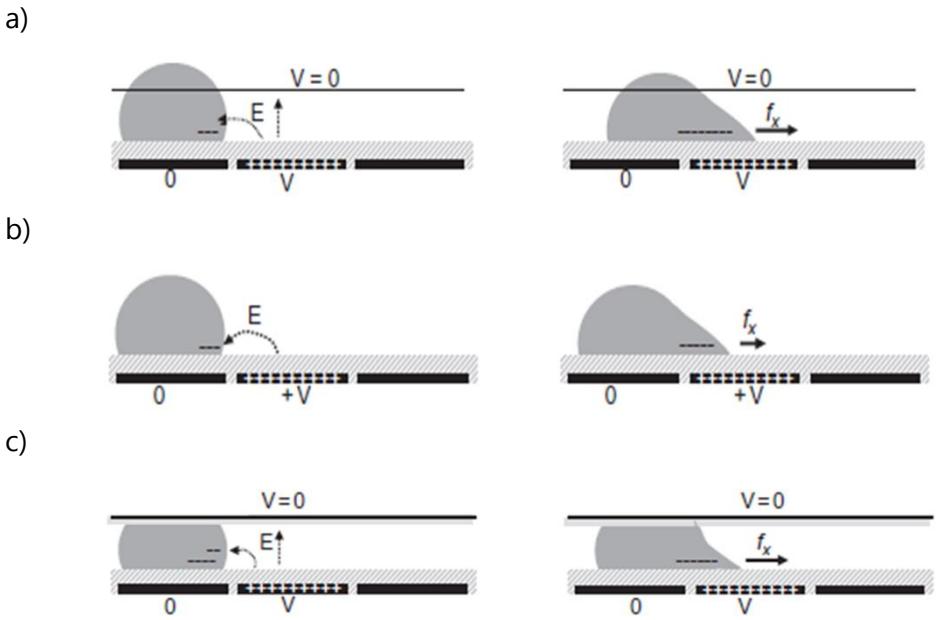

Figure 2.10: Comparison between single-plate and double-plate approaches. a) Single-plate approach, with a conductive wire as ground; b) Single-plate approach, with subsequent ground and actuator electrodes; c) Double-plate approach. Image retrieved with permission from[113], copyright Elsevier (2023).

2.4.1.1 Transporting droplets on double-plate configuration: required steps

As previously mentioned, in order to move droplets in EWOD-DMF devices, an electrical signal must be applied. Two signal types are possible: AC (alternating current) or DC (direct current). AC signals are generally preferred for several reasons: 1) AC leads to small droplet oscillations that reduce the contact line pinning, leading to less friction between the droplet and the contact surface; 2) charge injection is prevented, due to the constant shift in the direction of the electric field; 3) dielectric failure and electric fatigue are decreased and 4) for biological applications, AC signals prevent biofouling and improve in-droplet mixing[114–118]. However, regardless of the signal applied, the steps followed to move a droplet from one electrode to an adjacent one are the same: 1) first, deactivate the electrode where the droplet is standing; 2) activate the adjacent electrode, and the electric field will attract charges inside the droplet and 3) the droplet experiences a lateral force strong enough to pull it onto the adjacent, activated electrode. Figure 2.10 c) provides a good illustration of this phenomenon.

2.4.2 Actuation electrodes

Actuation electrodes are often underestimated, yet the correct electrode geometry and spacing between adjacent electrodes are fundamental to improve actuation, by increasing droplet transportation speed and reducing the required actuation voltage. Firstly, the distance separating electrodes must not be too large, or it will be extremely difficult (even impossible) to move droplets from one electrode to an adjacent one, as the electric field produced by activated electrodes will not be strong enough to attract droplets standing on deactivated electrodes; secondly, if said distance is too small, high cost and complex microfabrication processes will have to be employed, which is also undesirable. Thus, the adequate separation range has been estimated to fall between 10 μm and 30 μm[60]. Moreover, the distance between top and bottom plates, associated with the electrode geometry, will accurately define the volume of each droplet, and may be adjusted according to the intended application.

The electrode geometry has also been studied by several groups, in an attempt to further improve droplet actuation[119–130]. Let us consider the standard electrode design: a simple square. In this case, droplets will be limited by the electrode, as the gap to adjacent electrodes will have a hydrophobic nature. As such, the electric field applied by an activated electrode will have to be strong enough to surpass this hydrophobic region and attract the liquid droplet. Having this issue in mind, in the early 2000s, multiple groups developed crenellated electrodes[119,121,126–128,130], where each electrode includes small dents which occupy the area of the adjacent electrodes, in an interdigitated-like arrangement (see Figure 2.11). The idea behind this concept is to force droplets to partially occupy neighboring electrodes instead of remaining over a single electrode, meaning that when said neighboring electrodes are energized, the electric field is also partially generated directly beneath the droplet (instead of being generated next to the droplet), which considerably facilitates droplet motion from a deactivated electrode to an activated one. Multiple dent shapes have been extensively studied, namely squared, rectangular, triangular or wave-like, as well as their dimensions relatively to the remainder electrode, as to understand their effect on overall droplet motion[119,123–125,128], and novel electrode structures have been developed in recent years[120,122,129]. Unfortunately, the main drawback of crenellated electrodes is the significant complexity increase in the fabrication process, requiring higher resolution and control, which is why this work relies solely on square, non-crenellated electrodes.

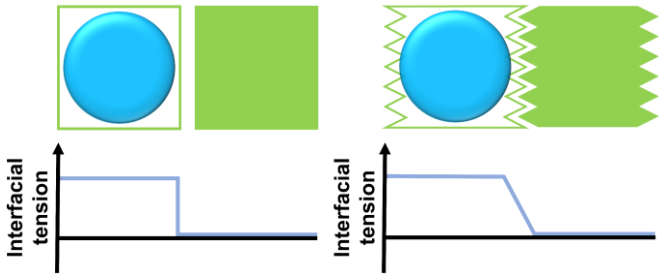

Figure 2.11: Average interfacial tension on a single droplet when it circulates over squared (left) or crenellated (right) electrode paths. Green-filled electrodes are energized whereas white-filled electrodes are not. Image adapted from [128].

The choice of the electrode material is crucial in the development of any DMF device, and several properties must be ensured: 1) good electrical conductivity; 2) strong adhesion to the substrate; 3) general coherence (the material must resist to the application of high voltage); 4) stability over time; 5) inertness towards the dielectric layer. Moreover, the electrode thickness should be adjusted to ensure good conductivity (surpass the effect of superficial imperfections and/or particle adsorption) while avoiding discontinuities during the dielectric deposition.

Depending on the selected substrate, the electrodes may be deposited through a multitude of techniques, ranging from screen-[131–134] or inkjet-printing[20,21,135,136] on flexible substrates to traditional thin film deposition techniques, such as electron-beam[17,48,137,138] or sputtering deposition[139–141]. Table 2.4 synthesizes some of the electrode materials used in EWOD-DMF devices, as well as thicknesses and deposition methods.

Table 2.4: Summary of common electrode materials used in EWOD-DMF devices, as well as respective thicknesses and deposition processes. Abbreviations and chemical symbols used: Au for gold, Cr for chromium, Ag for silver, Cu for copper, Ni for nickel, Al for aluminum, Ti for titanium, ITO for indium-tin-oxide, e-beam for electron-beam, PCB for printed circuit board, CNT for carbon nanotubes and PET for polyethylene terephthalate.

Electrode Material	Substrate	Thickness	Deposition method	Reference	Year
Au	Glass	120 nm	E-beam	[137]	2006
Au	Glass or silicon wafer	300 nm	-	[142]	2006
Au	Quartz wafer	100 nm	-	[59]	2002
CNT-based conductive ink (homemade)	Paper	≈ 800 nm	Inkjet printing	[20]	2014
Cr	Glass	200 nm	E-beam	[17]	2017
Cr	Glass	100 nm	Sputtering	[143]	2014
Cr	Glass	200 nm	-	[49]	2002
Cr	Glass	500 nm	Pre-deposited	[144]	2019
Cr/Ag	Glass	0.1/5 µm	Sputtering	[140]	2011
Cr/Au	Silicon wafer	5/300 nm	-	[145]	2006
Cr/Au	Glass	60/20 nm	E-beam	[138]	2008
Cr/Au	Glass	10/100 nm	Sputtering	[139]	2007
Cu	PCB	25 µm	Pre-deposited	[38]	2008
Cu	Glass slide	200 nm	Sputtering	[141]	2019
Cu	Flexible PCB	9 µm	Pre-deposited	[146]	2008
Cu/Ni/Au	PCB	43/185/3.6 µm	Etching	[147]	2014
ITO	Glass	300 nm	-	[148]	2020
Metalon JS-B25P silver nanoparticle ink	Novele IJ-220 inkjet printing media (PET-based)	≈ 1 µm	Inkjet printing and roll-coating	[135]	2016
Silver ink	Paper	> 500 nm	Inkjet printing	[21]	2014
Ti/AlCu	Silicon wafer	200 nm	Sputtering	[149]	2014

2.4.3 Dielectric layer

All layers composing a DMF device are relevant, however the dielectric layer is perhaps the most crucial for device functioning. As was mentioned on section 2.3.1, adding a dielectric layer between the electrodes and liquid droplets was the key to the success of EWOD-DMF, which enabled the large majority of applications requiring aqueous-based chemical or biological reactions. In this section, dielectrics in general will be discussed, as well as their role in EWOD-DMF devices.

A dielectric is essentially a non-conducting material able to store electric charges. On a molecular level, a dielectric can be characteristically seen as being composed of polar molecules (dipoles), that is, molecules which have a more negative region and a more positive region, despite being neutral overall. When no electric field is present, molecules are randomly oriented, however, when an electric field is applied, said molecules align with the direction of the field and the dielectric becomes polarized (Figure 2.12). This polarization induces opposite net surface charges, in opposite sides of the dielectric: one side becomes "positively charged" and the other "negatively charged", each of which will attract opposing charges[150,151]. Thus, even though no current passes through the dielectric material, droplets placed on top of the dielectric can still be affected by electric fields applied between an electrode and the top plate. Note that nonpolar molecules may also compose a dielectric.

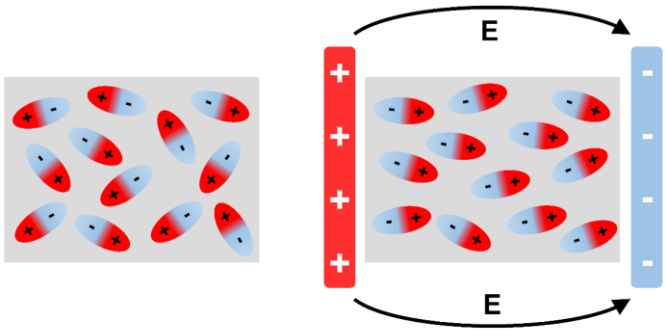

Figure 2.12: Schematic representation of a dielectric material with randomly oriented molecules (left) and polarization of the dielectric (right) in response to an external electric field (denoted as E). Image adapted from [151].

As mentioned in section 2.3.1, special attention must be given to the choice of the dielectric for a DMF device. This dielectric material should: 1) have a relatively high dielectric constant, to allow for lower voltage in droplet actuation; 2) have a high dielectric strength, as to endure the voltage required to move droplets; 3) be deposited conformally over the electrodes; 4) be stable; 5) have good adhesion to the electrodes and 6) be inert towards the electrodes

and hydrophobic layer. Table 2.5 is an increment of Table 2.2, presenting relevant properties of dielectrics used in the indicated references.

Table 2.5: Relevant properties of common dielectrics used in EWOD-DMF. Abbreviations used: ALD for atomic layer deposition; MOCVD for metal organic chemical vapor deposition; CVD for chemical vapor deposition; PECVD for plasma enhanced chemical vapor deposition; RF for radio frequency.

Dielectric material	Dielectric constant	Dielectric strength	Thickness	Deposition method	Reference	Year
Al_2O_3	3-9	4-5 MV/cm	300 nm/ 150 nm	ALD	[152,153]	2015/2013
BST	180	3 MV/cm	700 Å	MOCVD	[72]	2002
Parylene C	≈ 3	56 V/cm	Multiple	CVD	[17,37,41,42,46,49,138,139,143,153–159]	Multiple
Parylene HT	≈ 2.2	54 V/cm	50 nm 700 nm and 300 nm	CVD	[153,154]	2013/2011
PDMS	2.3-2.8	2.50-6.35 MV/cm	5 µm/ 10 µm / - /9 to 40 µm	Spin-coating	[140,141,160,161]	2011/2018/ 2019/2007
Si_3N_4	7.5	≈ 10 MV/cm	- / 500 nm 300 nm 0.15 to 0.3 µm 300 nm	PECVD	[137,149,162–164]	2012/2007 2008/2006 2014
SiO_2	3.9	≈ 10 MV/cm	1 µm/ 8 µm 100 nm/ 250 nm 100 nm/ 2 µm	Several: thermal growth, PECVD, RF-Sputtering	[35,72,132,165–167]	2002/2006 2016/2004 2010/2016
SU-8	≈ 4	4.4 MV/cm	300 nm/ 2 µm 10 µm / 1.6 µm	Spin-coating	[153,168–170]	2013/2014 2019/2015
Ta_2O_5	8-25	6 MV/cm	95 nm/ -* / Several*	Anodization, sputtering	[78,155,171]	2008/2011 2010

* For the signaled DMF devices, Ta_2O_5 was used as a dielectric, in parallel with Parylene C.

Note: the work of Schultz *et al.*[153] is an outstanding study comparing several types of dielectrics (Parylene C, Parylene HT, Al_2O_3 and SU-8) individually, as well as combinations of them for multi-layered dielectrics.

As can be seen on Table 2.5, Parylene C is by far the most widely used dielectric for EWOD-DMF. Parylene C may not have as high a dielectric constant as other dielectrics, however, it does not form a large number of pinholes, and due to the deposition process, highly developed by SCS coatings[172], it is an extremely conformable polymer, which is deposited onto the substrate at room temperature. Furthermore, Parylene C is biocompatible and resistant to water permeability, which is also a fundamental characteristic for biological applications[73,154,173]. Aiming to reduce actuation voltage, several authors have exploited different dielectrics, focusing mainly on the increase of the dielectric constant. However, due to deposition complexity or other constraints in substrate-dielectric compatibility for alternative dielectrics, Parylene C remains the first choice for EWOD users, even at the cost of a higher actuation voltage. Regarding this last aspect, it is noteworthy that EWOD-DMF devices do not consume current, due to the presence of the dielectric layer, and therefore larger actuation voltages do not mandatorily lead to high energy-consumption devices – a brilliant example of this was given by the Wheeler microfluidics group[41], that successfully implemented a portable EWOD-DMF platform for serological testing at a refugee camp in Kenya, using Parylene C as the dielectric.

2.4.4 Hydrophobic layer

The hydrophobic layer may not always be absolutely required, since some dielectrics such as Parylene already have a hydrophobic nature. Nevertheless, by adding such a layer, the droplet contact angle (without energization) is increased due to the decrease in surface energy (and droplet-surface friction) and the length of the contact line decreases (thus decreasing droplet pinning), therefore it is easier to move droplets from a deactivated to an activated electrode. Furthermore, if droplets are aqueous, a hydrophobic layer also acts as a barrier for water infiltration. Several hydrophobic materials are available for this layer, however Teflon® (or PTFE - polytetrafluoroethylene) is by far the most widely used, being a classic choice for increasing surface hydrophobicity in a variety of industries. Beyond Teflon®, other commercially available solutions have recently been proposed for DMF, such as Cytop®[42,152,162,171,174], Fluoro-Pel®[41,135,141], NeverWet®[175], Rain-X®[133,176],Nevosil® or Avam[177]. Superhydrophobic surfaces have also been achieved[178–182] by precise patterning of the surface in contact with droplets, yet the cost associated to this approach is very high, as well as the processing complexity.

In the case of biology-related applications, the role of the hydrophobic layer increases exponentially, since the risk of biofouling is much higher in such cases, and may hinder not only droplet motion, but also any reactions to be performed on-device. Biofouling essentially refers to the non-specific adhesion of biomolecules (e.g. proteins) to a specific surface[19,183].

This phenomenon is especially harmful for device operation, since the accumulation of biomolecules can lead to droplet pinning (thus hindering droplet motion) or even cross-contamination, not to mention that the electric field required for EWOD can increase said adhesion, interacting with biomolecular poles[183]. Proteins are particularly prone to adhere to hydrophobic layers, such as those required for EWOD-DMF devices, and special care should be taken when handling these biological elements – a very interesting and complete study of protein adsorption was performed by Rabe *et al.*[184]. The use of silicone oil as filler medium is one of the main strategies used in DMF for preventing biofouling, since said oil will create an encapsulation film, standing between the biofouling-prone droplet and the hydrophobic layer. Silicone oil also improves droplet movability, as it decreases friction between droplet and top/bottom plates.

2.4.5 Filler medium

In early EWOD and DMF studies, droplets were usually surrounded by air. Nevertheless, several issues arose, namely evaporation, biofouling and high operating voltages, therefore, to reduce said problems, an oil medium was added to the devices, similarly to the protocol followed in early low-volume tube PCR. Oil addition was first reported by Pollack and co-workers[49], who placed said oil between top and bottom plates in a double plate device, and later studies led to the creation of core-shell droplet structures, where liquid droplets are encapsulated by an oil shell, and can be moved in an air medium, while still preventing evaporation[185,186].

Several fillers are used in DMF devices (commonly silicone oil[16,17,37,43,155], light mineral oil[187,188] or hydrocarbons[38,152,159]), depending on the final application. For instance, proteins have the tendency for biofouling, and using oil as filler medium helps to prevent this phenomenon, as previously reported. Nevertheless, for high protein concentrations, oil is ineffective against biofouling, and additional strategies must be applied. One of the strategies employed to solve such problem consisted in loading the droplets themselves with compounds that prevent the phenomenon, typically Pluronic additives, as to decrease their surface tension[138,189–191]. Luk *et al.*[138] published a very interesting study on mixing Pluronic additives with droplets, in a low concentration, as an effective way to prevent biofouling in droplets bearing high protein concentration to be moved on DMF devices, and Ng[189] further studied optimal conditions of said additives for immunoassays and cell culture. In addition to high protein concentration and/or cell-based applications, oil alternatives may be required if oil-miscible elements are necessary on-chip, or if direct contact between the liquid droplet and the top layers is aimed

for[35,138,189]. Finally, for applications which require reagent dehydration, such as protein isolation, oil is also advised against[189].

2.5 DMF platforms

2.5.1 Control systems and user interfaces: home-made vs Industry-made

All DMF devices require a dedicated control system in order to function. Such system generally includes a signal generator (either DC or AC) connected to a signal amplifier (DMF voltages are usually high, sometimes reaching a few hundred volts) and a driving module (usually mediated by Arduino controllers), which receives instructions from a computer user interface and accordingly disperses the amplified signal to the assigned electrodes on the device. With the increase in popularity of DMF, several institutions or even mere enthusiasts have developed their own control systems, either for commercialization or in open-source format. One of the earliest control platforms was developed at the University of Toronto: DropBot[192]. DropBot is essentially a "black box" for driving DMF electrodes, which allows not only specific electrode driving according to instructions given to a Python-based user interface, but also impedance feedback, which is used to check droplet position and also to measure droplet velocity. Feedback systems are of utter relevance in DMF platforms and a key element for the laboratory automation revolution, since they will allow for true automation, providing information to the driving system on whether the droplet has moved or not, if splitting was successful, if all the reagents were dispensed, if droplet A merged with droplet B, if a certain detectable reaction occurred and many other possibilities. This first version of the system only included the driving module and required an external voltage amplifier, as well as a DMF device support and a camera. Furthermore, despite making all the designs public, including acrylic plates for the box, circuit board schematics and even a 3D-printable support for the DMF devices, it was still up to the researchers and hobbyists to buy all parts and assemble them. DropBot continued to evolve and is now on its third version, which is commercially available through the SciBots company[193] as part of a complete kit, the DropBot DB3-130 kit[194]. This kit includes all the necessary instrumentation for creating a DMF workstation, namely the control box itself (now equipped with a voltage amplifier), a power supply, a webcam, cables and even testing material to ensure that the system is working correctly. GaudiLabs also proposes a DMF platform, at a lower cost than the previous one, although with less functionalities: OpenDrop (now on version V3)[195]. This is a portable platform for allocating single-plate devices, which already includes all

voltage driving instrumentation. The kit contains connection cables as well as displays, audio features and small joysticks to control droplet movement with the user's finger, yet it does not include neither the hydrophobic coating nor silicone filler, which must be purchased separately. Yafia *et al.*[196] developed an extremely low-cost control platform for DMF devices, where all operations are smartphone-controlled. Taking advantage of the power and versatility of 3D printing for the external casing, and low-cost, commercially available electronic components, this platform costs approximately 62 USD (smartphone not included) and weights a mere 235 g. The smartphone is ingeniously converted into a high-resolution imaging system through the addition of a microscope lens to the embedded camera, and also acts as a user interface, sending commands to the control platform via Bluetooth™. Figure 2.13 illustrates the three examples mentioned. Digi.Bio[197] is another company that provides DMF control systems and also DMF chips, and they are currently offering their hardware and expertise to help Biotechnology and Chemistry companies to automate laboratory protocols or co-develop new products. Of course, numerous research groups working on EWOD-based DMF have developed their own setups[165,198], employing equipment and technology already existing at their respective laboratories, however, most of such setups are intended for internal use only.

a) c)

Figure 2.13: a) OpenDrop V3, from GaudiLabs[195] (copyright 2018 GaudiLabs); b) DMF control platform developed by Yafia and co-workers[196] (Creative Commons CC BY 4.0 license); c) DropBot DB3-120, from SciBots[194] (copyright 2022 SciBots).

2.5.2 Corporate DMF platforms

Thus far, only control platforms for DMF have been discussed, but even though some are commercially available, they have not been developed for a specific application, as is the case for the large majority of laboratory equipment. Nevertheless, several companies have seen the potential of the DMF technology, and have developed fully integrated platforms, ready-to-use for a number of applications. Digifluidic[199] is a Macau-based company that resorts to DMF platforms for nucleic acid analysis, aiming to achieve infectious disease detection, overall health analysis through detection of certain indicators (e.g. asthma or folic acid metabolism genes) and pathogen detection for agriculture and livestock. Their main equipment, the Virus Hunter™, is an all-purpose platform, which can receive multiple detection chips according to the final application. Also in the field of diagnostics, GenMark DX[200] has developed their own

EWOD-based system[201], the ePlex®, capable of performing all steps required from the patient sample to the final analysis result. ePlex® works with a panel system, where the same core equipment can receive multiple panels for detection of 1) common viruses and bacteria, responsible for upper respiratory infections; 2) sepsis-causing organisms in blood culture identification and 3) gastrointestinal pathogens. The system can now be integrated with a SARS-CoV-2 test, in response to the recent COVID-19 pandemic. Baebies[202] is another company focusing on diagnostic testing, specifically newborn screening. Their FDA-approved SEEKER® platform[203] enables automatic detection of Mucopolysaccharidosis Type I, Pompe, Gaucher or Fabry disease using a single droplet of blood from the newborn. This is merely an indicative summary of some of the companies currently using DMF technologies, and many others exist, either at a seed stage or at a highly developed stage[204–206], which is a very clear sign of the power and potential of this technology across a wide range of scientific and medical fields.

2.5.3 Temperature control in DMF platforms

Accurate temperature control is often a required functionality not only in DMF devices but also in other microfluidic setups, especially for biological reactions. As such, a plethora of heating strategies have been developed by research groups all around the world, ranging from simple Peltier modules or thin film resistors to complex SAW systems. Peltier modules are essentially heat pumps which resort to current to move heat from one extremity to the other, thus heating the first extremity and cooling the latter. They are also readily available in a wide range of formats and are therefore immensely popular in DMF systems[149,183,207]. Joule heating in thin metallic or semiconductor films is another extensively used technique for temperature control in DMF platforms[137,152,159,208], perhaps due to the small space occupation and the possibility of integration with high temperature coefficient materials as temperature sensors. Further alternatives include the use of PTC (positive temperature coefficients) heaters[169,209], and for isothermal amplification strategies, a simple water bath is sufficient, as was demonstrated by Fang *et al.*[210] for a disc microfluidic device. All the mentioned approaches are relatively well known, nevertheless, other research groups have developed innovative strategies to incorporate in DMF platforms. For instance, Sathyanarayanan and co-workers[211] developed a flexible and incredibly thin heater based on silver ink which was inkjet-printed onto a polyethylene terephthalate substrate. Being so thin and flexible, this heater was easily mounted under the DMF device itself, and provided localized heating, limited to the reaction area. Another revolutionary setup was achieved by Shen *et al.* [212], who placed the heating element on the top plate. This heating element was essentially composed of multiple platinum serpentine thin-

films, located directly above the regions where temperature control was required on-chip, and in order to prevent oxidation, the heating elements on the top plate were also covered by a dielectric layer (which is usually confined to the bottom plate), followed by a hydrophobic layer. Finally, an original and accurate temperature control system was developed by Sayad and co-workers[213], who resorted to a hot air gun to heat the samples in question. This approach was developed for a microfluidic disc, yet it is an interesting process to be applied on DMF systems. Nevertheless, there are numerous other possibilities for temperature control at small scales[214], undoubtedly representing innovation opportunities for further improvement of DMF devices.

2.6 DMF for nucleic acid exploitation: the last five years

As was mentioned before, DMF devices enable a wide range of applications in numerous fields of Biology and Chemistry (see sections 2.1 and 2.5). Nevertheless, considering the scope of this work, emphasis will be given to the use of DMF for nucleic acid exploitation, namely amplification.

Nucleic acid amplification refers to (quite literally) increasing the number of nucleic acid sequences from a low-concentration sample, via an amplification reaction. This allows for detection of said nucleic acid sequence, which is utterly relevant for disease diagnostics (either genetic disorders, viral infections or bacterial/fungal infections), forensic science, food safety, agricultural and livestock control, among others. The most widely used amplification reaction is the polymerase chain reaction (PCR), developed in 1986[215], whereby a thermostable enzyme resorts to available nucleotides in order to produce multiple copies of a certain sequence, delimited by two primers (forward primer and reverse primer). The reaction consists of successive repetition of three thermal steps: 1) the first step is denaturation of the target, held at 94-95°C, where target chains separate; 2) the second step is annealing, held at 40-60°C, where primers bind to the denatured chain; 3) the final step is extension, held at 70-74°C, where a new chain is synthesized[216,217]. Since the invention of this first methodology for nucleic acid amplification, several more followed, either requiring temperature cycling[218] or a single temperature[219–222].

Being an extremely versatile technology, DMF was quickly adapted to nucleic acid manipulation. Coelho *et al.*[16] present an exhaustive literature review for DMF applied to nucleic acid manipulation up to 2017, therefore this section will cover recent developments, from 2017 until the present.

Similarly to benchtop nucleic acid amplification, PCR continues to be one of the recurring amplification reactions in DMF platforms[223], however isothermal amplification procedures such

as LAMP[17,169,209] (loop-mediated isothermal amplification) or RPA[224,225] (recombinase polymerase amplification) have also been explored as viable DMF-based nucleic acid amplification strategies. Disease diagnostics through isothermal amplification methodologies has been the primary application of said DMF devices, either for cancer diagnostics[17], identification of genes conferring antibiotic resistance to pathogens[224,225] or parasite detection[169,209]. Furthermore, DMF-based manipulation of DNA has been used for pyrosequencing in the context of mutation detection[158], as well as DNA synthesis and error detection[223]. In the same time frame, another interesting study[160] revealed that resorting to liquid marbles instead of standard droplets in DMF is not only feasible, but also reduces and possibly eliminates cross-contamination. This feature would be vital for increasing specificity in nucleic acid amplification on DMF platforms, as well as decreasing the complexity of the respective electrode arrays, since contamination could be prevented without the need of single-paths for each reagent or wide separation between droplets carrying different reagents.

2.7 The next step: DMF for disease diagnostics through isothermal nucleic acid amplification

Although PCR has been the standard for nucleic acid amplification (NAA) since the invention of the technique in 1986[215], both Academia and Industry have demonstrated growing interest in isothermal amplification methodologies. Contrary to PCR, isothermal techniques do not require accurate and fast temperature cycling, therefore there is no need for costly thermocyclers – basic equipment, such as an oil bath or water bath, are enough to achieve nucleic acid amplification. Furthermore, the limit of detection (LOD), final copy number and reaction time of isothermal methodologies is comparable or even superior to those of PCR[226,227]. Such advantages are ideal for simple, low-energy consuming NAA, viable for low resource settings[219,222]. As was seen on section 2.5.3, a number of heating strategies have been fruitfully implemented on DMF platforms, ensuring stable and long-lasting temperature control, thus making DMF the ideal technology for portable, reliable and automatic NAA.

The first implementation of NAA on a DMF device was achieved in 2006 by Chang and co-workers[137]. Since then, a wide range of NAA strategies have been implemented on DMF devices, namely PCR and more importantly, isothermal strategies such as RPA[152,224,225], C2CA (circle-to-circle amplification)[143] and LAMP[17,169,209]. Among said strategies, LAMP is considered to be a highly robust, specific and sensitive technology, therefore an ideal candidate with great

potential for integration in DMF devices. LAMP was developed in 2000 by Notomi *et al.*[23], and it is essentially an isothermal NAA technique whereby a set of four primers (two inner and two outer primers) are used to recognize six different regions of a DNA chain. The other major player in LAMP is the catalyst enzyme, *Bst* polymerase, which possesses a high strand displacement activity and therefore eliminates the need of a denaturation step in the reaction. Said elements, along with stabilization agents (magnesium, betaine, buffer), enable an amplification of 10^9 times the initial copy number in just one hour, at a fixed temperature between 60 °C and 65 °C, the optimal temperature range for *Bst* enzyme activity. At the beginning of a LAMP reaction, one of the inner primers, FIP (forward inner primer), encounters its complementary DNA sequence and hybridizes to it. It is important to mention that the DNA double helix is not static, and the two chains can be briefly set apart in several regions, thus providing FIP opportunities to bind to the target sequence. After said hybridization, the enzyme proceeds to generating a complementary sequence to that beginning with FIP, while simultaneously separating the DNA duplex. Since the outer part of the FIP is not complementary to the initial DNA strand, this leaves enough room to allow for hybridization of one of the outer primers (F3) to the referred initial DNA strand. As previously, the enzyme proceeds to generating a new DNA sequence from the F3 primer, while separating the initial strand from the FIP-initiated sequence. This latter sequence is self-complementary on the FIP end (5′ end), thus forming a bell-like structure. The BIP (backward inner primer) can then freely hybridize to its complementary sequence next to the 3′ end of the FIP-initiated sequence, thus enabling the creation of yet another sequence (BIP-initiated sequence). Similarly to FIP, BIP primers are not fully complementary to the respective sequence, therefore leaving room for the other outer primer (B3) to hybridize and lead a B3-initiated sequence, while displacing the BIP-initiated sequence. This latter sequence now includes two self-complementary regions, leading to the formation of a dumbbell structure. FIP and BIP then hybridize to the bell moieties of this structure, thus proceeding to the amplification and elongation steps of the reaction, where multiple structures with several shapes and sizes will be produced, further leading to the characteristic vertical smear of LAMP amplification on an electrophoretic analysis. Figure 2.14 illustrates the above-mentioned amplification mechanism.

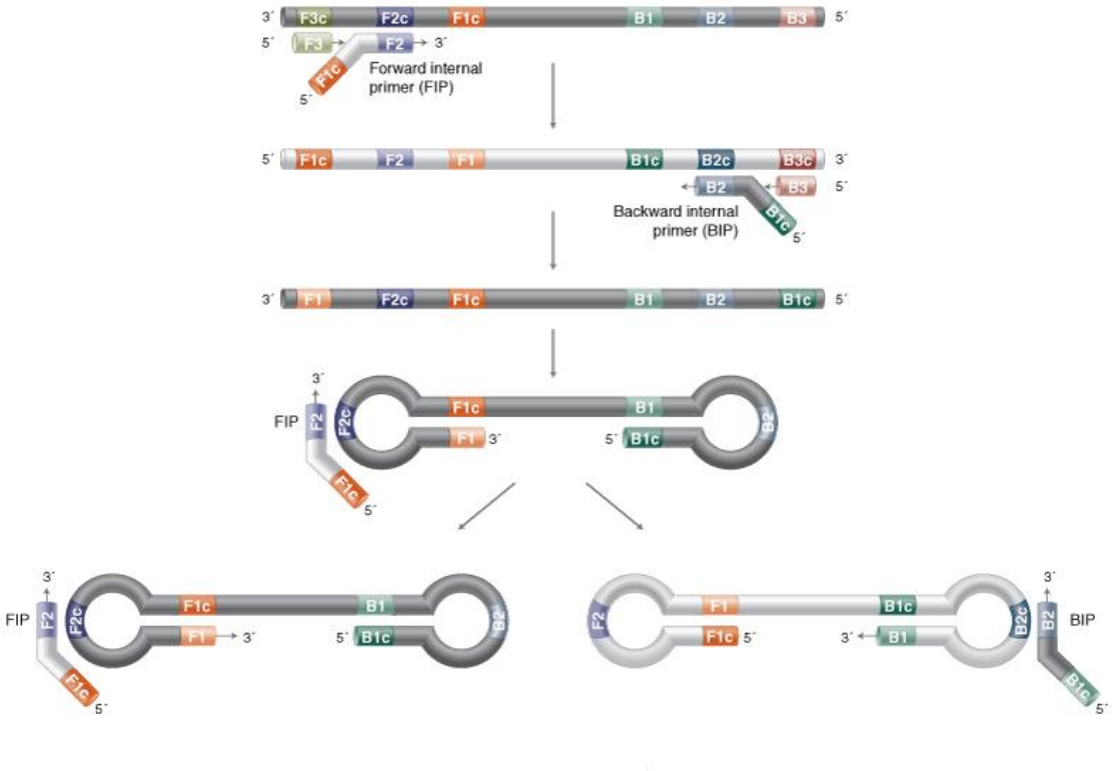

Figure 2.14: LAMP mechanism, from the beginning of the reaction until the formation of the dumbbell-like structures. Adapted from [228], copyright 2023 New England Biolabs, Inc.

Considering the robustness, specificity, sensitivity (down to a single target copy) and relatively low reaction time, this is deemed to be the perfect reaction for coupling with DMF devices and allow for automatic NAA anytime, anywhere. Furthermore, if amplification detection strategies are implemented within the DMF device, result interpretation will also be possible for anyone, with or without specific training.

Concerning target molecules, the LAMP methodology is capable of amplifying both DNA and RNA, the latter of which requires an additional reverse transcription step for successful amplification. This feature translates into the capability to detect any target based on nucleic acids, namely cancer biomarkers which may assist in early cancer detection. As previously stated, cancer biomarkers are biological molecules that signal mechanisms associated to cancer, or carcinogenesis (e.g. abnormal cell growth), and may be used for several applications such as detection of tumors, indication of tumor progression or even evaluation of treatment therapy[229]. Such biomarkers encompass proteins, enzymes, cell metabolites and nucleic acids, among others, which may be detected in a variety of biological samples such as blood, urine or saliva[230]. Considering the wide experience within the research groups associated to this PhD work, nucleic acids were the selected cancer biomarkers, and more specifically, the cancer

biomarker *c-Myc*. *c-Myc* encodes a transcription factor closely involved in cell differentiation, growth, metabolism and apoptosis. Overexpression of this oncogene has therefore been associated to abnormal cell growth and proliferation, strong indicators of tumorigenesis [27]. A multitude of cancers have been linked to this oncogene, including breast cancer, lung cancer and colorectal cancer[231–233]. Moreover, *c-Myc* overexpression is one of the hallmarks of Burkitt lymphoma, an extremely aggressive liquid cancer[234,235]. For all the previously-stated reasons, *c-Myc* was deemed a good starting point for proof-of-concept of the DMF devices produced in the scope of this work. Regarding samples, although *c-Myc* may be found in blood, it was also deemed reasonable to resort to biological instead of clinical samples, considering the relative ease of handling this gene in cellular models.

2.8 Loop-mediated isothermal amplification detection methods

Integrating LAMP into a DMF device, or any portable device, requires the adaptation of such device to detect nucleic acid amplification, in order to determine whether a given sample contains or not the target sequence. The main differentiation criterion in nucleic acid detection is continuity, that is, detection can be performed continuously throughout the reaction (in real-time) or at the end of the reaction (endpoint). The choice of detection method always depends on the application and also on available reagents and/or equipment. However, real-time detection is usually considered more advantageous, namely due to its higher sensitivity, the proportionality of fluorescence intensity regarding the number of amplicons, the absence of post-reaction processing, high resolution and possibility of automation[236–238].

Possible detection methods for LAMP include standard nucleic acid detection methodologies, namely gel electrophoresis (endpoint) or fluorescence detection (real-time), and additional methods such as turbidimetry (real-time or endpoint)[239]. In gel electrophoresis, the reaction product is placed into a polymeric matrix with a fixed-sized mesh (a gel), and a potential difference is applied between both extremities of the gel, thus forcing negatively-charged DNA to migrate from the negative potential to the positive potential. Considering that the mesh size is fixed, it is logical to conclude that smaller chains move further down the gel than larger chains, which is why this technique is commonly used for verification of chain size, by comparison with a known ladder. In fluorescence detection, on the other hand, intercalating dyes are added to the reaction master mix, which will bind to double-stranded DNA (dsDNA), as it is produced within the LAMP reaction. Said fluorescent dyes are usually quenched in the absence of dsDNA, thus producing minimal fluorescence, yet in the presence of dsDNA, the dyes'

structure is modified, and fluorescence occurs. Logically, an increase in dsDNA concentration will lead to an increase in the fluorescence signal. Similarly to dyes, molecular beacons may also be used to produce fluorescence as a result of target amplification. A molecular beacon is essentially comprised of a nucleic acid chain (complementary to a pre-determined sequence of the target chain), which is flanked by a reporter (fluorescent molecule) and a quencher. Thus, as amplification occurs, the fluorescence signal increases as a result of the binding of the beacon to the amplicons, which reduces quenching activity. Turbidimetry is another interesting methodology for target amplification monitoring, which relies on a LAMP by-product: pyrophosphates. This by-product is produced by the *Bst* polymerase enzyme during the construction of a new nucleic acid chain, and further reacts with magnesium ions present at the mix, yielding magnesium pyrophosphates (white precipitates)[240]. Equation 2.7 illustrates pyrophosphate production and Equation 2.8 elucidates the conversion of said pyrophosphates into magnesium pyrophosphates[240]:

$$(DNA)_{n-1} + dNTP \rightarrow (DNA)_n + P_2O_7^{4-} \quad (2.7)$$

$$P_2O_7^{4-} + 2Mg^{2+} \rightarrow Mg_2P_2O_7 \quad (2.8)$$

As was mentioned in section 2.1, portable devices are absolutely required in POC applications, and microfluidics is one of the main POC-enabling technologies. The first microfluidic device designed to accommodate LAMP reactions was developed by Huang and co-workers[241] in 2008, who not only achieved microfluidic-based LAMP, but also reported real-time reaction monitoring via fluorescence detection. Since this first publication, continuous flow microfluidics and other microfluidic approaches (paper microfluidics, droplet microfluidics) have constantly been upgraded and adapted[242], to allow for improved LAMP-based nucleic acid amplification, notably single copy detection[243,244] or multiplexing[245].

Novel detection methods have also been developed, such as electrochemical methods, lateral flow assays (LFA) and ELISA (enzyme-linked immunosorbent assay). The following table reports several methodologies for endpoint and real-time monitoring of LAMP reactions. As illustrated on Table 2.6, several interesting approaches have been developed to evaluate LAMP reactions. Endpoint results are particularly appealing for a yes/no response sensor, which is valuable in the context of rapid tests. When coupled to color-shifting mechanisms, endpoint methodologies become even more appealing, allowing for interpretation of the test result

without the need of any kind of equipment. Nevertheless, real-time monitoring provides more information on the profile of LAMP reactions and thus enables high-end applications such as initial copy number quantification, evaluation of gene expression or determination of viral load. Having this in mind, this PhD work will focus on real-time methods for monitoring LAMP, to be incorporated onto DMF devices. The gold standard fluorescence measuring method will be the starting point for on-chip reaction monitoring, yet other approaches will be studied such as a pH-sensitive electrochemical method and also an impedance measuring method. The fore-mentioned techniques and integration with DMF devices will be thoroughly discussed in the sections below.

Table 2.6: Brief summary of LAMP detection methods (both endpoint and real-time) and their respective characteristics. Abbreviations used: LFA for lateral flow assay, ELISA for enzyme-linked immunosorbent assay, FITC for fluorescein isothiocyanate, HNB for hydroxy naphthol blue, EBT for eriochrome black T, ssDNA for single-stranded DNA, dsDNA for double-stranded DNA, FET for field effect transistor. *Gel electrophoresis is a common method for amplification confirmation, and it is used in the large majority of references cited in this table.

Detection type	Detection method	Brief description of the technique	Advantages	Limitations	References
Endpoint	LFA	Strips containing immobilized biotin antibodies are used for binding with biotin-labelled nucleic acid chains, which have been further labelled with a fluorophore such as FITC. Other variants are possible	• Low-cost platform • Fast readout • Simple detection mechanism (naked eye) • Specific • Portable	• Requires prior double-labelling of LAMP products • May require enhancers for detection (e.g. nanoparticles)	[246–248]
	ELISA	LAMP amplicons are hybridized with a specific probe which binds to a labelled enzyme. This enzyme further reacts with a specific enzymatic substrate, leading to color changes	• Specific • Tendentially low-cost	• Usually requires specialized equipment for readout • Requires complex reagent preparation • Requires long post-LAMP incubations	[249–251]

Endpoint (cont.)	Electrophoresis	Voltage applied to a polymeric mesh induces DNA (negatively-charged) migration, depending on strand size	• Gold standard for end-point analysis • Extremely easy to perform • May be low cost, depending on agarose content per gel and efficient use of sample wells	• Requires specific equipment for readout • Unspecific to by-products such as primer dimers • Requires time for gel polymerization and further voltage run	*
	Colorimetric by pH indicator	A pH indicator such as phenol red is added to the LAMP master mix, changing color due to the pH variation during the reaction	• Simple detection mechanism (naked eye) • Portable • Does not require post-LAMP processing	• Still expensive when purchased as a kit • Unspecific	252–254
	Colorimetric by turbidity	A by-product of LAMP reactions, pyrophosphates, produce detectable white precipitates	• Resorts to a naturally-occurring phenomenon • Does not require post-LAMP processing	• Not always visible to the naked or untrained eye • May require specific equipment • Unspecific	240,255
	Ion-mediated colorimetric	Reagents are added to the LAMP master mix, which exhibit color changes due to ion concentration variations as a result of new strand production. Examples include calcein, HNB or EBT	• Low-cost • May resort to a naturally-occurring phenomenon • Does not require post-LAMP processing	• May lead to reaction inhibition • Unspecific	255–257

Endpoint (cont.)	Mediated by nanoparticles	Nanoparticles functionalized with ssDNA probes disaggregate in the presence of salt and the target DNA, leading to variations in optical properties	• Rapid • Specific • Simple post-LAMP processing • May allow for naked-eye detection	• May require specific equipment • Requires nanoparticle synthesis and proper functionalization	[258,259]
	Electrochemical based on redox reactions	Redox probes are added to LAMP products, and their respective oxidation/reduction current peaks are altered when probes bind to dsDNA	• Rapid • Low-cost	• Requires specific equipment • Unspecific	[260–262]
Real-time	Fluorescence (dyes or beacons)	DNA intercalating dyes (unspecific) or fluorescent probes (e.g. beacons, specific) are un-quenched in the presence of dsDNA, emitting fluorescence	• Gold standard for real-time monitoring • Medium-cost	• May inhibit LAMP • May be unspecific • Requires specific equipment	[263–265]
	Electrochemical based on redox reactions	Same principle as for the endpoint counterpart	• Same as for the endpoint counterpart	• Same as for endpoint counterpart	[266–268]
	Mediated by FET	pH changes occurring at a sensitive surface connected to the gate electrode produce measurable shifts on the current circulating between the drain and source electrodes	• Label-free • Compatible with industrial microfabrication	• Complex device fabrication • Unspecific • Requires specific equipment	[25,269]
	Turbidity	Same principle as for the endpoint counterpart	• Same as for the endpoint counterpart	• Same as for the endpoint counterpart	[240,270,271]

3

PROPOSED OBJECTIVES

Before stating any objectives, it is fundamental to highlight the context of this work. We are living in a data-driven world, where nations evolved towards a people-based economy, meaning that now, more than ever, services, products, and entire industries are focused on human well-being and comfort, and one major condition for said achievements is health.

Considering the previous paragraph, this PhD work aims to develop a portable platform for health monitoring, specifically based on nucleic acid amplification monitoring. The fore-mentioned platform is meant to be used by clinicians in health centres and hospitals, thus reducing dependency on central laboratories and consequently minimizing the time between collecting samples and achieving the final test result.

The main objective must be divided into sub-objectives, which constitute the several tasks of the PhD project:

- Task 1: design and development of a digital microfluidics platform allowing for nucleic acid amplification, and subsequent integration with multiple amplification detection methodologies.

- Task 2: study of several nucleic acid amplification monitoring methodologies, as well as possibilities for integration with the DMF platform (tasks 1 and 2 are intrinsically connected, as the structure of a DMF device may vary significantly according to the design adaptations required for the monitoring methodology).

- Task 3: for the most promising methodology, validation of the produced devices for isothermal nucleic acid amplification testing with biological samples to detect cancer biomarkers in real-time.

As a final task, it is vital to diffuse the results achieved in the PhD project by the scientific community, for peer validation and scientific divulgation. This task has been successfully achieved through scientific publications, as well as poster or oral presentations in both national and international conferences. Below is a listing of all major outputs from the author of this PhD thesis.

Scientific publications

Resulting from the PhD work

- Coelho, B. J.; Neto, J. P.; Sieira, B.; Moura, A. T.; Fortunato, E.; Martins, R.; Baptista, P. V.; Igreja, R.; Águas, H. *Hybrid digital-droplet microfluidic chip for dPCR applications: design, fabrication and characterization*. Sensors **2023**, 23 (10). https://doi.org/10.3390/s23104927.

- Coelho, B. J.; Pinto, J. V.; Martins, J.; Rovisco, A.; Barquinha, P.; Fortunato, E.; Martins, R.; Baptista, P. V.; Igreja, R. *Parylene C as a multipurpose material for electronics and microfluidics*. Polymers **2023**, 15 (10). https://doi.org/10.3390/polym15102277.

- Coelho, B. J.; Veigas, B.; Bettencourt, L.; Águas, H.; Fortunato, E.; Martins, R.; Baptista, P. V.; Igreja, R. *Digital Microfluidics-Powered Real-Time Monitoring of Isothermal DNA Amplification of Cancer Biomarker*. Biosensors (Basel) **2022**, 12 (4), 201. https://doi.org/10.3390/bios12040201.

- Coelho, B. J.; Veigas, B.; Bettencourt, L.; Águas, H.; Fortunato, E.; Martins, R.; Baptista, P. V.; Igreja, R. *Digital Microfluidics for Amplification Monitoring of Cancer Biomarkers*. Mater Proc **2022**, 8 (1). https://doi.org/10.3390/materproc2022008103.

- Coelho, B. J.; Pinheiro, T.; Marques, A. C.; Baptista, P. V.; Águas, H.; Igreja, R.; Martins, R.; Fortunato, E. Biossensores Com Incorporação de Microfluídica: Uma Mais-Valia No Diagnóstico Clínico. In *Novas Tecnologias da Saúde*; Fundação Amélia de Mello, Ed.; 2021.

Other publications

- Neto, J. P.; Mota, A.; Lopes, G.; Coelho, B. J.; Frazão, J.; Moura, A.; Oliveira, B.; Sieira, B.; Fernandes, J.; Fortunato, E.; Martins, R.; Igreja, R.; Baptista, P. V.; Águas, H. *Open-source tool for real-time and automated analysis of droplet-based microfluidic*. Lab Chip **2023**, 23 (14), 3238–44. https://doi.org/10.1039/D3LC00327B

- Pimentel, A.; Araújo, A.; Coelho, B. J.; Nunes, D.; Oliveira, M. J.; Mendes, M. J.; Águas, H.; Martins, R.; Fortunato, E. *3D ZnO/Ag Surface-Enhanced Raman Scattering on Disposable and Flexible Cardboard Platforms*. Materials **2017**, 10 (12), 1–19. https://doi.org/10.3390/ma10121351.

- Coelho, B. J.; Veigas, B.; Fortunato, E.; Martins, R.; Águas, H.; Igreja, R.; Baptista, P. V. *Digital Microfluidics for Nucleic Acid Amplification*. Sensors **2017**, 17 (7), 1–13. https://doi.org/10.3390/s17071495.

- Coelho, B. J.; Veigas, B.; Águas, H.; Fortunato, E.; Martins, R.; Baptista, P. V; Igreja, R. *A Digital Microfluidics Platform for Loop-Mediated Isothermal Amplification Detection*. Sensors **2017**, 17 (11), 1–11. https://doi.org/10.3390/s17112616.

Submitted

- Trêpo, I.; Pinto, J.; Santa, A.; Pareira, M.; Calmeiro, T.; Henriques, C.; Coelho, B. J.; Martins, R.; Fortunato, E.; Carey, M.; Marques, H.; Barquinha, P.; Neto, J. P. *Patterned Metal Grids for Flexible and Transparent Neural Microelectrode Arrays*. Submitted to Journal of Neural Engineering, pending editor decision.

In preparation

- I. Martins.; Figueiredo, C.; Coelho, B. J.; Rovisco, A.; Martins, J.; Barquinha, P.; Fortunato, E.; Martins, R.; Pinto, J. *Multifunctional Parylene C for conformable TFT devices.*

Scientific conferences

Oral presentations

- Coelho, B. J.; Pinto, J. V.; Martins, J.; Rovisco, A.; Barquinha, P.; Fortunato, E.; Baptista, P. V.; Martins, R.; Igreja, R. *Exploring Parylene C multi-functionality: from electronics to microfluidics*, **12th European School for Young Materials Scientists - Brno, Czech Republic** (9th to 10th November 2023).

- Coelho, B. J.; Neto, J. N.; Sieira, B.; Martins, R.; Águas, H., Baptista, P. V.; Igreja, R. *Hybrid digital-droplet microfluidics for nano-droplet generation*, **MATERIAIS 2023 - Guimarães, Portugal** (3rd to 6th April 2023).

- Coelho, B. J.; Veigas, B.; Bettencourt, L.; Águas, H.; Fortunato, E.; Martins, R.; Baptista, P. V.; Igreja, R. *Digital Microfluidics for Amplification Monitoring of Cancer Biomarkers*, **MATERIAIS 2022 - Marinha Grande, Portugal** (10th to 13th April 2022).

- Coelho, B. J.; Veigas, B.; Águas, H.; Fortunato, E.; Martins, R.; Baptista, P. V. & Igreja, R. *Digital Microfluidics for isothermal DNA amplification – closing in on automated multiplexing for cancer diagnostics*, **MATERIAIS 2019 – Lisbon, Portugal** (14th to 17th April 2019).

- Coelho, B. J. & Marques, A. C. *Introduction to Biosensors for Schools*, **III EU Conference of RM@Schools 3.0 – Bologna, Italy** (8th November 2018).

- Coelho, B. J.; Veigas, B.; Águas, H.; Fortunato, E.; Martins, R.; Baptista, P. V. & Igreja, R. *A Digital Microfluidics Platform for Loop-mediated Isothermal Amplification of DNA*, **Junior EUROMAT 2018 – Budapest, Hungary** (8th to 12th July 2018).

Poster presentations

- Coelho, B. J.; Veigas, B.; Bettencourt, L.; Águas, H.; Fortunato, E.; Martins, R.; Baptista, P. V.; Igreja, R. *Digital Microfluidics for Amplification Monitoring of Cancer Biomarkers*, **MATERIAIS 2022 - Marinha Grande, Portugal** (10th to 13th April 2022).

- Coelho, B. J.; Veigas, B.; Águas, H.; Fortunato, E.; Martins, R.; Baptista, P. V. & Igreja, R. *New Generation of Digital Microfluidics for Nucleic Acid Amplification*, **Encontro Ciência '20 – Online event, Portugal** (2nd to 4th November 2020).

- Coelho, B. J.; Veigas, B.; Águas, H.; Fortunato, E.; Martins, R.; Baptista, P. V. & Igreja, R. *Digital Microfluidics Devices for Nucleic Acid Amplification*, **Biosensors 2018 – Miami, USA** (12th to 15th June 2018).

- Coelho, B. J.; Veigas, B.; Águas, H.; Fortunato, E.; Martins, R.; Baptista, P. V. & Igreja, R. *Digital Microfluidics Sensing Devices*, **MNE 2017 – Braga, Portugal** (18th to 22nd September 2017).

Regular attendance (without poster or oral presentation)

- 2023 British-Iberian Bioelectronics Workshop (BIBio-e) - Lisbon, Portugal (17th February 2023).

- *Encontro Ciência 2022* – Lisbon, Portugal (16th to 18th May 2022).

- NOVA Science Day 2020 – Online, Portugal (22nd September 2020).

- *JORNADAS 2019* VII Annual Meeting – Aveiro, Portugal (14th December 2019).

- NOVA Science Day 2019 – Lisbon, Portugal (18th September 2019).

- NOVA Science Day 2018 – Lisbon, Portugal (10th September 2018).

- EurASc 2017 - Symposium: The Future in Science in the 21st Century: Science and Technology for the better future of Humankind – Lisbon, Portugal (26th and 27th October 2017).

Seminars presented by the author of this thesis

- Capacitive biosensors, electrowetting and digital microfluidics, presented at *Dia dos Bionanomateriais* – Caparica, Portugal (annual seminar, presented from 2017 to 2022).
- Digital microfluidics for DNA analysis, presented at BioSeminars@UCIBIO – Online, Portugal (17th February 2021).

Courses and Schools

- Project Management II course from NOVA Doctoral School - Online, Portugal (6th June to 18th July 2022).
- Project Management course from NOVA Doctoral School – Online, Portugal (4th October to 8th November 2021).
- Data Processing Automation course from NOVA Doctoral School – Lisbon, Portugal (23rd November to 7th December 2019).
- Theme school "Microfluidics 19" – Sète, France (13th to 18th October 2019).
- Research Skills Development course from NOVA Doctoral School – Setúbal, Portugal (9th to 12th July 2019).
- TCM-NET School on Materials for Flexible Electronics, Smart Surfaces and Sensing – Lisbon, Portugal (14th April 2019).
- Design Thinking course from NOVA Doctoral School – Lisbon, Portugal (10th to 17th November 2018).
- 4th ELBYSIER (Electronics for the Beyond Silicon Era) International Intensive Course in Nanoelectronics and Graphene Technologies – Caparica, Portugal (9th to 13th October 2017).

Scientific research projects

- dPCR4FreeDNA, Integrated Microfluidic Device for cancer detection from free circulating DNA using Digital PCR – financed by *Fundação para a Ciência e Tecnologia*, with reference PTDC/BTM-SAL/31201/2017.

Academic awards

- Best Oral Contribution at the 12th European School for Young Materials Scientists - Brno, Czech Republic (9th to 10th November 2023).
- Best Poster Award at the MATERIAIS 2022 conference - Marinha Grande, Portugal (10th to 13th April 2022).
- Most Innovative Project at the PrintoCent Innofest – Oulu, Finland (7th and 8th June 2018).

4

MATERIALS AND METHODS

Disclaimer

Some excerpts of this section have been published in the following publications:

Coelho, B. J.; Veigas, B.; Bettencourt, L.; Águas, H.; Fortunato, E.; Martins, R.; Baptista, P. V.; Igreja, R. *Digital Microfluidics-Powered Real-Time Monitoring of Isothermal DNA Amplification of Cancer Biomarker*. Biosensors (Basel) **2022**, 12 (4), 201. https://doi.org/10.3390/bios12040201.

Coelho, B. J.; Veigas, B.; Bettencourt, L.; Águas, H.; Fortunato, E.; Martins, R.; Baptista, P. V.; Igreja, R. *Digital Microfluidics for Amplification Monitoring of Cancer Biomarkers*. Mater Proc **2022**, 8 (1). https://doi.org/10.3390/materproc2022008103.

Coelho, B. J.; Neto, J. P.; Sieira, B.; Moura, A. T.; Fortunato, E.; Martins, R.; Baptista, P. V.; Igreja, R.; Águas, H. *Hybrid digital-droplet microfluidic chip for dPCR applications: design, fabrication and characterization*. Sensors **2023**, 23 (10). https://doi.org/10.3390/s23104927.

Coelho, B. J.; Pinto, J. V.; Martins, J.; Rovisco, A.; Barquinha, P.; Fortunato, E.; Martins, R.; Baptista, P. V.; Igreja, R. *Parylene C as a multipurpose material for electronics and microfluidics*. Polymers **2023**, 15 (10). https://doi.org/10.3390/polym15102277.

B. J. Coelho performed all the fabrication and characterization featuring the equipment described herein. She was also responsible for the optimization of all processes.

Throughout this PhD work, several structures were designed and produced, therefore multiple materials and methods were resorted to. This section, therefore, aims at exploring common techniques used in this work, and in light of fabrication variability, all experimental details for the different structures are described in each chapter. Even though some fabrication methods and conditions are common to multiple structures, for clarity and improved readability, the specific details are always mentioned in appropriate sections within chapters.

The LAMP reaction is, of course, a key method in this PhD work, however, the reaction was already discussed in sections 2.7 and 2.8, therefore it is not presented in this section. The reaction parameters vary according to the experimental assays, and all details are provided at the appropriate sections within each chapter. As previously stated, this strategy aims at improving clarity and readability of this thesis.

4.1 Fabrication methods

4.1.1 Electron beam

The electron beam (e-beam) deposition method is a physical vapor deposition (PVD) technique whereby a beam of electrons bombards a source material target, leading to the evaporation of the source material.

Briefly, an electron beam is first produced, typically by thermionic emission, which produces electrons through a filament heated to high temperatures by a high current supply. The resulting electron beam is accelerated and deflected by magnetic steering poles towards the crucible, which contains the material to be evaporated (evaporant)[272]. The electron beam bombards the evaporant, leading to localized heating of this material, and subsequent evaporation. The evaporated material is then deposited onto the substrate located above the crucible[273]. The evaporation rate can then be adjusted by the current passing through the filament, and of course, different materials will require different evaporation currents. The evaporation chamber remains under a high vacuum during the deposition, to avoid contamination of the substrate and to increase the mean free path of evaporated material[274]. Figure 4.1 illustrates the components within the deposition chamber.

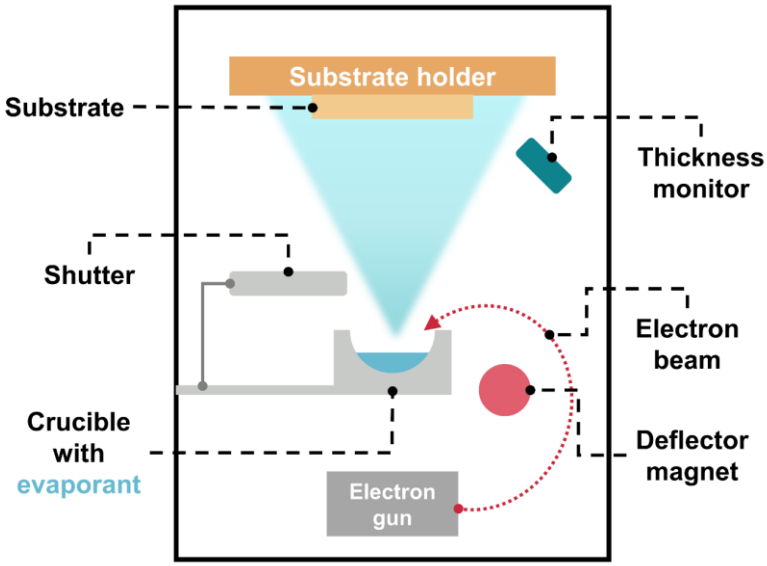

Figure 4.1: Schematic illustration of an electron beam deposition chamber, evidencing all the main components. Electrons produced by the electron gun create an electron beam, which is deflected towards the crucible containing the evaporant. This material then evaporates and is deposited on the substrate, as well as surrounding areas. The blue cone represents the path of the evaporated material until reaching the substrate holder. Image not to scale.

Throughout this PhD work, e-beam deposition was the method of choice for depositing electrodes, namely comprised of chromium. For all such depositions, a typical thickness of 200 nm was deposited, achieved with substrate heating at 100 °C and a low deposition rate. The deposition rate was always kept at a maximum of 0.05 nm/s, and the pressure within the deposition chamber was always kept under 0.9×10^{-7} mbar. Such conditions allowed for the deposition of conductive chromium thin films, with optimal adhesion to glass substrates. The choice of e-beam deposition over other deposition techniques (such as sputtering) is due to the higher number of substrates that may be loaded on the deposition chamber.

4.1.2 Parylene C deposition

The deposition technique used for Parylene C is based on the Gorham CVD method, first described in 1966[275]. The method is comprised of three steps performed in three inter-connected chambers, under a low vacuum. Briefly, the Parylene C precursor (dimer) is vaporized at the vaporizer, forming a dimeric gas. This gas is further pyrolyzed at an even higher temperature in the furnace, reducing to the monomeric form and finally, this gas enters the deposition chamber, which is at room temperature. In the deposition chamber, monomers bind to each other and form the final polymer on all available surfaces[276]. Since Parylene C tends to deposit on any cold surface, a cold trap is placed before the vacuum pump used to reduce the pressure

within the deposition chamber, effectively protecting the components of the pump. Within the deposition chamber, substrates are placed on a rotating holder that continuously rotates during the deposition process. Considering that the gas arrives at the deposition chamber from a single entrance (unilaterally), rotating the substrate holder ensures a homogenous deposition on the substrates. Figure 4.2 illustrates the components of a Parylene C deposition system.

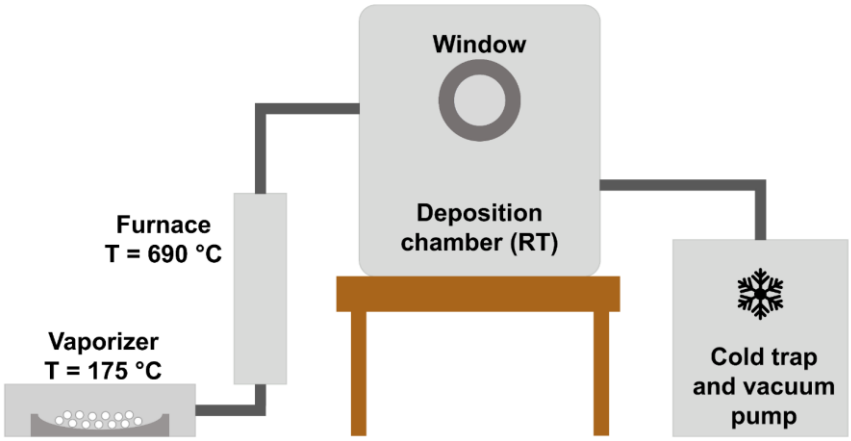

Figure 4.2: Schematic illustration of the Parylene C deposition system. The dimer is placed within the vaporizer (white dots) on an aluminum receptacle and is then vaporized. After suffering pyrolysis at the furnace, the gas enters the deposition chamber (at room temperature - RT) and polymerizes onto the substrate and chamber walls. A cold trap is placed before the vacuum pump to avoid Parylene deposition inside the pump. Image not to scale.

This process produces pure and conformal coatings, considering that the polymer is formed solely from its dimeric form, and the deposition is gas-mediated. The film thickness is defined uniquely by the initial dimer mass, thus requiring previous calibration.

All Parylene C depositions within this PhD work were performed using a Labcoater®-PDS 2010 from Specialty Coating Systems (SCS - Indianapolis, IN, USA), with constant temperatures of 175 °C and 690 °C for the vaporizer and the furnace, respectively, and with pressure at approximately 10 mTorr. The dimer was also purchased from SCS (CAS 28804-46-8). Moreover, to improve the adhesion of Parylene C to the glass substrates, an adhesion promoter (Silane A 174 from Merck KGaA, Darmstadt, Germany) was brushed on the deposition chamber with a standard acrylic paint brush. Silane promotes adhesion by creating covalent bonds between Parylene C radicals and the glass (as well as other materials)[277,278].

4.1.3 Photolithography

Photolithography is the gold standard technology for the definition of micro- and nano-features. Firstly, a photo-sensitive resin (photoresist) is used to cover the substrates. This resist

may be of positive or negative nature, meaning that the areas exposed to light (typically UV) will be weakened or strengthened, respectively. To select the areas exposed to UV light, photomasks are used, which contain transparent and black regions that will transmit or block the radiation. Such photomasks will therefore contain the pattern to be transmitted onto the resist. Before exposure, pre-baking may be performed to the substrate coated with photoresist, to improve adhesion to the substrate. Exposure to UV light follows, and a soft-baking step is required to evaporate the remaining solvent of the resist, and only after this baking step will the pattern be revealed. In the case of positive resist, the areas exposed to light are weakened, and after immersion into a developer bath, the weakened resist will be lifted from the substrate. In the case of negative resist, the contrary phenomenon will occur. The developing process is interrupted after immersion in ultrapure water, and the final pattern will be achieved[279].

For this PhD work, photolithography for electrode pattern definition was always used with positive resin and negative masks (masks where the metallic paths are transparent and the remaining area is black). The exact photolithographic conditions varied according to the structure in question, therefore the specific details will be described in appropriate sections within the chapters of this thesis. However, the positive resist employed was always AZ ECI 3012 1.2 µm grade photoresist from MicroChemicals (Ulm, Germany). Moreover, the development processes for this resist were performed with a bath of AZ726 MIF developer, also from MicroChemicals. For the fabrication of droplet microfluidic devices, SU-8 2150 resin was used, from MicroChem, recently acquired by Kayaku Advanced Materials (Westborough, MA, USA). All exposure protocols were performed with a Suss MA6 UV mask aligner (Suss MicroTec SE, Garching, Germany).

4.1.4 Spin-coating

Spin-coating is a widely used technique for the deposition of thin films, in the range of nano- to micrometers, without requiring a high vacuum. A common spin-coating setup includes a deposition chamber with a central holding place, connected to a vacuum pump located below the deposition chamber. The technique involves dispensing a liquid onto a substrate held by vacuum, which is then rotated at high speed, around an axis perpendicular to the substrate. The centrifugal force generated by this rotation leads to the spreading of the liquid over the substrate and often results in some degree of evaporation of the liquid[280]. Advantages of the technology include simplicity of use, uniformity of the thin film, thickness control, and low-cost operation. Typically, two spinning steps are required for spin-coating: one spinning step at a lower speed, for spreading the liquid over the substrate and another

spinning step at a higher speed and for a longer period of time, for defining the final thickness of the film. A post-baking step is also commonly performed, to evaporate the remaining solvent. The final properties of the thin film depend on deposition parameters such as spinning speed, acceleration, and time, as well as properties of the liquid, namely surface tension, viscosity, or drying rate[281].

In this work, spin-coating was frequently used, particularly in photolithography processes for coating glass substrates with photosensitive resins (photoresist or SU-8) and in coating the DMF devices with the hydrophobic PTFE-based layer. In the case of spin-coating, operation parameters were always constant for each process. In photolithography for DMF electrode patterning, the positive resist was deposited on glass substrates (cover about 90% of the surface), and spin-coated at 2000 rpm for 10 s and 4000 rpm for 20 s. The resist used for this purpose was deposited by spin-coating with a Suss Labspin6 from Suss MicroTec SE (Garching, Germany). If the photolithographic process relied on SU-8 resin, spin-coating occurred at 500 rpm for 7 s and 3260 rpm for 30 s, performed with a Suss CT62, also from Suss MicroTec SE. Lastly, for deposition of the hydrophobic layer in DMF devices, spin-coating was performed at 1000 rpm for 30 s, yet with a slow acceleration ramp where speed was increased by 100 rpm every second. This spin-coating process was performed with a WS-650MZ-23NPP spin-coater from Laurell (North Wales, PA, USA).

4.1.5 Sputtering

Sputtering is a PVD technique whereby a target composed of the material to be deposited is bombarded by ions, leading to atom release from the target, which will be deposited onto the substrate. Briefly, the process occurs within a deposition chamber placed under a high vacuum, where the target is located at the bottom of the chamber, directly opposite from the substrate. In the case of plasma sputtering (used in this PhD work), plasma of an inert gas is produced, leading to the generation of charged particles, namely ions, by employing a high electric field produced between the substrate (anode) and the target (cathode). Typically, Argon plasma is used due to its high van der Waals radius and relatively low cost, and Ar^+ ions are generated. The produced ions are then accelerated towards the target, also assisted by the electric field. By colliding with the target, the energized ions release atoms from the said target, which are further deposited onto the substrate, producing a uniform, conformal and dense thin film[273,282–284]. In this work, the RF (radio-frequency) sputtering variant was used, whereby an AC electric field is applied to the cathode. This allows for the deposition of dielectric materials such as Ta_2O_5, preventing charge buildup on the target. Moreover, in conjunction with RF,

the magnetron configuration was used, which relies on magnets placed behind the target to create a magnetic field close to said target, thus improving the plasma efficiency[283]. Figure 4.3 depicts a sputtering deposition chamber.

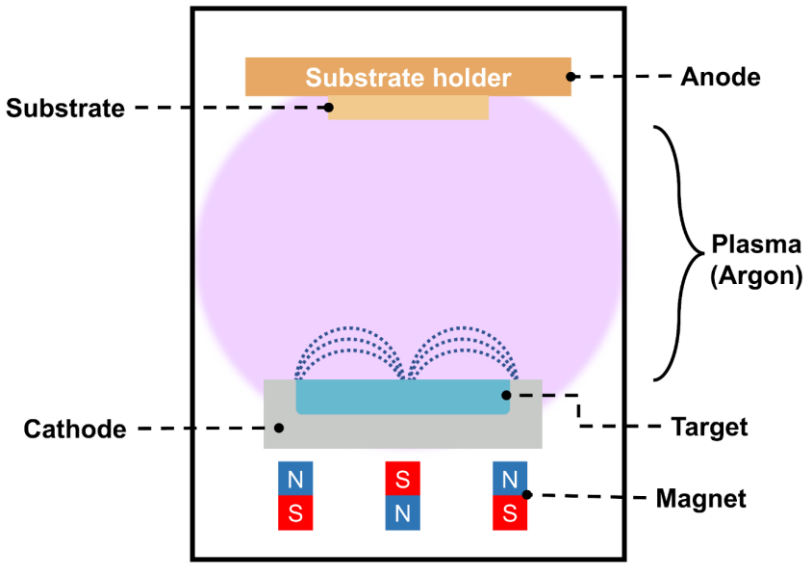

Figure 4.3: Illustration of a magnetron sputtering system. Plasma (lilac) from an inert gas is generated within the deposition chamber under vacuum, by the application of a strong electric field between anode and cathode. The target is thus bombarded with highly energized ions, which effectively remove material from the target. An additional magnetic field (dotted lines) is created by magnets close to the target, increasing the bombarding efficiency. Image not to scale.

In this PhD work, RF magnetron sputtering was used to deposit IGZO and Ta_2O_5, under conditions previously optimized[285]. The IGZO semiconductor was deposited by radio frequency magnetron sputtering (AJA ATC-1300F system by AJA International Inc., North Scituate, MA, USA) from a multicomponent ceramic target of IGZO (Indium:Gallium:Zinc Oxide in the proportion of 2:1:2 mol) and Ta_2O_5 was also deposited by radio frequency magnetron sputtering (same equipment), from a ceramic target of Ta_2O_5.

4.2 Characterization techniques

4.2.1 Electrochemical Impedance Spectroscopy

Electrochemical impedance spectroscopy (EIS) is a common methodology for measuring the impedance of a certain material or device over a range of frequencies. An AC signal with a small amplitude is applied to the material/device, and the resulting response is recorded. In this work, EIS was always performed by a potentiostat (Gamry Reference 600 from Gamry Instruments, Philadelphia, PA, USA). The potentiostat includes a total of four probes: working,

counter, working sense and reference electrodes. The working and counter electrodes handle current, while the working sense and reference electrodes handle voltage. In the context of this work, a two-probe configuration was used considering the structure of a DMF device, which will always include an actuated electrode and a ground electrode. Thus, the working and working sense probes were connected, as well as the reference and counter electrodes[286–288].

Within this PhD work, two subsets of EIS were used for device testing: potentiostatic EIS and Mott-Schottky EIS. The potentiostatic EIS allows for impedance measurement for a determined frequency range – this configuration was used to measure impedance with interdigitated electrodes. The Mott-Schottky EIS configuration allows for impedance measurement at a fixed frequency, for a range of DC voltages superimposed on the AC excitation signal. This configuration was used for metal-insulator-semiconductor and electrolyte-insulator-semiconductor device analysis. In this particular case, capacitance was the target property to be measured, thus the Echem Analyst software (also from Gamry) was used to determine the capacitance from the measured impedance.

4.2.2 Semiconductor parameter analyzer

A semiconductor parameter analyzer allows for evaluation of current and voltage of a wide range of materials, namely semiconductors, insulators or conductors. A single piece of equipment enables measurement of a plethora of parameters including current, voltage, capacitance, resistance or inductance[289].

In this work, a B1500A semiconductor parameter analyzer + Cascade Microtech EPS 150 manual probe station (Keysight, Santa Rosa, CA, USA) was used to perform capacitance and current measurements over a voltage range, to characterize metal-insulator-metal structures.

4.2.3 X-ray diffraction

X-Ray diffraction (XRD) is a non-destructive characterization technology for chemical and structural analysis. A typical XRD setup includes an X-ray source, a mobile stage where the sample is placed, and a detector. Briefly, X-rays are emitted toward the sample and suffer diffraction (their wavelength is of the same order of magnitude as the spacing within crystal planes) according to the structural properties of said sample. The diffracted radiation is then captured by the detector. According to the crystal planes present in the sample, the detector will receive diffracted X-rays forming different angles with the stage. As the stage and the

detector rotate, constructive interference between diffracted X-rays may occur, generating an intensity peak. This constructive interference may be predicted by the law of Bragg:

$$n\lambda = 2d \sin\theta \tag{4.1}$$

Where n is the diffraction order, λ is the X-ray wavelength, d is the distance between atomic planes and θ is the angle of X-ray incidence.

Such intensity peaks are used to identify the crystal planes of the material, and consequently, identify the structure of the material and the composition of the material[290].

In this work, an MPD X'Pert PRO powder diffractometer from PANalytical (Royston, UK), with a Cu Kα radiation source (λ = 1.540598 Å) and equipped with a 1D X'Celerator detector was used to assess the structure of Parylene C when exposed to different heating conditions. The XRD measurements were performed in the range of 10° to 65° (2θ) in the Bragg-Brentano configuration, with a scanning step size of 0.05° in 2θ.

4.2.4 Optical microscope (with fluorescence capability)

Fluorescence detection is one of the techniques employed for monitoring LAMP reactions. In this case, a standard optical microscope was used (model BX51 from Olympus, Tokyo, Japan), adapted for fluorescence detection, and equipped with a U-MWB2 wideband blue fluorescence filter cube, also from Olympus. Fluorescence microscopy is a technology that allows for the detection of fluorescence-emitting elements, or fluorophores – in this case, the EvaGreen® fluorophore. Briefly, radiation emitted by a light source is filtered by the excitation filter (here, a band-pass filter for the blue region of light) and directed toward the sample by the dichroic mirror. The excited sample emits radiation (in this case, in the green region of light) which passes through the dichroic mirror and is further filtered by the emission filter before reaching the detector of the microscope[291] (Figure 4.4).

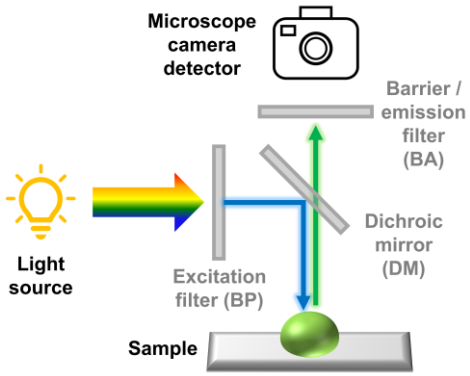

Figure 4.4: Schematic representation of the anatomy of a fluorescence microscope, evidencing all major filter components and radiation paths.

On a molecular level, if the sample is irradiated by the appropriate wavelength (i.e. photons with the appropriate energy), electrons will move from their ground state to an excited state, a process known as excitation. Once in the excited state, electrons will tendentially return to lower energy states, resulting in energy loss. Such loss may occur in various forms, namely energy dissipation through heat or energy decay through photon emission, leading to fluorescence. Non-radiative energy emission processes lead to electron energy decay to the lowest excited energy state, and further energy decay to a non-excited state results in the loss of a photon, thus fluorescence emission. Considering that photon emission is not the only process involved in the energy decay down to the ground state, the emitted photons will have lower energy (higher wavelengths) than the excitation photons – this is known as the Stokes shift[291,292].

In this work, fluorescence microscopy was used to monitor LAMP reactions within DMF devices, through the addition of a DNA-intercalating dye on the master mix, EvaGreen®. This dye was specifically engineered to fluoresce through binding to DNA chains, therefore the fluorescence intensity is proportional to the amount of DNA present in the sample.

4.2.5 Lock-in amplifier

The lock-in amplifier is one of the key elements in the impedance measuring system developed herein. Essentially, this equipment allows for measurement of a target signal (amplitude and phase), efficiently eliminating surrounding noise. The lock-in amplifier receives an input signal, i.e. the overall signal to be measured from the device under test (target signal and noise), and a reference signal, which should present a frequency behavior similar to the target

signal. The lock-in will then "lock" the reference signal, determine its frequency, and will further separate signals with a frequency similar to the reference frequency, from the remaining components of the input signal[293,294]. During signal processing, the input signal is commonly amplified, hence the term "amplifier".

In this PhD work, the lock-in amplifier is used for impedimetric measurements, as previously stated, considering the excellent measurement accuracy of the device in noisy environments. For such measurements, the voltage signal applied to the DMF electrodes includes the sum of two components, namely an actuation signal with 5 kHz and a measuring signal at another frequency. The reference signal is set with the measuring signal component. In this way, the measuring signal may be optimized to the best frequency for extracting the impedance of the droplet under test, while the droplet itself may be actuated at the best frequency for droplet motion or fixation in place (with some influence of the measuring signal). The SR830 DSP lock-in amplifier was used for such measurements, from Stanford Research Systems (Sunnyvale, CA, USA).

4.2.6 Contact profilometry

Contact profilometry is a widely used technique for accessing the topography of a thin film. This technique relies on a stylus that contacts the substrate to be measured with a predetermined force. A calibration step is commonly required, to identify the smoothest surface on the sample, which will be used as a baseline for height measurements. The tip will then move along the substrate, dislocating up- or downwards according to the presence of higher or lower planes, respectively. The displacement on X and Z axis is recorded by the profilometer and the corresponding profile is generated. For 3D measurements, several X-Z measurements may be performed for a range of distances in the Y axis, with a predetermined step. The conjunction of all the recorded X-Z measurements will result in a complete 3D profile of the substrate. Advantages of this technique include high vertical resolution, low cost, simplicity of use and adaptability to different surfaces. The greatest disadvantages of contact profilometry are the lower lateral resolution (limited by the size of the stylus tip) and the possibility of thin film degradation due to the use of higher-than-necessary stylus force or due to the soft nature of films[295].

In this PhD work, contact profilometry was the standard method for confirming film thicknesses, namely the metallic layers (e.g. chromium electrodes in DMF or interdigitated electrodes) and dielectric layers (e.g. Parylene C or tantalum pentoxide). An Ambios XP-Plus 200 Stylus was used for all measurements (Ambios Technology Inc, USA).

4.2.7 Contact angle measurement by drop shape analysis

Contact angle measurement is a qualitative methodology for evaluating the hydrophobicity (or hydrophilicity) of a surface, also known as the wettability of the surface. Briefly, whenever an interface between a solid surface and a liquid exists (in a gaseous medium), the angle defined between the surface and the liquid is named contact angle[296,297]. One possible method to determine such an angle is the drop shape analysis in sessile drop configuration[298]. With this method, a drop (in this case, of pure water) with a pre-determined volume is dispensed onto the solid surface, and the image of both droplet and contact surface is captured by a camera operating in a monochromatic regime. The contour of the droplet is assessed by the analysis software through the high contrast between the black droplet and the light background, and the contact line between the droplet and the surface is also identified (baseline). Lastly, the contact angle is determined [296–298]. Traditionally, a surface is considered wettable if the contact angle is below 90° and non-wettable if the contact angle is above 90°. The contact angle was previously explored in the section 2.3.

In this PhD work, contact angle measurement by drop shape analysis was used to determine the level of hydrophobicity of the Parylene C dielectric layer and the PTFE-based hydrophobic layer used in DMF devices, as well as the PDMS from droplet microfluidic devices. For this purpose, an OCA15plus contact angle measurement equipment was used, from Dataphysics (Filderstadt, Germany). An example of the interface of the equipment is shown in Figure 4.5.

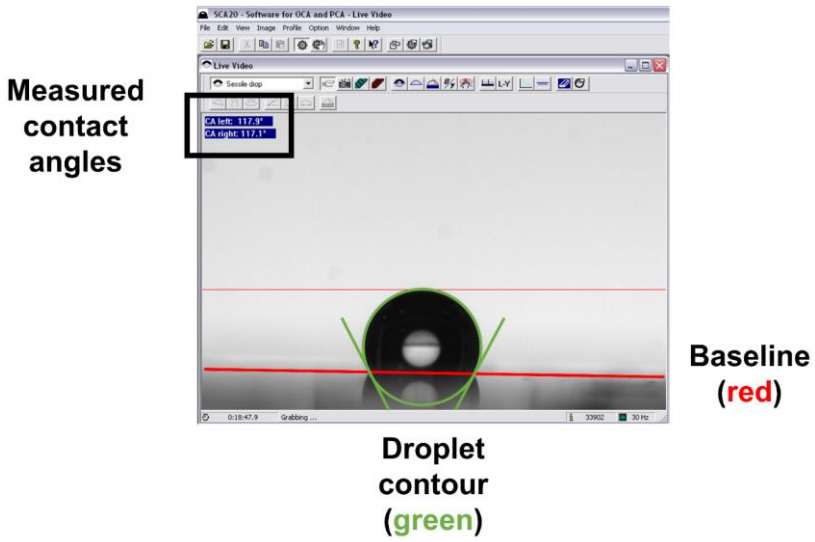

Figure 4.5: User interface from the OCA15plus contact angle measurement software, for contact angle measurement by the sessile drop method. The software identifies the baseline (line dividing the droplet and the substrate) as well as the contours of the droplet, and uses this information to further determine left and right contact angles.

4.2.8 Gel electrophoresis and gel imaging

Gel electrophoresis is a standard methodology in Molecular Biology with a wide range of applications such as nucleic acid purification or quantification. However, herein, the major focus will be endpoint analysis of nucleic acid amplification products, through agarose gel electrophoresis. The first step in agarose gel electrophoresis is the preparation of the gel itself, which involves heat-dissolving agarose powder in an appropriate solvent, in this case, TAE (Tris-Acetate-Ethylenediaminetetraacetic acid) buffer. The final concentration typically varies between 1% and 2% weight/volume. The solution solidifies at room temperature, creating a gel with an approximately fixed-sized mesh. An electrophoresis comb is added to one end of the gel during the solidification process, to create wells to accommodate samples.

As it is widely known, nucleotides are negatively charged at the phosphate groups, meaning that nucleic acid structures will also present a net negative charge (considering pH ≥ 7). Therefore, the electrophoresis process occurs by placing the agarose gel loaded with the sample in a casting tray connected to a voltage source. By applying a potential difference between the two ends of the casting tray, nucleic acids loaded onto the gel will migrate from the negative pole towards the positive pole. Smaller nucleic acid chains thus migrate faster than larger chains through the mesh pores, creating a migration pattern which may be compared to a reference ladder. The ladder is simply a reference solution comprised of several chains with known size, or base-pair (bp) number. Nucleic acid samples are often loaded with loading

buffer, which contains dyes that facilitate monitoring of the migration through the gel, and also include density agents to allow sample deposition on the bottom of the gel wells. Figure 4.6 illustrates a typical electrophoresis setup. After running the gel, imaging is required to evaluate the migration patterns. For this purpose, the agarose solution is typically mixed with a UV-sensitive dye that binds to nucleic acid chains. When subjected to UV radiation in a gel imaging system, the dye will emit fluorescence which is captured by the detector of the imaging system[299,300].

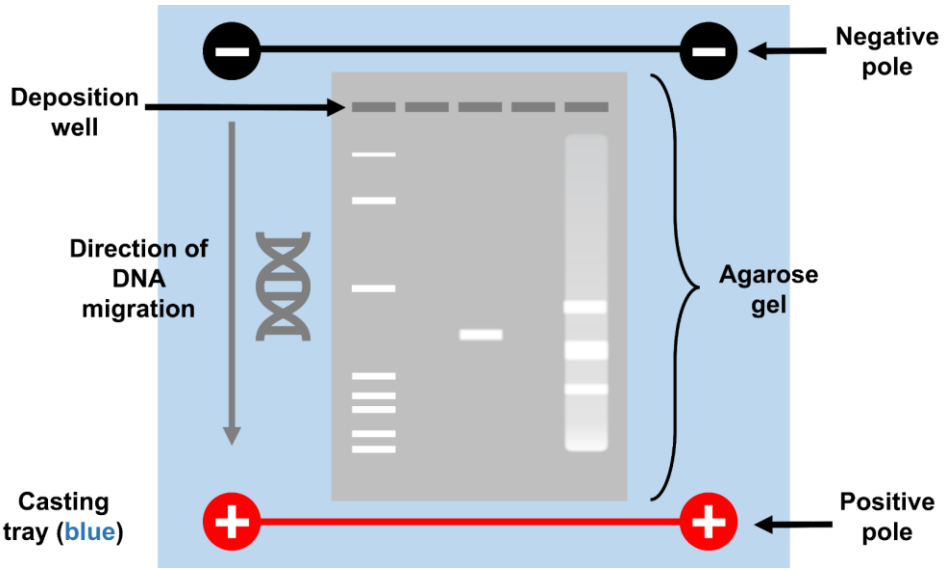

Figure 4.6: Illustration of a gel electrophoresis system. The agarose gel containing all samples (one per well) is subjected to a potential difference created between the negative and positive poles. Negatively-charged nucleic acids (e.g. DNA) migrate towards the positive pole, with smaller chains migrating faster than larger chains. The example gel contains a total of 5 lanes. The left lane presents an example of a DNA ladder, the middle lane presents an example of a PCR product band, and the right lane presents an example of a LAMP product band*. Image not to scale.

In this PhD work, gel electrophoresis was always used to confirm amplification or non-amplification for all LAMP reactions, performed on- or off-chip. For this purpose, 1% agarose gels (0.5 g of agarose dissolved into 50 mL of Tris-Acetate-EDTA) were prepared and loaded with a mix of 1 µL of each LAMP reaction product and 3 µL of gel loading dye. All gels were submitted to 70 V for 80 minutes, to ensure a good band separation. Horizontal electrophoresis systems were used, connected to a PowerPac™ basic power supply (both from BioRad, Hercules, CA, USA). Gel imaging was performed by a GelDoc™ EZ imaging system, also from BioRad.

* The LAMP band is essentially a smear due to the variety of shapes and sizes of the amplicons. However, within the smear, some brighter bands are often identified, corresponding to the most common amplicons – these are typically unique to the reaction target.

LAMP products present a wide variety of shapes and sizes (unlike single-sized PCR products) therefore the migration profile will form a full-length smear on the corresponding gel lanes.

4.2.9 Scanning electron microscopy

Scanning electron microscopy (SEM) relies on the detection of electrons instead of photons (as in common optical microscopy), which enables sample analysis at a nanometric scale. The wavelength of light is greater than that of electrons, therefore a higher resolution is obtained. SEM covers several applications, namely topographical surface analysis, chemical composition analysis or crystalline structure analysis. In this work, SEM is only used for topographical surface analysis, which will be the focus of this section.

A typical scanning electron microscope setup includes an electron gun, an anode and a set of coils and electromagnetic lenses (condenser and objective lenses), all of which are under vacuum. The electron gun produces highly energetic electrons which are accelerated by an anode, generating an electron beam directed towards the sample. The beam then passes through the condenser lens, which converges the electron beam and then through the objective lens, which focuses the beam onto the sample. The coils are used to deflect the electron beam towards different locations on the sample. The interaction of the electron beam with the sample results in several phenomena, and the most important for topographical analysis is the emission of secondary electrons (SE). SE are lower energy electrons that are emitted as a result of a collision with an incident electron from the electron beam. Since the emission of SE occurs only near the surface of the sample (lower energy results in a lower mean free path), they provide the highest resolution in SEM imaging. A specific detector (usually an Everhart–Thornley detector) is used to detect secondary electrons and further produce an image of the surface of the sample.

In this PhD work, SEM was used for imaging a cross section of the bottom plate of a DMF device. Considering that Parylene C is a soft polymer, DMF bottom plates were submerged in liquid nitrogen (a Teflon® beaker was used as vessel) and further broken through light pressure on the walls of the beaker. The pieces containing sections perpendicular to electrode paths (smaller than electrodes or reservoirs) were selected for SEM imaging, to enable individual visualization of all layers. Moreover, considering that the top layers of the bottom plates are not conductive, a thin coating of 15 nm of iridium was deposited before placing the sample on the SEM chamber.

5

DMF PLATFORM DEVELOPMENT

Disclaimer

Some excerpts of this section have been published in the following publications:

Coelho, B. J.; Veigas, B.; Bettencourt, L.; Águas, H.; Fortunato, E.; Martins, R.; Baptista, P. V.; Igreja, R. *Digital Microfluidics-Powered Real-Time Monitoring of Isothermal DNA Amplification of Cancer Biomarker*. Biosensors (Basel) **2022**, 12 (4), 201. https://doi.org/10.3390/bios12040201.

Coelho, B. J.; Veigas, B.; Bettencourt, L.; Águas, H.; Fortunato, E.; Martins, R.; Baptista, P. V.; Igreja, R. *Digital Microfluidics for Amplification Monitoring of Cancer Biomarkers*. Mater Proc **2022**, 8 (1). https://doi.org/10.3390/materproc2022008103.

Coelho, B. J.; Pinto, J. V.; Martins, J.; Rovisco, A.; Barquinha, P.; Fortunato, E.; Martins, R.; Baptista, P. V.; Igreja, R. *Parylene C as a multipurpose material for electronics and microfluidics*. Polymers **2023**, 15 (10). https://doi.org/10.3390/polym15102277.

B. J. Coelho designed and fabricated all the digital microfluidic devices, and supervised and contributed to the design of the support platform for the devices. She further designed, simulated, fabricated, tested and optimized the temperature control system, in terms of proportional–integral–derivative parameters, current/voltage supplied to the heating element and wire connections. Moreover, she supervised and contributed to the creation of the droplet control software, as well as the Arduino script used for the temperature control system. Lastly, she designed, fabricated, optimized and characterized all devices required for the study of the dielectric layer.

The basis of this PhD work is the DMF platform, which includes the DMF device (top and bottom plates, with all the required thin film layers), the DMF support system (i.e. the physical support needed to allocate the DMF devices and external connections), the droplet driving circuit and the user-interface software enabling droplet driving control. Such components are closely inter-dependent and must be carefully designed to fit the requirements of each detection method. It is also convenient to rely on easily adaptable fabrication technologies for all components, allowing minimum effort in adjusting any features, as demanded by the progression of the project.

5.1 DMF electrode architecture and device fabrication

5.1.1 Electrode architecture and intended purpose

The dominating element in the development of the DMF platform is the bottom plate electrode architecture, which will dictate the possibilities for droplet operation and consequently, dictate the on-device protocols. Thus, the starting point for the electrode pattern is the LAMP reaction itself. Standard DNA amplification strategies require a minimum of two test samples, typically a positive control, which contains the amplification reagents and the target DNA; and a negative control, which contains only the amplification reagents. The first control provides a verification of whether the reaction is functional, whereas the latter provides a verification of whether the amplification reagents are clean (i.e. no contamination with the target DNA occurred). Having such prerequisites in mind, a new electrode architecture was developed, allowing for two simultaneous reactions with no inter-crossing between droplets (to avoid contamination), as well as enough space for back-and-forth mixing. The proposed device is divided into seven large reservoirs, inter-connected by an array of nineteen smaller electrodes (see Figure 5.1). Communication with the droplet driving system was also a concern, therefore rectangular contact pads were developed to enable an easy fit of the DMF device onto PCB (printed circuit board) edge connectors. Lastly, it would be desirable for the device to allow straightforward reagent insertion and also withdrawal, as to transfer reaction products to a redundant amplification control methodology, gel electrophoresis. To address this issue, holes were drilled on the top plate, partially overlapping relevant reservoirs. Figure 5.1 illustrates top and bottom plates for the proposed DMF device, separated by a polyimide tape spacer.

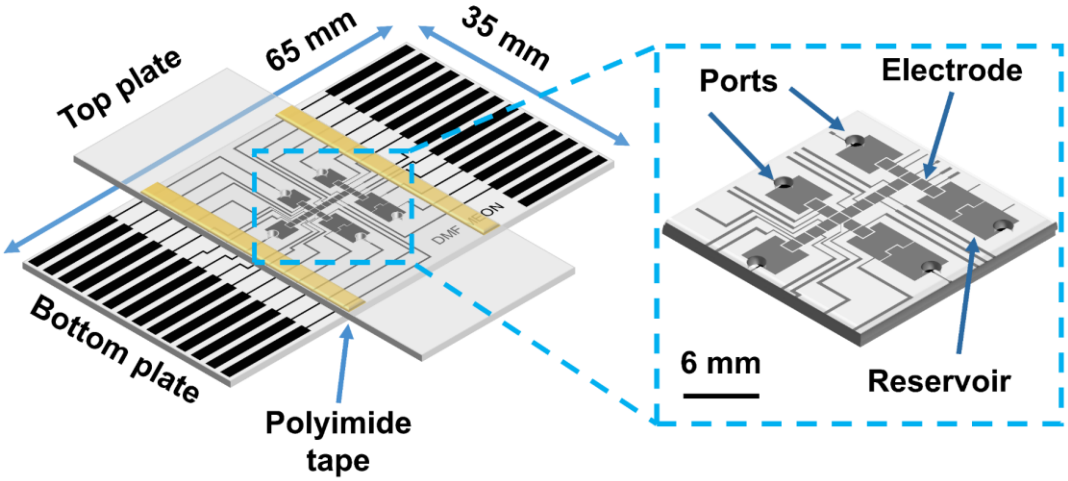

Figure 5.1: Proposed DMF device layout, consisting of seven larger reservoirs, connected by nineteen electrodes. The inset shows a zoom of the electrode and reservoir area.

With the design represented in Figure 5.1, the three top reservoirs aim to receive the LAMP reagents (master mix), as well as the two control samples: a DNA solution containing the target *c-Myc* gene fragment for the positive control and LAMP reaction buffer for the negative control (Figure 5.2 a)). It is noteworthy to state that the DNA solution consists of the *c-Myc* fragment resuspended in reaction buffer instead of water, since the reaction buffer is more conductive and therefore easier to move than pure water: 3.56 mS/cm for the 1x buffer solution vs 31.5 µS/cm for pure water as measured by the HI 98312 multi-parameter analyzer (Hanna Instruments, Woonsocket, RI, USA) and the Elix Advantage 5 pure water dispenser (Merck KGaA, Darmstadt, Germany), respectively. The intended on-device LAMP protocol is as follows: 1) the LAMP master mix is divided into two partitions, which are then moved towards the reaction areas, and one small droplet is dispensed from both the 1x reaction buffer and the DNA solution (Figure 5.2 b)). Said small droplets are merged with the LAMP master mix partitions at the reaction areas and mixing is performed (Figure 5.2 c) and d)). The device is then subjected to heating, to perform the LAMP reaction, and DNA detection is performed according to the chosen detection method.

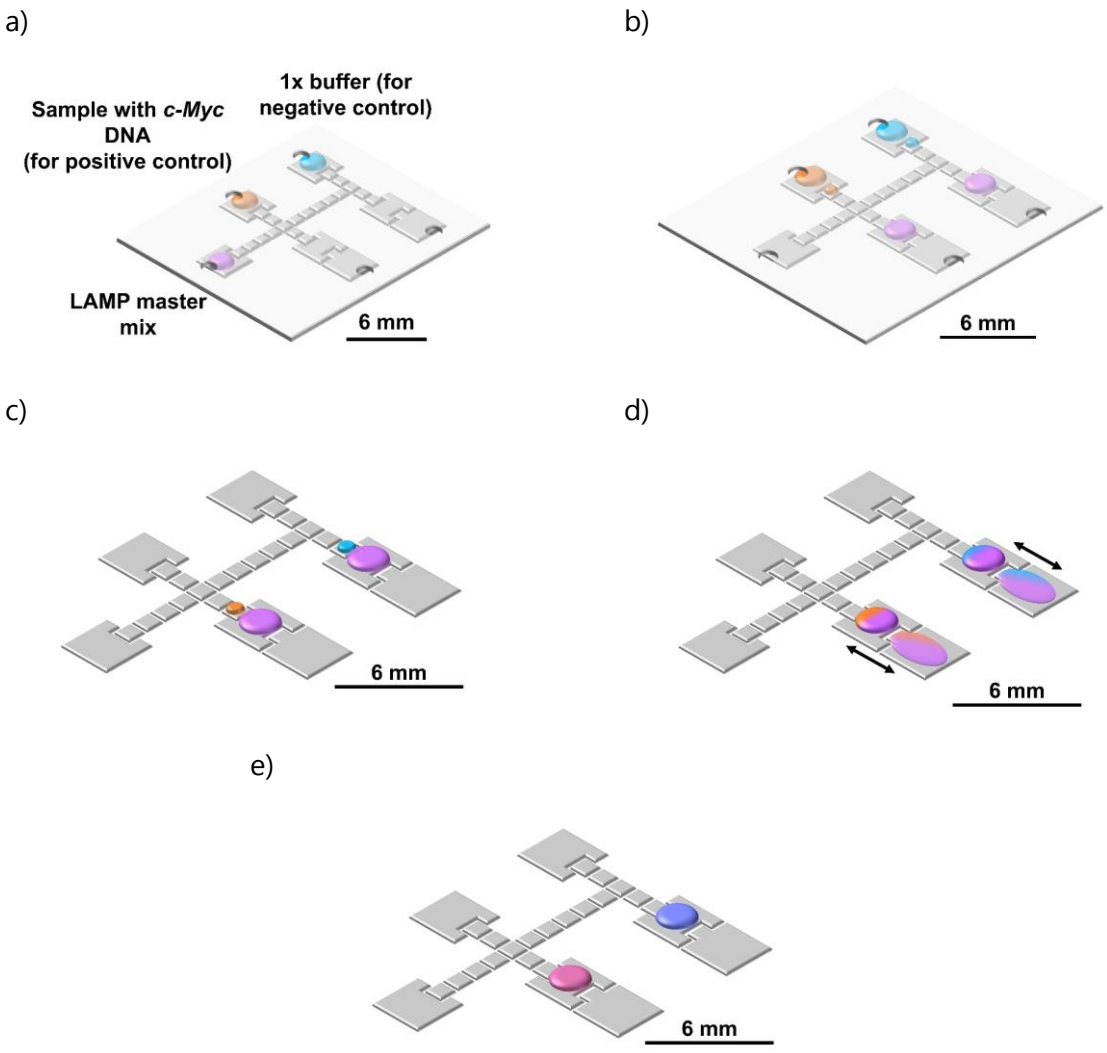

Figure 5.2: Steps required for on-device LAMP amplification of sample DNA. Firstly, droplets containing the LAMP master mix are withdrawn from the left reservoir and moved towards the reaction areas (a-c). Secondly, small droplets containing the sample DNA solution (for the positive control) and reaction buffer (for the negative control) are withdrawn from their respective reservoirs and mixed with the LAMP master mix (d-e). Finally, the DMF chip is heated for LAMP to occur. Note that the top plate was omitted from c) to e) for better visualization.

5.1.2 DMF device fabrication

The first step in device fabrication is the design of the photomask pattern, with the electrodes, reservoirs and connection lines represented in Figure 5.1 (bottom plate). The pattern was designed using the Adobe Illustrator® software (Adobe Inc., San José, CA, USA) and transferred onto film photomasks by JD Photodata (Hitchin, UK) for photolithography. For device fabrication, common dishwashing detergent (an outstanding surfactant) was used to gently rub glass substrates, which were then rinsed in ultrapure water and blow-dried with a nitrogen jet. Substrates were then cleaned with acetone and isopropyl alcohol baths under ultra-sound

for 15 min each, rinsed with ultrapure water and blow-dried with a nitrogen jet. Heating at 180 °C followed, to ensure evaporation of any water molecules on the surface, and after brief cooldown, substrates were coated with AZ ECI 3012 1.2 µm grade photoresist by spin-coating at 2000 rpm for 10 s, followed by 4000 rpm for 20 s. Pre-baking was then performed at 115 °C for 75 s. Exposure was carried out under UV radiation on a Suss MA6 UV mask aligner for 8 s. Following exposure, substrates were post-baked at 115 °C for 35 s and further developed in AZ726 MIF developer, also for 35 s. Afterwards, a 200 nm chromium layer was deposited via a home-made electron beam deposition system (substrate heating at 100 °C), and the final conductor patterns were achieved after lift-off with acetone.

For the dielectric layer, a 2 µm layer of Parylene C was deposited over the chromium pattern. This deposition was performed either in a single- or double-layered format, according to the intended applications. For single-layered devices, the Parylene C dimer mass was adjusted to achieve a 2 µm thickness, and to improve adhesion to the substrate, 6 drops (dispensed with a common dropper) of adhesion promoter (silane) were brushed on the deposition chamber with a standard acrylic paint brush. For double-layered Parylene C devices, two 1 µm layers were deposited sequentially, for pinhole reduction. Prior to each deposition, 3 drops of adhesion promoter were brushed on the deposition chamber.

Lastly, for the hydrophobic layer, a solution of 0.6% wt/wt of PTFE (polytetrafluoroethylene) AF 1600 in Fluorinert™ FC-40, (both from Merck KGaA, Darmstadt, Germany) was spin-coated over the dielectric at 1000 rpm for 30 s to achieve a 50 nm thickness, and post-baked at 160 °C for 10 min. For the top plates, ITO(Indium-Tin-Oxide)-coated glass was used, and was also covered by a PTFE-based hydrophobic layer, through the same process described above.

The 180 µm gap between top and bottom plates was set by polyimide tape (Pro-Power Farnell, Leeds, UK), and both plates were sealed together by simply using nail polish, dried at 55 °C for 10 min. Since the nail polish was placed around the reservoirs, this layer also isolates the central area of the chip.

5.2 DMF support platform

The DMF chips require a support platform, i.e., the physical structure that will accommodate the DMF devices and enable reactions to occur and be monitored. Considering that the purpose of this PhD project is to create a DMF platform suited for multiple strategies in nucleic acid amplification monitoring, the support platform must be extremely versatile and rely on fabrication methods allowing for swift feature adaptation, when necessary. Thus, 3D printing

was the chosen fabrication technology, and the final support system (Figure 5.3) consists of two major parts: the cover and the base. The base is further subdivided into three components: 1) ground connector, 2) ground connector base, 3) thin film resistor support; 4) PCB and outer connection support.

a)

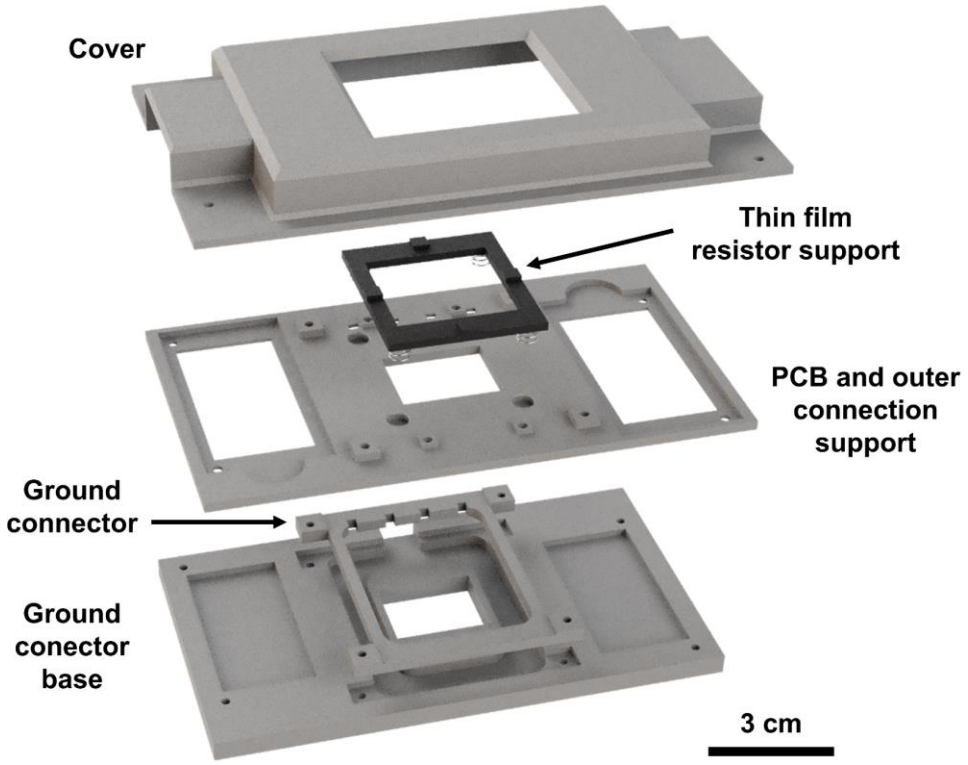

b)

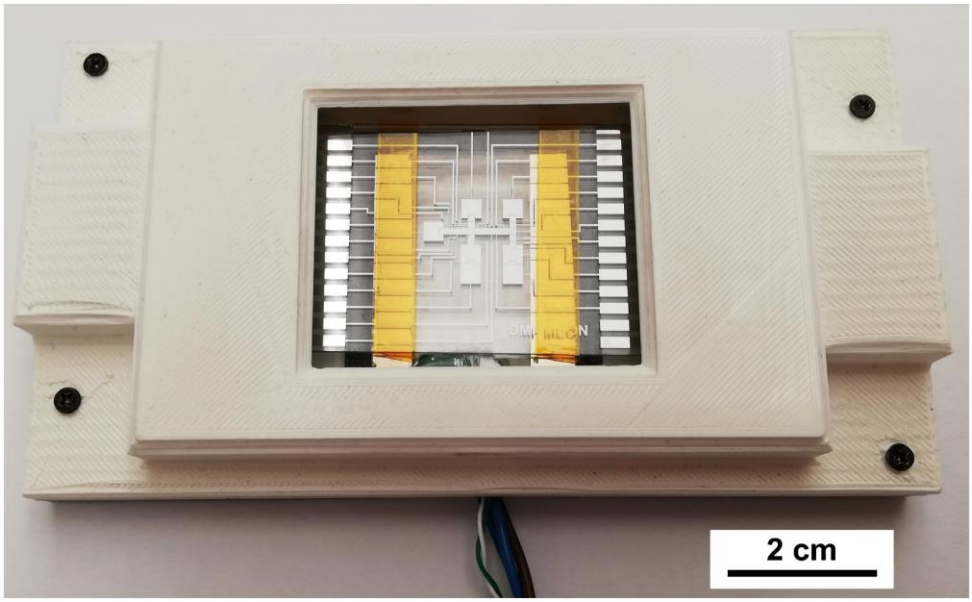

Figure 5.3: a) 3D model of the support system for DMF chips, evidencing all separate components, by fitting order. b) Photograph of the assembled DMF support system, integrated with the DMF device. Note that the top plate of the DMF device was omitted for better visualization.

The purpose of the ground connector is essentially to short-circuit all the conductive pogo pins providing electrical contact with the ITO layer from the top plate (Figure 5.3 a) and

Figure 5.4), and also to connect the fore-mentioned elements to the ground. The ground connector base simply provides a casing for wire protection and fixation, while maintaining a flat, straight foundation for the entire platform. Considering that the nucleic acid amplification assay requires heating (in this case, via a thin film resistor), a physical support was specifically designed to hold the heater and keep it as close to the DMF chip as possible, while providing an air gap to dissipate heat beneath the heater, thus protecting the integrity of surrounding materials. Finally, the PCB and outer connection support is yet another separate piece, which includes room to incorporate a specially designed PCB that allows connection between the DMF chip (through 2 PCB edgecard connectors – 28 contacts, 2.54 mm pitch; Weald Electronics, Horsham, UK) and the driving hardware (through 2 PCB connectors – 16 contacts, 2.54 mm pitch, male; Harting, Espelkamp, Germany). This component also includes dedicated areas to fit 4 springs suspending the thin film resistor support, as well as 4 pogo pins (P70-2100045R - 5.5 mm free height, Harwin, Portsmouth, UK) for connecting the top plate to the ground, exerting an upward force onto the top plate of the DMF chip. The cover protects both the DMF chip and electronic circuitry, includes an open window so that fluorescence may be captured and also lodges another 4 pogo pins, slightly shorter than the previous ones (P70-21000045R - 3.6 mm free height, Harwin, Portsmouth, UK), that exert downward force onto the top plate. The 8 pogo pins (4 on the cover and 4 on the base) fixate the top plate of the DMF chip, and since all contain internal springs, the top plate can move just enough to respect the gap between plates, defined by polyimide tape (180 µm). All parts are inter-connected through a set of 8 screws. Figure 5.4 illustrates the fully assembled base, including the DMF chip and related outside connections.

a)

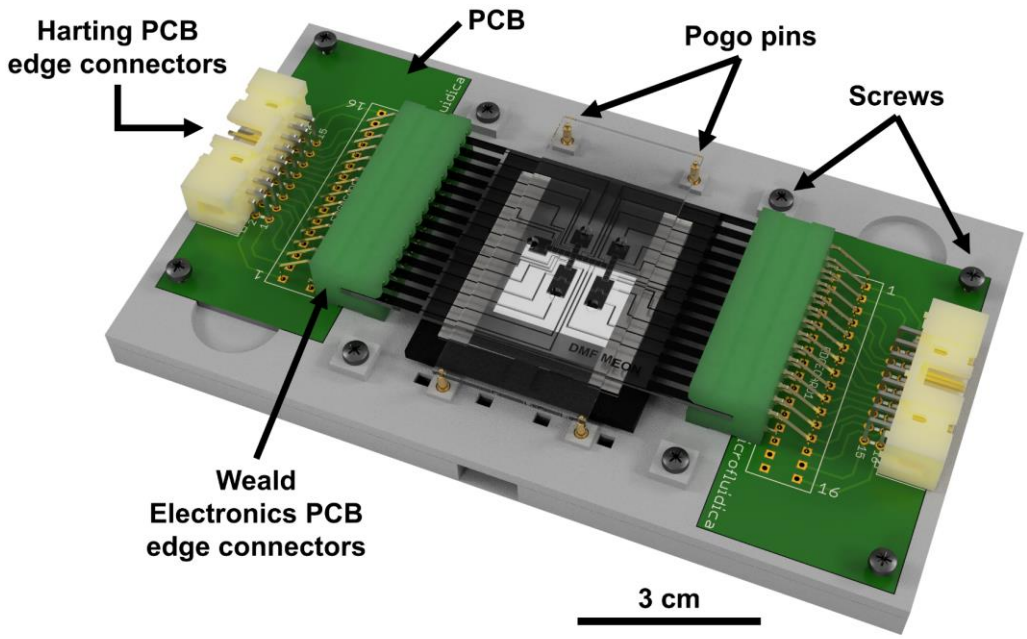

b)

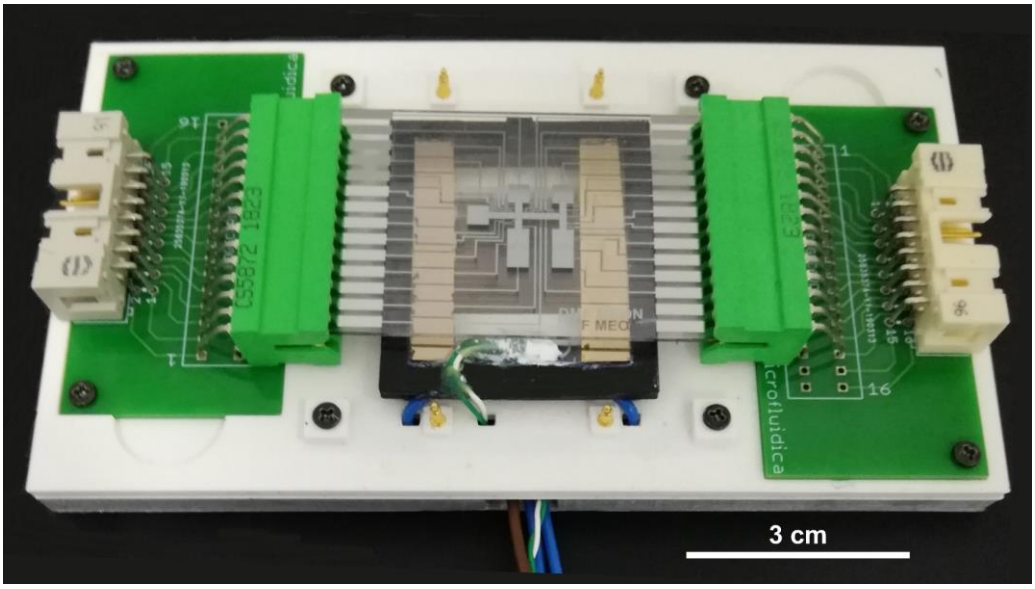

Figure 5.4: 3D illustration (a) and photograph (b) of the uncovered DMF support system, evidencing connections from the pads of the chip to PCB edge connectors and outer-support system connectors, mediated by a PCB.

Base and cover were designed to fit under a microscope if required, measuring 13.2 cm x 7.3 cm, with a total thickness of only 1.9 cm. All parts were printed with an Ultimaker 2+® 3D printer (Ultimaker B.V., Utrecht, Netherlands), in polylactic acid (PLA), except for the thin film resistor support, which was printed in acrylonitrile butadiene styrene (ABS), since this polymer can withstand higher temperatures.

5.3 Choice of device materials

Determining the most appropriate materials for the various layers of a DMF device is fundamental for producing functional devices. Figure 5.5 illustrates the typical layers present on a DMF device.

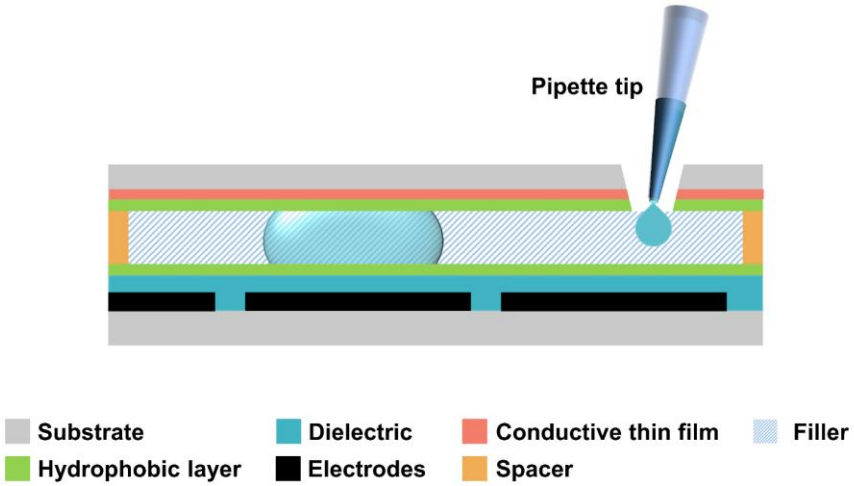

Figure 5.5: Schematic cross-section of a standard DMF device, evidencing all constituting layers, as well as an example sample insertion through an inlet at the top plate, with a pipette. Image not to scale.

Regardless of the architecture, DMF bottom plates generally include a physical substrate on which are deposited: a metallic electrode layer to ensure electrical connections, a dielectric layer to avoid short circuits as well as liquid electrolysis, and a hydrophobic layer, to increase the contact angle between the liquid droplet and the bottom plate. As for the substrate, soda lime glass was chosen, due to its robustness, hardness, availability, and low cost. Chromium was chosen as the electrode/reservoir metal, mostly considering its exceptional adhesion to glass, a highly required property for sliding the DMF devices onto the PCB edge connectors without damaging or rising the metallic pads. Moreover, chromium presents a high conductivity, which is also ideal for DMF applications. Several materials were readily available as dielectrics, namely silicon dioxide, aluminum oxide, Parylene C and innovative in-house developed electrolytes based on cellulose[301,302]. Nevertheless, cellulose-based dielectrics are permeable hydrogels, which invalidates their usage for DMF applications. Silicon dioxide and aluminum oxide are good candidates, however they would require very low vacuum conditions and an increase in deposition complexity due to the generally required control of O_2 pressure on the deposition chamber. As was discussed in section 2.4.3, Parylene C cumulatively presents outstanding conformability, biocompatibility, low permeability and ease of deposition[73], thus

remaining the most common dielectric in DMF applications, and the chosen option for this PhD work. As explained above (and on section 2.4.4), the hydrophobic layer also has a relevant role in DMF, increasing the contact angle of the liquid droplet and therefore reducing the surface energy. For this PhD project, Teflon® was the immediate choice, considering its wide applications in industry[303,304] and academics, particularly in the field of DMF and overall electrowetting applications[103,122,129]. Moreover, Teflon® is stable in contact with biological tissues, and has been used for decades in medical devices[305]. Please note that along this PhD work, Teflon® (registered trademark from The Chemours Company FC, LLC) was replaced by its constituting compound, PTFE (polytetrafluoroethylene) AF 1600. The hydrophobic layer used throughout this endeavor (prepared as described in section 5.1.2) will be referred to as only PTFE for simplicity. As for the filler medium, a non-polar filler would be preferrable, to avoid an excessive increase on the droplet-filler surface energy, which would hamper sample introduction on DMF chips through the holes drilled on the top plate. Low viscosity is also relevant to reduce the actuation voltage required, as well as a high breakdown voltage, and of course biocompatibility is always preferred. Silicone oil was the selected filler, as it is able to withstand high voltage electric fields[306–308], presents relatively good biocompatibility[309,310] and is readily available in a wide range of viscosities[311], namely 5 cSt as applied to this work. Regarding the spacer, polyimide strips were selected, considering their good adhesive properties at high temperatures and ease of processing and spacing control (spacing may be easily increased or decreased by simply adding or removing strips). Lastly, the top plate is fabricated from soda lime glass with a pre-deposited layer of ITO (100 nm), due to its overall transparency and availability. The following tables present the materials considered for the substrate, electrodes, dielectric and hydrophobic layers, and filler medium, as well as relevant properties for comparison. Note that the selected materials for each layer have been highlighted in green.

Table 5.1: Materials considered for the substrate and relevant properties. Abbreviations used: PEN for polyethylene naphthalate, PET for polyethylene terephthalate.

	Robustness	Low-cost	Ease of processing
Glass	++	+	-
Paper	--	++	++
PEN	+	+	++
PET	+	-	++

Table 5.2: Materials considered for the electrode layer and relevant properties.

	Conductivity	Adhesion to glass	Ease of processing
Chromium	++	++	-
Aluminum	++	-	-
Titanium/Gold	++	+	-
Molybdenum	++	-	+
Copper	++	-	-

Table 5.3: Materials considered for the dielectric layer and relevant properties.

	Dielectric strength	Biocompatibility	Water permeability	Ease of processing
Parylene C	+ (220.5 V/µm)	++	+	+
Silicon Dioxide	++ (950 V/µm)	++	+	--
Aluminum Oxide	-- (16 V/µm)	++	-	--

Table 5.4: Materials considered for the hydrophobic layer and relevant properties. PTFE: polytetrafluoroethylene.

	Availability	Biocompatibility	Use in EWOD
PTFE/Teflon®	+	++	++
AquaPel	--	?	+
Cytop	--	?	+

Table 5.5: Materials considered for the filler medium and relevant properties.

	Availability	Biocompatibility	Viscosity	Low-cost	Use in EWOD
Silicone oil	++	++	Variable	--	++
Light mineral oil	++	++	-	-	+
Pluronic additives	-	++	Variable	++	+

5.4 DMF droplet driving system

Controlling droplets within a DMF chip requires a multi-component driving system, typically consisting of a voltage source and voltage amplifier, which will determine the potential applied to the electrodes (and droplets, consequently); a high voltage switching unit (HVSU), to compute between ON and OFF electrode states; a control board, to determine electrode

addressing and finally an electrical connection to the DMF chip. In this PhD work, a previously reported driving system[17] was improved, by increasing the driving capability from 16 to 28 electrodes, by redesigning the chip connections to PCB edge connectors and also by adding an impedance measuring unit (see section 7). Briefly, the driving system is fully controlled by a specific software developed within the group (see section 5.5), which is connected to an Arduino Mega control board. The Arduino board translates input information from the software to output commands, further transmitted to the HVSU. The HVSU receives an amplified AC signal and according to the commands provided by the Arduino board, activates/deactivates the corresponding electrodes on the chip, by enabling/disabling the connection to the AC signal, respectively. Moreover, the impedance measuring unit includes a lock-in amplifier which receives a voltage readout from the DMF device and determines the voltage amplitude of actuated electrodes at a specified frequency. Impedance may further be calculated from the readout values. Note that the impedance measuring unit is only used when impedimetric measurements are required. Figure 5.6 illustrates all the components of the driving system, as well as connections between them.

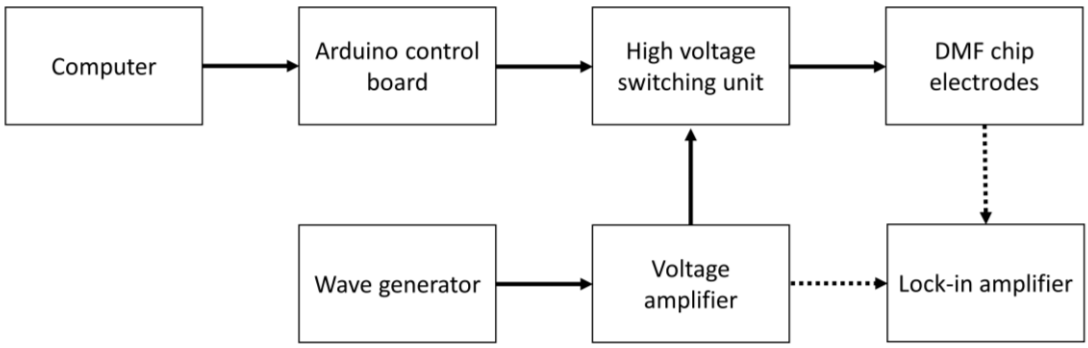

Figure 5.6: Schematic representation of the multi-component DMF droplet driving system, evidencing connections between distinct components.

5.5 DMF droplet control software

Electrode switching for droplet control is fully automatic, relying on a software specifically designed for this purpose. This software was implemented through the Python programming language, which includes a specialized module for Graphical User Interface (GUI) implementation: Tkinter. This module allows for straightforward creation of operation menus, and facilitates communication with any external hardware (cameras, Arduino boards, other electronic equipment). Figure 5.7 illustrates the user interface of the software.

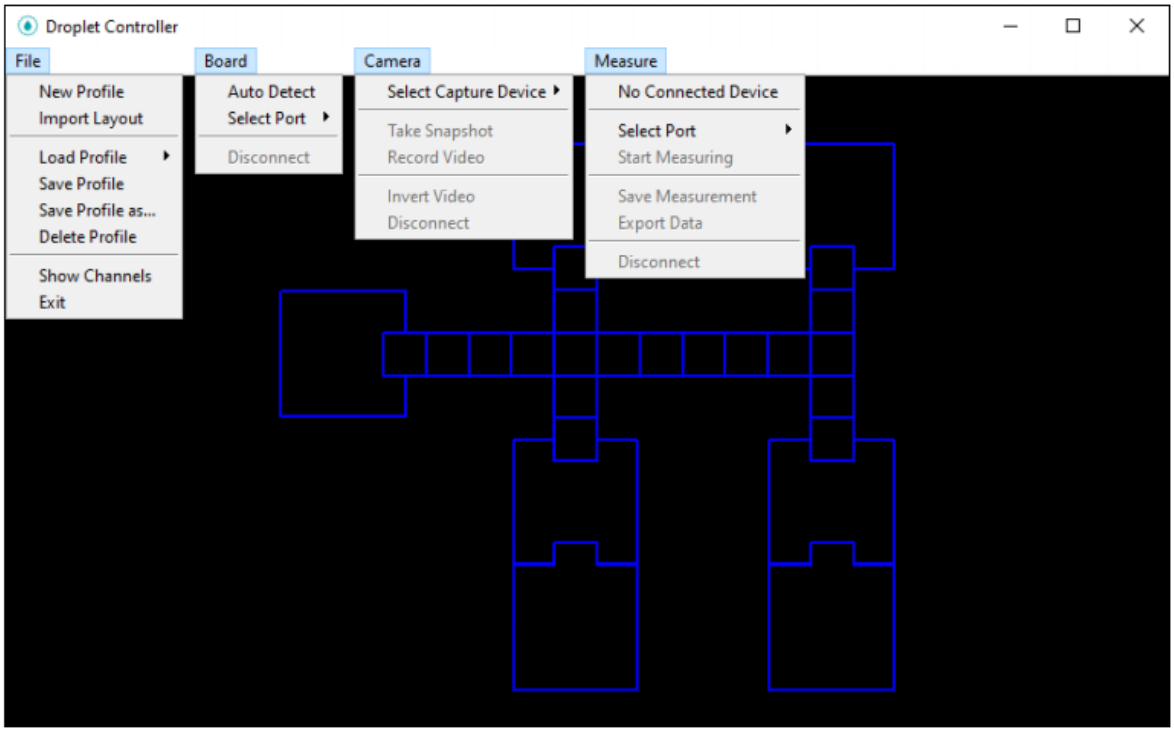

Figure 5.7: Edited screenshot of the software with the configured device profile, to display all available options in the top menu bar.

As can be seen on Figure 5.7, the software enables four different main operations: 1) profile uploading, which allows the user to create an .svg file containing any bottom plate electrode configuration. The software assumes designed shapes as addressable entities, which may be turned ON or OFF as desired; 2) board detection, enabling communication with an Arduino board, which in turn will control the high voltage switching unit and ultimately allow for switching ON/OFF any set of electrodes; 3) camera control, which enables selection of any USB-connectable camera device, as well as video and snapshot capturing; 4) measuring setup, which enables communication with the impedance analyser via GPIB (General Purpose Interface Bus).

5.6 Temperature control setup

Heating is a cardinal requirement for all nucleic acid amplification methodologies, even those that occur at lower temperatures[312,313]. Whether thermal cycling is required, or a single temperature suffices, it is of the utmost relevance to maintain the setpoint temperature stable, since even slight temperature disturbances may lower the reaction efficiency. Joule heating in thin metallic or semiconductor films is one of the most extensively used techniques for temperature control in DMF platforms[137,152,159,208], perhaps due to the small space occupation and the possibility of integration with high temperature coefficient materials as temperature sensors. Considering such benefits, the chosen strategy for heat production on the DMF platform was Joule heating, through a commercially available glass substrate with a 100 nm ITO thin film deposited on one of the glass faces.

5.6.1 Initial simulations

As mentioned in section 2.7, the LAMP amplification methodology relies on a *Bst* polymerase, which functions optimally at a temperature ranging from 60 to 65 °C. According to New England Biolabs®, the enzyme activity varies with temperature as described below[314]:

Table 5.6: Enzyme activity according to temperature for *Bst* DNA polymerase, large fragment.

Enzyme activity	Temperature (°C)
10-15%	37
30-45%	50
100%	60-65
20%	70
Heat-inactivation	>70

As specified on Table 5.6, enzyme activity falls abruptly outside the optimal temperature range (60-65 °C), particularly for higher temperatures. Thus, control simulations are required to determine the ideal temperature to be applied by the thin film heating element in order to ensure that the temperature gradient at the droplet respects the optimal range. Moreover, it is relevant to understand whether the silicone oil surrounding the reaction droplet will significantly hinder heat transfer. COMSOL Multiphysics 5.4® was selected for running the necessary simulations, resorting to the heat transfer in solids and fluids module, in a 2D space. The model designed for this study includes a droplet that would fit on a bottom plate electrode (1 mm ×

180 µm), sandwiched between fractions of the bottom and top plates, and surrounded by silicone oil. Figure 5.8 illustrates said model.

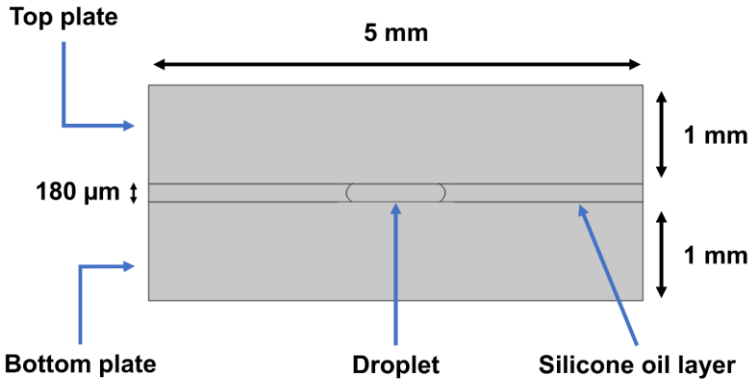

Figure 5.8: COMSOL® model used to assess temperature distribution along a reaction droplet on a DMF chip.

For this model, silicone oil and water were added as constituting materials, with the properties stated in Table 5.7.

Table 5.7: Relevant properties of simulation materials for the COMSOL® module for heat transfer in solids and fluids.

	Silicone oil	Water
Thermal conductivity, κ [W/(m·K)]	0.12[315]	0.5861[316]
Density, ρ [kg/m^3]	913[315]	998.2[316]
Heat capacity at constant pressure, *Cp* [J/(kg·K)]	1.8E6[315]	4183[316]

In this simulation, room temperature was defined as 20 °C, and thermal insulation was assumed for all the boundaries which were only in contact with air. The temperature boundary was set on the downside face of the bottom plate, assuming thermal equilibrium with the heating element, at a test temperature of 65 °C (the top temperature in the optimal operation range of the *Bst* enzyme - Table 5.6). The mesh was adjusted to "extremely fine" due to small-sized features, namely the droplet edges, and included 12768 domain elements, 596 boundary elements, and 16 vertex elements. The simulation results are presented on Figure 5.9, where the area surrounding the droplet was zoomed in for better visualization of the temperature profile within said droplet.

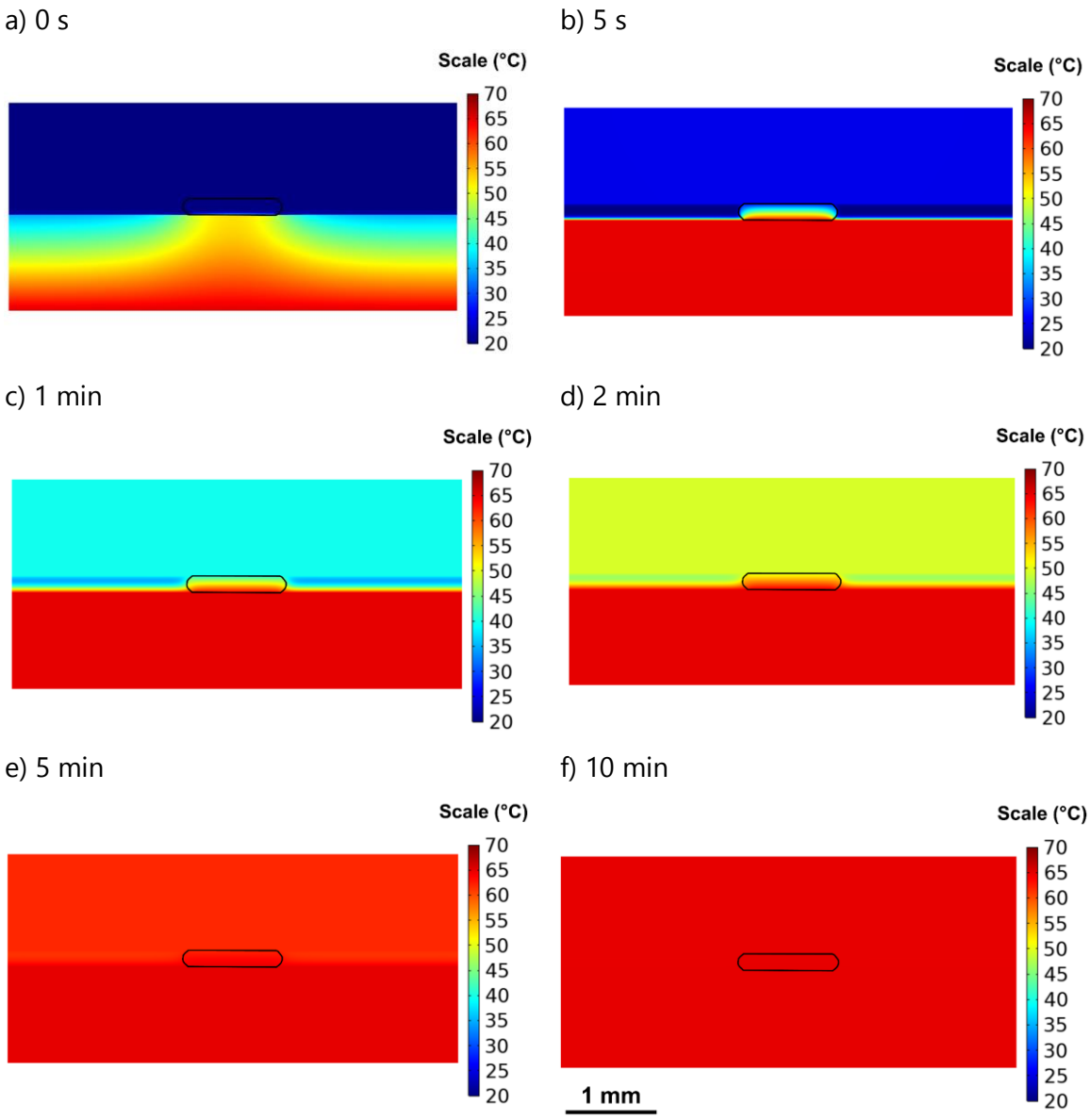

Figure 5.9: Evolution of the temperature distribution between top and bottom plates of the DMF chip. The droplet region has been highlighted in black. Note that the dimension scale in f) is valid for the whole Figure.

The filler oil indeed acts as a barrier for the propagation of heat from the bottom to the top plate, with the reaction droplet becoming the path of least thermal resistance. Nevertheless, the droplet reaches the bottom of the optimal temperature range for the *Bst* enzyme (60 °C) relatively quickly, after 2 min. Moreover, the entire area surrounding the droplet (as well as the droplet itself) reaches thermal equilibrium after 10 min. Surely the conditions within the produced DMF devices will be slightly different from this simulation, considering the variations from reality, however, this simulation is deemed a good starting point, and the vertical temperature distribution within the droplet and surrounding areas is quite satisfactory for on-chip LAMP reactions.

Furthermore, it is relevant to simulate and study the temperature distribution along the area of the bottom plate where the electrodes and reservoirs are located, i.e., where LAMP reactions will occur. Uniform heating must be guaranteed, so that both test samples are subjected to the same conditions. For said simulations, only three elements were used in the simulation model: the thin film heating element, the heating support and the bottom plate of the DMF chip (Figure 5.10).

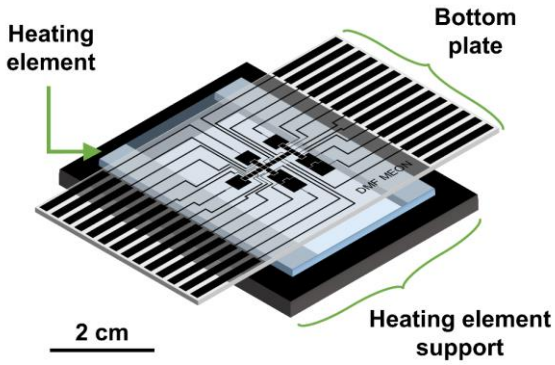

Figure 5.10: Elements used for the COMSOL® simulation of temperature distribution from the heating element to the surroundings.

Using the model depicted on Figure 5.10, COMSOL Muptiphysics 5.4® simulations were run for temperature gradient evaluation over time, resorting to the heat transfer in solids module, in a 3D space. Room temperature and insulation conditions are the same as for the previous simulations. Only two materials were considered for this simulation, i.e., window plate glass (COMSOL® base material) and ABS (added material), with the model properties described in Table 5.8. Note that all units of the presented properties are consistent with the COMSOL® software requisites.

Table 5.8: Relevant properties of simulation materials for the COMSOL® module for heat transfer in solids.

	Window plate glass	ABS
Thermal conductivity, κ [W/(m·K)]	1.06[317]	0.25[318]
Density, ρ [kg/m^3]	2500[317]	1.05E3[318]
Heat capacity at constant pressure, Cp [J/(kg·K)]	870[317]	1.655E3[319]

A temperature boundary of 65 °C was set on the downside face of the heating element, assuming uniform heating along the ITO thin film with current flow. The mesh was set to the "finer" setting, thus including 41506 domain elements, 22504 boundary elements, and 2199 edge elements. The relevant parameter to be studied here is the temperature distribution in

the XY axis, at the bottom plate, and not the horizonal temperature variation. The simulation results are presented on Figure 5.11.

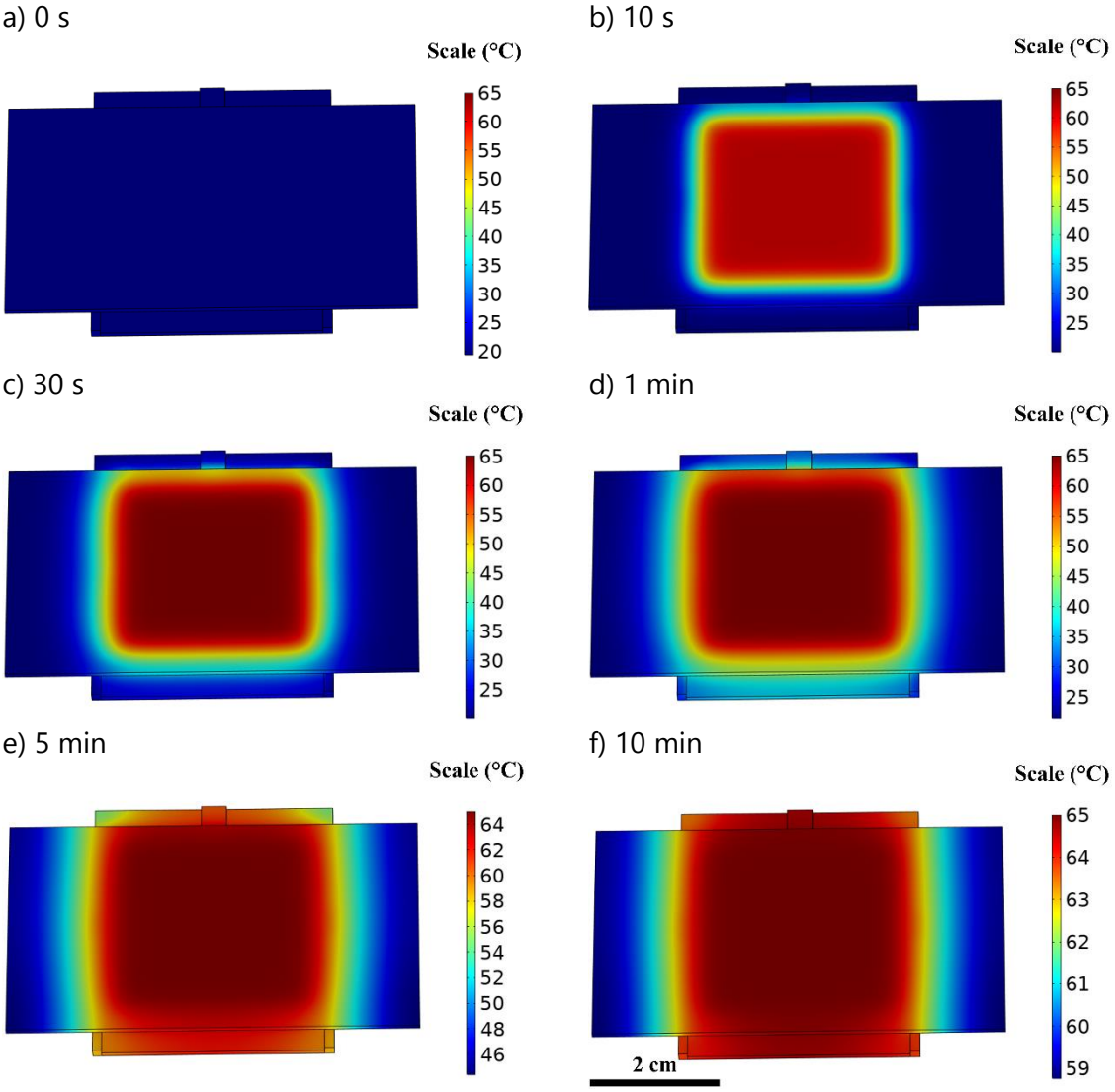

Figure 5.11: Evolution of the temperature distribution along the heating system and bottom plate of the DMF chip. Note that the dimension scale in f) is valid for the whole Figure.

As can be seen on Figure 5.11, the central area of the bottom plate is the first to achieve thermal equilibrium with the heating element, reaching 65 °C in 30 s. Temperature continues to rise around the central area of the bottom plate and also throughout the thin film support until reaching equilibrium after 10 min of heating. Although the left and right edges of the bottom plate remain at lower temperatures, the area where amplification reactions will occur presents a uniform temperature distribution, suggesting that the proposed temperature control system is indeed capable of providing the temperature required for LAMP.

In summary, the previous COMSOL® simulations suggest that the proposed heating system, based on a thin film heating element that provides heat for the entire DMF chip, is a

promising candidate for performing LAMP assays, considering that: i) temperature is uniformly distributed along the area directly beneath the electrodes and reservoirs (where the reaction will occur) and ii) despite presenting inferior density and thermal conductivity, as well as superior heat capacity, the temperature barrier effect of the oil matrix is surpassed after some minutes.

5.6.2 Assembly of the temperature control system

Essentially, (30 x 35) mm^2 pieces were cut from commercially available ITO-coated glass by means of a glass cutter (Silberschnitt® 2000 Special Glass Cutter), to fit within the thin film resistor support. A 66 nm titanium-gold (6 nm of titanium for glass adhesion and 60 nm of gold for improving electrical conduction properties) layer was then deposited on each side of the ITO-coated glass pieces by electron beam deposition, as contacts. Following this, multifilament cable wires were bonded to Ti-Au contacts by means of silver ink (PELCO® Conductive Silver Paint, Ted Pella. Inc., Redding, CA, USA) and high-temperature epoxy glue (Ceys high temperature contact glue, Ceys, Barcelona, Spain), which were left drying for 24 hours. Figure 5.12 illustrates the thin film resistor and cable connections.

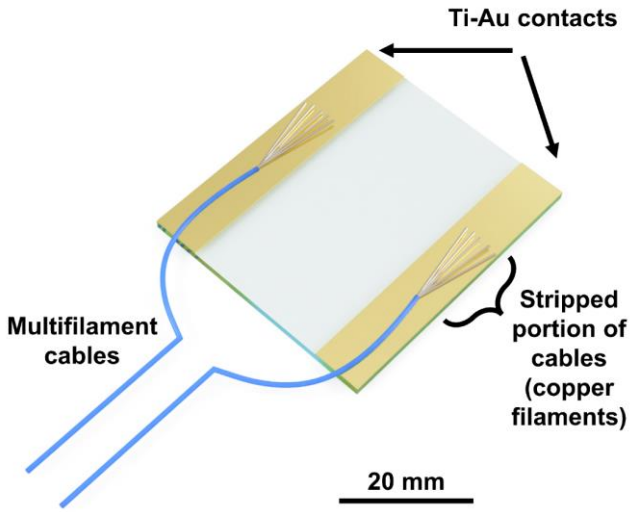

Figure 5.12: Schematic representation of the connection between multifilament cables and Ti-Au contacts. The ends of each cable were stripped, exposing the Cu filaments for electrical contact with the Ti-Au contacts.

Temperature at the thin film heating element is dependent on the current passing between the contacts, therefore, to maintain a certain temperature setpoint, a feedback system is required, where current is adjusted according to temperature readings. In this project, the temperature control system relies on two separate temperature sensors: a PT100 sensor (RS PRO PT100 class B 2 platinum chip – 2 mm diameter) responsible for providing feedback

readings and a thermocouple (RS PRO Type K Thermocouple, RS Components, Corby, UK) glued to the edge of the thin film heating element for redundant monitoring. Both temperature sensors respond to temperature shifts with internal resistance variations, meaning that a driver module is required to convert said resistance variations to corresponding temperature variations, which are further converted into voltage signals interpretable by an Arduino board. For this reason, specific breakout circuits (MAX31855 for the thermocouple and MAX31865 for the PT100, both from Maxim Integrated, San Jose, CA, USA) are added to the control system, between the temperature sensors and the Arduino board. As for the temperature control system working principle, current drawn from a power supply passes through an IRF 520 MOS (Metal-Oxide-Semiconductor) module which mediates current flow to the heating element via a MOS transistor. The transistor in turn responds to temperature readings from the PT100 temperature sensor, mediated by an Arduino control board. The code written in Arduino operates a proportional–integral–derivative (PID) controller that receives input temperature readings from the PT100 sensor and correspondingly adjusts the MOS transistor to allow more or less current to flow. Thus, if the temperature sensed by the PT100 is above the setpoint, less current will be drawn from the power supply until temperature decreases and reversely, if the temperature sensed by the PT100 is below the setpoint, more current will be drawn from the power supply, until temperature increases. Figure 5.13 illustrates all the components of the temperature control system, as well as inter-connections.

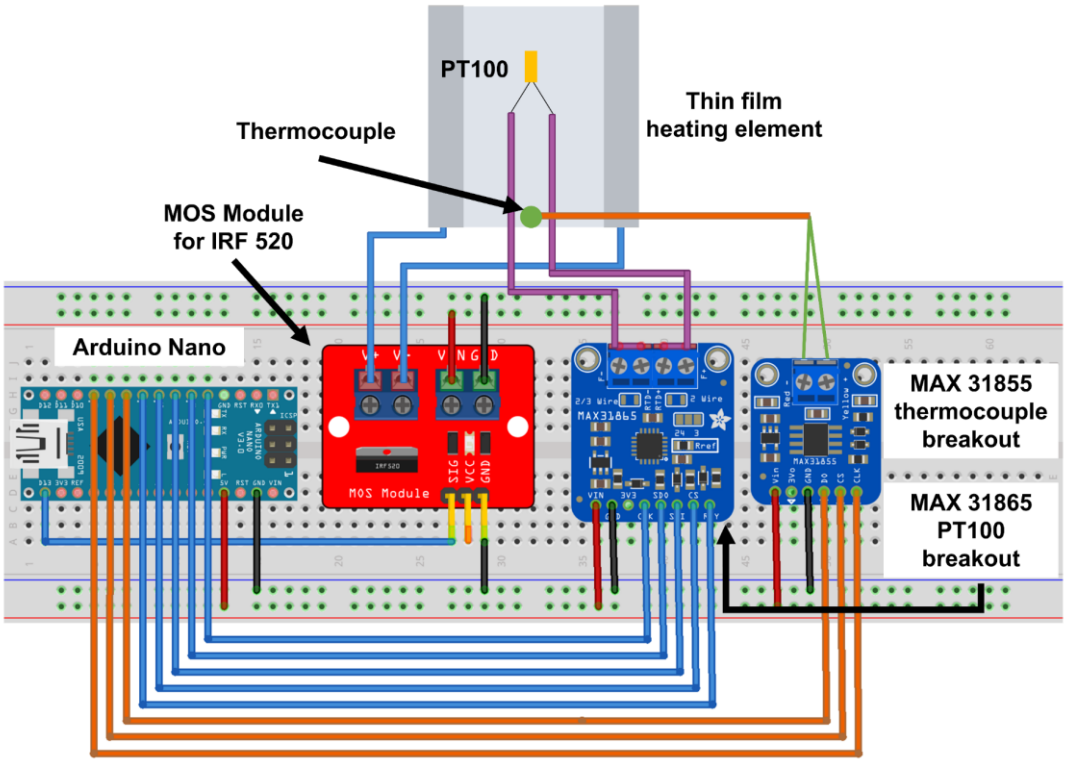

Figure 5.13: Breadboard model of the temperature control system used for DMF-LAMP, evidencing all electronic components and connections, as well as connections for the thin film heating element.

5.6.3 Testing the temperature control system: heating distribution along the thin film heating element

In order to understand the temperature distribution along the fabricated thin film resistor, an infrared camera (PYROVIEW 380L compact+, DIAS Infrared Systems, Dresden, Germany) was used to film the thermal profile of the resistor during heating, from room temperature up to 65 °C. The higher temperature limit was tested, considering that heat will be dissipated from the measuring point to the real reaction area. To confirm the readings from the infrared camera, the PT100 temperature sensor was bonded to central area of the thin film, at approximately the same location corresponding to the reaction areas on the DMF device. Figure 5.14 shows a compilation of frames evidencing the evolution of temperature within the thin film heating element.

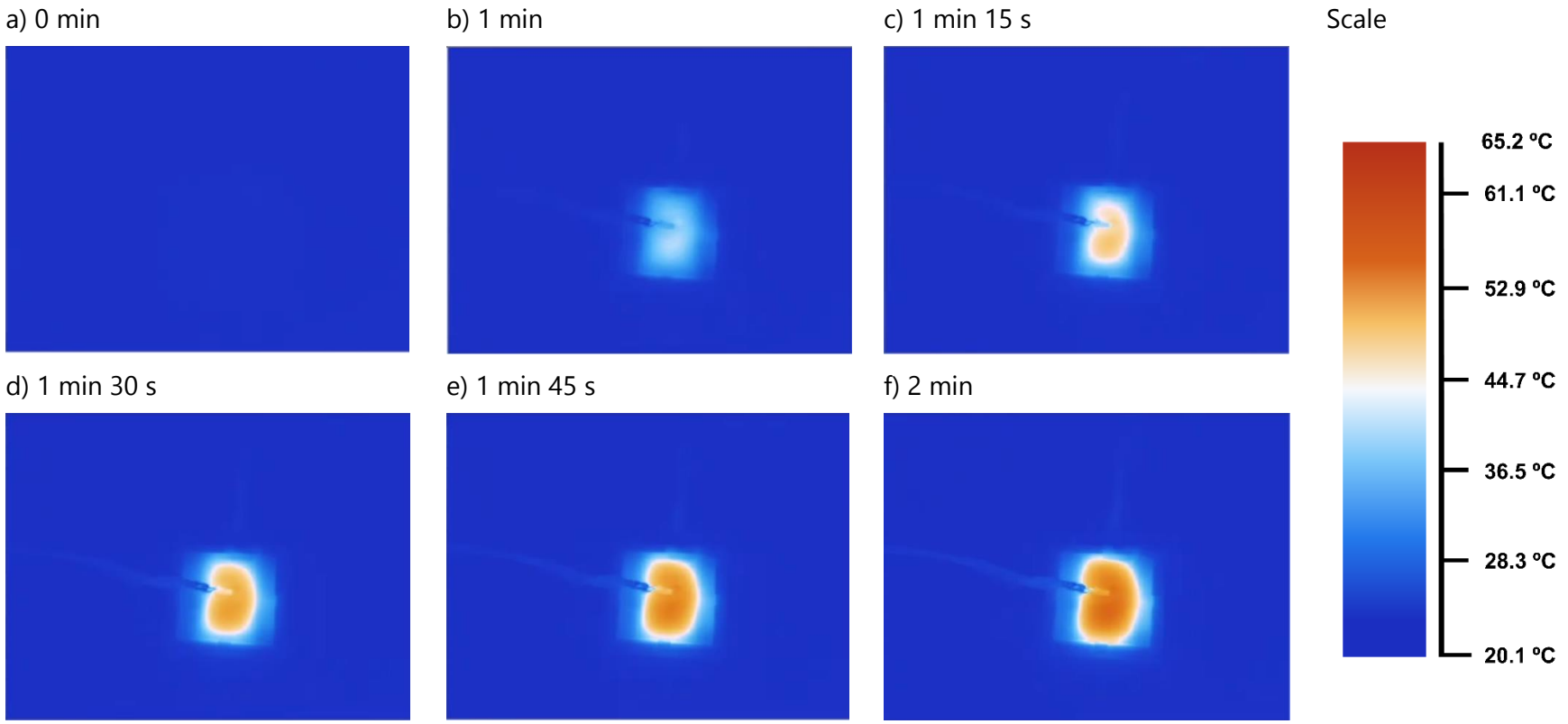
a) 0 min
b) 1 min
c) 1 min 15 s
Scale
65.2 ºC
61.1 ºC
52.9 ºC
44.7 ºC
36.5 ºC
28.3 ºC
20.1 ºC
d) 1 min 30 s
e) 1 min 45 s
f) 2 min

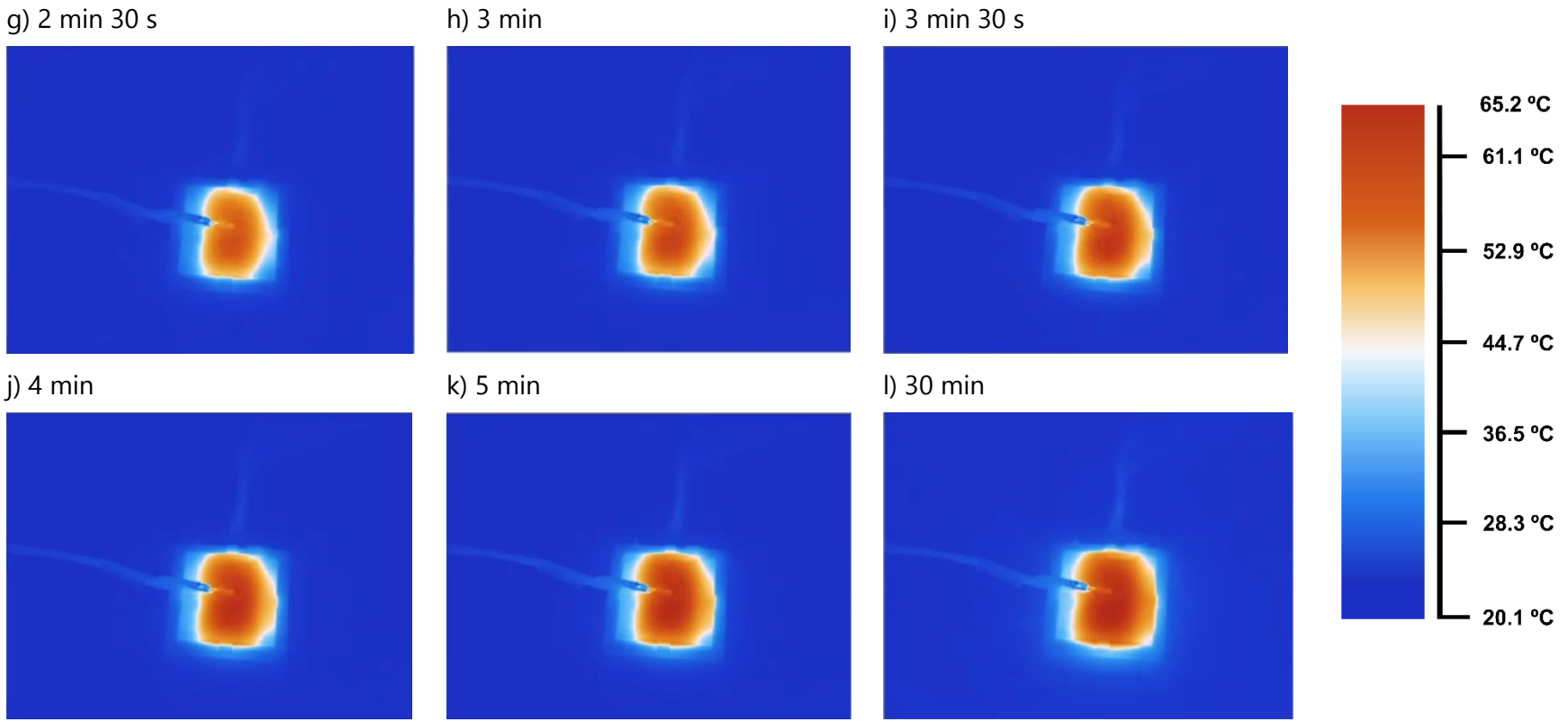

Figure 5.14: Video frames acquired through the PYROSOFT software, companion to the PYROVIEW camera family, displaying the temperature distribution along the thin film heating element, from room temperature to a 65 ºC setpoint.

Temperature initially rises in the middle section of thin film resistor (Figure 5.14 b) to c)) and rapidly spreads along the entire area, reaching the setpoint (around 65 ºC) in about 5 minutes, which is confirmed by the PT100 sensor readings. The area directly beneath the reaction region of the DMF chip is uniformly heated, therefore the thin film resistor appears to be a viable option for on-chip nucleic acid amplification reactions. Temperature measured by the thermal camera was also confirmed by a PT100 sensor placed on top of the heating element, directly beneath the area where LAMP reactions will occur (Figure 5.15).

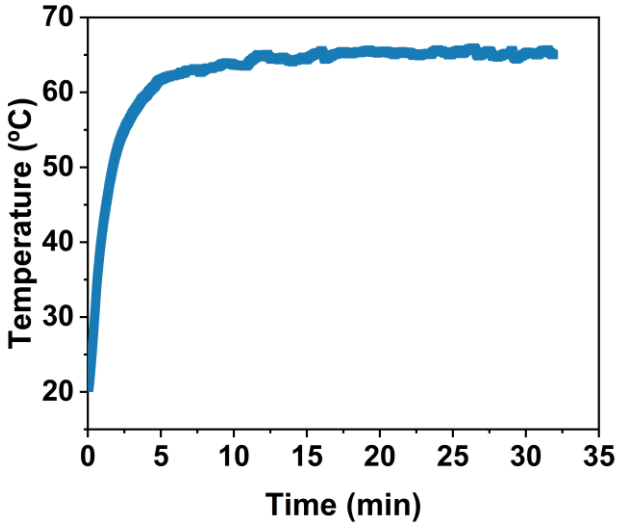

Figure 5.15: Temperature measured by the PT100 sensor placed directly on top of the thin film resistor.

5.6.4 Testing the temperature control system: configuration for LAMP amplification

In order to prepare the temperature control system for a LAMP reaction, the assembled thin film resistor was placed downwards on the respective support, so that the non-coated part would be in contact with the DMF device. The thermocouple remained glued to the thin film resistor, thus allowing for a better understanding of the temperature gradient across the entire DMF chip. The DMF chip and temperature system were then assembled to the final configuration: 1) the bottom plate was placed directly on top of the thin film heating element; 2) the top plate was placed above the bottom plate, with a 180 µm height provided by the polyimide tape spacers; 3) the PT100 sensor was bonded to the top plate, above the reaction area. In this configuration, heat generated by the ITO thin film will dissipate through two 1 mm-thick glass substrates (firstly the resistor substrate and then the electrode substrate) and all the layers composing the bottom plate until reaching the base of the droplet containing the master mix

for the reaction. Heat will then dissipate through the droplet and the top plate glass until attaining the temperature sensor. Such heat dissipation must be taken into consideration while pursuing a LAMP reaction and bearing in mind that optimal LAMP occurs between 60 and 65 ºC, the setpoint temperature was adjusted to 59.5 ºC for the PT100, thus ensuring that the temperature gradient within the reaction droplet falls between the above-mentioned range. As an additional control measure, a thermocouple was attached to the edge of the thin film resistor. Figure 5.16 illustrates the fore-mentioned setup.

a)

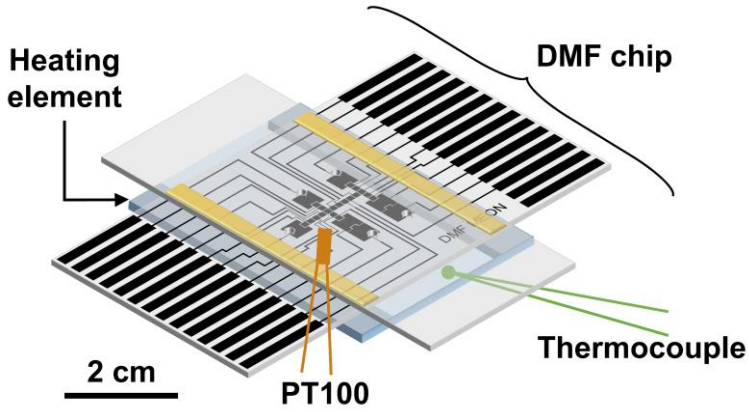

b)

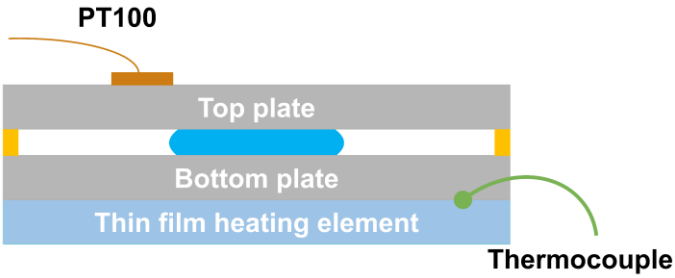

Figure 5.16: a) Schematic view of the DMF chip and the temperature system configuration for on-chip LAMP reactions, consisting of a thin film heating element placed directly below the bottom plate and two temperature sensors. b) Cross section of the same configuration, evidencing the location of the temperature sensors, namely the PT100 sensor on the top plate and the thermocouple on the heating element. Image not to scale.

Resorting to this setup, the PID parameters were adjusted to prevent temperature overshoot, thus preventing degradation of the LAMP reagents, and to achieve low steady-state error, thus maintaining the reaction temperature constant. Figure 5.17 represents the average temperature measured by both PT100 and thermocouple, in a total of 3 experiments.

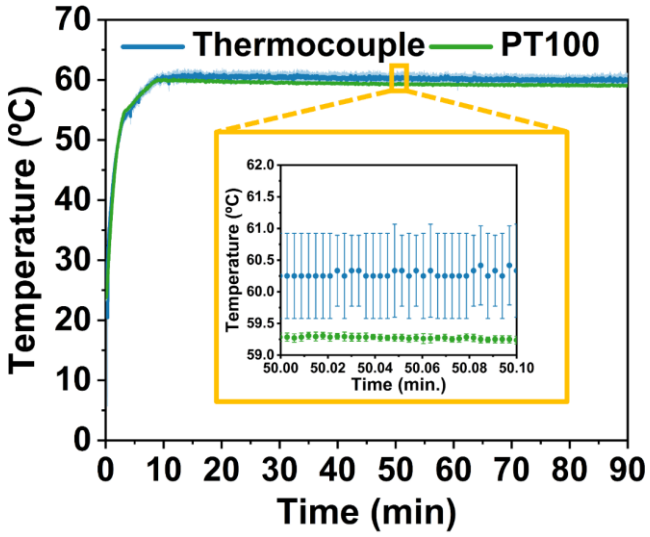

Figure 5.17: Average temperature measured on two separate locations of the DMF system, by two distinct temperature sensors, a PT100 and a thermocouple, for three trials. On the inset, the region around the setpoint temperature is enlarged for better visualization. Error bars correspond to the 90% confidence interval, for a total of three experiments.

As can be seen on Figure 5.17, temperature quickly rises to 55 °C, after which temperature steadily reaches the setpoint of 59.5 °C in approximately 4 min with a good steady-state error on the top plate level (maximum deviation of 0.9 °C from 10 min to 90 min).

5.7 DMF device operation

The operating protocol for DMF devices is of extreme relevance to reduce issues associated to high-voltage control of liquid droplets. Firstly, before sample insertion on the chip, the latter is filled with 5 cSt silicone oil (Sigma-Aldrich, St. Louis, MO, USA), previously degassed in low vacuum for at least 3 hours. Subsequently, 2 µL of the sample in question may be inserted onto the chip via access orifices on the top plate, by using a pipette. For droplet motion, an AC signal with 40 V_{RMS} and 5 kHz is used, whereas during the course of a LAMP reaction, the signal amplitude is reduced to 20 V_{RMS}, to prevent degradation of any of the layers comprising the device.

5.8 Characterization of the dielectric layer

As previously stated, the dielectric layer is one of the most critical layers in DMF devices based on EWOD, considering that it is strictly necessary to prevent water electrolysis due to

the use of a strong electric field[320]. Consequently, the breakdown of the dielectric is a major constraint in DMF[116], leading to immediate loss of functionality for the devices and interruption of any on-chip protocol. Therefore, it is fundamental to study the dielectric layer of the DMF devices developed in this work, particularly when exposed to temperature and actuation signals for an extended period of time, as would happen during a LAMP reaction on-chip. LAMP reactions require heating at a temperature between 60 °C and 65 °C, and on-chip LAMP reactions reach 90 minutes, or even 120 minutes for complex targets. During this time period, not only will the dielectric be subjected to heating, but reaction sites will also be constantly subjected to electric fields, since voltage actuation is required to keep droplets in place. Of course, a lower-amplitude signal is used for such purpose, to prevent device degradation, typically 20 V_{RMS} in comparison to 40 V_{RMS} used for droplet motion. The 20 V_{RMS} signal is high enough to prevent droplets from moving, but low enough to help preventing device degradation. Moreover, a breakdown-prevention strategy must be implemented to assure proper device function during all DMF protocols thus avoiding unnecessary costs and time consumption. Considering that pinholes are decisive in the breakdown of a dielectric layer, the proposed breakdown-prevention strategy consists of depositing Parylene C in double- instead of single-layer. The chosen thickness for the Parylene C layer was 2 µm, deposited in one deposition process in the case of single-layered devices, or in two consecutive deposition processes (1 µm each).

5.8.1 Influence of heating and electric stress

To evaluate the influence of applying temperature and electric stress to the dielectric layer, MIM (metal-insulator-metal) structures were fabricated with Parylene C as the insulating layer.

5.8.1.1 MIM structure fabrication and characterization protocols

Fabrication steps include glass cleaning, as previously described, and deposition of chromium bottom contacts (200 nm) by e-beam, also as previously described, but resorting to mechanical masks. Parylene C was deposited over the bottom contacts (connection pads were covered) and the top chromium contacts were deposited by e-beam at room temperature. The effective areas of the MIM structures are as follows: 0.0625 mm^2, 0.25 mm^2, 0.5625 mm^2 and 1 mm^2. Figure 5.18 illustrates the structures produced.

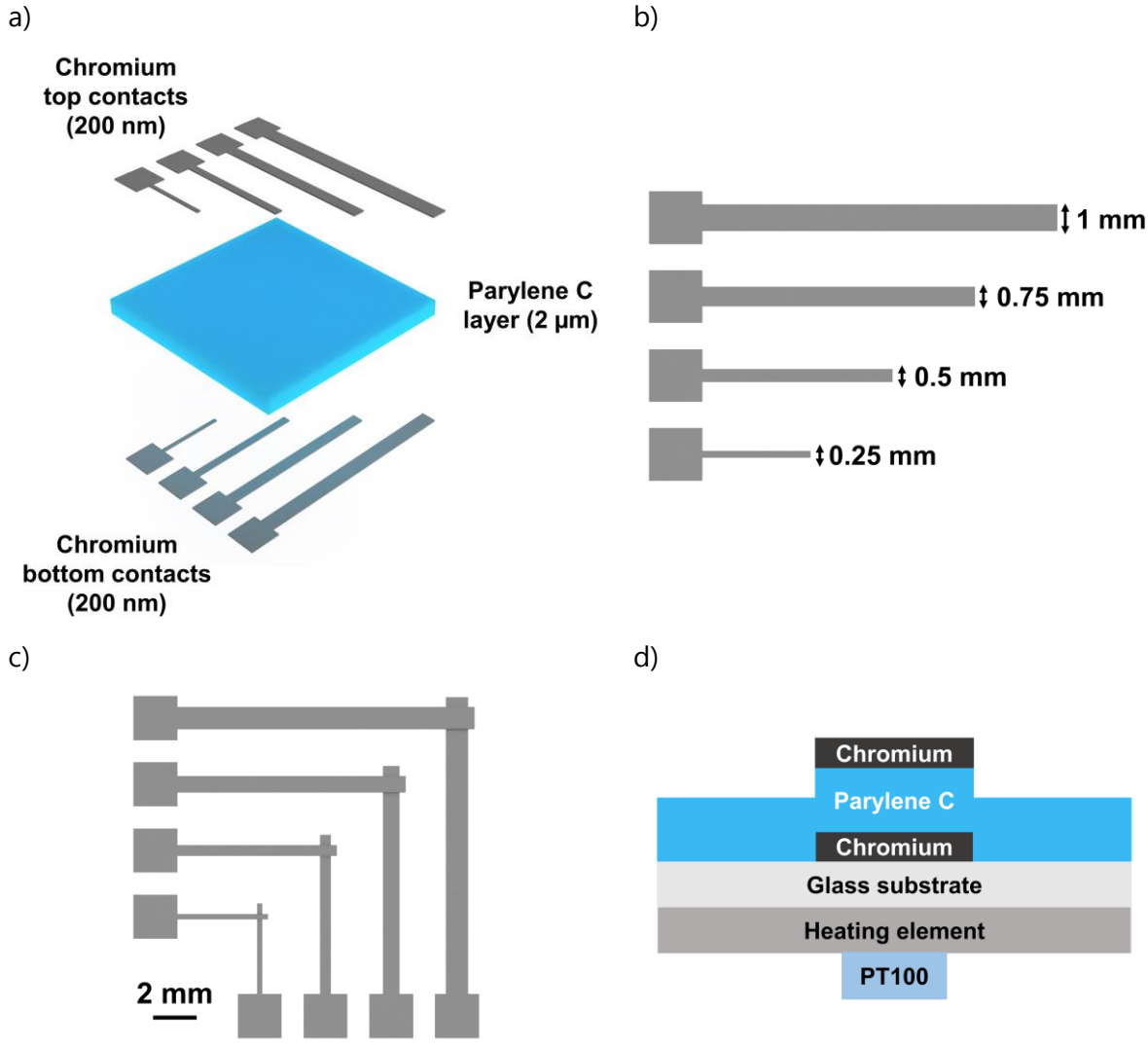

Figure 5.18: Schematic representation of the MIM structures produced for testing the Parylene C dielectric layer. a) 3D view of all layers comprising the MIM structures, as well as respective thicknesses. Image not to scale. b) Depiction of chromium contacts and respective lateral dimensions. c) Overlap of chromium contacts, evidencing the area corresponding to the MIM capacitors (the Parylene C layer was omitted for better visualization). d) Cross section of a MIM structure, placed over the temperature setup. Image not to scale.

The MIM structures were exposed to three different settings: 1) constant temperature (62 °C); 2) constant AC actuation (20 V_{RMS}) and 3) both stimuli simultaneously, which corresponds to the DMF-LAMP operation parameters. The temperature was fixed at 62 °C, considering that this is the mid-range temperature for the optimal temperature spectrum for the *Bst* enzyme. All three conditions were applied to the devices for two hours, anticipating the use of the devices for detection of low concentration DNA targets. The temperature system differs only from the previously reported in the location of the PT100 sensor, which has been moved to below the heating element, as shown by Figure 5.18 d). A 20 V_{RMS} AC signal was applied to the bottom contacts of the MIM structures, whereas the top contacts were grounded. Lastly,

for dual stimulation (temperature and AC signal), the same DMF platform was used to mimic on-chip LAMP conditions. All characterizations were performed using the Keysight B1500A semiconductor parameter analyzer. *C-V* (capacitance-voltage) measurements were performed, for a voltage range of -5 V to +5 V (step of 0.5 V), followed by another voltage loop from +5 V to -5 V. Dielectric breakdown was then attempted, by applying a high voltage DC signal with a total range amplitude of 200 V. During this measurement, the leakage current was recorded for a step of 2 V (current-voltage or *I-V* measurements). Said measurements were performed for each sample, before and after applying the stimuli. Moreover, Parylene C is known to crystallize with temperature, therefore a structural analysis was performed by XRD. Diffraction spectra were collected in continuous mode from 10° to 20° (2θ), for a step of 0.002°, with a generator voltage of 45 kV and a tube current of 40 mA.

5.8.1.2 Characterization of the heating influence

C-V measurements were performed on each sample before and after applying the stimulus (temperature and/or AC signal). Briefly, for each tested condition, a minimum of three samples were tested, and the results obtained for the capacitance were averaged and normalized to the corresponding area (capacitance per unit area, *C/A*). The *C/A* obtained after applying the stimulus was further normalized to the *C/A* obtained before applying the stimulus, according to Equation 5.1:

$$\Delta\frac{C}{A} = \frac{\left(\frac{C}{A}\ post\ stimulus\right) - \left(\frac{C}{A}\ pre\ stimulus\right)}{\frac{C}{A}\ pre\ stimulus} \times 100 \qquad (5.1)$$

For simplification, the capacitance per unit area will from now on be referred to as *C/A* and the relative variation of the capacitance per unit area, obtained through Equation 5.1, will be denoted as Δ*C/A*. Figure 5.19 illustrates the average Δ*C/A*. For pre-stimulus device characterization in terms of capacitance, relative permittivity, and loss tangent, please refer to Appendices A, B and C, respectively.

a) Temperature stimulus: 62 °C for 2h

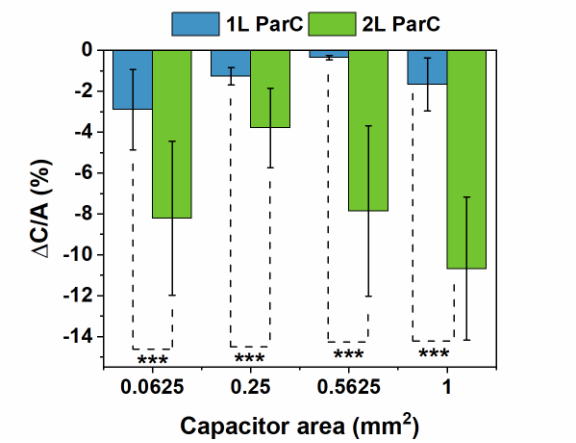

b) AC stimulus: 20 V_{RMS} for 2h

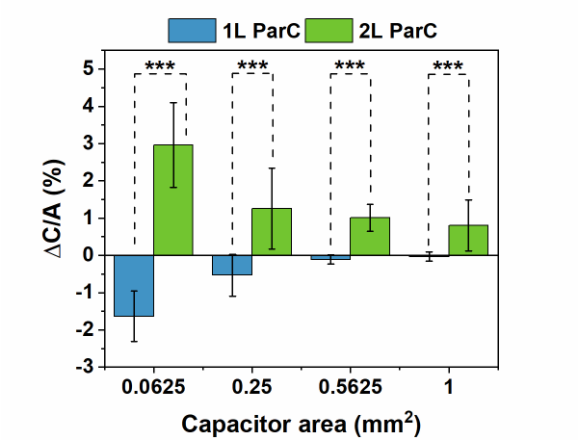

c) Dual stimuli: temperature + AC signal for 2h

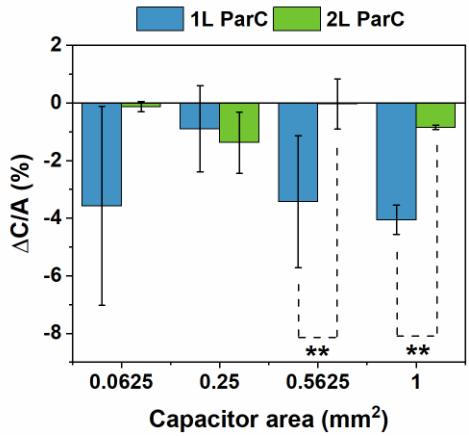

Figure 5.19: Δ*C/A* for the dielectric layer (Parylene C and PTFE) with Parylene C (ParC) deposited as a single (blue bars) or double layer (green bars), for four different MIM capacitor areas†: 0.0625 mm², 0.25 mm², 0.5625 mm² and 1 mm². a) Δ*C/A* with temperature (62 °C applied for 2h). b) Δ*C/A* with AC signal (20 V_{RMS} applied for 2h). c) Δ*C/A* with both stimuli (62 °C and 20 V_{RMS} applied for 2h). Error bars correspond to the standard error. For a) and b), all capacitor areas demonstrate statistical differences between single- and double-layered Parylene C; *** represents *p* values ≤ 0.001. For c), there are no statistical differences for 0.0625 mm² and 0.25 mm², whereas ** represents statistical difference, with *p* values ≤ 0.01. Please note that physical quantities have not been italicized in the graphics for ease of visualization.

Figure 5.19 a) illustrates the relative variation of the capacitance per unit area (Δ*C/A*) with temperature, for all tested areas, with Parylene C deposited as a single or double layer. Overall, the *C/A* decreases with temperature for both single and double layered Parylene C (as inferred by the negative Δ*C/A*), and larger areas seem to promote a greater variation, despite the area-normalization of the data. Moreover, double-layered Parylene C reveals a slightly larger

† Considering that not all data follow a normal distribution (likely due to the measurement of capacitance in loop), Kruskal-Wallis H Test with a significance level of 0.05 was performed to evaluate the differences between single- and double-layered Parylene C for each condition.

decrease in *C/A* as the MIM area increases. This could be due to the interface between both Parylene C layers, which represents a discontinuity of the thin films and is possibly more prone to defect propagation, leading to small decreases in capacitance. Nevertheless, the maximum average decrease in *C/A* in all samples is of about -11%, which does not represent a meaningful variation. However, Parylene C is known to crystallize with temperature, and an increase in crystallization of the polymer could explain the general decrease in *C/A* with this stimulus. Thus, XRD analysis was performed to pristine samples, without chromium electrodes. Said samples were subjected to the same temperature stimulus, and the obtained diffractograms are presented in Figure 5.20. This figure also includes diffractograms for the dielectric layer before and after the annealing step required for PTFE curing during the fabrication of DMF devices (see section 5.1.2).

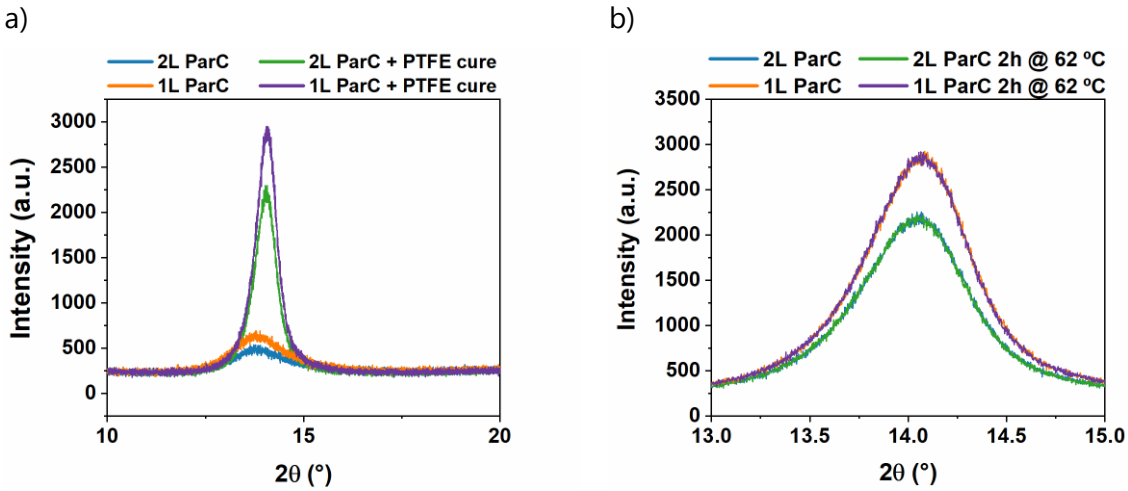

Figure 5.20: XRD diffractograms for the dielectric layer comparing all steps in the fabrication process involving temperature, with Parylene C deposited as a single ("1L ParC") or double ("2L ParC") layer. a) Diffractograms prior to ("ParC") and following PTFE curing at 160 °C for 10 minutes ("ParC + PTFE cure"). b) Diffractograms for the dielectric layer after PTFE curing, prior to and following the temperature stimulus, i.e., heating at 62 °C for 2 hours ("2h @ 62 °C").

Figure 5.20 a) shows that the un-annealed dielectric layer presents XRD intensity peaks at 13.85° and 13.84° for double- and single-layered Parylene C, respectively. Data are in accordance with the literature results reported for Parylene C only[321–323], which suggests that for XRD analysis, the PTFE layer is not substantial. This was expected considering the extremely thin nature of the PTFE coating (50 nm), which falls out of the operation range of the diffractometer. Furthermore, the X-Ray diffraction peak detected at around 2θ = 14° has been associated with the (020) plane of the monoclinic unit cell for Parylene C only[324,325]. The peak for double-layered Parylene C is less intense than its single-layered counterpart (see Figure 5.20 and Table 5.9), which could be due to the interface between both layers. This interface produces

a gap that could be translated to an apparent loss in crystallinity, hence the lower diffraction peak. The full width at half maximum (FWHM) is also slightly larger for double-layered Parylene C, with or without curing, supporting the apparent loss of crystallinity for double-layer structures. After being subjected to curing at 160 °C, samples present a considerable rise in peak intensities, suggesting an increase in the crystallinity of the polymer for both single- and double-layered Parylene C. Similarly to what is observed in as-deposited samples, the double layer structure post-curing presents a lower peak than for single layer structures, again suggesting a seeming loss in crystallinity. Accordingly, the FWHM also decreased after curing, indicating an increase in crystallinity as well. A right shift in the peak position (higher 2θ) is also observed for both structures after curing, which is usually an indication of a contraction of the lattice. Such observation is reflected by the slight decrease in spacing between atomic layers, d-spacing (Table 5.9). Finally, the crystallite size is also increased after the curing process.

Table 5.9: Parameters associated with X-Ray diffractograms, for as-deposited and 160 °C cured single- and double-layered Parylene C.

	Peak height (a.u.)	Peak position (2θ)	FWHM (2θ)	d-spacing (Å)	Crystallite size (Å)
Single layer	252.15	13.84°	1.54	6.39	43
Double layer	164.27	13.85°	1.70	6.39	40
Single layer + cure	1691.37	14.03°	0.66	6.31	116
Double layer + cure	1277.65	14.01°	0.67	6.32	110

Figure 5.20 b) and Table 5.10 compare the cured dielectric layer before and after being subjected to the temperature stimulus, i.e., 2 hours at 62 °C. The pre- and post-temperature stimulus XRD spectra overlap, indicating that low temperature heating does not critically affect the crystallinity of the dielectric lattice, despite the duration of the stimulus. Therefore, the decrease in the capacitance of the dielectric layer after applying the temperature stimulus may not be entirely related to differences in crystallization. Other factors could be triggering the decrease in capacitance, such as a decrease in the dielectric constant, because of the lower polarization of the polymer molecules due to the increase in thermal energy.

Table 5.10: Parameters associated with X-Ray diffractograms, for 160 °C cured single- and double-layered Parylene C before and after applying the temperature stimulus (62 °C for 2 h).

	Peak height (a.u.)	Peak position (2θ)	FWHM (2θ)	d-spacing (Å)	Crystallite size (Å)
Single layer + cure	1691.37	14.03°	0.66	6.31	116
Double layer + cure	1277.65	14.01°	0.67	6.32	110
Single layer + cure + 62 °C for 2 h	1700.28	14.03°	0.65	6.31	116
Double layer + cure + 62 °C for 2 h	1259.11	14.00°	0.68	6.32	112

Turning back to Figure 5.19, Figure 5.19 b) illustrates the variation of the capacitance with AC actuation. For single-layered Parylene C, there is an overall decrease in the capacitance of the dielectric layer after applying the stimulus, however, the variation in capacitance becomes less pronounced as the area of the MIM structures increases. Regarding double-layered Parylene C, the capacitance increases after applying the stimulus. One possible explanation is the disorientation of the polymer molecules with the AC field, which could contribute to the increment of the capacitance. This phenomenon may be more expressive in double-layered Parylene C due to the additional interface between the two layers, which could facilitate molecule rearrangement, in comparison to the single-layer counterpart. Overall, both capacitance variations (for single- and double-layered Parylene C) tend to decrease as the area increases. This observation could be due to the decrease of the influence of the parasitic capacitances that may occur in the overlapping electrodes region.

It should be noted that the maximum absolute variation in capacitance is of around 3%, which is a good indication of the stability of the dielectric layer when subjected to an AC signal stimulus, as opposed to thermal stimulation, which may lead to three times higher variations in capacitance. This observation is in accordance with the literature, where AC signals are advised for droplet motion in electrowetting-based devices, for a number of reasons including: 1) contact angle saturation occurs for higher voltages[326]; 2) prevention of charge injection on the dielectric layer[327]; 3) reduction of the biofouling phenomenon (adhesion of biomolecules to the dielectric layer)[117] and 4) improvement of mixing within the droplet[115].

Lastly, Figure 5.19 c) illustrates the variation in the capacitance when a dual stimulus is applied, merging both temperature and AC signal stimuli. For both single- and double-layered Parylene C, capacitance decreased after applying the stimuli to the MIM structures.

Nevertheless, this is more expressive for single-layered Parylene C, even though at a very small scale, with a maximum absolute variation of merely 4% approximately. Indeed, single-layered Parylene C presents a more stable behavior regarding capacitance variations for individual stimuli, consistently close to 0%, with a maximum variation around 3%. This tendency is only reversed when both stimuli are applied simultaneously, and in this case, the double-layered Parylene C clearly presents higher stability, with a maximum absolute capacitance variation which does not reach 2%, indicating that this approach could be a safer choice for electro-wetting applications such as DMF. Interestingly, for the double-layer, there seems to be an approximate sum of the capacitance variance for each individual stimulus. The maximum absolute variation in capacitance is of about 1.4%, which is an intermediate value between -11% measured for the thermal-only stimulus and +3% measured for the AC signal-only stimulus. Nonetheless, this is a small variation percentage, which suggests that the dielectric layer under test is perfectly capable of withstanding heating and an AC electric field over a period of two hours.

The maximum leakage current (total range of 200 V) was measured to further characterize the MIM structures produced. Please note that, in this case, data were not normalized since the absolute differences in leakage current are relevant to understanding whether devices are close to reaching dielectric breakdown. Figure 5.21 illustrates the maximum leakage current measured for all stimuli applied to the MIM devices.

a) Temperature stimulus: 62 °C for 2h

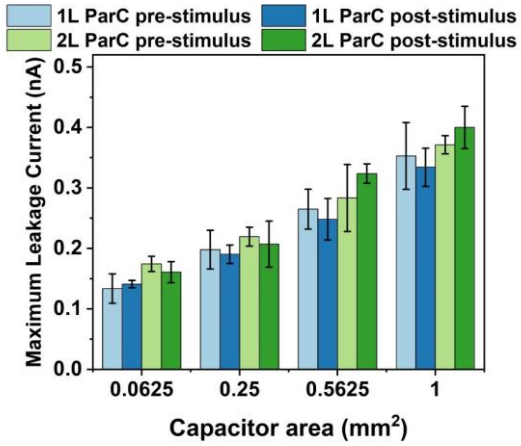

b) AC stimulus: 20 V_{RMS} for 2h

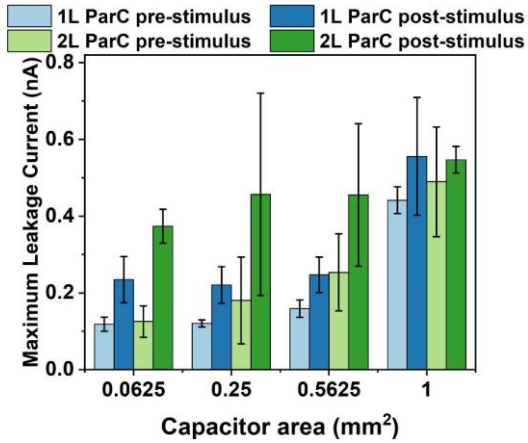

c) Dual stimuli: temperature + AC signal for 2h

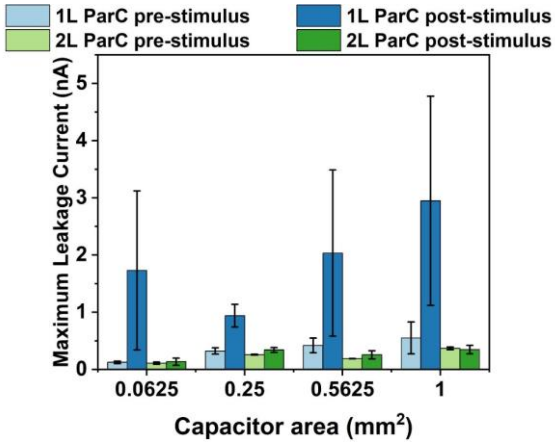

Figure 5.21: Maximum leakage current for the dielectric layer (Parylene C and PTFE) with Parylene C (ParC) deposited as a single ("1L") or double layer ("2L"), for four different MIM capacitor areas. Leakage measurements were performed before ("pre-stimulus") and after ("post-stimulus") applying the stimulus. a) Maximum leakage current measured for the temperature stimulus (62 °C applied for 2h). b) Maximum leakage current measured for the AC stimulus (20 V_{RMS} applied for 2h). c) Maximum leakage current measured for both stimuli (62 °C and 20 V_{RMS} applied for 2h). Error bars correspond to the standard error.

Generically, the maximum leakage current measured increases with the area of the MIM capacitors. This is expected since for larger areas there is a higher probability of reaching defect-rich spots that promote current flow through the dielectric layer. Considering the temperature stimulus (Figure 5.21 a)), for both single- and double-layered Parylene C, the maximum leakage current is low, below 0.4 nA, and does not considerably vary after applying the stimulus. Such observation suggests that the decrease in capacitance (namely for double-layered Parylene C) is mostly due to molecule rearrangements within the polymer lattice and not to the occurrence of current pathways through the dielectric layer. As for the AC signal stimulus

(Figure 5.21 b)), the maximum leakage current is consistently below 0.6 nA, indicating good isolation of said layer. Nevertheless, there appears to be a constant increase in the maximum leakage current after applying the AC stimulus, for both single- and double-layered Parylene C. This is consistent with subjecting the dielectric layer to an electric field, which may remove some electrons from their positions within the molecular structure, thus creating paths for current flow through the insulation layer. Nevertheless, this effect remains negligible considering that the leakage currents are acceptable for dielectrics. Lastly, for two stimuli applied to the dielectric layer (Figure 5.21 c)), the leakage current becomes considerable in the case of single-layered Parylene C, even though current does not reach high levels, with a maximum average below 3 nA. However, this finding suggests that when an AC signal and temperature are simultaneously applied to a dielectric layer comprising single-layered Parylene C, the leakage current could become a relevant mechanism for the decrease in capacitance. It is also noteworthy that double-layered Parylene C remains on a low leakage current regime after the dual stimulus, which again suggests that this could be a safer option for electrowetting-based DMF devices than single-layered Parylene C. Of course, it should be noted that leakage currents were measured by applying much higher voltage (200 V total range) to the insulator than for measuring the capacitance (10 V total range), therefore further studies would be required to pinpoint the exact weight of this mechanism on the final reduction of the capacitance of the MIM structures.

5.8.2 DMF devices produced with double-layered Parylene C

DMF devices were produced exactly as previously disclosed (section 5.1), with double-layered Parylene C. Of course, in this case, a hydrophobic layer of PTFE was applied to increase the droplet contact angle and facilitate motion. As discussed in section 2.4.4, the hydrophobic layer reduces the surface energy in contact with the droplets. Lower surface energy leads to less friction between the droplet and the surface, and consequently, droplet motion at lower voltages[61,328]. PTFE is also a dielectric, however, as demonstrated further below, this layer will not expressively influence the overall dielectric behavior of the devices. Briefly, Parylene C and the hydrophobic layer form parallel capacitors, with similar dielectric constants, therefore the capacitance of a 50 nm layer of the PTFE in FC-40 solution will be negligible in comparison to the 2 µm layer of Parylene C (as confirmed by Figure 5.22).

Parylene C presents a very high dielectric strength (approximately 220.5 V/µm[276]), thus enabling droplet motion at relatively high actuation voltages, ideally with low risk of dielectric breakdown. Of course, the choice of Parylene C thickness is paramount for device operation,

and for the DMF devices developed herein, an optimal thickness of 2 µm was chosen. This thickness enables a large voltage operation range (breakdown will theoretically occur at around 441 V). Figure 5.22 represents the behavior of the dielectric layer according to the thickness of Parylene C, in terms of breakdown voltage and actuation voltage required for a 20° shift in contact angle (from 120° to 100°) in EWOD conditions. An initial angle of 120° was chosen considering that it is the approximate initial contact angle with the hydrophobic PTFE layer (further discussed in section 9.5). The EWOD actuation voltages per Parylene C thickness were determined in accordance to the Lippmann-Young equation (Equations 2.4 and 2.5). Two EWOD conditions are represented: 1) voltage required to achieve a 20° shift in contact angle for a Parylene C-only dielectric layer ("EWOD ParC") with varying thickness and 2) voltage required to achieve a 20° shift in contact angle for a dielectric layer comprised of a 50 nm layer of the hydrophobic layer plus a Parylene C layer with varying thickness ("EWOD ParC + 50 nm PTFE"). Considering that the hydrophobic layer is based on a 0.6% wt/wt solution of PTFE AF 1600 (ε_R = 1.93[329]) in Fluorinert FC-40 (ε_R = 1.9 [330]), a relative permittivity of 1.9 was considered in calculations with the hydrophobic layer.

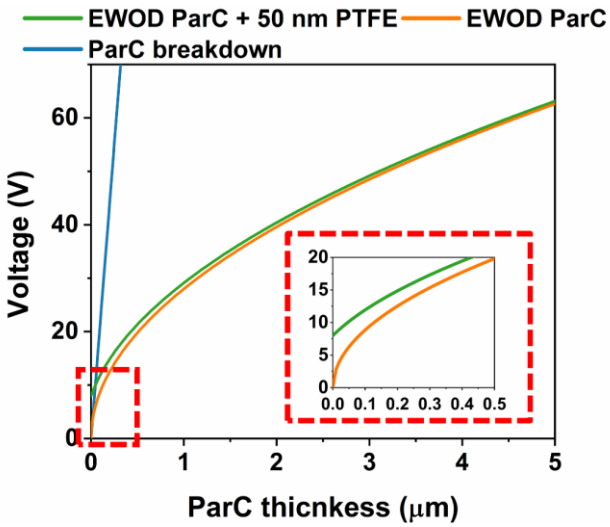

Figure 5.22: Behavior of Parylene C with varying thickness in terms of breakdown voltage ("ParC breakdown"), and voltage required to induce a contact angle shift of 20°, in EWOD conditions. For the last case, two situations are represented: a dielectric layer comprised of Parylene C only ("EWOD ParC") with varying thickness and a dielectric layer comprised of 50 nm of PTFE plus a Parylene C layer with varying thickness ("EWOD ParC + 50 nm PTFE"). The inset shows the small region where the difference in required actuation voltage for Parylene C only and Parylene C + PTFE is more relevant. The breakdown voltage line was omitted for better visualization. Please note that for the breakdown voltage, only Parylene C was considered, since the breakdown voltage is considerably high.

Figure 5.22 clearly illustrates the great advantage of using a dielectric layer featuring Parylene C, with a high dielectric strength, which allows for a wide range of EWOD actuation voltages, suitable even for low-conductivity solutions that may require higher actuation voltages. Also, adding a hydrophobic layer results in little variations to the actuation voltages required, which is also a good indicator for the suitability of the chosen PTFE layer to the Parylene C dielectric. This also attests that the results obtained for MIM structures may also be associated to the dielectric layer of DMF devices, comprised of Parylene C and the hydrophobic layer, with minor error.

Double-layered devices were also characterized in terms of droplet speed and the ability to withstand long LAMP reactions, up to 2 hours (Figure 5.23). For determination of droplet speed, videos of droplets moving back and forth from one electrode to an adjacent one were captured by a digital microscope (Handheld Digital Microscope Pro from Celestron, Torrence, CA, USA). Such videos were then used to determine the time required for both the head and the tail of droplets to start moving from an unenergized electrode to the adjacent energized electrode. Speed was determined by dividing the travelled distance by the time required to travel it. Results of long LAMP reactions will be further discussed in section 6.3.

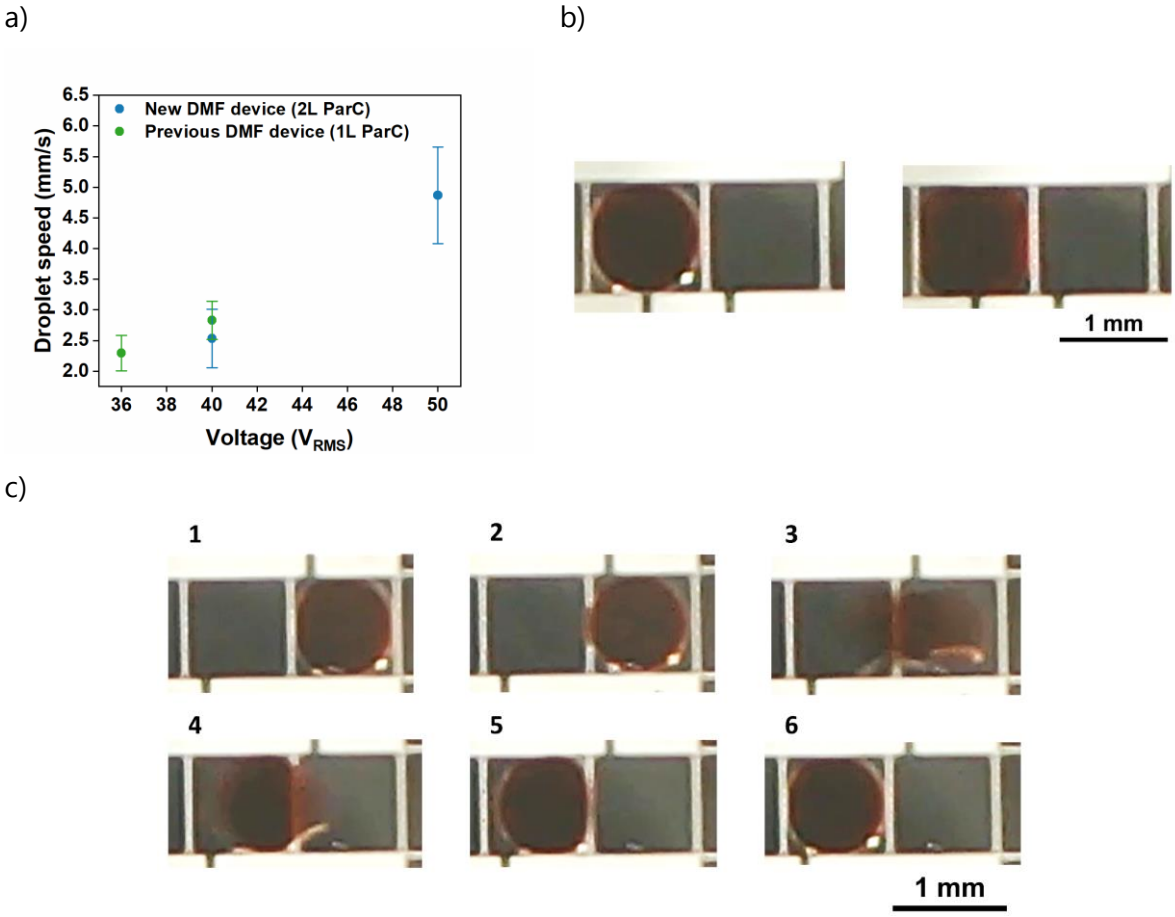

Figure 5.23: Aspects of DMF devices based on double-layered Parylene C. a) Droplet speed achieved on the new DMF devices, featuring Parylene C deposited in double-layer ("2L ParC"), in comparison to droplet speed achieved on previous DMF devices, with single-layered Parylene C ("1L ParC"). b) Shape acquired by a droplet under a 40 V_{RMS} (left) or 50 V_{RMS} (right) signal. c) Sequence of video frames showing droplet motion on a DMF device based on double-layered Parylene C (40 V_{RMS} applied to the droplet).

As will be demonstrated on section 6.3, the great advantage of using double-layered Parylene C on DMF devices is the possibility of performing longer isothermal nucleic acid amplification reactions (in this case, LAMP reactions) without device degradation. In general, longer reactions may be required for very low-concentration targets, or for standard concentration targets which are more difficult to amplify due to a number of factors such as sample complexity or pH, among others[331,332]. Moreover, double-layered Parylene C allows for the application of a higher amplitude voltage signal without device degradation, which in turn results in higher droplet motion speeds (Figure 5.23 a)). This increase in droplet motion speed can be relevant to prevent reagent degradation (e.g. photobleaching during dislocation to reaction sites in the case of DMF-LAMP) or other undesirable effects in time-sensitive reactions. Figure 5.23 b) demonstrates that applying 50 V_{RMS} to droplets, instead of 40 V_{RMS}, leads to a higher coverage of the electrode due to the lower final contact angle (Equations 2.4 and 2.5), which

may be relevant for applications where a fixed area is required (e.g. impedance measurements). Lastly, Figure 5.23 c) illustrates the droplet motion process from one electrode to an adjacent one, in a DMF device comprising double-layered Parylene C, which is as straightforward as for devices with single-layered Parylene C.

SEM (scanning electrode microscopy) images of the bottom plate of double-layered DMF devices are available in Appendix D.

Having completed the design and production of an adaptable DMF platform, the next logical step was to experiment multiple nucleic acid amplification monitoring strategies, thoroughly analyse each one and finally discover which one provides the most accurate results.

6

FLUORESCENCE MEASUREMENTS

Disclaimer

Some excerpts of this section have been published in the following publications:

Coelho, B. J.; Veigas, B.; Bettencourt, L.; Águas, H.; Fortunato, E.; Martins, R.; Baptista, P. V.; Igreja, R. *Digital Microfluidics-Powered Real-Time Monitoring of Isothermal DNA Amplification of Cancer Biomarker*. Biosensors (Basel) **2022**, 12 (4), 201. https://doi.org/10.3390/bios12040201.

Coelho, B. J.; Veigas, B.; Bettencourt, L.; Águas, H.; Fortunato, E.; Martins, R.; Baptista, P. V.; Igreja, R. *Digital Microfluidics for Amplification Monitoring of Cancer Biomarkers*. Mater Proc **2022**, 8 (1). https://doi.org/10.3390/materproc2022008103.

B. J. Coelho produced all the required digital microfluidic devices, and further designed, optimized and performed all loop-mediated isothermal amplification reactions, either on- or off-chip. She also designed, tested and optimized all on-chip protocols, as well as fluorescence reading protocols. She further created the software used for processing all images acquired by microscopy. Lastly, she designed, tested and optimized the new temperature control system.

Since its discovery in 1993[333], fluorescence detection quickly became the gold standard methodology for real-time nucleic acid amplification monitoring, leading to the subsequent development of specialized equipment[334–337] and reagents[337,338], in search for faster and more accurate detection. Considering this gold standard, as well as the foundational concept of this PhD thesis to achieve a wider scientific community by means of general-purpose technologies, fluorescence microscopy through a standard optical microscope was the chosen detection strategy.

6.1 Off-device optimization of fluorescence measurements

As might be expected, a standard microscope with the possibility for fluorescence analysis is not the optimal choice for such a sensitive application, thus before proceeding to on-chip fluorescence measurements, it is paramount to optimize fluorescence readout outside the DMF devices. As a first approach, transmission spectra from the available microscope filter set (U-MWB2 wideband blue fluorescence filter cube) were compared to the absorption and emission spectra for the EvaGreen® fluorophore. Figure 6.1 illustrates the fore-mentioned spectra, as provided by the respective manufacturers.

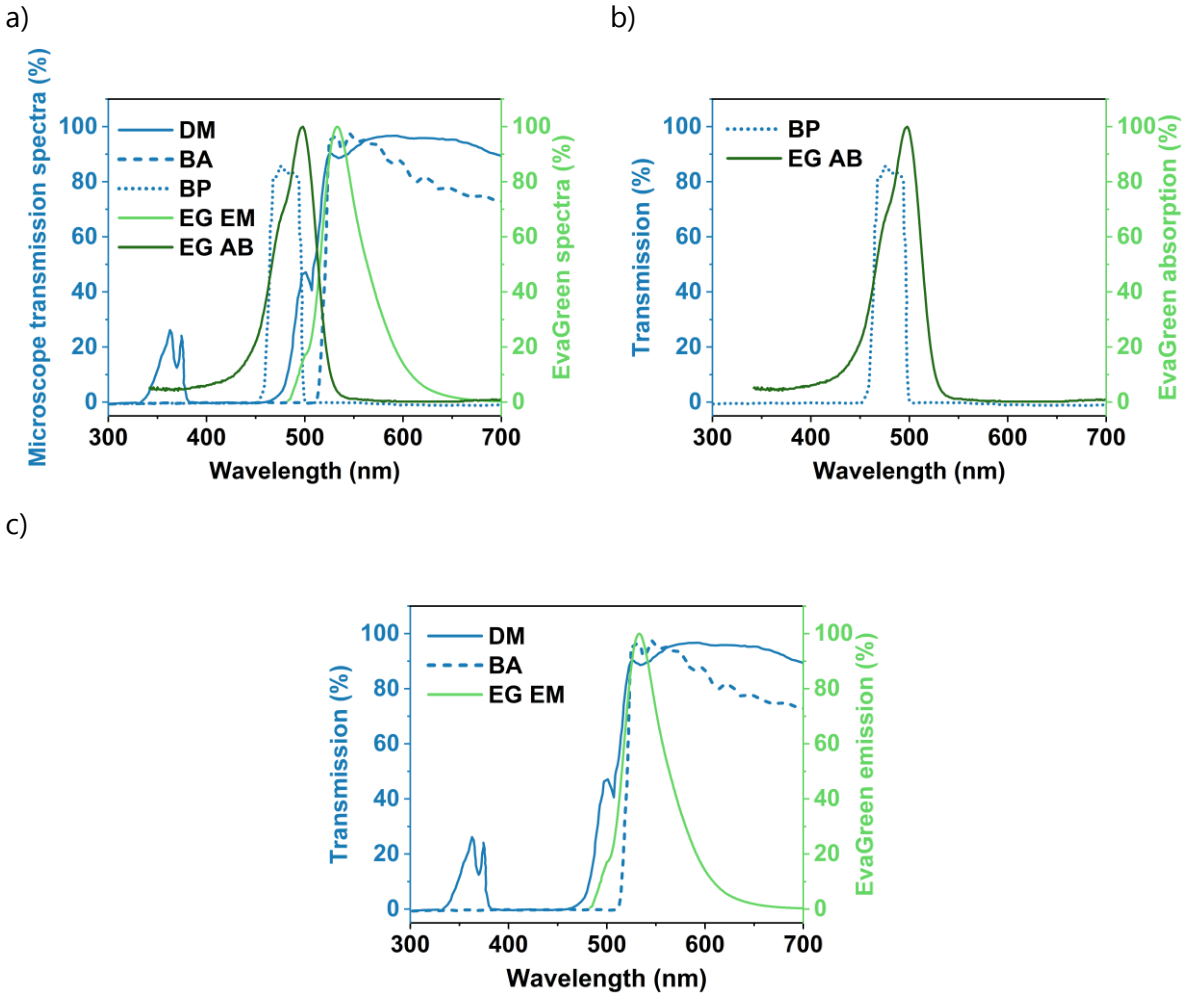

Figure 6.1: Schematic representation and transmission spectra for all filter components of the U-MWB2 filter cube according to manufacturer specifications, as well as absorption ("EG AB") and emission ("EG EM") spectra for the EvaGreen® fluorophore, also according to manufacturer specifications. Transmission spectra include the dichroic mirror ("DM"), the barrier/emission filter ("BA") and the band-pass excitation filter ("BP"). a) Representation of all spectra, related to both the microscope and the fluorophore. b) Focus on the elements involved in the excitation of the EvaGreen® fluorophore, i.e., the spectrum of the microscope band-pass emission filter and the EvaGreen® absorption spectrum. c) Focus on the elements involved in the emission readout of the EvaGreen® fluorophore, i.e., the spectrum of the microscope barrier/emission filter and the EvaGreen® emission spectrum.

As illustrated on Figure 6.1 a), the U-MWB2 filter cube appears to be adequate to detect fluorescence from the EvaGreen® fluorophore with both absorption and emission spectra falling within the respective filter transmission areas. According to Figure 6.1 b), a relatively large area of the absorption spectrum of the EvaGreen® fluorophore falls out of the range of the band-pass excitation filter, and therefore the excitation of the fluorophore will not attain maximum efficiency. Nevertheless, the excitation filter still covers a large portion of the absorption spectrum of the EvaGreen® fluorophore, which is a good indicator of the compatibility between the fluorophore and the available microscopy filters. Regarding Figure 6.1 c), it is clear that the

barrier filter will block a small fraction of the emission spectrum of the fluorophore, which will not be transmitted to the detector of the microscope. Nevertheless, most of the emission area of EvaGreen® will be successfully transmitted. Thus, the agreement between the fluorophore characteristics and the U-MWB2 filter cube is satisfactory enough to proceed with experimental tests to optimize the EvaGreen® fluorescence measuring conditions.

For such purpose, several LAMP reactions were performed, with multiple conditions, and fluorescence for each sample was measured with a fluorescence microscope. All reactions were performed by adding the following reagents, in the presented order (master mix): 1× of ThermoPol® reaction buffer (New England Biolabs, Ipswich, MA, USA), 1 M betaine (Sigma–Aldrich, St. Louis, MO, USA), 4 mM magnesium sulfate ($MgSO_4$, New England Biolabs), 0.8 µM of both FIP and BIP, 0.4 mM of dNTP mix (ThermoFisher Scientific, Waltham, MA, USA), 0.2 µM of both FP and BP, 1.5x EvaGreen® (Biotium, Fremont, CA, USA) and 8 U of *Bst* DNA polymerase (large fragment; New England Biolabs). Note that all primers were obtained from Stab Vida (Caparica, Portugal). The concentration of EvaGreen® was optimized to fit the operation range (further details below). For the positive controls (amplifying samples), a DNA fragment containing the target sequence derived from the *c-Myc* gene was added to the master mix for a final concentration of 0.5 ng/µL; whereas for the negative controls (non-amplifying samples), PCR-grade water was added instead. The *c-Myc* fragment used in this study was obtained from a plasmid vector, also containing an antibiotic resistance gene, which was further introduced in *E-coli* bacteria. Bacteria were selected through the addition of ampicillin to the respective growth medium, and were further cultured prior to DNA extraction, yielding thousands of copies of the target DNA. Amplifying and non-amplifying samples were heated at 65 °C for 60 min, on a thermal cycler. All primer sequences are described in Table 6.1.

Table 6.1: Primer sequences used for the LAMP-amplification of the *c-Myc* oncogene.

Primer	Sequence (5´- 3´)
FP	TCTGAAGAGGACTTGTTGC
BP	TTCAGTCTCAAGACTCAGC
FIP	CTTTTCCTTACGCACAAGAGTTCC-GGAAACGACGAGAACAG
BIP	ACGATTCCTTCTAACAGAAATGTCC-CAAGGTTGTGAGGTTGCA

For EvaGreen® concentration optimization, 1 µL droplets of both positive and negative LAMP controls were sandwiched between dummy bottom and top plates (180 µm height), mimicking on-chip conditions. This setup was further placed under the fluorescence

microscope and samples were irradiated by an EXFO X-Cite Series 120 Q lamp (Excelitas, Waltham, MA, USA). Both excitation and emission were processed through the above-mentioned U-MWB2 blue broadband filter cube. Three different concentrations of EvaGreen® fluorophore were tested (1x, 1.5x and 2x) by adding a suitable volume at the end of the reaction time. This procedure was repeated in triplicate for all conditions. For each condition, droplet fluorescence images were processed by an in-house designed software which essentially divides the image into two color channels (green for the fluorescent droplet and black for the background) following an Otsu segmentation algorithm and subsequently determines the median fluorescence intensity for both droplet and background, subtracting the latter to the first. Figure 6.2 represents the output results of the above-mentioned experiment.

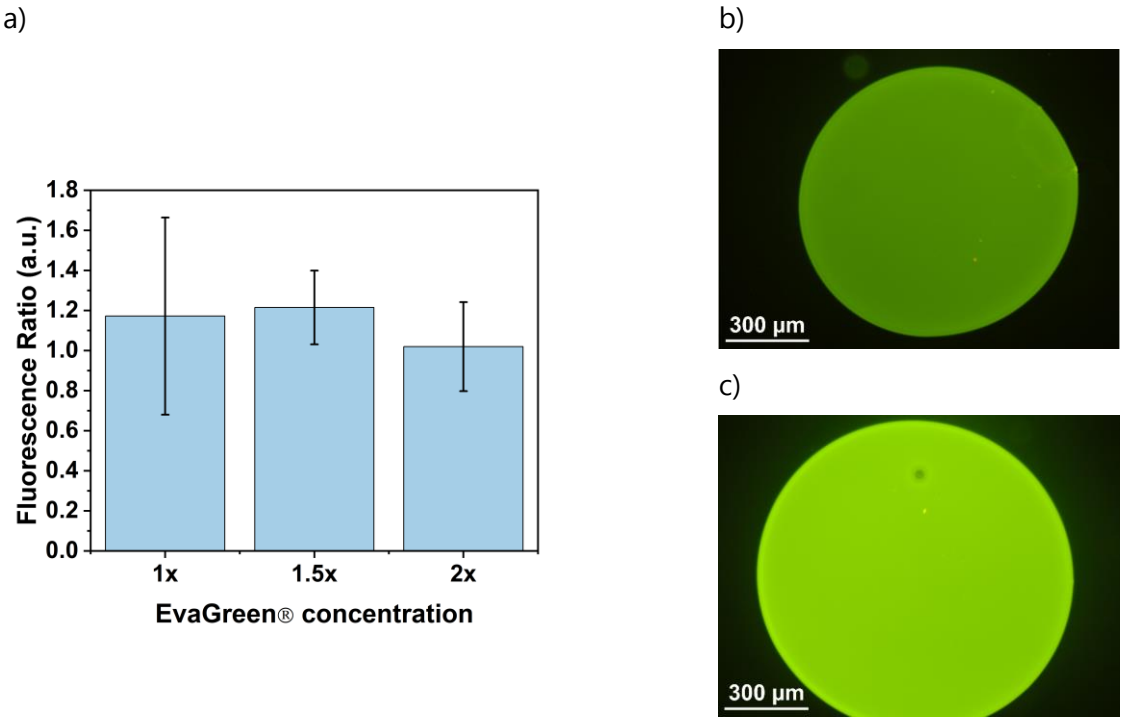

Figure 6.2: Fluorescence ratio between amplifying and non-amplifying samples[‡] for multiple EvaGreen® initial concentrations (1x, 1.5x or 2x). Error bars correspond to the confidence interval at 90% for each case, for a total of three experiments. Example of non-amplifying (b) and amplifying (c) samples.

One striking remark from this experiment is that the basal fluorescence for EvaGreen® is rather high for any initial concentration of the fluorophore, as can be deduced by the relatively small variation in intensity, as well as small fluorescence ratio for all tested conditions. This could be due to unspecific binding of the fluorophore to primers or primer-generated

[‡] The fluorescence ratio between amplifying and non-amplifying samples is determined by $\frac{Amplifying\ average\ fluorescence}{Non-amplifying\ average\ fluorescence}$

structures, or other reagents that allow for the formation of hydrophobic domains where the EvaGreen® fluorophore may undesirably emit radiation. Nevertheless, amplifying samples generally achieve higher fluorescence intensity than non-amplifying samples, regardless of EvaGreen® concentration (fluorescence ratios above 1). However, EvaGreen® at 1.5x cumulatively presents a reasonable difference in fluorescence between amplification and non-amplification, as well as a less significant error.

6.2 On-device monitoring of nucleic acid amplification through fluorescence

As can be seen on section 6.1, performing a LAMP reaction involves mixing the LAMP master mix with the test sample, either PCR-grade water for negative controls or a solution containing the target DNA for positive controls. Mixing can be performed on- or off-chip, nevertheless, due to the low volume of droplets carried by DMF, laminar flow is predominant on-chip, meaning that merging two or more droplets does not immediately lead to mixing of droplet content, or uniformization of molecule distribution along the merged droplet[339–342]. Several strategies have been developed to address the mixing issue, namely AC signal frequency tuning[341–345] or specific electrode path architectures[339,340,346]. Herein, active mixing is included in the DMF-LAMP routine through the combination of two mixing strategies: low AC frequency mixing and straightforward back-and-forth motion, to ensure uniform and efficient mixing of the LAMP master mix with test samples. The efficiency of mixing LAMP reagents inside the DMF device versus mixing reagents off-chip by vortex agitation (before performing the LAMP reaction on-chip) is also compared. In both cases, the pre-LAMP preparation of the chip is similar, and was previously explained in section 5.1. Briefly, three strips of polyimide tape are placed on each side of the electrode area at the bottom plate, ensuring a 180 µm spacing between top and bottom plates. Simple nail polish is then applied around the electrode area, after which the top plate is positioned over the bottom plate, aligning the drilled holes with corresponding reservoirs on the bottom plate. The DMF chip is then heated at 55 °C for 10 min to dry the nail polish and seal the electrode area. Before sample addition, each chip was filled with 5 cSt silicone oil previously degassed in low vacuum for at least 3 h.

For on-chip reagent mixing, three different solutions were prepared: 1) LAMP master mix (see section 6.1); 2) DNA solution consisting of the target *c-Myc* gene fragment resuspended in 1x ThermoPol® reaction buffer and 3) standard 1x ThermoPol® reaction buffer. All three

solutions were inserted on separate reservoirs, as illustrated by Figure 6.3 a). The LAMP master mix was divided into two partitions (each containing nine droplets of approximately 180 nL each, considering the electrode area and top/bottom plate spacing), which were moved towards the reaction areas, and one droplet from both the 1x reaction buffer and the solution containing the DNA target were added to the master mix partitions. Excess from all three solutions remaining on the reservoirs was removed to prevent air bubble formation due to device heating for LAMP, and degassed silicone oil was used to cover the inlets as to avert the entrance of air. The small droplets (DNA solution and the buffer solution) were merged with the LAMP master mix partitions at the reaction areas and mixing was performed by shifting the frequency of the actuation signal to 0.5 Hz for 6 s, followed by back-and-forth motion of the droplets between the larger reservoirs at the bottom part of the chip (Figure 6.3 b)). Since a general-purpose microscope was used in this work, the fluorescence detection performance was far from ideal, and the maximum excitation intensity from the light source had to be used in order to detect the fluorescence emitted by the sample. This approach leads to severe photobleaching of the samples, which in turn hinders the detection of amplifying nucleic acids (see Appendix E for more information regarding photobleaching). To prevent said photobleaching, the resulting fully mixed droplets were further sub-divided into three smaller droplets (Figure 6.3 c)). The DMF platform (chip and support system) was then placed under the microscope and heated for a 59.5 °C setpoint measured at the top plate, for 90 min. During the LAMP reaction, every 10 min, one small droplet from each control is irradiated (Figure 6.3 c)) and the emission captured by the microscope detector is stored in image format. With this protocol, during the 90 min of reaction, each droplet is irradiated a maximum of three times, which greatly contributes to reduce photobleaching resulting from the use of non-specialized equipment such as a real-time cycler. For droplet motion, an AC signal with 40 V_{RMS} and 5 kHz was used, whereas during a LAMP reaction, the signal amplitude was reduced to 20 V_{RMS}, to prevent device degradation. Finally, the endpoint LAMP products (i.e. all droplets from each reaction) were pulled together by DMF, removed from the device and submitted to agarose gel electrophoresis analysis.

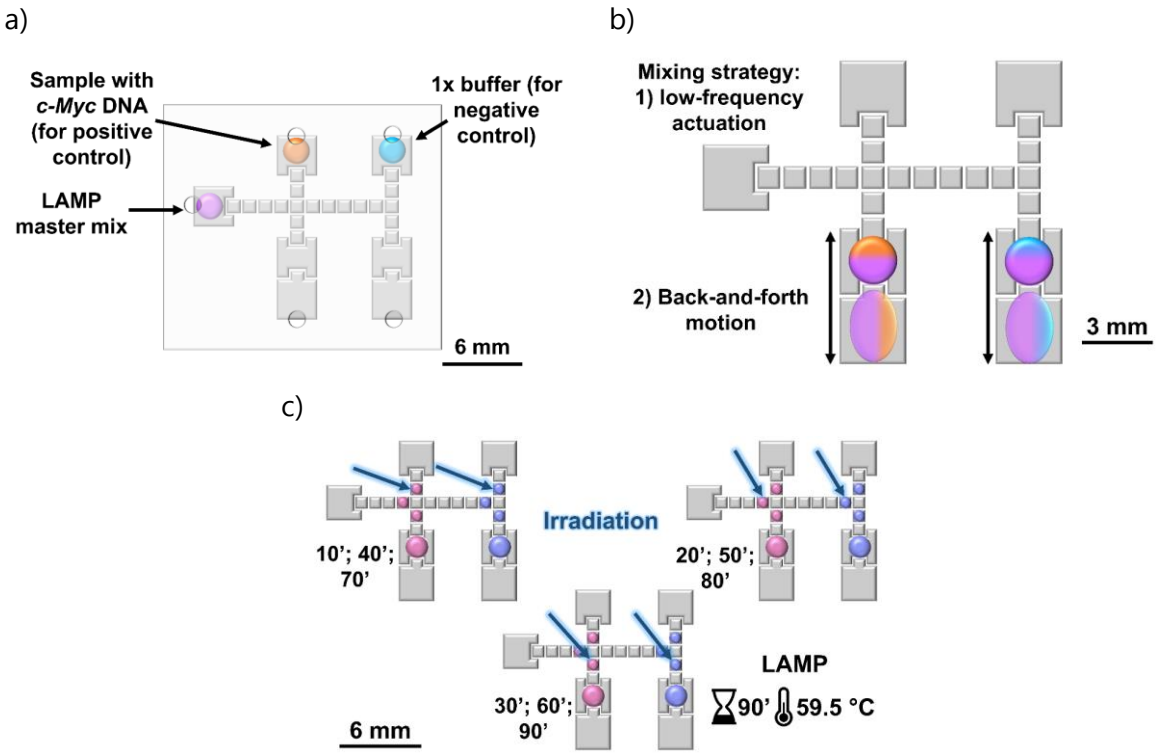

Figure 6.3: Steps required for on-chip LAMP amplification with on-chip reagent mixing. Droplets containing the LAMP master mix, *c-Myc* DNA and 1x reaction buffer are inserted onto the respective reservoirs (a). The LAMP master mix is then moved towards the two reservoirs at the bottom of the chip (1.62 µL per large droplet, achieved with nine small 180 nL droplets). For the positive control, a small droplet of DNA solution is merged with one partition of the LAMP master mix, whereas for the negative control, a small droplet of 1x reaction buffer is merged with the second partition of the LAMP master mix. Mixing is performed by low AC frequency actuation followed by back-and-forth droplet motion (b), and three droplets are withdrawn from each control and moved towards irradiation sites (c). The DMF chip is then heated for a 59.5 °C setpoint measured at the top plate, for 90 min and droplets are sequentially irradiated (c). Note that for figures b) and c), the top plate was omitted for better visualization.

For off-chip reagent mixing, positive and negative controls were prepared as described in section 6.1 and reagents were mixed through vortex mixing. Both controls were then added to the DMF chip, and the protocol followed as above, except for the steps required for on-chip mixing. Appendix F provides a more detailed insight on this protocol.

After determining the ideal conditions for fluorescence measurements, DMF-LAMP reactions were performed with reagent mixing on-chip and off-chip. In both cases, for each 10 min, one positive droplet and one negative droplet were quickly exposed, and the resulting emission was captured as an image. At the end of the LAMP reaction, all images were processed by the previously mentioned in-house designed software. Each experiment was performed at least four times. The Z score for fluorescence was then determined, according to Equation 6.1:

$$Z\ score = \frac{X - X_i}{SD_{X_i}} \quad (6.1)$$

where X is the current fluorescence measurement, Xi is the first fluorescence measurement and SD_{Xi} is the standard deviation for the first fluorescence measurement. The Z score was chosen as the primary statistical treatment for the fluorescence data, as it illustrates the capacity of the system to detect changes in fluorescence intensity, by normalizing the data to the standard deviation of the baseline (i.e. the first measurement, at 10 min).

Figure 6.4 summarizes the results achieved for fluorescence measurements.

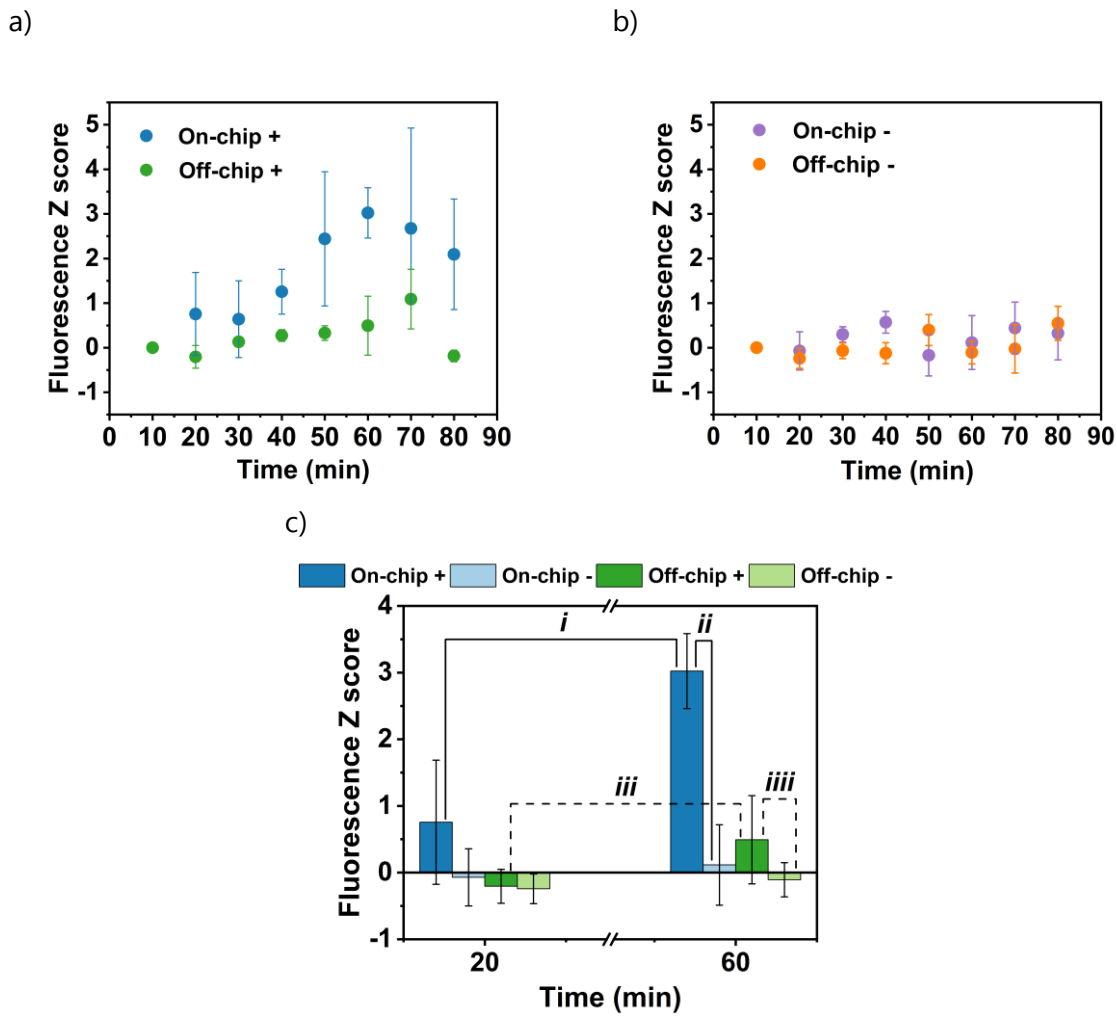

Figure 6.4: Fluorescence Z score analysis for LAMP reactions. a) Z scores for amplifying "+" samples, where reagents were mixed either on-chip or off-chip. b) Z scores for non-amplifying "-" samples, also comparing reagent mixing on-chip and off-chip. c) Fluorescence Z scores for early and final stages of DMF-LAMP reactions, concerning all tested conditions, namely amplifying and non-amplifying samples, as well as off-chip and on-chip reagent mixing. Statistical analysis was performed through one-way ANOVA (analysis of variance) and means comparison by the Tukey method, after non-rejection of normality and variance homogeneity by Shapiro-Wilk[347] and Brown-Forsythe[348] tests, respectively. *i*: $p = 0.048$, *ii*: $p = 0.002$, *iii*: $p = 0.210$, *iiii*: $p = 0.139$ for a significance level of 0.05. In all cases, error bars correspond to the 90% confidence interval of a minimum 4 experiments for each time frame.

Figure 6.4 a) shows that on-chip mixing yields a greater variation in fluorescence for amplifying samples, and therefore a superior capacity to detect the production of double-stranded DNA as a result of LAMP amplification. With on-chip mixing, DNA amplification is clearly visible from 40 min onwards, with the fluorescence amplification plateau reached at 60 min. As for off-chip mixing, the largest increase in fluorescence occurs from 60 min to 70 min, at which point the plateau is reached. Cumulatively, lower Z scores are observed for off-chip mixing, influenced by greater fluctuations in the initial fluorescence measurements,

possibly suggesting an increase in mixing efficiency on-chip versus its off-chip counterpart. Data in Figure 6.4 b) demonstrate that fluorescence in non-amplifying samples remains mostly unchanged as expected, with Z scores close to 0, regardless of on-chip or off-chip mixing. Still, some background noise of the system is observed, probably due to the formation of primer dimers resulting from the initial molecular steps of the LAMP reaction, as the EvaGreen® fluorophore intercalates into double-stranded DNA[349] (see Appendix G). Appendix H provides additional information regarding relative fluorescence.

Figure 6.4 c) outlines the fluorescence Z scores of all tested conditions (on-chip and off-chip mixing, amplifying "+" and non-amplifying "-") for early and final stages of the DMF-LAMP reactions. The DMF platform allows for distinction between amplifying and non-amplifying samples, whether mixing is performed on-chip or off-chip. In both cases, fluorescence increasingly deviates from the baseline, nevertheless, said deviation is larger for on-chip reagent mixing, as previously observed. Data presented on Figure 6.4 suggest that the proposed DMF platform is suitable for performing real-time LAMP using 0.5 ng/µL (or 90 pg) of the *c-Myc* proto-oncogene template, a fair amount of DNA considering the range reported in the literature[25,26]. Moreover, the proposed dual on-chip mixing strategy based on low frequency signal actuation and back-and-forth motion for mixing the LAMP master mix with test sample seems to promote a relevant decrease in initial fluorescence variability as reflected by overall larger Z scores. This suggests that the proposed system seems to be able to detect smaller changes in fluorescence when LAMP master mix and sample are mixed on-chip. The dual mixing strategy has thus proven to be successful in overcoming laminar flow, a significant constraint for mixing in microfluidic systems[342,345]. The simplified setup still requires some optimization as to increase the dynamic range of the signal acquisition, mainly by reducing the background noise for the non-amplifying reactions. Once this signal-to-noise ratio is improved, the proposed system might be of use for nucleic acid detection and semi-quantification (comparison) between samples. Furthermore, the integration of said nucleic acid detection onto a portable DMF platform equipped with fluorescence detection capability is envisioned. This could be achieved through the miniaturization of all the DMF operating hardware (i.e. signal wave generator, signal amplifier, power source, voltage control hardware and temperature control hardware – see sections 5.4 and 5.5), following the lead of other portable DMF systems such as PortaDrop[350], LampPort[169] or the DropBot DB3-120 kit[351].

6.3 Adding a control gene: the case of *18S*

In the previous section, it was proved that the developed fluorescence detection system is capable of detecting the fluorescence of samples circulating within DMF devices, as well as following the progression of LAMP reactions. Thus, considering that the DMF devices produced can accommodate two different samples, it would be interesting to add a second gene for detection. This would be particularly relevant if the second gene considered were a control gene, which would open the path for gene expression analysis. Several criteria have been defined in the literature for the classification of "control gene" (commonly known as a "housekeeping" gene or reference gene), namely a threshold cycle close to the target or a low expression variability between tissues. However, the most important criterium is maintaining a constant expression regardless of experimental conditions, obviously with a sequence different from that of the target[352,353]. A plethora of control genes have been identified and discussed in the literature, namely *GAPDH* (glyceraldehyde-3-phosphate dehydrogenase), *ACTB* (β -actin), *28S rRNA* (28S ribosomal RNA) or *18S rRNA* (18S ribosomal RNA), just to name a few[352–354]. The latter, *18S rRNA* (referred to as *18S* for simplicity) was chosen control gene, considering immediate availability of such gene, as well as the high degree of experience in handling this gene within the group.

For on-chip gene expression analysis, complementary DNA (cDNA) was used, instead of plasmid DNA used so far, since the control gene is ribosomal RNA. Thus, total RNA was extracted from HCT116 cells containing both *c-Myc* and *18S* fragments and was further reverse-transcribed to cDNA. The optimal amplification conditions for *18S* are different from *c-Myc*, however *c-Myc* also produces LAMP amplification with this protocol. Considering that *18S* does not produce any amplification with the LAMP protocol used so far, the new protocol (optimized for *18S*) was selected for amplification of both genes on-chip. This new protocol is as follows: 1× of ThermoPol® reaction buffer, 0.8 M betaine, 2 mM $MgCl_2$, 0.64 µM of both FIP and BIP, 0.64 mM of dNTP mix, 0.2 µM of both FP and BP, 1x EvaGreen® and 8 U of *Bst* DNA polymerase. Moreover, the sequences of primers used for *18S* are described below:

Table 6.2: Primer sequences for amplification of the *18S* gene.

Primer	Primer sequence (5' to 3')
FIP	TTCGTCACTACCTCCCCGGGCTACCACATCCAAGGAAGGC
BIP	CAGGACTCTTTCGAGGCCCTGTGCCCTCCAATGGATCCTC
F3	AGGGTTCGATTCCGGAGAG
B3	GAATTACCGCGGCTGCTG

6.3.1 Development of a new temperature control system

Initial on-chip reactions with the *18S* gene did not produce any amplification, whereas their thermocycler counterpart always revealed successful amplification. Such evidence suggested that the reason for non-amplification resided with the DMF devices. After multiple attempts at adjusting reagent concentration and temperature settings, it became clear that the temperature system in use was not efficient enough to allow for amplification of the *18S* control gene. An improved temperature system was then implemented, relying on a PT100 sensor placed below the heating element, as illustrated in the following figure. As an extra control, the thermocouple was kept on top of the heating element.

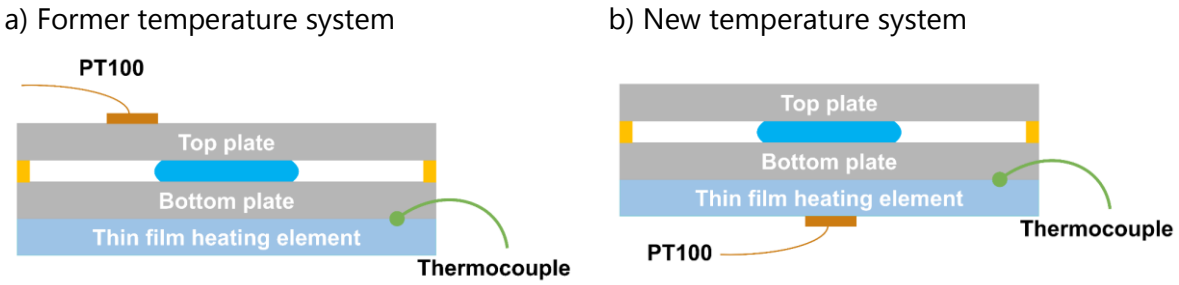

Figure 6.5: Schematic cross-section of the former (a) and new (b) temperature control systems used for on-chip LAMP reactions.

The temperature distribution within the heating element is similar to the one presented in section 5.6.3 (results not shown), and the PID parameters were adjusted to ensure a swifter temperature rise until the setpoint, with minimum overshoot, and optimal stability over time. Figure 6.6 represents the temperature profile measured by both sensors, for a setpoint of 61.5 °C. This setpoint was chosen specifically since it is the optimal temperature for the dual-gene LAMP reactions, as discussed in the following section.

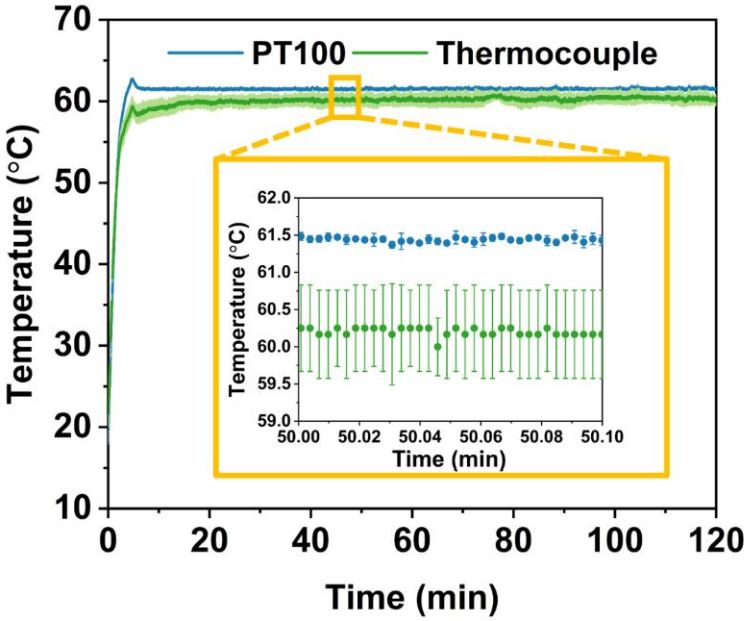

Figure 6.6: Temperature measured by the PT100 and thermocouple sensors, for a setpoint of 61.5 °C. Error bars represent the 90% confidence interval for a minimum 3 experiments.

As illustrated by Figure 6.6, the temperature rise is much faster than previously, reaching the setpoint in about 6 min. Focusing on the PT100 sensor, there is a small temperature overshoot until approximately 62.7 °C, merely 1.2 °C above the intended setpoint. Moreover, both sensors demonstrate that the new PID parameters enable a stable temperature over a tested period of 120 min (2 h), close to the setpoint defined for the PT100 sensor.

6.3.2 Dual amplification: *c-Myc* and *18S*

Following optimization of the LAMP master mix and the temperature control system, on-chip dual reactions were performed. A master mix containing all reagents mentioned previously was prepared off-chip and divided in two partitions: to one partition, primers for *c-Myc* were added; to the other, primers for *18S* were added. For positive controls, 1 µL of cDNA (1000 ng) was added to both partitions, whereas for negative controls, an equal volume of water was added (20 µL of total volume). All controls were vortex-mixed off-chip. The positive controls were then loaded onto the DMF chips (2 µL each), whereas the negative controls and the remainder of positive controls were transferred to a thermal cycler for the benchtop reaction counterpart. Regarding the positive *c-Myc* and *18S* controls on-chip, the reaction protocol is essentially the same described in section 6.2. Briefly, both controls were further mixed on chip by frequency actuation and back-and-forth motion, sub-divided into 3 smaller droplets

and irradiated every 10 min. The first assays performed on-chip aimed at finding the ideal temperature setpoint. For this purpose, several DMF-LAMP reactions were performed between 60 °C and 65 °C, in steps of 0.5 °C. Amplification for *18S* occurred only for 61 °C, 61.5 °C and 62 °C, with earlier amplification at 61.5 °C (data not shown). After determining the optimal amplification temperature, dual-gene amplification was performed on-chip, and the results are presented in Figure 6.7.

a) b)

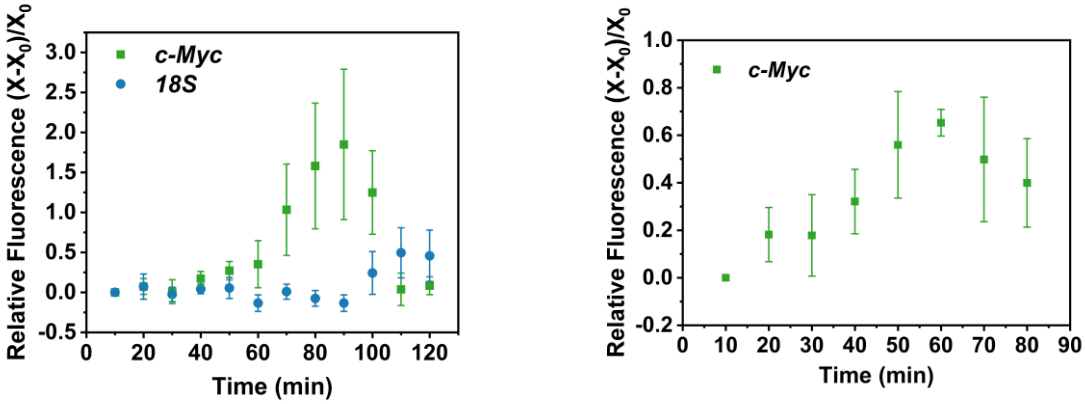

Figure 6.7: Relative fluorescence analysis for on-chip LAMP reactions with *c-Myc* and *18S* genes, for *18S* optimal amplification conditions (a) used for the present experiments and *c-Myc* optimal amplification conditions (b) used for previous experiments. Error bars correspond to the 90% confidence interval of a minimum 3 experiments for each time frame.

With the proposed amplification protocol, *c-Myc* begins to amplify at 60 min reaction time, achieving a fluorescence peak at 90 min, as illustrated by Figure 6.7 a). In comparison to the previous experiments, the amplification curve moved rightwards, which is probably due to the adjustment of the LAMP master mix to optimal amplification conditions for *18S*, which are sub-optimal for *c-Myc*. After the peak at 90 min, there is a decrease in the relative fluorescence, which may be attributed to photobleaching. Interestingly, the relative fluorescence peak for *c-Myc* is higher for dual-gene reactions (Figure 6.7 a)) than for the previous reactions (Figure 6.7 b)), with optimal amplification conditions for this gene. The average initial fluorescence for optimal and sub-optimal amplification conditions in *c-Myc* is similar (12.7 a.u. vs 12.9 a.u. - results not shown), and do not justify the differences in peak fluorescence. This may be due to the changes in the LAMP master mix, namely regarding salt concentration, which is a known factor affecting the quantum yield of fluorophores[355,356]. This could also be the case for the EvaGreen® fluorophore. Another hypothesis is that the increased concentration of EvaGreen® used in the previous assays lead to screening of most inner molecules, preventing their excitation and subsequent fluorescence emission. The author postulates that perhaps both factors

affect fluorescence, since initial optimizations did not reveal great differences in the fluorescence ratio for LAMP products with EvaGreen® at 1x and 1.5x (see Figure 6.2). Regarding the *18S* gene, amplification appears to begin only after 90 min, achieving a local fluorescence peak at 110 min. The reaction clearly begins at a much later stage than would be acceptable for a POC system, rendering the *18S* gene inappropriate as a control gene for gene expression analysis. Considering that off-chip LAMP reactions for the *18S* gene produced amplification before 90 min with the implemented protocol (knowledge from the research group), it was hypothesized that lowering the reaction volume could lead to a decrease in the efficiency of this specific reaction. Thus, a LAMP master mix was prepared and divided into two positive controls with different volumes (5 µL and 20 µL) and a negative control (20 µL). All controls were placed on a thermal cycler set for heating at 65 °C, adjusted to the lower volume (5 µL). The resulting reaction products were submitted to gel electrophoresis (1 µL each), and the gel was further subjected to UV light illumination. The image obtained by the gel imaging system is represented below.

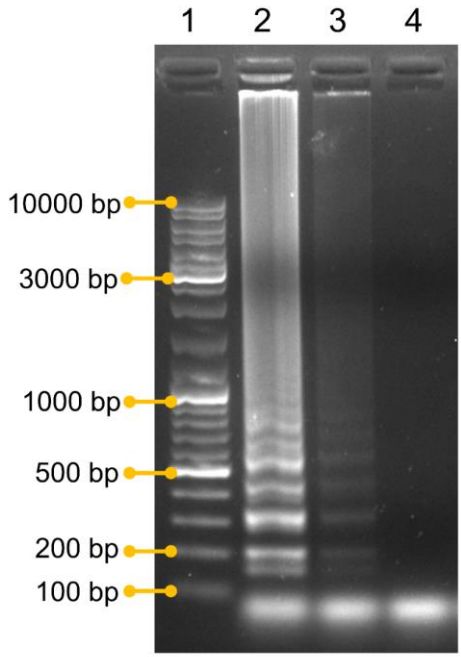

Figure 6.8: Electrophoresis gel resulting from the evaluation of reaction volume on the amplification of the *18S* gene by LAMP. 1) DNA ladder and some representative base-pair (bp) markers. 2) *18S* positive control for a reaction volume of 20 µL. 3) *18S* positive control for a reaction volume of 5 µL. 4) *18S* negative control for a reaction volume of 20 µL.

Figure 6.8 clearly shows that the reaction volume is a relevant parameter for amplification of the *18S* gene by LAMP. For the same sample volume loaded onto the electrophoresis gel (1 µL), the positive control for a total reaction volume of 20 µL presents a much brighter band

than the positive control for 5 µL, suggesting higher DNA amplification for the larger volume. Moreover, the lower bp smears (typically attributed to primer dimers, as previously discussed) appear to present different intensities for the positive controls, with the smear for the lower volume being more intense than the one for the higher volume. As a LAMP reaction progresses, primers are consumed and become part of the newly created DNA strands. Higher intensity of the low bp smears is an indicator of low primer consumption, therefore low DNA strand production. Such smears were analyzed by a standard image analysis software (ImageJ), developed by the National Institutes of Health (NIH, USA). The mean gray value measured for the 5 µL low bp smear is higher than the 20 µL low bp smear (211.7 a.u. and 194.7 a.u., respectively), confirming the difference in intensity. Thus, evidence suggests that lowering the reaction volume is a limiting factor for the amplification of *18S* by LAMP. The author postulates that a combination between the low available space and the GC content may be influencing the amplification of *18S*. Lower volumes lead to a decrease in the entropy of the system, and therefore affect the mixing efficiency (mixing between liquids is a widely known issue in microfluidics[357,358] as stated earlier). Even though the heating of the DMF chips increases entropy, this may not be enough to compensate for the initial effect. Furthermore, the GC content of the *18S* target sequence and respective primers is higher than that of *c-Myc* (Table 6.3), which could also contribute to the decrease in reaction efficiency for *18S*. GC structures have higher thermal stability due to the three hydrogen bonds between bases, against two hydrogen bonds for AT structures. Further studies are required to fully understand this phenomenon, which fall out of the scope of the present work. The main conclusion to be drawn is that for this specific device and LAMP reaction, the *18S* gene is not a suitable endogenous control.

Table 6.3: GC content of amplicon and primers relative to LAMP amplification of *c-Myc* and *18S*.

	c-Myc	*18S*
Amplicon	41.8%	53.0%
Combined primers	46.3%	59.8%
Amplicon and primers	43.5%	55.4%

Other control genes may be further evaluated, such as *GAPDH* or *ACTB*. Nevertheless, the objective of this work is to develop and study sensing methodologies to be integrated within DMF devices, for monitoring of LAMP reactions. Thus, the focus of the PhD project was

redirected towards another sensing technology with high potential for sensing in DMF: impedance measurements.

7

Impedance measurements

B. J. Coelho fabricated, optimized and tested all devices used for impedance measurements. She further optimized the impedance measuring conditions in all cases, and performed all the impedimetric modelling.

The term impedance (from the verb impede) was first conceived by Oliver Heaviside in 1886, and later published in his book Electrical Papers[359] (1894), where the concept is described as "the ratio of the impressed force to the current in a line when electrostatic induction is ignorable". To a more modern interpretation, impedance can be seen as the opposition that a certain element or circuit presents to the passage of current[360,361]. Typically associated with electronics, the potential of impedance in Biology has met an exponential growth in the last decades as a methodology for evaluating biological conditions[361–366], namely antibody-antigen interactions[367–369], enzyme-mediated reactions (commonly applied for glucose[370,371] and urea detection[372,373]), cell-related applications[364,365] (such as cell count, differentiation, metabolic activity, cytotoxicity, among others), bacteria detection[374] and finally nucleic acid sensing[363,375]. Regarding nucleic acid detection, research has mainly focused on identifying the specific hybridization between single strands of DNA bound to metallic electrodes and complementary strands present in a solution placed on top of said electrodes[363,375]. In the field of DMF, the potential of impedance has been thoroughly explored[192,350,376–389], ranging from droplet shape[385] and volume[350,382,383,387] identification, droplet electrochemical characteristics[350,376,378,381,383,386], droplet motion[192,350,376,388,389] (through the impedance difference between a naked electrode and an electrode covered with a droplet) and even evaluation of cells placed above the electrodes[380,390]. Nevertheless, impedimetric nucleic acid detection within DMF platforms has yet to be explored.

7.1 Preliminary investigation of LAMP impedance

In this work, continuous impedance measurements for real-time evaluation of nucleic acid LAMP amplification are investigated. Nevertheless, LAMP solutions are extremely complex, with high ionic strength, containing a variety of salts, proteins, nucleic acids and further require pH buffer capability, to maintain the enzyme activity in the optimum region. Such constraints will hinder the differentiation between amplifying and non-amplifying samples, therefore preliminary testing is required to understand whether amplification is distinguishable from non-amplification via impedance measurements and, if affirmative, determine which conditions (namely in terms of frequency) would improve measurement of the droplet impedance over the remaining layers' impedance. EIS using inter-digitated electrodes (IDEs) was the chosen methodology for the above-mentioned tests (EIS is specifically discussed in section 8). Briefly, 200 nm-thick chromium interdigitated electrodes were fabricated following the same procedure previously described for DMF devices, but with a lower exposure time, 4s, and a 100 nm

Parylene C layer was subsequently deposited over said electrodes. Figure 7.1 illustrates such inter-digitated electrodes, as well as relevant geometrical parameters.

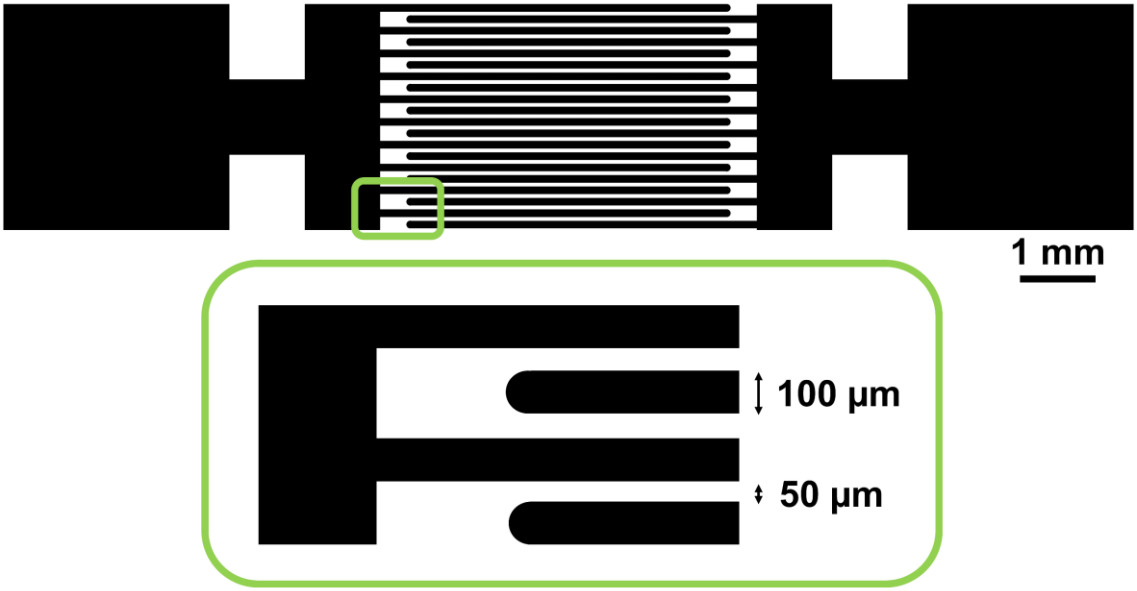

Figure 7.1: Inter-digitated electrode structure used for EIS, evidencing digit height and distancing.

A custom-made PDMS frame with approximately 2 mm height was placed around the digit area of the inter-digitated electrodes, to accommodate the solution to be measured via EIS. To evaluate the progression of LAMP reactions, four positive LAMP mixes were prepared according to section 6.1, but without the use of EvaGreen® fluorophore. The first mix was not placed on the thermal cycler (t = 0), the second mix was thermal-cycled for 30 min (t = 30), and the third and fourth mixes were thermal-cycled for 60 min (t = 60) and 90 min (t = 90), respectively. These four mixes were placed sequentially on top of the inter-digitated area within the PDMS frame, and EIS measurements were performed following a strict protocol: 1) air blow the devices, to remove any dust or particles; 2) resorting to two-probe EIS configuration, connect working and working sense probes to the left IDE contact and reference and counter probes to the right IDE contact; 3) place 10 µL of t = 0 solution on the IDE device, surrounded by the PDMS frame; 4) wait 2 min; 5) perform 3 consecutive EIS measurements; 6) carefully remove solution with a micropipette; 7) immediately rinse device with 20 µL of PCR-grade water; 8) carefully remove all the water, including that which typically accumulates near the edges of the PDMS frame; repeat steps 3) to 8) for remaining LAMP solutions. Furthermore, the room conditions should be adjusted to a maximum of 19 °C and 50% humidity. Chemical and biological sensors are often affected by the drift phenomenon, which is essentially a variation of the behavior of the sensor under constant stimuli[391,392]. To study said phenomenon on

the proposed IDEs, the previously-described protocol was performed with a negative LAMP control (without DNA amplification) at endpoint, on another set of devices. Specific EIS measurement parameters used for all assays are described on Table 7.1.

Table 7.1: EIS measurement parameters for monitoring LAMP reactions on IDE devices.

Equipment	Potentiostat Gamry Reference 600 (Gamry Instruments, Philadelphia, PA, USA)
Frequency	From 1 MHz to 1 kHz
Points per decade	30
AC voltage	500 mV_{RMS}
DC voltage	0 V vs E_{oc}*
Area	0.15 cm^2
Conditioning	Off
Delay	30 s
Mode	Normal

* E_{oc} represents the open circuit potential.

Figure 7.2 illustrates the results obtained with the described experiment.

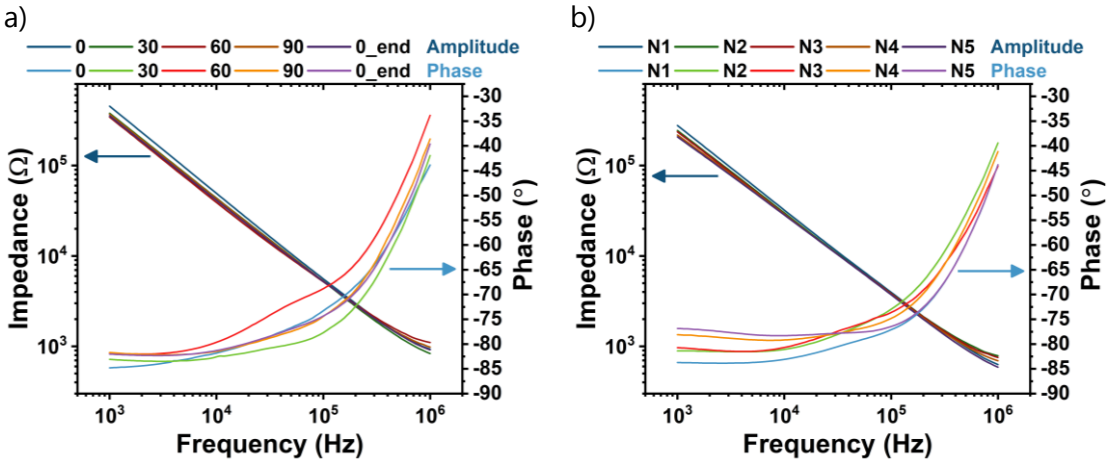

Figure 7.2: Impedance module and phase variation with frequency, for IDE structures in contact with: a) positive LAMP reaction products at several stages of the reaction (0 min, 30 min, 60 min, 90 min and again 0 min); b) negative ("N") LAMP reaction products (at endpoint) measured with the same protocol as for a) – device drift. Note that each plot corresponds to the average of three measurements per test condition, performed on a minimum of four devices. Error bands are not presented for ease of visualization.

Impedance assumes a linear behavior with frequency (logarithmic scale), decreasing with the increase in frequency, as expected in a capacitor (section 7.2 provides a theoretical insight on impedance). As for phase, lower frequencies lead to negative phases, close to -90° (perfect

capacitor) whereas higher frequencies lead to an increase in phase, tending towards 0° as the resistive component of the liquid droplet becomes dominant. It is thus possible to conclude that the system under test, comprised of IDEs and liquid solutions, overall exhibits an expected performance. Nevertheless, a fixed frequency must be selected for further integration with the lock-in amplifier used for on-chip impedance measurements. This particular frequency should fulfill several requirements: 1) enable distinction between amplifying and non-amplifying samples; 2) be high enough to prevent biofouling; 3) be low enough to prevent production of satellite droplets[343]. Considering said requirements, 10 kHz was deemed a good measuring frequency, and has been proven to be biocompatible with EWOD actuation[156,158,393,394]. Isolating this frequency, the variation of impedance was analyzed for each one of the set LAMP solutions, as illustrated in Figure 7.3.

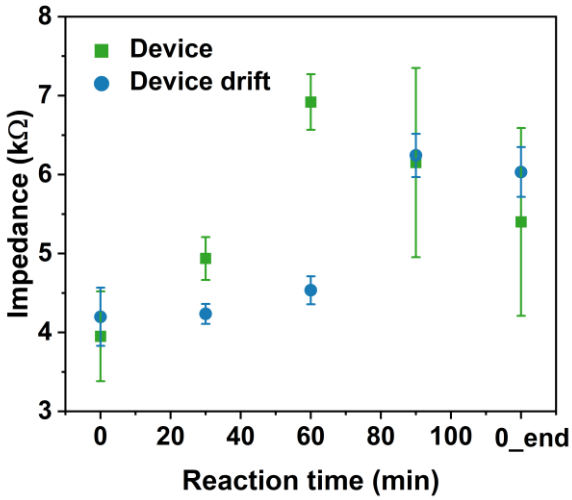

Figure 7.3: IDE impedance module at a fixed frequency of 10 kHz, for both positive LAMP test measurements and device drift measurements. Please note that for the device drift, the reaction times do not apply, since all measurements were performed with negative endpoint LAMP products.

As can be seen on Figure 7.3, the proposed IDE devices trace the LAMP amplification profile, presenting an increase in impedance for a reaction time of 30 min, and an even more evident impedance increase for a reaction time of 60 min. This increase is in conformity with the theory accepted within the research group, according to which impedance increases throughout a LAMP reaction due to reagent consumption (needed to build new strands of DNA), namely charge-bearing molecules and ions. Having less charge-bearing elements, the conductivity of the solution decreases, therefore the overall impedance increases. Interestingly, for the fourth and fifth sets of measurements (corresponding to 90 min and the final 0 min), there is an overlay of the drift impedance with the device impedance. This evidence suggests

that the IDE apparatus only functions correctly for a limited number of measurements, after which the interaction between liquid solutions and Parylene leads to irreversible damage of the dielectric layer. Such damage is clearly visible, as shown in Figure 7.4.

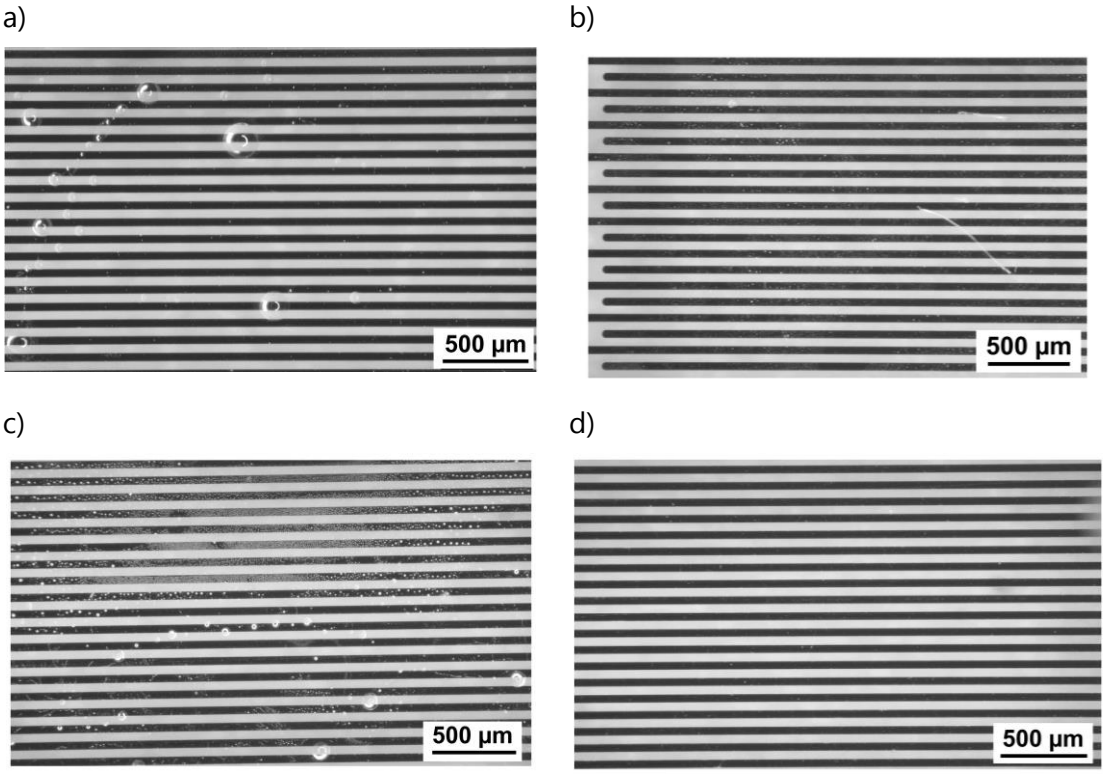

Figure 7.4: Evidence of degradation in different IDE devices after LAMP measurements (a, b, c), in comparison with a pristine device (d).

Regardless of the limited number of measurements that the IDE devices enable, this study demonstrates that it is possible to follow the progression of a LAMP reaction through impedance, which is a good indicator for transferring impedance measurements onto a DMF device. However, some adaptations of the impedance measurement system will be required to ensure correct readouts within a DMF device, as explained in the following section.

7.2 Novel impedance measuring system: dual-signal

One of the major drawbacks in existing impedance-measuring circuits for DMF is the lack of versatility and adaptability of the measuring signal to the droplet characteristics. Since the same signal is employed for measuring and moving the droplet, it is quite difficult to ensure that optimal conditions are being used for each application. To overcome this problem, the impedance measurement circuit proposed herein resorts to a novel dual-tone measuring methodology, whereby two distinct signals are applied to the DMF device: one signal to move

droplets and another signal to measure the droplet impedance. As can be seen on Figure 7.5, both signals are summed and applied to the DMF device (and working droplets), and current flowing through the top plate will be sent to the lock-in amplifier, after current-voltage conversion by a transimpedance amplifier. The lock-in will then isolate the reference frequency (that is, the measurement signal frequency) from the summed signal received and analyze its amplitude and phase.

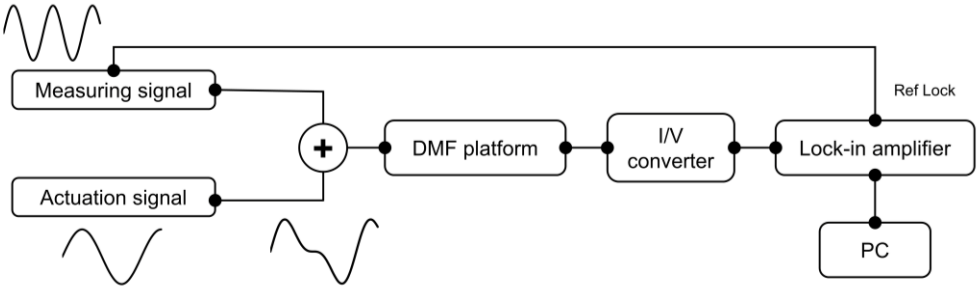

Figure 7.5: Block diagram of the droplet driving and analysis system.

The signal read by the lock-in amplifier will contain information not only regarding the droplet, but also the surrounding materials. Figure 7.6 illustrates a cross-section of a droplet placed on top of an electrode, in a DMF device, as well as the equivalent circuit model.

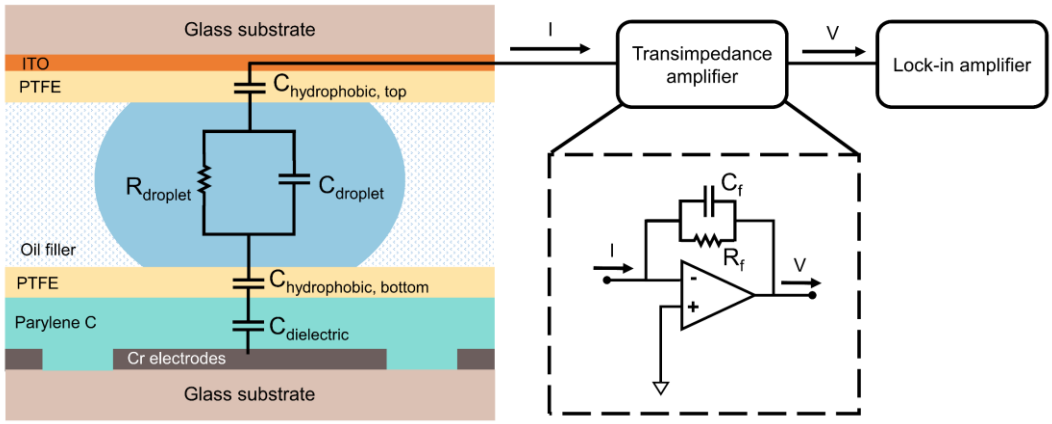

Figure 7.6: Cross-section of a DMF device, with overlapping equivalent electric circuit for all layers, as well as connections to the measuring system. Image not to scale. Please note that physical quantities have not been italicized in the images for ease of visualization.

As was mentioned previously, the closed configuration was chosen for this work, in which droplets move between two plates. Any signal applied will therefore cross multiple layers before readout. In this case, the signal is applied on the bottom plate electrodes and will cross the dielectric layer (Parylene C), the hydrophobic layer (PTFE), achieve the droplet and finally cross the second hydrophobic layer on the top plate before reaching the top plate common ground electrode, which in turn is connected to the lock-in amplifier. A home-made

transimpedance amplifier was used (see schematic on Figure 7.6), composed of a buffer and the parallel of a feedback resistor (R_f = 989 Ω) and a feedback capacitor (C_f = 560 pF). The buffer is essentially an operational amplifier, and assuming its characteristics to be ideal: 1) the loop gain is infinite; 2) the input resistance is also infinite and 3) the output resistance is null. The loop gain is given by Equation 7.1:

$$Avo\ (\infty) = \frac{v_{out}}{v_{in}} \tag{7.1}$$

where v_{out} is the output voltage and v_{in} corresponds to the potential difference between the inverting input (v_-) and the non-inverting output (v_+). Thus, Equation 7.1 may be simplified to Equation 7.2:

$$Avo\ (\infty) = \frac{v_{out}}{(v_+ - v_-)} \tag{7.2}$$

Further developing of Equation 7.2 leads to the major consequence of an infinite loop gain: the buffer will force the inverting input to equal the non-inverting input ($v_+ = v_-$). Such equality, allied to the infinite input resistance (no current flows to the buffer input), allows the output voltage to be determined by Equation 7.3:

$$v_{out} = -\left(Z_{Rf} // Z_{Cf}\right) \times I \tag{7.3}$$

Where $Z_{Rf}//Z_{Cf}$ represents the equivalent impedance resulting from the parallel of feedback resistor and capacitor. As it is widely known, the impedance of a resistor equals its resistance, and the impedance of a capacitor is determined by Equation 7.4:

$$Z_C = \frac{1}{2\pi f C} \tag{7.4}$$

Where f is the frequency of the applied signal and C is the capacitor's capacitance.

This parallel will also act as a low pass filter, since for high frequencies, the impedance of the capacitor will tend to zero, and the equivalent impedance $Z_{Rf}//Z_{Cf}$ will also tend to zero, whereas for low frequencies, the impedance of the capacitor will tend to infinite, and the equivalent impedance $Z_{Rf}//Z_{Cf}$ will in turn tend to Z_{Rf}. The lock-in amplifier will then read the amplitude and phase of the output signal, for a pre-determined reference frequency.

Prior to applying the impedance measuring system to on-chip LAMP reactions, theoretical modelling of the impedance shift for a LAMP reaction droplet inside the DMF chip was

performed. According to Zhang *et al.*[395], the conductivity of a LAMP reaction varies between 0.260 S/m and 0.231 S/m from the beginning to the end of the reaction, respectively. This is a good starting point to approximate the impedimetric behavior of the system in early and final stages of LAMP. The model used for calculations is the one depicted on the left side of Figure 7.6, that is, a reaction droplet represented by a resistor in parallel with a capacitor, in series with the dielectric and hydrophobic layers, represented by another three capacitors. The total impedance will therefore be determined by:

$$Z_{Total} = 2Z_{PTFE} + Z_{Droplet} + Z_{ParC} \tag{7.5}$$

Where Z_{Total} is the total impedance of the considered system, Z_{PTFE} is the impedance of the PTFE hydrophobic layer, $Z_{Droplet}$ is the impedance of the droplet and Z_{ParC} is the impedance of the Parylene C dielectric layer.

Considering the PTFE and Parylene C layers as ideal capacitors, Equation 7.4 may be used to determine their respective impedances, considering that the capacitance C, may be determined by:

$$C = \frac{\varepsilon_0 \varepsilon_R}{d} A \tag{7.6}$$

Where ε_0 is the permittivity of vacuum, ε_R is the relative permittivity, d is the thickness of the layer and A is the area. ε_0 and A are common to all layers, yet the remaining parameters vary.

The impedance of the droplet will be determined as follows:

$$Z_{Droplet} = Z_{R_{Droplet}} // Z_{C_{Droplet}} \tag{7.7}$$

The results obtained from this modelling are presented in Figure 7.7:

a)

b)

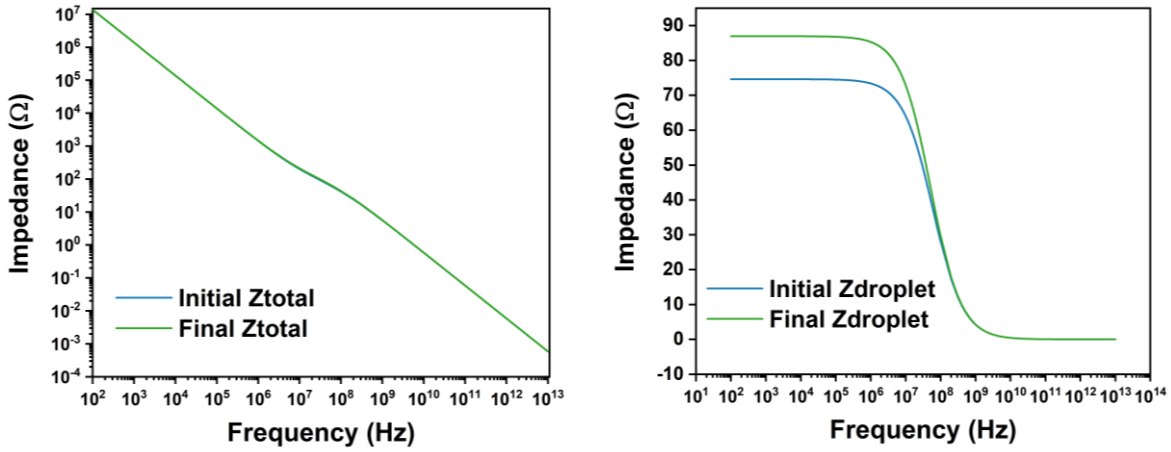

c)

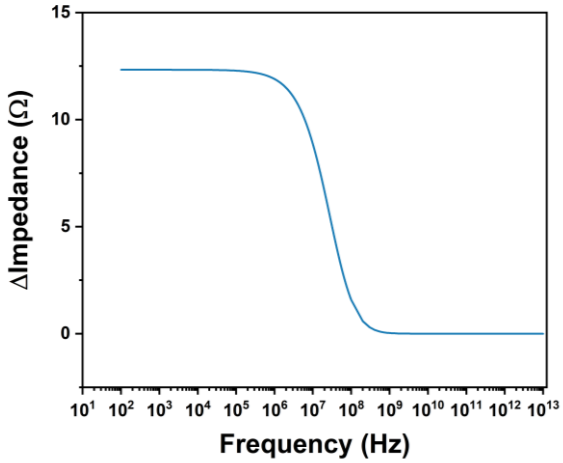

Figure 7.7: Results obtained from modelling the impedance of the DMF system and reaction droplets over frequency. a) Impedance determined for the whole system (Figure 7.6, left) for initial and final stages of a LAMP reaction. b) Impedance determined for the reaction droplet only, for initial and final stages of a LAMP reaction. c) Impedance difference between final and initial stages of a LAMP reaction, for the whole system (Z_{final} - $Z_{initial}$).

According to the models presented above, the maximum variation of impedance is considerably lower than the overall impedance of the system considered. In fact, a maximum variation of around 12 Ω is expected for a LAMP reaction. Such conditions reveal the importance of resorting to a slightly more complex, and undoubtedly accurate system for impedance measurement, as the one developed in this work. Surely the parameters of the LAMP reaction considered for such models differ from the ones used in the specific LAMP reactions studied herein. However, the basic principle remains that DNA strands are produced in several shapes

and sizes, consuming reactants in the process, and the final amount of DNA largely surpasses the initial amount of DNA. Thus, the error associated should be minimal.

With the proposed system, continuous impedance measurements for on-chip LAMP were performed for the pre-determined frequency of 10 kHz, in the frequency region where the impedance varies more expressively. Higher frequencies were also tested, namely 50 kHz and 100 kHz, however, devices suffered severe degradation in the first 30 minutes for such conditions. The frequency of the actuation signal was adjusted to 5 kHz, and the combination of both signals allowed for good droplet motion, without perceived delay. Note that similarly to the protocol used for IDE measurements, EvaGreen® was not added to the LAMP mixes, considering that fluorescence was not required. On-chip LAMP was performed simultaneously for negative (non-amplifying) and positive (amplifying) samples in each experiment. Figure 7.8 illustrates the impedance measured in amplifying and non-amplifying samples, and corresponding error bands.

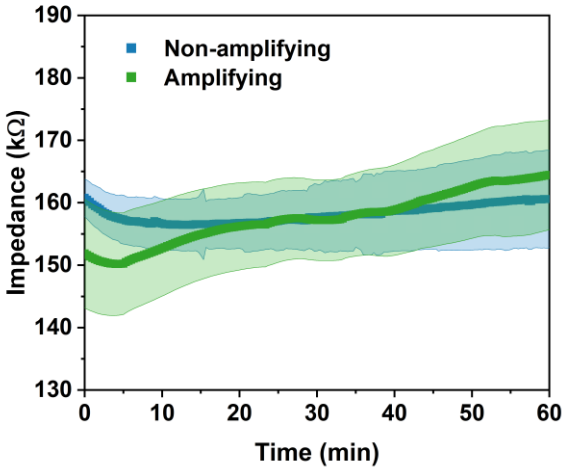

Figure 7.8: Impedance measured with the dual signal method, throughout a LAMP reaction, for both amplifying and non-amplifying samples. Error bands correspond to the 90% confidence interval in each case.

As illustrated by Figure 7.8, there appears to be an impedance increase tendency for both amplifying and non-amplifying samples, however the increase observed for amplifying samples seems to be slightly more expressive than that observed for non-amplifying samples. This is consistent with the working theory within the group, according to which droplet impedance should increase in amplifying samples, considering the consumption of ions present in the LAMP solution during amplification, and the production of a negatively charged, larger and less mobile molecule: double-stranded DNA. Nevertheless, the error associated with amplifying samples is also larger, and both error bands remain close at the end of the reaction. Additionally, the overall shape of the curves obtained does not correspond to the expected

progression of LAMP reactions, previously reported by label (such as fluorescence measurements[396]) and label-free (such as pH measurements[25]) methodologies. In both cases, real-time LAMP reactions are characterized by an initial low-signal phase where the reaction either has not yet begun or if it has begun, the signal is still not detectable, followed by a significant increase in signal with the formation of numerous new copies of the target strand in several shapes and sizes (from cauliflower clusters to extremely long strands)[23,239]. Nevertheless, to the knowledge of the author, the impedance measurement system presented herein has never been adapted to digital microfluidics nor used for real-time monitoring of LAMP, therefore further analysis is required before rejecting this methodology. Thus, statistics was applied to evaluate the statistical relevance of impedance at the beginning (t = 10 min) and at the end (t = 60 min) of the LAMP reaction, for amplifying (Amp) and non-amplifying samples (NAmp). A Shapiro-Wilk normality test was first applied to all data sets, and for a significance level of 0.05, normality could not be rejected. Please note that the Shapiro-Wilk test was chosen due to its adequacy for a small sample number[397], which corresponds to the current case: 3 non-amplifying assays and 5 amplifying assays. The difference between assay numbers is due to the occurrence of non-specific amplification in the non-amplifying controls, as confirmed by gel electrophoresis performed after the on-chip reactions. Following non-rejection of normality in the distribution of the data sets, Student's t-tests were performed to determine whether significant differences existed between any of the data sets.

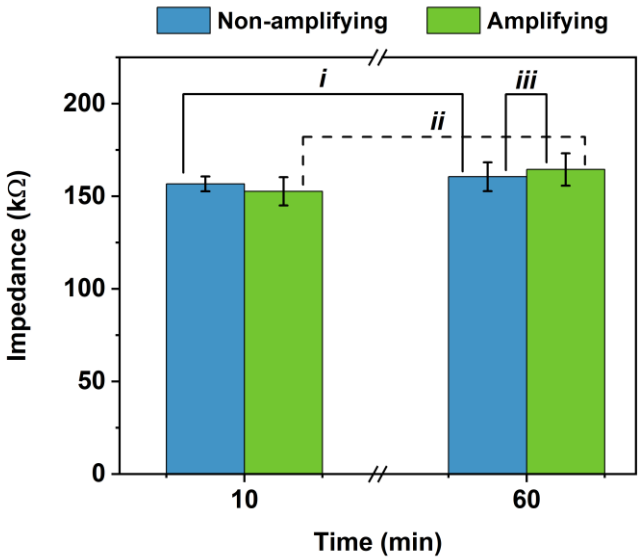

Figure 7.9: Measured impedance for the initial (t = 10 min) and final (t = 60 min) phases of the LAMP reaction performed on-chip concerning all tested conditions, namely amplifying and non-amplifying samples. Statistical analysis was performed through Student's t-test. *i*: p = 0.543, *ii*: p = 0.188, *iii*: p = 0.198 for a significance level of 0.05. In all cases, error bars correspond to the 90% confidence interval of a minimum 3 experiments for each time frame.

As can be observed on Figure 7.9, t-tests were performed on three different sets of data: 1) initial and final impedance of non-amplifying samples (expected to remain equal); 2) initial and final impedance of amplifying samples (expected to increase with time); 3) final impedance of amplifying and non-amplifying samples (as previously discussed, impedance is expected to be higher for amplifying samples). For all data sets, t-tests revealed that the population means are not significantly different (significance level of 0.05). Although a small difference between amplifying and non-amplifying samples is visible at the end of the reaction, the hypothesis test reveals that such difference is not statistically different, meaning that for a sufficient number of experiments, the impedance curves for both cases could possibly overlap. The difference in impedance between the beginning and end of the LAMP reaction is also not statistically meaningful neither for amplifying samples nor for non-amplifying samples. This result suggests that the small increase in impedance observed in both cases is likely due to random factors, such as some liquid evaporation or volume loss due to satellite droplet production (the two phenomena were observed during experimentation). This would overall result in a reduction of the droplet contact area, and subsequently lead to an impedance increase. Additional factors could have affected the impedance measurements, namely the degradation of the layers comprising the DMF device. As confirmed in section 7.1, the Parylene dielectric deteriorates when in contact with LAMP reactants, and even though the DMF devices are comprised of a much thicker

layer (2 µm as opposed to 100 nm in IDE devices), electrode corrosion was observed in some devices, which is irrevocable proof of reactant permeation in PTFE and Parylene. Both polymers are recommended for biological applications due to their biocompatibility[73,305], however, aggravating aspects such as high voltage actuation or temperature increase, coupled with liquid contact, could promote deterioration. Further increase in the thickness of the dielectric layer is not advisable, considering the accompanying increase in actuation voltage required, as well as the greater difficulty in moving droplets and measuring LAMP-related impedance. Nevertheless, said electrode corrosion was not observed in all devices, which does not imply that some degree of vertical degradation of the layers was involved, not only due to LAMP reactant action, but also possibly due to the influence of strong electric fields required for droplet motion and the additional temperature required for LAMP. Unfortunately, said hampering effects could not be properly studied, since acetone- and surfactant-based cleaning is always required at the end of device usage, to remove the filler oil and dissolve the reaction chamber sealant. Thus, it would be fairly complex to distinguish the damage resulting from cleaning, from the damage resulting from device usage. It should also be mentioned that LAMP samples possess a high ionic strength and are dependent on the use of buffers, which specifically counter variations in pH (ionic variations). This could also contribute to a greater difficulty in identifying amplification via impedance measurements in DMF. Considering all the above-mentioned issues, measuring device impedance with the proposed system and associated parameters is not deemed an efficient method to monitor DMF-LAMP in real-time. Modifications in the layers surrounding the droplet are too significant to accurately evaluate the progression of a LAMP reaction by impedance. Nevertheless, the impedance measuring system is still an extremely high-quality setup, which can (and should) be applied to other purposes. Section 10.2 further explores additional purposes for the impedance measuring system developed herein.

Considering the incompatibility of impedance measurements with DMF, electrochemical measurements were proposed, taking advantage of the commonly used sensitive layers in the field, which could achieve the required sensitivity to changes arising from LAMP amplification.

8

ELECTROCHEMICAL MEASUREMENTS

B. J. Coelho designed, fabricated, optimized and tested all the metal-insulator-semiconductor and electrolyte-insulator-semiconductor devices used for electrochemical measurements.

Electrochemical impedance spectroscopy (EIS) is a widely used technique for measuring impedance over a certain range of frequencies, which relies heavily on the work of Heaviside regarding impedance, admittance and conductance[359], and was applied experimentally for the first time in 1894, by Walther Nernst[398]. EIS covers an impressive span of applications, namely corrosion[399], battery technology[400], fuel cell technology[401] and biosensing[361]. Particularly, in the field of biosensing, EIS has been used for DNA-related applications, commonly to detect hybridization phenomena[402], which is further employed for cancer biomarker detection, gene expression analysis, bacteria detection, toxin detection, among others[402–405]. Nevertheless, as previously stated, one of the major mechanisms for DNA detection is hybridization, whereby a conductive (or semiconductive) surface is functionalized to allow for immobilization of single-stranded DNA, complementary to the target strand. If the target DNA is present, hybridization with the immobilized ssDNA strand will occur, inducing a local shift in ionic conductivity, which is translated to a shift in the surface impedance[403]. Of course electrochemical DNA detection mechanisms other than EIS are possible, such as several types of voltammetry or field-effect ion-sensitive devices[25,404,406–408]. Interestingly, a predominant aspect in a great number of the electrochemical devices presented in literature is the use of a sensitive layer[402,405,407], which specifically interacts with the intended target, namely due to surface functionalization (e.g. with complementary DNA strands, as discussed previously) or due to innate surface sensitivity (e.g. proton exchanges between liquid solutions and oxide surfaces). Detection of DNA amplification in real-time through electrochemical measurements such as EIS has been described by some authors[409,410], as well as DNA amplification monitoring in real-time with DMF devices[16,265], however a sensitive layer (SL) has never been added to the equation (at least to the knowledge of the author), resulting in SL-mediated DMF-LAMP detection by EIS. Among the spectra of EIS methodologies is Mott-Schottky EIS, which can be simply described as a capacitance measurement at a set frequency, in response to a constant voltage or range of constant voltage points[411]. Coupling Mott-Schottky EIS with a sensitive layer placed on the reaction area of the DMF device could enable the specificity and sensitivity required to follow the profile of a LAMP amplification reaction in real-time. In comparison with the previous impedance measuring system, using a potentiostat for Mott-Schottky EIS through a sensitive layer should increase specificity and sensitivity of the measurement, and the sensitive layer will be in direct contact with the sample, which should improve the signal-to-noise ratio. As a disadvantage, a thorough frequency optimization is required, to achieve a compromise frequency which simultaneously allows for optimal measuring and good droplet motion.

8.1 Preliminary investigation of electrochemical measuring conditions

Considering all the hindering conditions discussed in the previous sections regarding the evaluation of LAMP droplets within a DMF device, preliminary studies were performed to assess the optimal measuring parameters. Said studies were performed with specifically designed metal-insulator-semiconductor (MIS) devices. Before delving into the working principle of a MIS device, it is relevant to briefly explain the physical behavior of the composing materials, namely the insulator and the semiconductor. An insulator can be simply defined as a non-conductive material, which will effectively stop the flow of charge carriers. Dielectric materials, discussed in section 2.4.3, are examples of insulator materials. Semiconductor materials possess conductivity values between those of insulating and conductive materials. On a more in-depth approach, band theory of solids may be used to represent all three classes of materials, as illustrated below.

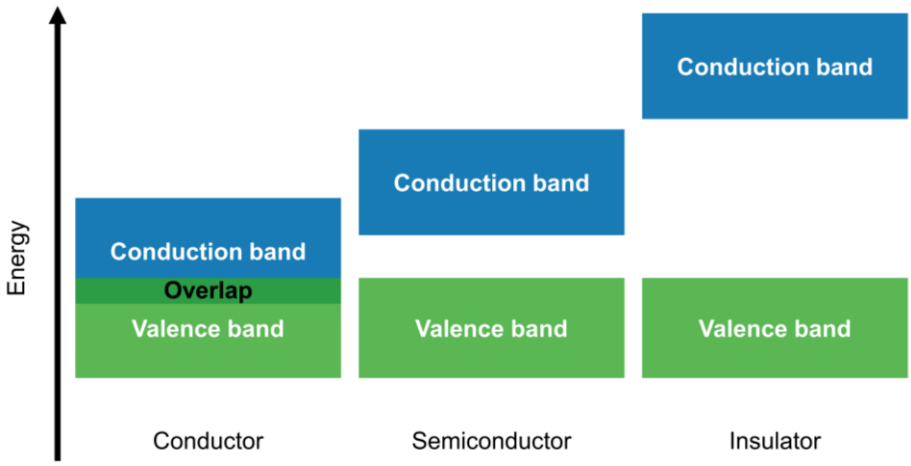

Figure 8.1: Schematic representation of energy bands for conductor, semiconductor and insulator materials.

According to band theory, charge carriers are commonly distributed on a low energy (non-conduction) band, the valence band, but may be transferred to higher energy states located at the conduction band if the right amount of energy is applied to them. Conductor materials feature an overlap between valence and conduction bands, therefore such materials are naturally conductive (charge carriers move freely), even if no external energy is applied. Semiconductor materials are naturally non-conductive, since there is an energy gap between the valence and conduction bands. However, if the right amount of energy is supplied to charge carriers, they may be transferred onto the conduction band, and the semiconductor

material becomes conductive. Finally, on insulator materials, the energy gap is larger, and therefore charge carriers may not be transferred to the conduction band, therefore the material remains non-conductive. The MIS device structure takes advantage of all three types of materials, in order to produce a device with variable capacitance, due to the presence of the semiconductor. The goal here is to implement an EISm (electrolyte-insulator-semiconductor) structure within a DMF device, where at the reaction areas, the electrode acts as metal back contact, an IGZO (Indium-Gallium-Zinc-Oxide) semiconductor is deposited over the back contact, the dielectric is replaced by the sensitive layer and the LAMP solution assumes the role of the second contact, or electrolyte. The MIS structure can therefore be used to the determine the measuring conditions that lead to the most significant device response, which may then be applied to an EISm structure with LAMP, to measure changes in the reaction. IGZO was chosen as a semiconductor considering the vast experience within the group in depositing excellent quality thin films of this material[285,412], and for the sensitive layer, Ta_2O_5 (tantalum pentoxide) was he chosen material, also considering the experience within the group in using said material as an ion-sensitive layer for DNA amplification detection[25,285,408,413]. Nevertheless, for preliminary understanding of the working principles and optimal measuring parameters of the system, MIS-based devices were developed, as illustrated in Figure 8.2.

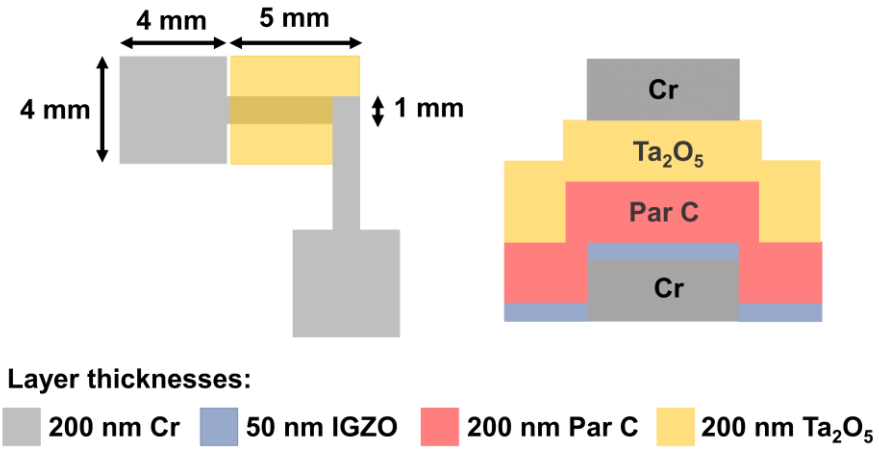

Figure 8.2: Schematic representation of the produced MIS devices, in top view (left) and cross-section (right). The useful area of the devices corresponds to a 1 mm x 1 mm square resulting from the overlapping between two chromium (Cr) contacts. In the middle of the contacts is the semiconductor (IGZO) and the insulator consisting of two insulating layers: one of Parylene C (Par C) and another of Ta_2O_5. Please note that the schematic on the right is not to scale.

8.1.1 MIS device fabrication and testing parameters

The first step in the fabrication of the MIS devices (Figure 8.2) is the deposition of the chromium (Cr) back contact. Cr was deposited by electron-beam deposition with heating of the glass substrate at 100 °C to improve adhesion. Mechanical masks were used during the deposition, comprised of PEN cut by laser with the shape illustrated in Figure 8.2. The overlapping area of the two Cr contacts was kept at 1 mm^2, mimicking the area of a DMF electrode. The IGZO semiconductor was then deposited by radio frequency magnetron sputtering from a multicomponent ceramic target of IGZO. A 200 nm layer of Parylene C was further deposited by CVD, as reported previously, after which the Ta_2O_5 insulating layer was deposited (200 nm), also by radio frequency magnetron sputtering (same equipment). Finally, the second Cr contact was deposited with the same conditions as the back contact. This way, simultaneously to the deposition of Cr, annealing of the structure was performed, at 100 °C for 2 hours. This annealing step is important in promoting crystallization of the Ta_2O_5 layer (and the remaining layers, consequently), which has been associated to improved pH sensitivity[285]. Annealing is also a common fabrication step in electronic devices (namely transistors) due to the improvement of layer interfaces and overall device stability[414,415].

Ta_2O_5 is known for producing the drift phenomenon, according to which, in biosensing, the sensitive layer in contact with liquid solutions suffers compositional changes with time, which in turn induce error in the electrochemical measurement[413]. Leakage tests performed

with interdigitated electrodes covered with 200 nm Ta_2O_5 showed a significant increase in the leakage current when a water droplet is placed on top of the dielectric, as opposed to a dry dielectric (results not shown). Thus, the dielectric is composed of two layers: a Ta_2O_5 layer for sensing and a Parylene C layer to prevent leakage. For this initial study, smaller thicknesses (200 nm) were used for each layer, since a smaller dielectric layer will facilitate signal acquisition. Should this preliminary study yield promising results, the Ta_2O_5 and Parylene C thickness will then be adjusted to DMF requirements (within measuring limits).

Resorting to the devices illustrated in Figure 8.2, Mott Schottky EIS analysis was performed for several frequencies and excitation signal amplitudes, according to the parameters illustrated on Table 8.1, in order to determine the optimal measurement conditions.

Table 8.1: Mott Schottky EIS parameters for measurement optimization.

Equipment	Potentiostat Gamry Reference 600
Measuring configuration	Two-electrode 
Voltage range	From -2 V to 2 V
Voltage Step	0.2 V
AC Voltage (excitation signal)	Several: 10 mV_{RMS}, 50 mV_{RMS}, 100 mV_{RMS} and 150 mV_{RMS}
Frequency	Several: 100 Hz, 500 Hz, 1 kHz and 5 kHz
Area	0.01 cm^2
Conditioning	0 V vs E_{oc}, for 10 s
Delay	30 s
Mode	Low noise

8.1.2 MIS device characterization

Figure 8.3 illustrates the results obtained with this study, where the output capacitances measured for several frequencies are grouped according to the excitation voltage.

a) 10 mV_{RMS}

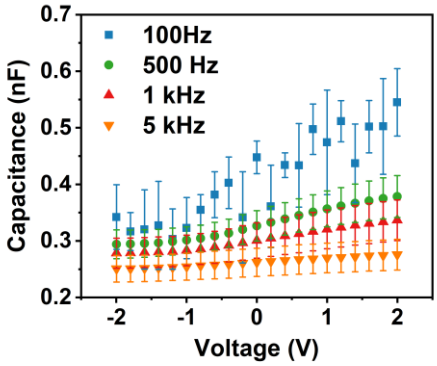

b) 50 mV_{RMS}

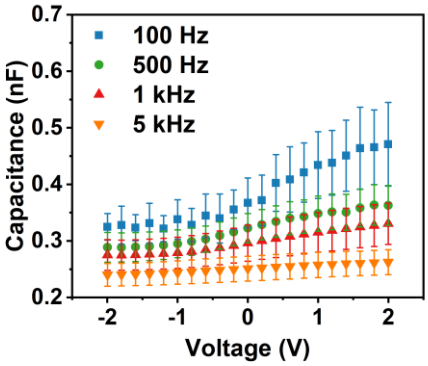

c) 100 mV_{RMS}

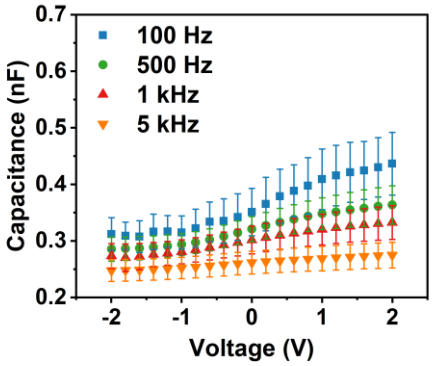

c) 150 mV_{RMS}

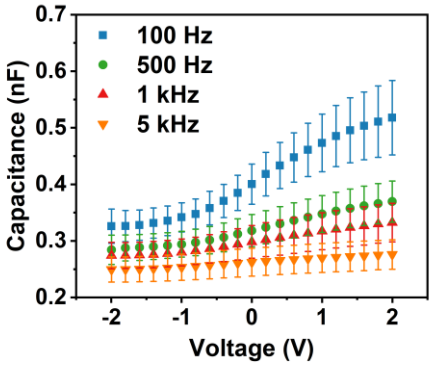

Figure 8.3: Capacitance of the MIS devices measured at several frequencies and excitation voltages, namely 10 mV_{RMS} (a), 50 mV_{RMS} (b), 100 mV_{RMS} (c) and 150 mV_{RMS} (d). Error bars correspond to the standard deviation of at least 5 independent measurements.

As can be seen on Figure 8.3, for any excitation amplitude, the capacitance of the MIS devices suffers a larger variation for a frequency of 100 Hz. This result is in accordance with the theory, since lower excitation frequencies are a synonym of slower charge displacement. For higher frequencies, the electric field applied varies quickly and for the same time frame, charges are also displaced faster. The capacitance response of the MIS devices for 100 Hz is also higher than for other frequencies, for any given voltage. Another interesting observation is that the stability of the measured capacitance increases with the excitation voltage, with the capacitance curve for 150 mV_{RMS} being smoother and more consistent than the curve for 10 mV_{RMS}. As a matter of fact, for 150 mV_{RMS}, capacitance for -2 V to 0 V is essentially inverse to the capacitance for 0 V to 2 V, which is the ideal behavior expected in this type of structure. Considering the masking of the 100 Hz frequency regarding the remaining frequencies, this frequency was removed for better visualization in the following Figure 8.4.

a) 10 mV_{RMS} b) 50 mV_{RMS}

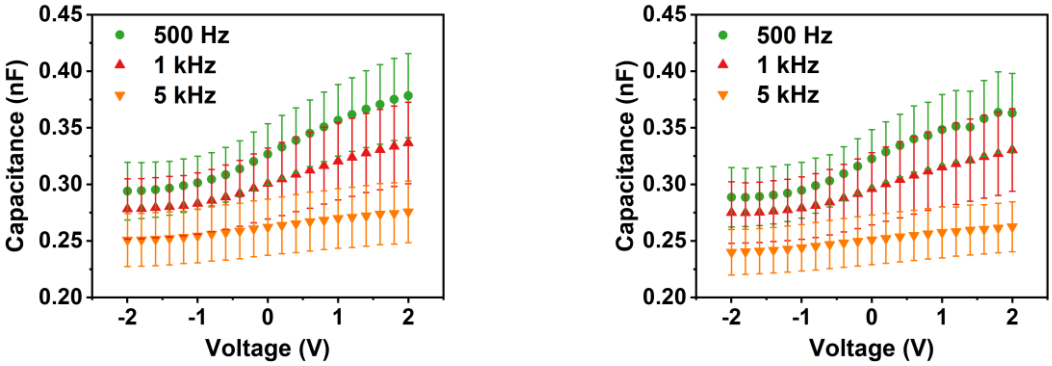

c) 100 mV_{RMS} c) 150 mV_{RMS}

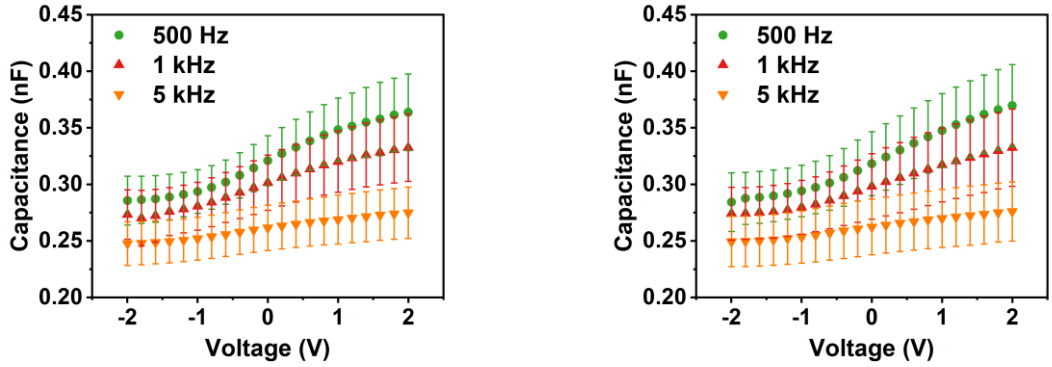

Figure 8.4: Capacitance of the MIS devices measured at several frequencies (500 Hz, 1 kHz and 5 kHz) and excitation voltages, namely 10 mV_{RMS} (a), 50 mV_{RMS} (b), 100 mV_{RMS} (c) and 150 mV_{RMS} (d). Error bars correspond to the standard deviation of at least 5 independent measurements.

Removing the 100 Hz frequency, the capacitance variation for the remaining tested frequencies becomes much clearer. Regardless of the excitation signal, the capacitance variation decreases with frequency, as previously observed. Nevertheless, for the selected frequencies, the overall capacitance curve is more stable than for 100 Hz, remaining virtually unchanged for the tested range of AC excitation signals. Moreover, for any given frequency and excitation signal, the devices behave exactly as expected in terms of capacitance, with an inversion of the capacitance curve in response to a shift in the voltage sense. Table 8.2 displays the maximum difference in capacitance (on average) measured for each of the tested condition, according to the following equation:

$$\Delta C = C_{(2V)} - C_{(-2V)} \tag{8.1}$$

where C represents capacitance.

Table 8.2: Maximum difference in capacitance (on average), ΔC, for the tested range of excitation signal parameters (frequency and AC voltage).

		Signal frequency			
		100 Hz	500 Hz	1 kHz	5 kHz
AC signal voltage	10 mV_{RMS}	0.20 nF	0.084 nF	0.058 nF	0.025 nF
	50 mV_{RMS}	0.15 nF	0.074 nF	0.055 nF	0.020 nF
	100 mV_{RMS}	0.12 nF	0.078 nF	0.059 nF	0.027 nF
	150 mV_{RMS}	0.19 nF	0.085 nF	0.058 nF	0.027nF

Briefly, Table 8.2 confirms that lower frequencies lead to a higher ΔC, however, voltage variations do not seem to produce significant improvements to capacitance measurement. Nevertheless, as was observed on Figure 8.3, measuring capacitance at 100 Hz leads to a fairly unstable signal acquisition, which is an undesirable effect for future integration with DMF devices. Thus, further studies are required to evaluate the impact of such instability on the measurement of capacitance in liquids.

8.2 Preliminary electrochemical measurements with varying pH

To evaluate the influence of liquids on the capacitive response of the sensitive layer, the two most promising frequencies were chosen, i.e. 100 Hz and 500 Hz, and the AC signal voltage was kept at 150 mV_{RMS}. This excitation voltage was chosen considering that it consistently lead to higher ΔC, despite the little variation to the ΔC achieved for other voltages. Furthermore, a different device architecture was designed and produced, which allowed for encapsulation of liquid solutions in direct contact with the Ta_2O_5 dielectric layer. This novel architecture is comprised of the same layers illustrated in Figure 8.2, except for the top Cr contact, which is replaced by the liquid solution in test. Said structure is surrounded by an SU-8 frame to confine the liquid solution, and an ITO-coated glass is placed on top of the frame, to prevent evaporation. The ITO is essentially the second electrical contact and is further connected to the potentiostat through a flat spring connector. Moreover, the ITO-coated glass includes two apertures that allow for introducing the liquid onto the device and expelling the air within the SU-8 frame. Figure 8.5 illustrates the fore-mentioned device.

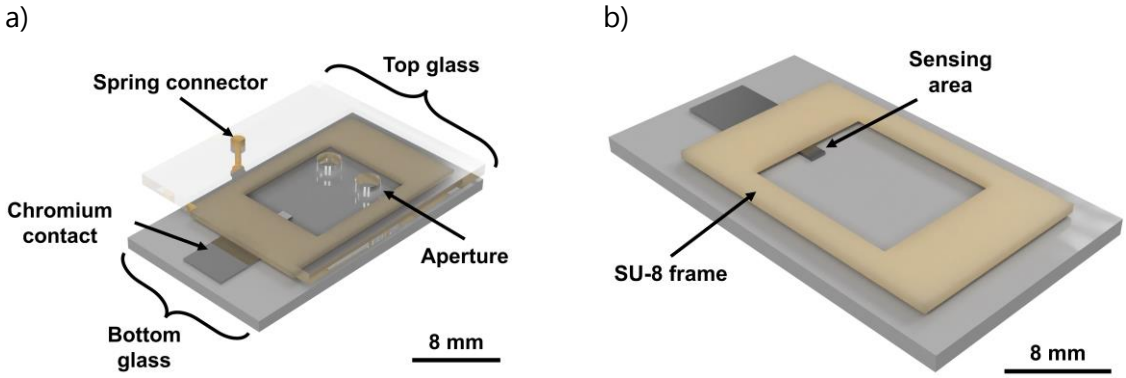

Figure 8.5: 3D illustration of the produced device architecture for capacitance measurements on liquid solutions, with (a) and without (b) the top glass.

8.2.1 EISm device fabrication

By replacing the top Cr electrode with a test solution, the MIS structures are converted to EISm (electrolyte-insulator-semiconductor) structures, where the electrolyte corresponds to the solution. The fabrication of the EISm devices illustrated in Figure 8.5 involves three major steps: 1) Cr deposition; 2) Deposition of semiconductor (IGZO) and insulator (Parylene C and Ta_2O_5) layers; 3) Fabrication of the SU-8 frame; 4) drilling of the apertures on the top glass and 5) assembly of the device. Cr was deposited by e-beam, as previously disclosed (section 8.1.1), for a final thickness of 200 nm, consistent with the DMF devices. The semiconductor and insulator layers were then deposited, also as previously disclosed. Fabrication of the SU-8 frame followed, with photolithography performed with masks consisting of three overlapping acetate sheets, printed with the layout of the frame. The SU-8 frame was processed according to the instructions of the manufacturer for SU-8 2100 (former MicroChem, acquired by Kayaku Advanced Materials, Westborough, MA, USA). Briefly, the SU-8 resin was spin-coated over clean glass substrates at 500 rpm for 7s and 1500 rpm for 30s. After a resting period of 10 min, soft-baking was performed by heating the substrates at 65 °C for 22 min and 95 °C for 60 min. A cooldown period followed, after which the resin was exposed on the mask aligner for 30 s. Post-baking was then performed by heating the substrates at 65 °C for 1 min and 95 °C for 15 min. The development step followed, by immersing the substrates in propylene glycol monomethyl ether acetate (Sigma-Aldrich, St. Louis, MO, USA) for 17 min, on a rotation table rotating at 50 rpm. The top plate, consisting of commercially-available ITO-coated glass, was drilled with a diamond-tip drill to open the apertures, and finally, the device was assembled.

8.2.2 EISm device characterization

LAMP reactions rely on a specific enzyme (*Bst* polymerase), which sequentially adds free nucleotides to an existing nucleic acid strand – a process known as DNA polymerization. During this process, hydrogen ions are generated as a by-product, according to Equation 8.2:

$$(DNA)_{n-1} + dNTP \rightarrow (DNA)_n + P_2O_7^{4-} + H^+ \quad (8.2)$$

Hydrogen ion production leads to changes in the solution pH, which may be used to follow the nucleic acid amplification reaction[25,26].

Resorting to the setup represented on Figure 8.5, commercial solutions of fixed pH (pH 4, 7 and 10) were tested, using the previously identified measuring parameters, i.e. 100 Hz or 500 Hz, and 150 mV_{RMS}. Commercial solutions were selected for this initial approach, considering their high stability in pH, which is fundamental in assessing the real capability of the device in detecting pH changes. Moreover, highly stable solutions facilitate the identification of changes in the properties of the device itself (device drift), which lead to erroneous readouts. As previously stated, the measuring protocol is of extreme relevance in data acquisition with liquid samples. Prior to measurements, top and bottom glass pieces were lightly blown with a nitrogen jet. After assembling the fore-mentioned glass pieces according to Figure 8.5, the pH solution in question was slowly inserted through one of the apertures, leaving air flow from the other aperture. The solution was allowed to rest for 5 minutes, allowing for stabilization of phenomena occurring at the solution-oxide interface, and only then were measurements performed. To exchange pH solutions, the new pH solution was directly inserted through one of the apertures, and the old solution was collected through the other aperture with a paper cloth. To remove all of the old solution, this process was repeated twice. The 5 minutes waiting time followed, after which new measurements were performed. Typically, in EISm systems, there is a shift of the capacitance-voltage (*C*-*V*) curve either to the right or to the left (voltage axis), indicating a pH variation. In the present case, where n-type IGZO is used as a semiconductor and Ta_2O_5 is used as the pH-sensitive layer, the capacitance should increase with the increase of applied voltage, and a *C*-*V* right shift is indicative of a decrease in pH. The pH measurement is therefore achieved by reading the voltage shift for a fixed capacitance. However, the behavior of the devices produced in this work was unstable and the traditional method was not applicable. Appendix I includes more information regarding this issue. Thus, a different methodology was chosen to evaluate the produced EISm devices as pH meters: for each *C*-*V* curve, three

different voltages were chosen (-2 V, 0 V and +2 V) and the difference in the capacitance between subsequent pH solutions was determined, according to the following equation:

$$pH\ x\ to\ pH\ y = Capacitance_{pH\ y} - Capacitance_{pH\ x} \quad (8.3)$$

Figure 8.6 illustrates the variation in capacitance per applied voltage, for the two selected frequencies (100 Hz and 500 Hz), with decreasing or increasing pH conditions. A set of three known pH solutions were used, namely pH10, pH7 and pH4. For the increasing pH condition, measurements began with pH4, followed by pH7 and pH10. However, after pH10, pH7 and pH4 solutions were measured again, to verify if the devices were truly capable of detecting pH changes, as opposed to capacitance variations due solely to drifting phenomena. For example, if capacitance increases linearly from pH4 until pH10, and continues to increase linearly when pH7 and pH4 are tested once more, then drifting would likely be the measured phenomenon, instead of the pH change. For the decreasing pH conditions, the reverse pH order was followed, i.e., measurements began with pH10, followed by pH7, pH4, and again pH7 and pH10.

a) 100 Hz, decreasing pH

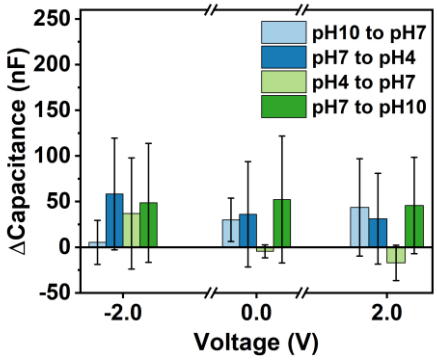

b) 100 Hz, increasing pH

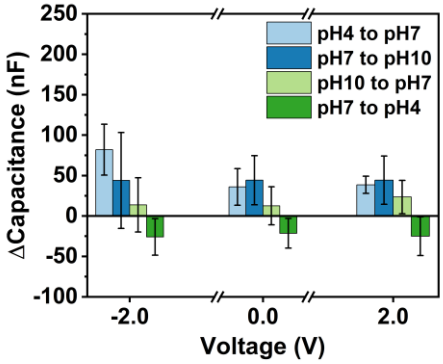

c) 500 Hz, decreasing pH

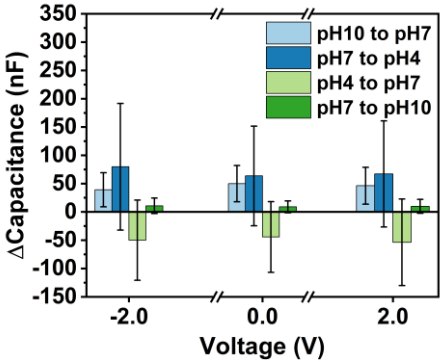

d) 500 Hz, increasing pH

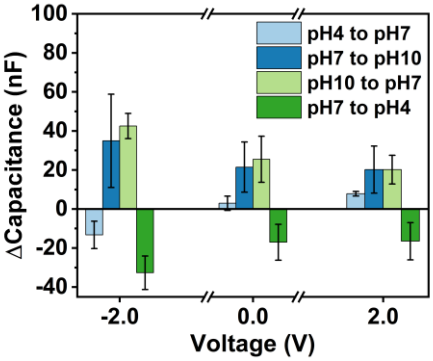

Figure 8.6: Variation of capacitance measured according to shifts in pH test solutions, for different voltage conditions, using the capacitance measurement devices (see Figure 8.5). Each bar on the bar chart corresponds to the capacitance variation obtained by changing the test solution from one pH to the following, as indicated by Equation 8.3. Three pH solutions were used (pH4, pH7 and pH10) and four sets of conditions were tested, by varying the measurement frequency and the pH order of the test solutions: a) 100 Hz and decreasing pH order; b) 100 Hz and increasing pH order; c) 500 Hz and decreasing pH order; d) 500 Hz and increasing pH order. Please note that "increasing" and "decreasing" terms refer to the initial tested conditions (as previously stated, the pH order is reversed for the last measurements, as to detect drifting). Error bars correspond to the confidence interval at 90%.

For a frequency of 100 Hz and decreasing pH condition (Figure 8.6 a)), the variation in capacitance (Δ capacitance) does not appear to follow any specific trend. For instance, at -2 V, there appears to be a difference in capacitance only from pH10 to pH7 whereas for the remaining pH shifts, the capacitance remains virtually unchanged. A similar phenomenon occurs for 0 V and +2 V, where capacitance only varies significantly for a single pH shift, from pH4 to pH7. Moreover, for any given voltage applied, Δ capacitance from pH7 to pH4 and pH7 to pH10 remain virtually unchanged, whereas more significant changes occur from pH10 to pH7 and pH4 to pH7. Nevertheless, due to the high degree of fluctuation in the results (as may be inferred by the considerable error bars), no definite conclusions may be withdrawn from this

condition. Remaining on a frequency of 100 Hz and reversing the pH order (Figure 8.6 b)) reveals interesting patterns. Specifically, for -2 V, the Δ capacitance consistently decreases as pH is increased from pH4 to pH7 and from pH7 to pH10. However, this tendency is repeated when the pH order is reversed (pH10 to pH7 and pH7 to pH4), which is suggestive of device drifting. As for a frequency of 500 Hz, the decreasing pH condition (Figure 8.6 c)) reveals initial assay stability, with very similar Δ capacitance from pH10 to pH7 for all tested actuation voltages. Further decreasing pH, from pH7 to pH4, generally leads to an increase in Δ capacitance, nevertheless the error associated is considerable, therefore no definite conclusions may be drawn. Reverting the pH order appears to produce a relevant effect, with an expressive drop in Δ capacitance from pH 4 to pH7, to negative values. From pH7 to pH10, the Δ capacitance increases until close to 0, yet still remains largely inferior to the first tested pH order. In summary, for this specific set of conditions (500 Hz, initial decreasing pH and any applied voltage), devices appear to distinguish between the initial pH decrease and the reverse pH order. Nevertheless, the associated error is still quite expressive, mainly in intermediate conditions, which prevents any clear conclusions to be drawn. Lastly, for 500 Hz and increasing pH order (Figure 8.6 d)), devices appear to distinguish between the two extremes of pH conditions, that is, between the initial pH4 to pH7 and the final pH7 to pH4. The two intermediate conditions are very close to each other, with overlapping error bars, which does not suggest statistically relevant differences. Interestingly, in comparison to the 100 Hz counterpart (Figure 8.6 b)), the Δ capacitances appear to repeat the pattern of positive and negative values, from pH4 to pH7 and pH7 to pH4, respectively (with the exception of pH4 to pH7 at -2 V).

In an effort to determine whether exact correlations could be extracted from the capacitance variations arising from pH shifts, statistical analysis was performed to all data sets. Table 8.3 summarizes the results of ANOVA tests, only for statistically relevant data sets. For the complete output of the analysis of variance (ANOVA) performed to assess whether statistical differences exist between pH shifts on the developed devices, please consult Appendix J. For all cases, one-way ANOVA was performed to the totality of data sets per applied voltage, for a significance level of 0.1. Means comparison by the Tukey test was further performed for each combination of pH shifts, also with a significance level of 0.1. Please note that ANOVA and Tukey tests were performed only after confirming that all data sets followed a normal distribution through the Shapiro-Wilk normality test (advised for a small number of samples[397]), and confirming the homogeneity of variance by the Brown-Forsythe test. Further note that the minimum number of experiments per pH shift is 4.

Table 8.3: Statistical evaluation of the capacitance variation for statistically significant pH shift combinations, for several measuring frequencies and applied voltages. Of course, in this case the ANOVA tests always revealed statistical differences, therefore only the post-hoc Tukey test results are shown, as well as respective *p*-values. "Yes" indicates statistical relevance.

Measuring condition	Applied voltage	pH shift	Tukey test result
100 Hz, increasing pH	-2 V	pH4 to pH7 vs pH7 to pH4	Yes (p = 0.0960)
	+2 V	pH4 to pH7 vs pH7 to pH4	Yes (p = 0.0883)
		pH7 to pH10 vs pH7 to pH4	Yes (p = 0.0619)
500 Hz, increasing pH	-2 V	pH7 to pH10 vs pH7 to pH4	Yes (p = 0.0785)
		pH10 to pH7 vs pH7 to pH4	Yes (p = 0.0565)
	0 V	pH7 to pH10 vs pH7 to pH4	Yes (p = 0.0987)
		pH10 to pH7 vs pH7 to pH4	Yes (p = 0.0960)
	+2 V	pH7 to pH10 vs pH7 to pH4	Yes (p = 0.0718)
		pH10 to pH7 vs pH7 to pH4	Yes (p = 0.0975)

As illustrated by Table 8.3 (and Appendix J), very few of the pH variations produced significant differences, and the large majority of significant results is concentrated on the 500 Hz and increasing pH measuring condition. Focusing on said measuring condition, it is clear that the key element for statistical difference is the last pH shift (pH7 to pH4) which presents a Δ capacitance statistically different from the intermediate pH shifts (pH7 to pH10 and pH10 to pH7). However, this observation does not fully satisfy the requirements for following a LAMP reaction, neither at endpoint nor in real-time, as will be discussed below. Moreover, the lack of a clear and uniform tendency in the behavior (e.g. systematic increase of Δ capacitance with decreasing pH) presents a critical barrier to the adaptation of this measuring system to a DMF device. It is important to remember that the sensing area of the devices would have to be incorporated into a dedicated region of a DMF device, which would imply a large increase in the fabrication complexity. This would involve feature alignment and more lithographic steps, which would mandatorily require covering of the sensing area, possibly with a sacrificial layer, for deposition of the 2 µm layer of the dielectric. Of course, it would be advisable not to increase the thicknesses of the EISm layers to match the dielectric layer, since the ion exchanges leading to pH detection occur at the interface between the solution and the oxide layer. Thus, increasing the distance of the measuring electrode from this interface will lead to a loss in signal strength. The increase in fabrication complexity is also accompanied by the possibility

of damage to the EISm layers, further contributing to measurement instability. Lastly, for real-time measurements of a LAMP reaction, the sensing area could also be affected by temperature changes.

Focusing on the LAMP reaction itself, the pH of a LAMP reaction is expected to vary from an initial pH of 8 to 9 pH units (the pH range for LAMP reaction buffers, to assure optimal activity of the *Bst* enzyme) and further decrease around 2 to 3 pH units (Table 8.4).

Table 8.4: pH variation associated with LAMP reactions reported in multiple scientific publications, for amplifying samples (positive controls).

Reaction target	Initial pH (pH units)	Absolute pH variation (pH units)	Reference	Notes
Escherichia coli O157	8	Maximum 1.2	[416]	-
Multiple	8.8	2.3 - 2.8	[254]	-
Salmonella	≈ 9	≈ 2.0 - 3.0	[417]	Several pH indicators used
α^0-thalassemia	8.8	≈ 2.0 - 3.0	[253]	Fails to report pH variation, but resort to WarmStart® Colorimetric LAMP 2X Master Mix, from New England BioLabs[418]
SARS-CoV-2	8.8	≈ 2.0 - 3.0	[252]	Fails to report pH variation, but resort to WarmStart® Colorimetric LAMP 2X Master Mix, from New England BioLabs[418]

Please note that the WarmStart® Colorimetric LAMP kit relies on phenol red as a pH indicator which changes from pink to yellow from pH 9/pH 8 to pH 6. Moreover, the initial pH was considered to be 8.8, since this is the pH reported by the manufacturer for amplification buffers using the WarmStart® DNA polymerase supplied with the kit[419].

Considering data from Table 8.4, the pH-sensing region to be incorporated within a DMF device would have to be capable of detecting a pH variation from pH8/pH9 to pH7/pH6. For real-time LAMP monitoring, detection of 0.5 units of pH variation (or even less) would be desirable. In light of such requirements, as well as the process needed to incorporate a pH-

sensing area on a DMF device, the electrochemical method in question does not appear to be a good fit for evaluation of a LAMP reaction within a DMF device, neither for endpoint evaluation (yes or no response) nor for real-time monitoring of the reaction.

9

THE NEXT STEP: HYBRID DMF-DRMF PLATFORMS FOR NUCLEIC ACID AMPLIFICATION AND MONITORING

Disclaimer

Some excerpts of this section have been published in the following publication:

Coelho, B. J.; Neto, J. P.; Sieira, B.; Moura, A. T.; Fortunato, E.; Martins, R.; Baptista, P. V.; Igreja, R.; Águas, H. *Hybrid digital-droplet microfluidic chip for dPCR applications: design, fabrication and characterization*. Sensors **2023**, 23 (10). https://doi.org/10.3390/s23104927.

B. J. Coelho fabricated and tested all the digital microfluidic sections, and finalized the fabrication of the hybrid devices. Moreover, she designed, fabricated and tested the new physical support for the hybrid devices, and handled its incorporation onto the experimental setup. She further characterized all the standalone droplet microfluidic devices as well as all hybrid devices.

Section 5 revealed a fully functional DMF device, capable of performing all fluidic operations and also heating, as required for LAMP reactions. Section 6 further clarified that the best methodology for monitoring the progression of LAMP reactions is fluorescence measurement, by intermediate of an intercalating dye (EvaGreen® in this case). At this point, the logical evolution would be an escalation of the capabilities of the device, namely through the improvement of reaction output. An interesting way to improve the capabilities of the DMF devices is the integration with other microfluidic technologies. Several microfluidic methodologies are available for integration, namely paper microfluidics (PMF), continuous-flow microfluidics (CMF) or droplet microfluidics (DrMF)[420–422]. Examples of already existing hybrid approaches include PMF and DMF[423], PMF and CMF[424], and DMF and CMF or DrMF[425–429]. The fusion between DMF and DrMF is quite exciting from the application point of view, and the reasoning for this conclusion will be explained in the following sentences. One important aspect in nucleic acid amplification testing is absolute quantification of the initial copy number of the target sequence. Such quantification is useful for a plethora of applications such as viral load determination, detection of rare mutations or copy number variation analysis[430,431]. Thus, it would be highly valuable to produce single-substrate DMF-DrMF hybrid devices, where the DMF portion can mix all the LAMP reagents and test samples, perform the reaction by heating and finally supply the reaction products to the DrMF portion. DrMF can then create nano-droplets at a flow-focusing region, thus enabling determination of the exact number of copies of the target sequence within the sample, by the droplet digital methodology[432].

9.1 Joining DMF and DrMF

It is of extreme relevance to specifically join DMF and DrMF, since this fusion allows to overcome major disadvantages of the separate technologies, particularly the difficulty in mixing different reagents due to the predominance of laminar flow in microfluidic channels (associated with a low Reynolds number), frequently highlighted as one of the main disadvantages of channel-based microfluidics[357,358]. Typically, for small diameter microchannels featuring a Reynolds number below 2300, laminar flow increasingly prevails[358], which in practical terms indicates that fluids passing through the same channel will not be mixed, but rather flow in parallel. Double-plate DMF technologies (where droplets flow sandwiched between two plates) are capable of solving the mixing issue, since droplets may be voltage-actuated to perform mixing protocols, ranging from back-and-forth motion[339], circular motion[433], frequency-assisted mixing[342] or combinations of the latter[265]. Section 6.2 specifically covers an effective DMF

mixing technique developed in the scope of this PhD work. Moreover, DrMF typically allows for lower-volume droplets than DMF, with a higher and faster droplet throughput. Thus, by uniting both technologies, advantage is taken from the higher mixing efficiency in DMF and the higher throughput and lower volume droplets of DrMF to create a hybrid system, envisioning nucleic acid amplification and quantitative detection.

As the name suggests, droplet microfluidics refers to droplet generation in microfluidic systems, as opposed to continuous-flow microfluidics, where an uninterrupted flow of liquid circulates within microfluidic channels. The mechanism behind droplet formation in droplet microfluidics is immiscibility between two fluids. Briefly, both fluids flow simultaneously, and due to interfacial instabilities between these fluids coupled with the surface energy of the microfluidic channel, one fluid will form droplets (the dispersed phase) and the other fluid will circle said droplets (the continuous phase), thus creating an emulsion[434]. Oil is commonly used as a continuous phase, whereas aqueous liquids are used as a dispersed phase. Of course, additional microfluidic design is required to achieve droplet formation. Several systems have been developed for this purpose, which can be roughly divided into passive and active methodologies[434–436]. Passive methodologies rely solely on the design of microfluidic channels, intrinsic properties of the circulating fluids and flow rates for fluid control. Fluid control usually relies on devices external do the microfluidic chips (e.g. syringe pumps), however this is the only off-chip equipment required for passive droplet generation. Active methodologies combine passive droplet generation with auxiliary external fields (magnetic or electrical), mechanical forces or thermal gradients[435]. Passive methods were chosen as a first approach to the hybrid devices, considering their simplicity and ease of implementation.

Within passive methodologies, three major categories may be defined, based on the architecture of the microfluidic channels: co-flow, cross-flow (sub-divided into Y-junctions and T-junctions) and flow-focusing droplet generation (Figure 9.1).

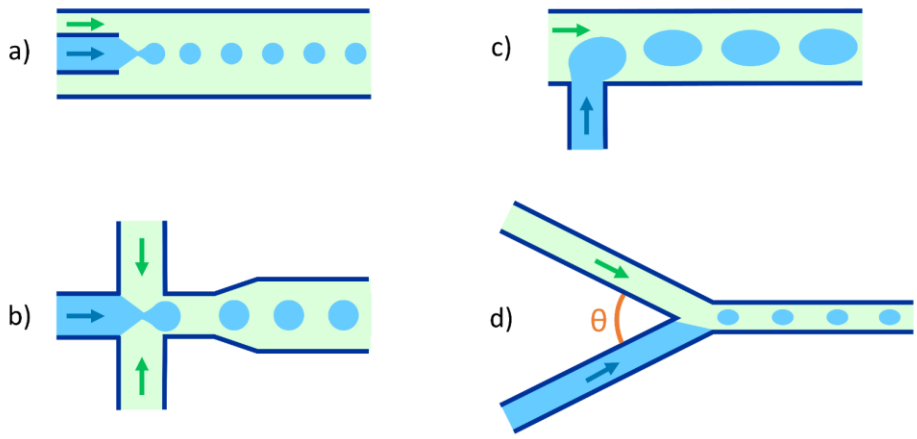

Figure 9.1: Schematic representation of passive droplet generation methodologies: a) co-flow; b) flow-focusing; c) cross-flow T-junction and d) cross-flow Y-junction. Blue and green arrows represent the flow direction of the dispersed and continuous phases, respectively. Light blue and light green represent the dispersed and continuous phases accordingly.

In the co-flow method, a small-diameter channel is inserted in a larger-diameter channel, and dispersed and continuous phases flow in parallel. Droplets are formed at the end of the smaller channel, where the dispersed phase flowing in the smaller channel is enclosed by the continuous phase flowing in the larger channel[436,437]. For the flow-focusing method, dispersed and continuous phases flow perpendicularly, with the continuous phase intercepting the dispersed phase in opposite directions. Droplets are formed due to pinching of the dispersed phase by the continuous phase. A narrowing channel is commonly present, to improve control over droplet size and parameters such as droplet circulation speed[436,437]. Lastly, the cross-flow method (for any junction architecture) is characterized by the intersection of continuous and dispersed phases at an angle θ, as represented in Figure 9.1 d)[435]. General characteristics of each method are summarized in the following table.

Table 9.1: Comparison between droplet generation methodologies according to selected parameters.

	Co-flow	Flow-focusing	Cross-flow
Droplet shape	Spherical or non-spherical	Mostly spherical	Non-spherical
Droplet size	Adjustable	Adjustable	Adjustable
Droplet size dispersion	Depends on operating regime	Low	Low
Fabrication	Easy	Can be difficult	Standard

Each methodology presents advantages and drawbacks; however, the final choice must take into consideration the integration with the DMF device. DMF is meant to provide the liquid for the dispersed phase, meaning that the droplet generator for DrMF will ideally operate with negative pressure, pulling the dispersed phase from the DMF (e.g. DMF-CMF hybrids produced by Abdelgawad *et al*.[426]). From the above-mentioned methodologies, flow-focusing has been demonstrated to operate with negative pressure for the dispersed phase and positive pressure (pushing force) for the continuous phase[438,439]. Moreover, spherical and monodisperse droplets are possible, which will facilitate droplet analysis. Difficulties in fabrication arise mostly from the pinching region, which may include challenging features (angles must be accurate and corners must be perfectly straight), however the facilities available at CEMOP allow for fabrication of this kind of feature. In light of the above-mentioned arguments, flow-focusing was the chosen droplet generation system.

9.2 Architecture of the DMF-DrMF hybrid devices

As concluded in the previous section, the hybrid platform will include a DMF section coupled with a DrMF section featuring a flow-focusing area for droplet generation. This DMF-DrMF platform should be capable of generating nano-liter spherical droplets, fed by DMF electrodes and controlled by a combination of positive pressure (pushing flow) for the oil phase and negative pressure (pulling flow) for the aqueous phase. In a first approach, a simple design will be implemented, to study the interface between the two microfluidic technologies, optimize operation parameters (e.g. syringe pump flows for the DrMF section, DMF voltage applied at the interface) and solve any unforeseen problems.

9.2.1 The DrMF section: emphasis on the flow-focusing region

One of the most pressing issues in the architecture of this platform is the flow-focusing region. This region must be carefully designed, since channel dimensions and angles between channels are greatly relevant for droplet formation[440,441]. The design of the flow-focusing region was thus adapted from the work of Teo *et al.*[442], and dimensions were adjusted for: a) width of the channel interfacing DMF of 180 µm, matching the bottom-top plate distance in DMF; b) input/output apertures with 1 mm radius, in conformity with the available tubing for connection with syringes; c) maximum length of 4 cm, to fit within the visibility window of a DMF support (adapted to a 10 cm length window glass); d) maximum width of 3.6 cm, to be compatible with the available edge connectors. Initially, only the DrMF section was produced

(standalone DrMF devices) in order to optimize conditions for producing high-throughput nano-droplets with negative pressure (pulling force), prior to integration with the DMF section. The final design for the DrMF standalone devices is depicted in Figure 9.2.

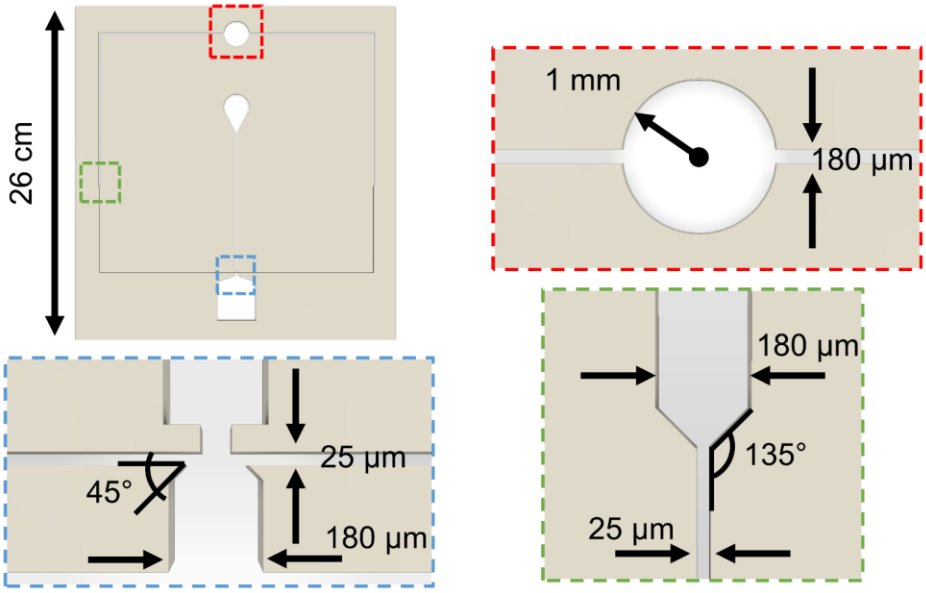

Figure 9.2: Representation of DrMF standalones, evidencing relevant features and dimensions. The flow focusing region (highlighted in blue, bottom left) receives the aqueous phase from the squared reservoir at the bottom of the device and the oil phase from the left and right channels. The access point for the oil phase is represented on the top right (highlighted in red), and the channel width reduction zone is represented on the bottom right (highlighted in green).

Briefly, the DrMF section includes two access points for the two phases required to create nanoliter droplets at the flow-focusing region (region highlighted in blue). The oil phase is inserted on the circular inlet (region highlighted in red) and flows laterally both right- and leftwards, down to the flow-focusing area; the aqueous phase enters by the squared reservoir at the bottom of the device. The aqueous samples experience a pulling force exerted by a syringe-pump connected to the tear-shaped access point, located below the circular inlet highlighted in red. Considering the small size of features in relation to the area of the device, a large print image of said device was added to Appendix K, for better visualization.

Standalone devices were also used to assess the influence of semi-passive liquid supply (i.e. not driven into the device by assistance of a syringe pump at the entry point), by using the squared reservoir (with approximately the same dimensions as the DMF electrodes) to store the liquid phase, which in turn is dispensed from a previously-filled pipette tip - Figure 9.3.

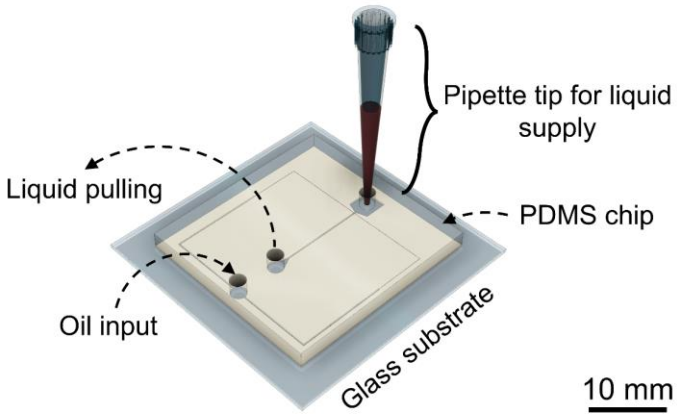

Figure 9.3: 3D illustration of a standalone DrMF device. The oil phase is inserted through the oil input by means of a syringe pump (pushing force), liquid is passively supplied by a pre-filled pipette tip connected to an additional squared reservoir, and a pulling force is applied through the outlet.

9.2.2 DMF-DrMF hybrids

The proposed DMF-DrMF hybrid device follows an in-line approach, where both moieties of the device (DMF and DrMF sections) are built on the same standard glass substrate. Thus, sample fluid flows directly from the DMF section to its DrMF complement - Figure 9.4. Please note that the only difference between standalone DrMF devices and the DrMF section of the hybrid devices is that the region of the squared reservoir was cut and replaced by the DMF-DrMF interface.

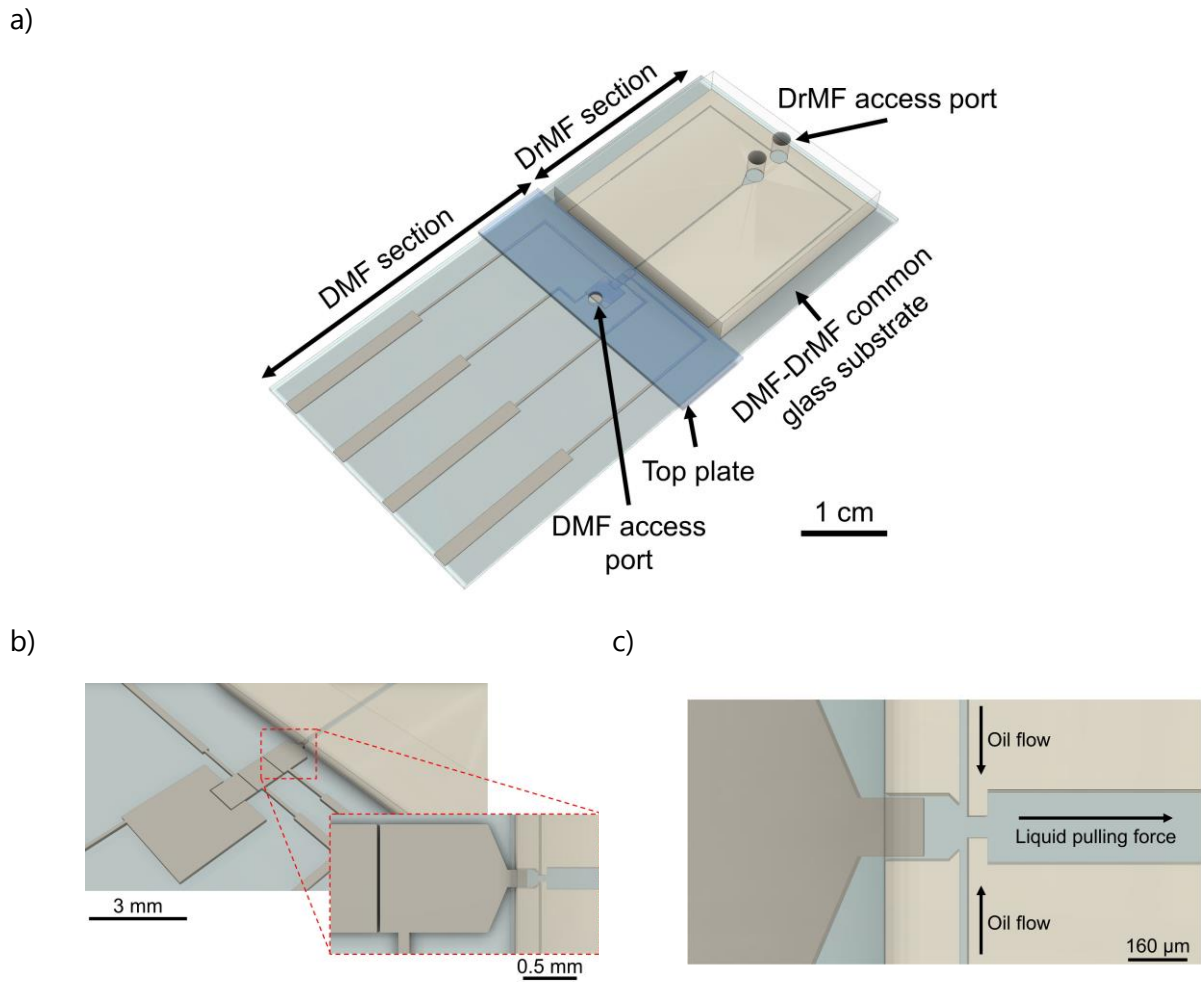

Figure 9.4: 3D illustration of a DMF-DrMF hybrid device. a) General view of the hybrid device, evidencing all constituting parts. b) Close-up view of the DMF electrodes, without the top plate. The inset image represents the electrode specifically designed for the DMF-DrMF interface, which includes a triangular end shape that directs droplets towards the droplet generation site within the DrMF section. An additional protuberance enters the DrMF cavity and further assists the liquid transference from the DMF to DrMF. c) Interface between DMF and DrMF, evidencing the flow focusing area (droplet generator structure), as well as the direction of the oil phase flow, and the flow direction of the droplets. Briefly, the oil phase is inserted through the access port closest to the edge of the DrMF section and flows bilaterally to the flow focusing region, whereas the aqueous phase is pulled from the DMF section, through the second (inward) access port. Both pulling of the aqueous phase and insertion of the oil phase are mediated by syringe pumps.

The design includes a DMF section with a bottom plate comprising 3 working electrodes and a larger reservoir (Figure 9.4 b)). An access port was drilled on the top plate, directly above this larger reservoir, thus enabling sample insertion. The final electrode was optimized to facilitate the transference of the aqueous phase from the DMF section to the DrMF section. This electrode features a triangular termination that directs the sample towards the DrMF section, and further includes a rectangular protuberance that enters the DrMF section, also assisting liquid transference (Figure 9.4 b) and c)). The DrMF section consists of the flow focusing device

previously discussed, where phase and flow rate differences should allow for the generation of nanoliter droplets at the junction area. The DMF-DrMF hybrid is mounted onto a 3D-printed casing similar to the one presented in section 5.2, which was enlarged to accommodate a glass piece with 10 cm of length. Essentially, this meant extending the length of all 3D-printed components by 3.5 cm and adjusting the position of the pogo pins to match the size and location of the new top plates (see Figure 9.4 a)).

9.3 Fabrication of the DMF-DrMF hybrids and assembly of the experimental setup

Before performing any fabrication step, the glass substrates were subjected to a thorough cleaning process, as previously described (section 5.1.2). After cleaning, the DMF section is fabricated on the glass substrate, and the DrMF section is fabricated separately and further mounted onto the substrate, as described below. Please note that some of the fabrication steps, such as the deposition of the dielectric layer (Parylene C) are common to both sections.

9.3.1 Fabrication of DMF and DrMF sections

The DrMF section consists of a set of microchannels embossed on a PDMS substrate, which is then sealed to the glass substrate containing the DMF electrodes. Such PDMS-based microchannels were produced from primary SU-8 molds. Briefly, SU-8 2150 (Kayaku Advanced Materials, Westborough, MA, USA) was spin-coated at 500 rpm for 7 s and 3260 rpm for 30 s, after which the resist was allowed to rest for 10 min. Soft-baking followed, with heating at 65 °C for 5 min and 95 °C for 20 min. After a brief cooldown, the SU-8 resin was exposed on a mask aligner with a constant dose of 240 $mJ \cdot cm^{-2}$. After exposure, two additional baking steps were performed, with heating at 65 °C for 5 min and 95 °C for 10 min. Finally, the molds were developed in propylene glycol monomethyl ether acetate for 10 min, on a rotation table rotating at 50 rpm. Such molds were then used to fabricate the PDMS microchannels. Firstly, base and curing agent from the SYLGARD®184 silicone elastomer kit (Dow, Midland, MI, USA) were mixed on a 10:1 proportion and deposited over the SU-8 molds, previously placed on a plastic petri dish. The petri dish was then placed in vacuum until all air bubbles were eliminated. Following this step, mold and elastomer were placed in a drying oven at 70 °C for approximately 1 hour, after which the PDMS elastomer could be successfully peeled from the SU-8 mold. The photolithographic mask includes a guiding line at the interfacial region with DMF, which is

transferred onto the PDMS and creates a groove. This groove allows for accurate cutting of the polymer without damaging the flow focusing region at this point in fabrication. Access ports to the DrMF were then opened on the PDMS with an appropriate puncher (Darwin Microfluidics, Paris, France). Sealing of the PDMS microchannels onto the glass substrate followed, through plasma exposure with 30 SCCM of O_2 for 70 s at 1000 mTorr and 25 W (Phantom III RIE from Trion Technology, Tempe, AZ, USA). 7 µL of isopropyl alcohol (IPA) were placed between the DrMF section and the glass substrate, for alignment of the flow focusing region with the interface electrode (see Figure 9.4 c)) of the DMF section, under a microscope (the IPA creates a sacrificial layer that allows the user to adjust the DrMF section on the glass substrate if necessary). Another heating step followed, for approximately 2 hours at 115 °C in a hot plate with added weight on top. The DrMF section was thus fabricated, and the remaining DMF fabrication steps followed. Please note that this protocol was also used to fabricate standalone DrMF devices.

The fabrication of the DMF section essentially follows the same steps described in section 5.1.2, with some minor adaptations: exposure time was decreased from 8 s to 6.5 s, and post-baking time was also reduced from 35 s to 30 s. Following electrode patterning, the DrMF section was aligned with the connection electrode and sealed onto the glass substrate, and prior to the dielectric deposition step, the top of the DrMF section was covered with polyimide tape. Covering the top of the DrMF section prevents the deposition of Parylene C on top of the microfluidic channel where droplets circulate, which creates a blurring effect that subsequently hinders video capture of the droplet shapes. For the dielectric layer, a 2 µm layer of Parylene C was deposited as previously disclosed, followed by the PTFE hydrophobic layer, also as previously described. Prior to use, the DMF section was filled with degassed 5cSt silicone oil.

9.3.2 DMF-DrMF experimental setup

Two separate control systems were used to operate the hybrid DMF-DrMF devices, one applied to each section. For the DMF section, the same custom control system was used (sections 5.4 and 5.5). The second control system was applied to the DrMF section, and was comprised of two syringe pumps (Legato 210 P from KD Scientific, Holliston, MA, USA): one used to push oil into the DrMF section, and another one to apply negative pressure to the system, thus effectively pulling the aqueous phase. For both oil and aqueous phase, specific syringes were used (0.5 mL volume, model GASTIGHT® 1750TLL, PTFE luer lock from Hamilton, Reno, NV, USA) coupled with microfluidic tubes (reference LVF-KTU-13 from Darwin Microfluidics, Paris, France) and blunt-end luer lock syringe needles (reference AE-23G-100x, also from

Darwin Microfluidics). For standalone DrMF experiments, only the latter control system was used, with the aqueous phase being supplied by a pre-filled pipette tip instead of the DMF section, as previously stated. The oil phase circulating within the DrMF section consists of mineral oil (light oil for molecular biology, reference M5904 from Sigma-Aldrich, St. Louis, MO, USA) and Span80® (Croda International PLC, Snaith, England) at 0.5% wt/wt whereas the aqueous phase consists of LAMP buffer diluted to 1x (ThermoPol® reaction buffer). The DMF-DrMF devices and physical support were placed on a clear acrylic base, mounted on an optical breadboard (model MBH3060/M from ThorLabs, Newton, NJ, USA). Below the acrylic base, a custom-built lighting base with multiple LED lights allowed for optimal illumination and contrast control of the DrMF droplets, for further image-based droplet analysis. Finally, a 25 mm optical construction rail (ThorLabs) was mounted on the optical table, to hold a Chameleon3 USB3 monochrome camera (model CM3-U3-13Y3M-CS, Python 1300 from Teledyne FLIR, Wilsonville, OR, USA), coupled with a MLM3X-MP magnification lens from Computar (Cary, NC, USA) to acquire videos.

After mounting the experimental setup described above, silicone oil should be slowly introduced into the DMF section, thus filling the DMF cavity without the production of air gaps. An additional hole may be drilled on the top plate to facilitate the exit of air between the DMF top and bottom plates, as silicone oil is introduced. Mineral oil should be inserted into the DrMF section at a relatively low rate (500 nL/min), thus slowly expelling air from the device without air bubble formation. Devices are only used after ensuring that no air bubbles are observed on either section. Despite some contact between the oils used in both moieties at the interface, they are immiscible, and this contact does not significantly affect the operation of the device.

As for the liquid phase, LAMP buffer diluted to 1x was used for these initial assays. After inserting the oil phase, LAMP buffer should then be inserted onto the DMF section of hybrid devices by activating the larger reservoir and then inserting the buffer through the hole drilled on the top plate, by means of a micropipette. By sequentially activating and deactivating neighboring electrodes, the LAMP buffer should be moved towards the interfacing electrode (see Figure 9.4 b) and c)) and only then should the respective syringe pump be activated (negative pressure, pulling force). For droplet motion in DMF, the standard AC signal of 40 V_{RMS} was used, at a frequency of 5 kHz. This signal was kept constant at the interfacial electrode during droplet generation, to ensure a constant supply of LAMP buffer from the DMF section to the DrMF section. Moreover, regarding the testing of different fluidic flows on the DrMF section, tests should always be performed from the smaller to the larger flows to avoid excessive pressure

increase within the device. This increase in pressure could result in abnormal droplet formation, accompanied with larger volume and speed variability.

9.3.3 Data acquisition and analysis

Data acquisition and processing was fully centralized into an in-house developed offline software. Firstly, a connection to the camera was established, and the acquired video (20 s to 25 s duration) was cropped to ensure that only the region where droplets flowed was captured. After cropping, the video frames were converted to grayscale, to facilitate the definition of a threshold between the droplets and the surrounding medium. To achieve a fair droplet threshold, it is essential to adjust the LED lighting source to ensure that the edge of droplets is well defined, with a dark droplet contour and a bright droplet. Visual confirmation of the identified droplet contour may be performed by the user. After isolating the droplets from the background, the software determines the volume of droplets, the droplet speed and the droplet production frequency. Finally, results obtained from the image processing may be exported to a .csv file for further analysis.

9.4 Characterization of the DrMF section through standalone devices

As previously mentioned, standalone DrMF devices were used to optimize the droplet generator design, by determining the optimal conditions for producing high-throughput nano-droplets with negative pressure (pulling force). Regarding droplet production, two major parameters require optimization: the pulling flow for the LAMP buffer and the pushing flow for the oil phase. Several combinations of both were tested, and the droplet-forming conditions relied on pulling flows in the order of µL/min and pushing flows in the order of nL/min. Figure 9.5 illustrates the droplet volume, speed and frequency obtained for several droplet-forming conditions (i.e., flow ratios), as well as a representative video frame of the droplets produced by the DrMF device. Droplet volume was determined from the diameter (d) measured by the image analysis software, in two different conditions: if the droplet diameter is larger than the channel dimensions (height and width), the volume was determined as suggested by Crawford *et al.*[443]; otherwise, the volume was approximated to the volume of a sphere with radius $d/2$. Please note that the frequency represents the number of droplets formed per second, denoted

as dr/s for simplicity. The optimal flow for pulling the aqueous phase was determined to be 1000 nL/min[§], and several flows for pushing the oil phase were further tested.

a) DrMF standalone: droplet volume

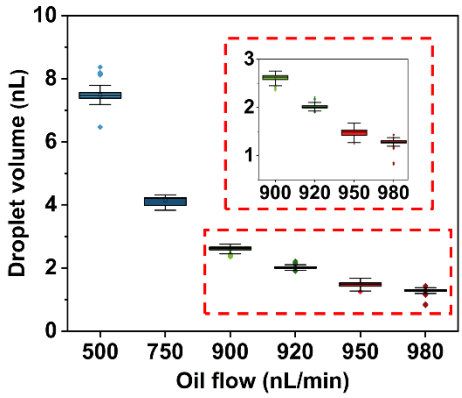

b) DrMF standalone: droplet speed

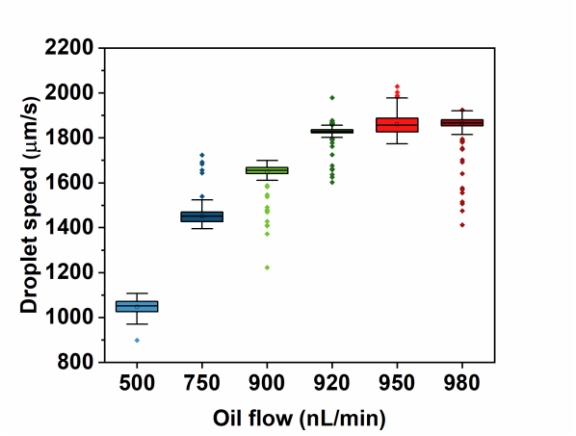

c) DrMF standalone: droplet frequency

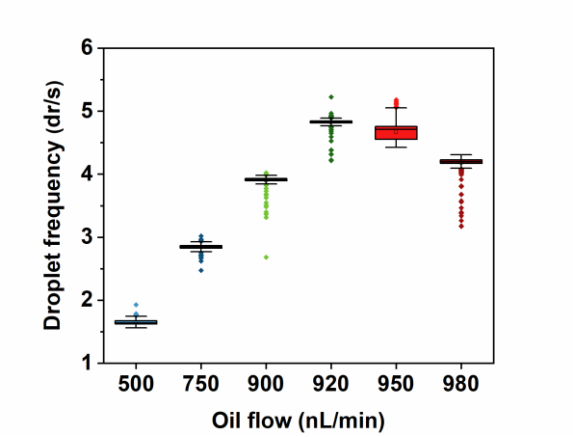

d) DrMF standalone: video frame of droplets generated at 920 nL/min oil flow

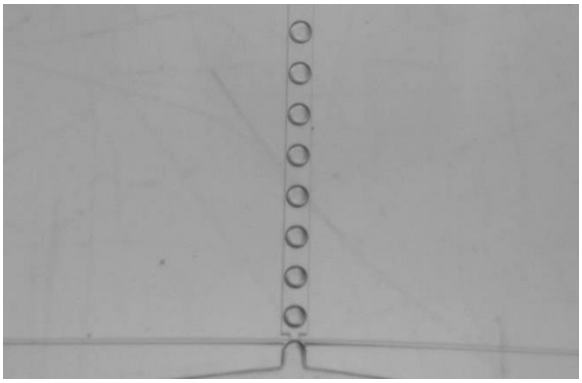

Figure 9.5: Box plots for droplet volume (a), speed (b) and frequency (c) as determined by the software developed for this work. The pulling flow for the LAMP buffer was kept constant at 1000 nL/min whereas the pushing flow for oil varied from a minimum of 500 nL/min to a maximum of 980 nL/min. Below and above this range of pushing flows, droplet formation was unstable. Outliers were determined by the interquartile range (IQR) method[444], and were kept in the data presentation, represented by colored points in line with the respective data set. For each experiment, a minimum of 1000 droplets were evaluated. d) represents a video frame evidencing droplets produced with standalone DrMF devices, for a randomly selected oil flow of 920 nL/min.

As illustrated by Figure 9.5, for each tested condition in both droplet volume and droplet speed, the data is narrowly distributed, suggesting that these standalone DrMF devices can

[§] Below 1000 nL/min, droplets are not spherical as intended, but assume a rectangular shape with round corners. Above 1000 nL/min, droplet speed becomes too high and internal pressure increases enough to hinder the uniformity of the droplet production (results not shown).

generate stable droplets. Regarding the volume of the produced droplets, there is a decrease with increasing pushing flows. If the oil flow at the flow focusing region (Figure 9.2) is increased for a constant buffer flow, the buffer will be divided into smaller droplets (smaller volumes). Furthermore, this decrease in droplet volume is accompanied with an increase in droplet speed – Figure 9.5 b). This may be explained by the increase of lateral pressure at the flow focusing region as the pushing flow increases, which leads to faster droplet production and consequently, faster droplet motion[445–447]. It is observable that the increase in droplet speed does not always increase linearly with the increase in oil flow. As a matter of fact, the increase in speed accompanying the flow change from 900 nL/min to 920 nL/min is almost as large as the one from 750 nL/min to 900 nL/min (the median[**] speed value increases approximately 204 μm/s and 173 μm/s, respectively). This tendency will be explored further ahead.

Droplet frequency is also a relevant parameter to measure, as it represents the number of droplets formed by the flow focusing region, per second. For DrMF standalone devices, an interesting behavior is observed: the frequency steadily increases as the oil flow increases, until reaching a maximum for an oil flow of 920 nL/min. After this maximum, droplet frequency decreases for higher oil flows. It was expected that higher oil flows would lead to a higher number of droplets produced per time-period, considering that the aqueous phase (LAMP buffer) will be disrupted at increasing rates. One possible explanation for the decrease in frequency after 920 nL/min of oil flow is the equilibrium of pulling and pushing forces acting upon the aqueous and oil phase, respectively. As the pushing oil flow approaches the pulling flow for the LAMP buffer (1000 nL/min), the opposite forces tend to balance with each other and thus droplets are formed at an increasingly slower ratio. However, even though the frequency of droplet formation decreases, the droplet speed is kept stable. This suggests that it is possible to individually control the frequency of droplet formation, as well as the droplet speed.

9.5 Characterization of DMF-DrMF hybrid devices

Knowing the flow combinations that lead to droplet formation, studied with DrMF standalone devices, the same flow combinations were applied to DMF-DrMF hybrid devices. As mentioned in section 9.3.2, in hybrid devices, the LAMP buffer must first be moved towards the interface electrode of the DMF section, and only then can the DrMF syringe pumps be

[**] The median value was selected as a means of comparison since it is less affected by the outliers than the mean value.

activated for droplet formation. For all the oil flows tested on standalone DrMF devices, LAMP buffer was successfully supplied by the DMF section to the DrMF section, where nano-liter droplets were further produced. This is a reasonable indicator that the union of both microfluidic moieties is at the very least able to match their standalone capabilities. Figure 9.6 illustrates the droplet volume, speed and frequency obtained for the mentioned hybrid devices, as well as an example of the droplet-forming interface.

a) DMF-DrMF hybrids: droplet volume

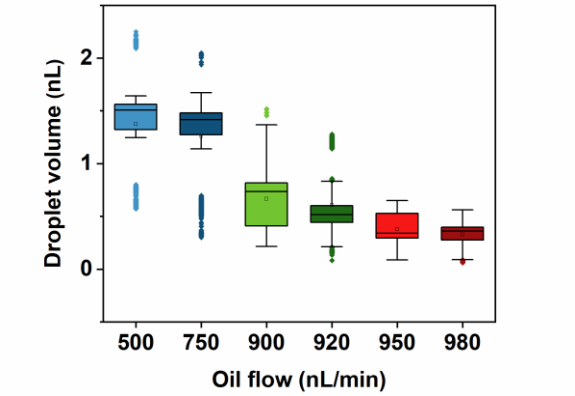

b) DMF-DrMF hybrids: droplet speed

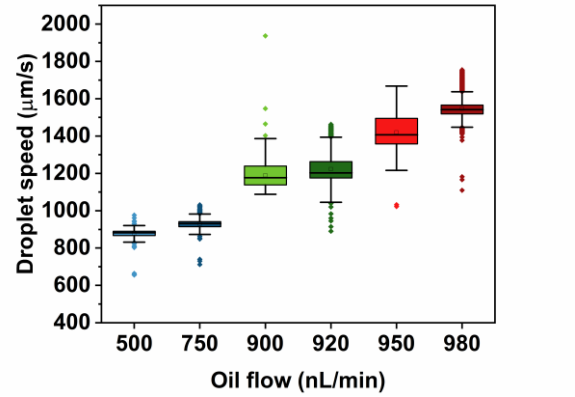

c) DMF-DrMF hybrids: droplet frequency

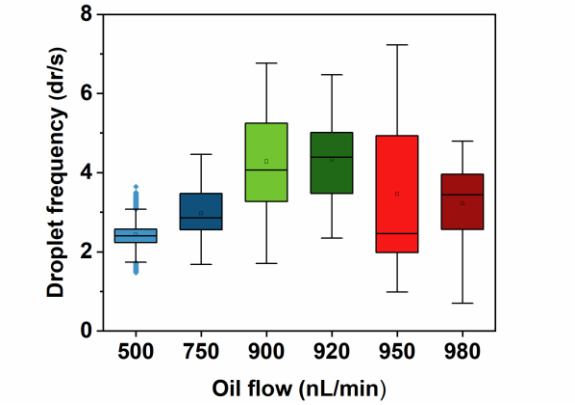

d) DMF-DrMF hybrids: video frame of droplets generated at 920 nL/min oil flow

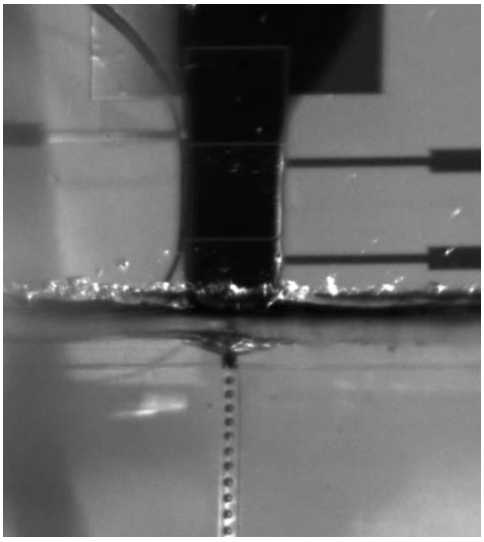

Figure 9.6: Box plots for droplet volume (a), speed (b) and frequency (c) in DMF-DrMF hybrid devices, as determined by the software developed for this work. As experimented for DrMF standalone devices, the pulling flow for the LAMP buffer was kept constant at 1000 nL/min whereas the pushing flow for oil varied from a minimum of 500 nL/min to a maximum of 980 nL/min. Once more, outliers were determined by the interquartile range (IQR) method[444], and were kept in the data presentation, represented by colored points in line with the respective data set. For each experiment, a minimum of 1000 droplets were evaluated. d) represents a video frame evidencing droplets produced with hybrid DMF-DrMF devices, for a randomly selected oil flow of 920 nL/min. LAMP buffer is supplied by the DMF section on top, droplets are formed on the near-interfacial flow focusing region (not visible), and further flow through the DrMF microfluidic channel on the bottom.

DMF-DrMF hybrid devices also produce stable droplets, as evidenced by the low dispersion of data in both droplet volume and speed for all tested conditions. This attests to the quality and robustness of the developed devices. A deeper analysis of the volume shows that there is a clear tendency for decrease as the oil flow is increased (see section 9.6). Nevertheless,

this tendency is quite smooth and the decrease in the average droplet volume from the first to the last tested oil flow condition (500 nL/min and 980 nL/min respectively) is not very expressive – Figure 9.6 a). As a matter of fact, there is very little variation in the populations obtained for 500 nL/min and 750 nL/min (median droplet volume of 1.5 nL and 1.4 nL, respectively), despite the large increase in oil flow. This might be due to the reduction of the microfluidic channel dimension at the interface between DMF and DrMF. Since both Parylene C and PTFE are deposited on the hybrid devices after bonding of the DrMF section to the glass substrate (see Figure 9.4 a)), two supplementary layers of thickness are added to the walls of the PDMS. Appendix L includes a study on the variation of the microfluidic channel width as a result of Parylene C and PTFE depositions. This decrease in the diameter of the DrMF microfluidic channel at the flow focusing region leads to a decrease in the maximum droplet volume when compared with standalone DrMF devices. Moreover, PTFE is even more hydrophobic than PDMS, reducing interaction of the aqueous phase with DrMF channel walls, which could also contribute to the non-decrease of the droplet volume with the increase of oil flow. Appendix M includes information regarding the contact angle of the discussed materials, as a measure of their respective hydrophobicity. The droplet volume only decreases for oil flows from 900 nL/min onwards, as illustrated on Figure 9.6 a). Regarding droplet speed, as discussed above (see section 9.4), speed increases with the increment in oil flow. However, for DMF-DrMF hybrid devices, speed presents little variation between 500 nL/min to 750 nL/min of oil flow (1274.1 µm/s and 1212.6 µm/s median speed, respectively), and even between 900 nL/min and 920 nL/min (1258.3 µm/s and 1378.8 µm/s median speed, respectively). This could be explained by the activation of the interface electrode during the droplet generation process, which could exert an additional force on the droplets, thus attracting them to the activated DMF electrode. Such additional force could act as a barrier to the increase in droplet speed for sequentially larger oil flows, without influencing the droplet volume. Regarding droplet frequency (Figure 9.6 c)), the number of droplets produced per second increases as the oil flow is increased until 920 nL/min. After such oil flow, the droplet frequency decreases, which could also be explained by the equilibrium between pushing and pulling forces, as the pushing oil flow becomes closer to the pulling flow of the LAMP buffer (1000 nL/min). However, this decrease in droplet production does not affect droplet speed, which continues to increase after 920 nL/min of oil flow. Data thus suggests that the hybrid DMF-DrMF devices enable on-demand nano-droplet formation with tunable droplet production rate and speed. However, it is observable that there is a higher dispersion of values than for standalone devices, which will be further analyzed in the following section.

9.6 Comparing standalone DrMF and hybrid DMF-DrMF devices

After individually studying the droplet parameters of standalone DrMF and hybrid DMF-DrMF devices, a comparison between both was performed. Figure 9.7 contains graphical representations of the average droplet volume, speed and droplet production frequency for each tested oil flow.

a)

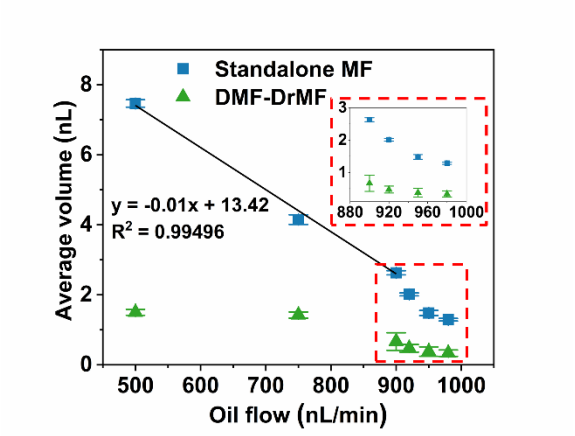

b)

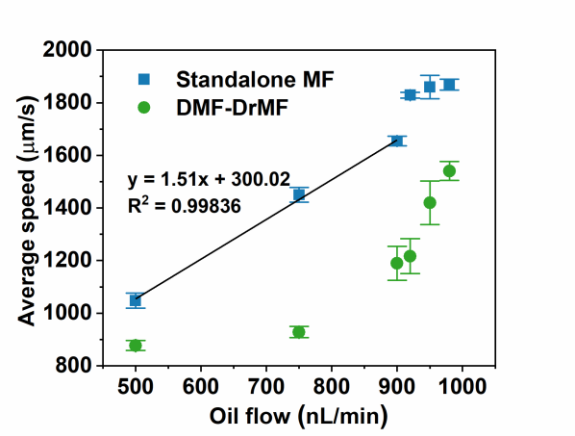

c)

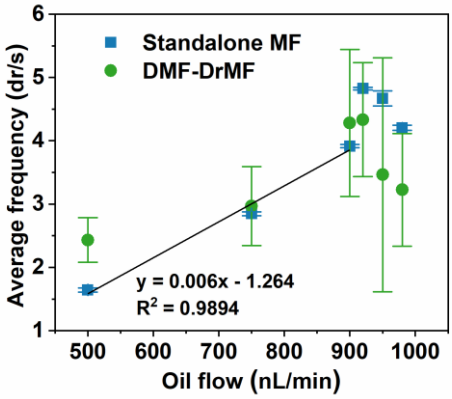

Figure 9.7: Average droplet volume (a), speed (b) and frequency (c) for variable positive pressure oil flows and constant negative pressure for LAMP buffer (1000 nL/min), in standalone DrMF devices and hybrid DMF-DrMF devices. Outliers were removed from all data sets, considering their large influence on the averaged results. The inset on a) represents an enlarged plot of the area highlighted in red (between 880 nL/min and 1000 nL/min oil flows). On a), b) and c), the equations correspond to the linear fit obtained for the first three oil flow conditions (500 nL/min, 750 nL/min and 900 nL/min) for standalone DrMF devices, also represented by the black lines. Error bars correspond to the standard deviation of data.

As depicted in Figure 9.7 a), there is a significant difference in droplet volume between standalone and hybrid devices, for 500 nL/min of oil flow. This difference decreases with the increase in oil flow; however it remains statistically significant until the final tested oil flow,

980 nL/min. This difference in droplet volume between both types of devices can be explained by the thinning of the DrMF microfluidic channel in DMF-DrMF hybrid devices, due to the deposition of Parylene C and PTFE (see Appendix L). Standalone DrMF devices present a clear decrease in droplet volume (almost linear) as the oil flow increases until 900 nL/min. From this point forward, the linear tendency appears to be lost, however lower oil flows continue to produce smaller droplets. As for hybrid devices, there is no linear tendency for droplet volumes, which again could be related to the decrease in the microfluidic channel diameter. From 900 nL/min to 980 nL/min, the difference in the average droplet volume between standalone and hybrid devices is less pronounced, however there is still a clear distinction in the behavior of the two types of devices. In this oil flow regime, the decrease in volume is smoother in hybrid than in standalone devices, probably due to the difference in the initial volume. As for Figure 9.7 b), in standalone DrMF devices, there is a linear tendency for increase in droplet speed as the oil flow increases, until 900 nL/min. After 900 nL/min flows, the linear tendency appears to be lost, and is replaced for what seems to be a saturation plateau tending towards approximately 1900 µm/min. For hybrid DMF-DrMF devices, the average droplet speed remains relatively stable for 500 nL/min and 700 nL/min, increasing only after the latter oil flow. This could be due to the force exerted by the activated interfacial electrode on the LAMP buffer, as previously stated (section 9.5). Moreover, droplet speed in hybrid devices is consistently lower than in standalone DrMF devices. This suggests that despite the presence of PTFE at the beginning of the DrMF microfluidic channel (which in the form of the solution prepared for this work presents a higher degree of hydrophobicity than PDMS alone - see Appendix M), the force exerted by the activated interfacial electrode is dominant, leading to the overall lower droplet speeds. Also regarding hybrid devices, the speed does not seem to reach any saturation plateau, however, the maximum average speed achieved in such devices is still far from the plateau where standalone devices appear to saturate. As illustrated in Figure 9.7 c), frequency in standalone DrMF devices presents a closely linear increase with the increase in oil flow, from 500 nL/min to 900 nL/min. For higher oil flows, consistently with droplet volume and speed, the linear tendency is lost, and the maximum droplet production frequency is achieved for 920 nL/min oil flow. After reaching this maximum, droplet frequency decreases, which as previously stated (section 9.4), is likely related to the equilibrium of positive and negative pressure applied to the oil and LAMP buffer, respectively. Moreover, it is interesting to note that contrary to droplet volume and speed, the frequency of droplet production is similar in both standalone and hybrid devices. DMF-DrMF devices thus match the high throughput production of droplets achieved by standalone DrMF devices, yet with a slower progression of

speed with oil flow increase. This implies that hybrid devices provide the same droplet throughput, with a more controlled progression of droplet volume and speed, since such characteristics do not fluctuate as much as for standalone DrMF devices. In both cases, the maximum droplet production rate is achieved for 920 nL/min of oil flow. Furthermore, frequency in DMF-DrMF devices presents higher variability than for DrMF devices, as suggested by the larger standard deviation. One possible explanation is the activation of the interface electrode. The activation signal could be sufficient to introduce variations in the number of droplets produced per time unit - further investigation would be required to confirm this theory. Nevertheless, regardless of the type of device tested, droplet volume, droplet speed and droplet frequency can be successfully controlled by simply adjusting the oil flow.

In summary, by comparing droplets produced by standalone DrMF devices with hybrid DMF-DrMF devices and after analysis, it is possible to conclude that both methodologies provide controllable droplet production. The standalone DrMF devices provide a wider range of droplet sizes and circulation speeds, whereas DMF-DrMF devices provide a stabler and more controlled droplet production - both technologies provide similar droplet throughputs. This is a proof-of-concept for the working principles of hybrid DMF-DrMF devices; however, it is important to consider that DMF enables a wide range of electrode pathways and consequently a wide range of protocols, and DrMF further enables high-throughput nano-droplet production, which may flow in any desired microfluidic channel path. The hybrid DMF-DrMF devices herein presented opens the path to a new range of applications featuring nucleic acid amplification, where the DMF section may be used to mix the required reagents and further supply the mix to the DrMF section, which is then able to produce nano-liter droplets, required for digital droplet reactions such as droplet digital LAMP[448] or droplet digital PCR[432]. By adding a heating element, a fluorescence detection system and by associating a software for droplet analysis, DNA quantification by in-line droplet-digital LAMP should be possible. With this setup, droplet fluorescence could be measured as droplets flow through the microfluidic channels after heating, as opposed to traditional fluorescence measurement in a wider chamber, where all droplets are gathered[432,449,450].

10

FINAL CONSIDERATIONS AND FUTURE PERSPECTIVES

10.1 Final considerations

This PhD project aimed at developing and studying sensing methodologies to be incorporated with digital microfluidics, for monitoring isothermal nucleic acid amplification. For such purposes, the first step was to design and fabricate the DMF devices, as well as a physical support for the devices. After screening multiple materials for all device layers, the final structure was set to comprise two plates: for the bottom plate, a glass substrate was selected, as well as chromium electrodes, a Parylene C dielectric layer and a PTFE-based hydrophobic layer; for the top plate, ITO-covered glass was selected, also with a PTFE-based hydrophobic coating. The electrode pathway was designed to allocate three entry points for reagent insertion, two points for reactions to occur, and two points for reaction product withdrawal. Various entry and exit points allow for redundancy paths in case of device failure in a specific region, as well as multiple options for on-chip reaction protocols. The final design included seven larger reservoirs, namely three for inserting reagents, two for performing reactions and another two for withdrawing reaction products. All reservoirs were interconnected by a network of nineteen electrodes, allowing for droplet motion from/to any reservoir. A physical support was then designed to accommodate the DMF devices, as well as the required connections from each electrode/reservoir control pad to the voltage driving system. Briefly, the physical support consists of a 3D-printed casing including a cover with a window opening (for visualization and/or fluorescence measurements) and a layered bottom support, which holds the DMF devices in place and accommodates the heating element. Voltage driving was based on an open-source voltage control unit, specifically designed for DMF devices, which essentially mediates the application of an AC signal or ground voltage to each electrode (ON and OFF states, respectively) according to user instructions provided through a graphical user interface. For heating, an ITO thin film resistor was used, which produced heat according to the current provided by a MOSFET driver working on temperature feedback from a temperature sensor.

The Parylene C dielectric layer was also evaluated under thermal and electric stress, considering that performing LAMP reactions on-chip requires heating the device and also maintaining the AC signal to the reaction regions, in order to fixate the reaction droplet. The dielectric layer proved to be resistant to both sources of stress, enduring with minimal loss of capacitance after a test period of two hours. However, considering that the presence of liquid and oil over the hydrophobic and dielectric layer will also promote damage to the DMF devices, namely dielectric breakdown, a prevention strategy was tested: deposition of Parylene C in

double-layer. This dual deposition should contribute to the interruption of pinholes and surface impurities which would otherwise lead to vertical current paths and consequently, breakdown. Such strategy proved to be successful in enduring thermal and electric stress, and allowed to perform long LAMP reactions (two hours) without any visible damage to the DMF devices, contrary to the single-layered counterparts, which frequently suffered dielectric breakdown and complete destruction of the droplet-bearing electrodes.

The developed DMF platform was the base for the study of monitoring methodologies for isothermal nucleic acid amplification by loop-mediated isothermal amplification. Three distinct methodologies were studied: fluorescence measurements, impedance measurements and electrochemical measurements.

The starting point was, of course, the gold standard for nucleic acid amplification monitoring: fluorescence. Fluorescence measurement parameters were firstly studied off-chip, namely the concentration of the fluorophore EvaGreen® for detection with an optical microscope. The temperature control system was adjusted specifically for on-chip LAMP reactions, with a PT100 temperature sensor glued to the top plate, controlling temperature feedback. The adjusted temperature control system enabled a steady temperature rise until the setpoint of 59.5 °C, and further kept temperature stable during the reaction, with a maximum error under 1 °C. The DMF physical support was also engineered to be as thin as possible (1.9 cm height), thus fitting an optical microscope and respecting its focal distance. On-chip LAMP was then performed with positive and negative controls simultaneously, for the *c-Myc* proto-oncogene. After moving the appropriate volume of LAMP master mix towards the two reaction regions, positive and negative controls were defined by mixing either target DNA or reaction buffer with the mix, respectively. To overcome the mixing difficulty in microfluidic systems, a new DMF mixing protocol was implemented, joining back-and-forth motion with frequency tuning of the AC signal. Essentially, back-and-forth motion between neighboring electrodes/reservoirs mimics a shaking movement, whereas the decrease in frequency of the AC signal down to 0.5 Hz allows for elements within the droplet to accompany the electric field applied, further increasing the mixing efficiency. In fact, at such low frequencies, the droplet itself can physically react to the signal, performing a "dance" on a single reservoir visible with naked eye. Nevertheless, despite the improvement of on-chip mixing, photobleaching was still a persistent issue, due to the use of sub-ideal equipment for fluorescence detection, which required maximization of intensity of the excitation light. To overcome this problem, another strategy was implemented, consisting of the division of the controls in three smaller droplets, dispersed through the DMF electrodes, which were irradiated in turn so that each droplet would only be irradiated

three times during the LAMP reaction. Both mixing and fluorescence detection strategies were validated by fluorescence monitoring of the *c-Myc* LAMP amplification, with a target concentration of 0.5 ng/µL or 90 pg, and a total reaction time of one hour. Two conditions were tested, with mixing performed off-chip, prior to on-chip LAMP, and mixing performed on-chip, in-line with the LAMP reaction. As a result, a clear distinction between positive and negative controls was achieved, as well as a larger increase in fluorescence readout for amplifying samples with on-chip mixing in comparison with standard off-chip vortex mixing. Furthermore, an overall decrease in fluorescence fluctuation was achieved with on-chip mixing.

The next methodology studied for following the on-chip LAMP reaction profile was impedance measuring. The first step in this approach was to verify whether DNA amplification by LAMP lead to a variation in the impedance of the solution. This initial screening was performed resorting to a simple yet effective structure: interdigitated electrodes. Such electrodes were comprised of chromium and covered with a dielectric Parylene C layer, to approach the conditions in DMF devices. The thickness of the Parylene C layer was reduced considering that the sensitivity of interdigitated electrodes decreases as the distance from the sample increases, due to the loss in intensity of the electric field applied. Resorting to this simplified setup, it was confirmed that the impedance of a LAMP reaction does increase as the reaction progresses, suggesting that impedimetric measuring methods could be promising for reaction monitoring in DMF devices. However, considering that the conditions in a DMF device are substantially more hindering to impedance measurements (due to thick dielectric layers, multiple materials comprising the device or the presence of silicone oil surrounding the reaction droplet), an improved system for impedance measuring was implemented. This system was based on an impedimetric scheme featuring a lock-in amplifier able to isolate signals with a certain frequency. Thus, it is possible to apply two distinct signals to the DMF devices, one signal for optimal droplet motion and another signal for optimal droplet measurement, and use the lock-in amplifier to isolate the measurement signal. The impedance measuring system was applied to *c-Myc* LAMP reactions, with positive and negative controls performed simultaneously. Unfortunately, even though some differences were visible between the impedance profiles of positive and negative controls during LAMP, such differences were not statistically relevant. This suggests that for a higher number of experiments, the impedance profiles of both controls could possibly overlap.

Following impedimetric attempts, the last methodology to be tested was based on electrochemical measurements. Electrochemistry is also a promising methodology for the evaluation of LAMP reaction profiles, considering the pH variation resulting from the production of

new DNA strands. Similarly to previous studies, the first step consisted of determining optimal measuring conditions, through the evaluation of solid metal-insulator-semiconductor structures (ideal structures, unaffected by contact with liquids). The best measurement conditions were then applied to electrolyte-insulator-semiconductor structures, to evaluate commercial-grade buffer solutions with different pH. If the proposed devices could differentiate between highly stable solutions with pH4, pH7 and pH10, this would be a good indicator of their suitability for following a LAMP reaction profile, and subsequent integration onto DMF devices. Nevertheless, the produced EISm devices were not satisfactory in distinguishing the pH of different solutions, despite several attempts at evaluating the data and thorough statistical investigation. This suggests that incorporating an electrochemical measurement area within a more complex system such as a DMF device would not provide an accurate representation of LAMP profiles.

Lastly, hybrid platforms combining digital and droplet microfluidics were engineered, envisioning in-line reagent mixing and subsequent high-throughput nucleic acid amplification. Since continuous-flow and droplet microfluidic platforms present difficulties in mixing, and the throughput of DMF platforms in undeniably lower than that of droplet microfluidics, the proposed hybrid platform would take advantage of the superior mixing capabilities of DMF (namely mixing protocols developed within this PhD work) to mix all the required reagents and feed them to a nano-liter droplet generator, which would form thousands of droplets, thus increasing throughput. By integrating this hybrid platform with an adequate fluorescence measurement system, capable of faster image processing to analyze flowing droplets, it would be possible to evaluate the fluorescence intensity in each droplet and enable quantification of the target nucleic acid sequence.

Following the experimental line of thought used thus far, the first step in this final endeavor was to resort to a simpler setup for preliminary studies of the hybrid platforms. Thus, a simple four-element DMF section (one reservoir and three electrodes) was integrated with a simple flow-focusing droplet generator, and LAMP buffer was used as a liquid sample. With this initial hybrid device, the DMF portion successfully transmitted the LAMP buffer to the DrMF section, which further generated droplets with volumes below 2 nL. Such nano-liter droplets could further be controlled in terms of production rate and circulating speed, achieving maxima of approximately 4 dr/s and approximately 1500 μm/s for each parameter, respectively. This attests to the high throughput capabilities of the hybrid platform, comparable to the throughput obtained for DrMF platforms only, as well as the moveability and interchangeability between sections of a key component in LAMP reactions: the reaction buffer.

In conclusion, fluorescence proved to be the best alternative for monitoring DMF-LAMP reactions, providing accurate distinction between positive and negative controls, as well as distinction between target genes. Nevertheless, this does not mean that impedimetric and electrochemical methods should be forever abandoned for integration with DMF. The knowledge resulting from this PhD work may be used as a base for new ideas, new perspectives and new research lines. Perhaps not for LAMP reaction monitoring, perhaps not even for any nucleic acid amplification scheme, but for novel and innovative applications surpassing the scope of this PhD work and the vision of the author. Finally, the integration of DMF with another microfluidic system, DrMF, was proved and provided encouraging results for future in-line reagent mixing and droplet generation for droplet digital nucleic acid amplification and absolute quantification of the initial target copy number.

10.2 Future perspectives

This PhD work paved the path for several improvements, which of course will not be limited to the vision of the author presented in this chapter. The following suggestions are merely that, suggestions, and may be used as a starting point or be completely discarded in favor of original and bold new ideas.

The first improvement should be the miniaturization of the voltage driving system, in order to achieve a truly field-deployable device. In the hands of a good electrical engineer, the Arduino processor, as well as the voltage driving boards, may be replaced by a single board, with the possibility to control even more electrodes. The signal generator may also be miniaturized and replaced by commercially-available components, namely a battery, a DC/AC converter and a voltage amplifier. The DMF devices can also be re-designed to a more ubiquitous architecture, comprised of an electrode grid (e.g. 10 x 10 electrodes) including sample insertion/withdrawal reservoirs and reaction regions. This may be achieved by outsourcing PCB bottom plates, with vertical connection lines to the electrodes in the middle. Increasing the electrode and reservoir number of the DMF devices allows for full automation of nucleic acid amplification protocols, with devices being capable of mixing all the reagents required, and not only a master mix prepared off-chip with a sample. Extreme attention must be given to this type of on-chip protocol, considering the delicate nature of reagents, which quickly degrade when not preserved in cold conditions.

The heating system may also be further optimized, by using commercial thin film heaters for heating, over which commercial thin film resistance temperature detectors (RTD) may be

placed, thus ensuring that temperature is measured over the entire surface of the heating element and not just at one or two points.

Upgrading the fluorescence detection system is also a relevant aspect to consider, aiming once again for miniaturization, that is the key feature of field-deployable devices. This may be achieved in one of two ways: 1) by using existing miniature fluorescence detection systems[451] or 2) (the personal choice of the author) by designing a fluorescence detection system customized to the parameters of the EvaGreen® fluorophore, in terms of excitation light and emission detection. For the second option, the author recommends a partnership with a research group specialized in optics, since several sensitive parameters will have to be carefully designed, such as the focal point or the irradiation and detection angles.

After miniaturizing the DMF platform and fluorescence detection system, the next step will be to pursue dual-gene amplification for gene expression analysis. An endogenous control gene compatible with DMF should be screened and used to evaluate the expression of *c-Myc* (or yet another cancer biomarker) in healthy and cancerous cells. Decreasing the reaction time would also be interesting, in the case of LAMP by adding loop primers and/or screening different *Bst* enzymes in search of the one with the fastest amplification rate.

Building on the previous ideas, the integration of droplet microfluidics should also be considered. Thus, not only LAMP reagents may be mixed by DMF, but the reaction throughput may be increased to thousands of droplets. LAMP may be fully performed on the DMF section (reagent mixing and heating) and the reaction products may be further partitioned by the DrMF section, enabling the full capabilities of digital droplet analysis, including absolute quantification of the initial target copy number. This may be achieved by creating a droplet accumulation zone in the DrMF section, and using the fluorescence detector to evaluate the fluorescence in this area. Alternatively, high resolution real-time monitoring of the reaction may be performed, by placing the fluorescence detector in a fixed region at the DrMF section (where heating would be performed), reading the average droplet fluorescence with time. In all cases involving fluorescence detection, some time should be spent in developing automated image processing methods, either by direct programming or by using existing open-source image processing tools such as Bonsai[452,453]. Further building on the previous ideas, sample pre-processing (DNA extraction or RNA extraction and conversion to cDNA) may be incorporated into the DMF moiety, allowing for clinical samples to be screened, namely blood, urine or saliva.

Impedance measurements should not be discarded, considering the promising results achieved for interdigitated electrodes. Even if integration with DMF devices proves to be excessively complex, biosensing elements based on simple interdigitated electrodes covered by

a dielectric such as Parylene C and surrounded by a PDMS frame, may be used for endpoint analysis. Briefly, considering that there is clear degradation of the devices with usage, perhaps real-time monitoring would not be ideal, but endpoint LAMP products may easily provide a yes/no answer, informing the user whether there was amplification or not. For the LAMP reaction studied herein, IDE devices could differentiate a positive from a negative control by more than 2.3 kΩ on average, a very good margin to detect variations. Several initial target concentrations may be evaluated for the same reaction time point, or even several nucleic acid sequences or different amplification methodologies, other than LAMP. All of such conditions may be mechanistically evaluated in terms of impedance, providing a thorough study of the electrical behavior of the reactions under evaluation. Regarding electrochemical detection, further improvements of the detection system are clearly required, such as the increase in sample volume, allowing for the inclusion of a reference electrode. Alternatively, mediation of signal detection by more sensitive elements could be pursued, for example using MOSFET transistors, which are highly sensitive to voltage variations[26].

In summary, the future development of the DMF platform developed in this PhD work should be entirely focused primarily on miniaturization, thus creating a portable system for nucleic acid amplification analysis. Following miniaturization, clinical validation of the platform will be required to create a true point-of-care device. Fluorescence should be the main monitoring methodology, whereas the remaining methods studied herein should be directed to different applications, as described above.

Finally, it should be reminded that the perspectives previously mentioned are simple suggestions, fully open to different interpretations and integration with new ideas and lines of research.

Bibliography

1. World Health Organization. The top 10 causes of death. https://www.who.int/news-room/fact-sheets/detail/the-top-10-causes-of-death (2020).
2. Ferlay, J. *et al.* Cancer statistics for the year 2020: an overview. *Int J Cancer* **149**, 778–789 (2021).
3. Center for Systems Science and Engineering at Johns Hopkins University. COVID-19 Dashboard. https://www.arcgis.com/apps/dashboards/bda7594740fd40299423467b48e9ecf6 (2021).
4. Crosby, D. *et al.* A roadmap for the early detection and diagnosis of cancer. *Lancet Oncol* **21**, 1397–1399 (2020).
5. Rubin, G. *et al.* The expanding role of primary care in cancer control. *Lancet Oncol* **16**, 1231–1272 (2015).
6. Bossmann, S. H. & Troyer, D. L. Point-of-care routine rapid screening: The future of cancer diagnosis? *Expert Rev Mol Diagn* **13**, 107–109 (2013).
7. Gubala, V., Harris, L. F., Ricco, A. J., Tan, M. X. & Williams, D. E. Point of care diagnostics: Status and future. *Anal Chem* **84**, 487–515 (2012).
8. Wang, P. & Kricka, L. J. Current and emerging trends in point-of-care technology and strategies for clinical validation and implementation. *Clin Chem* **64**, 1439–1452 (2018).
9. Yager, P., Domingo, G. J. & Gerdes, J. Point-of-Care Diagnostics for Global Health. *Annu Rev Biomed Eng* **10**, 107–144 (2008).
10. Gauglitz, G. Point-of-Care Platforms. *Annual Review of Analytical Chemistry* **7**, 297–315 (2014).
11. Henry, N. L. & Hayes, D. F. Cancer biomarkers. *Mol Oncol* **6**, 140–146 (2012).
12. Mordente, A., Meucci, E., Martorana, G. & Silvestrini, A. Cancer Biomarkers Discovery and Validation: State of the Art, Problems and Future Perspectives. in *Advances in Cancer Biomarkers: From biochemistry to clinic for a critical revision* (ed. Scatena, R.) (Springer Science+Business, 2015). doi:10.1007/978-94-017-7215-0.
13. Choi, K. *et al.* Automated digital microfluidic platform for magnetic-particle-based immunoassays with optimization by design of experiments. *Anal Chem* **85**, 9638–9646 (2013).
14. Choi, K., Ng, A. H. C., Fobel, R. & Wheeler, A. R. Digital Microfluidics. *Annual Review of Analytical Chemistry* **5**, 413–440 (2012).
15. Abdelgawad, B. M., Wheeler, A. R., Abdelgawad, M. & Wheeler, A. R. The digital revolution: A new paradigm for microfluidics. *Advanced Materials* **21**, 920–925 (2009).

16. Coelho, B. J. *et al.* Digital Microfluidics for Nucleic Acid Amplification. *Sensors* **17**, 1–13 (2017).
17. Coelho, B. J. *et al.* A Digital Microfluidics Platform for Loop-Mediated Isothermal Amplification Detection. *Sensors* **17**, 1–11 (2017).
18. Jebrail, M. J. & Wheeler, A. R. Let's get digital: digitizing chemical biology with microfluidics. *Curr Opin Chem Biol* **14**, 574–581 (2010).
19. Jebrail, M. J. *et al.* Digital microfluidics: a versatile tool for applications in chemistry, biology and medicine. *Lab Chip* **12**, 2452 (2012).
20. Ko, H. *et al.* Active digital microfluidic paper chips with inkjet-printed patterned electrodes. *Advanced Materials* **26**, 2335–2340 (2014).
21. Fobel, R., Kirby, A. E., Ng, A. H. C. C., Farnood, R. R. & Wheeler, A. R. Paper microfluidics goes digital. *Advanced Materials* **26**, 2838–2843 (2014).
22. Abdelgawad, M. Digital Microfluidics: Automation of Liquid Handling on the Microscale. *IEEE Nanotechnol Mag* **14**, 6–23 (2020).
23. Notomi, T. *et al.* Loop-mediated isothermal amplification of DNA. *Nucleic Acids Res* **28**, e63 (2000).
24. Notomi, T., Mori, Y., Tomita, N. & Kanda, H. Loop-mediated isothermal amplification (LAMP): principle, features, and future prospects. *Journal of Microbiology* **53**, 1–5 (2015).
25. Veigas, B. *et al.* Ion sensing (EIS) real-time quantitative monitorization of isothermal DNA amplification. *Biosens Bioelectron* **52**, 50–55 (2014).
26. Veigas, B. *et al.* Quantitative real-time monitoring of RCA amplification of cancer biomarkers mediated by a flexible ion sensitive platform. *Biosens Bioelectron* **91**, 788–795 (2017).
27. Miller, D. M., Thomas, S. S. D. S., Islam, A., Muench, D. & Sedoris, K. c-Myc and Cancer Metabolism. *Clinical Cancer Research* **18**, 5546–5553 (2012).
28. Dang, C. v., Le, A. & Gao, P. MYC-induced cancer cell energy metabolism and therapeutic opportunities. *Clinical Cancer Research* **15**, 6479–6483 (2009).
29. Dang, C. v. MYC, Metabolism, Cell Growth, and Tumorigenesis. *Cold Spring Harb Perspect Med* **3**, 1–15 (2013).
30. Dang, C. V. MYC on the path to cancer. *Cell* **149**, 22–35 (2012).
31. Gabay, M., Li, Y. & Felsher, D. W. MYC activation is a hallmark of cancer initiation and maintenance. *Cold Spring Harb Perspect Med* **4**, 1–14 (2014).

32. Tavassoli, M. & Pezzella, F. Oncogenesis and tumour suppression. in *Oxford Textbook of Cancer Biology* (eds. Pezzella, F., Tavassoli, M. & Kerr, D. J.) 136–154 (Oxford University Press, 2019).
33. Abdelgawad, M. & Wheeler, A. R. The digital revolution: A new paradigm for microfluidics. *Advanced Materials* **21**, 920–925 (2009).
34. Wheeler, A. R. *et al.* Digital microfluidics with in-line sample purification for proteomics analyses with MALDI-MS. *Anal Chem* **77**, 534–540 (2005).
35. Moon, H., Wheeler, A. R., Garrell, R. L., Loo, J. A. & Kim, C. J. An integrated digital microfluidic chip for multiplexed proteomic sample preparation and analysis by MALDI-MS. *Lab Chip* **6**, 1213–1219 (2006).
36. Luk, V. N., Fiddes, L. K., Luk, V. M., Kumacheva, E. & Wheeler, A. R. Digital microfluidic hydrogel microreactors for proteomics. *Proteomics* **12**, 1310–1318 (2012).
37. Sista, R. S. *et al.* Heterogeneous immunoassays using magnetic beads on a digital microfluidic platform. *Lab Chip* **8**, 2188–2196 (2008).
38. Sista, R. *et al.* Development of a digital microfluidic platform for point of care testing. *Lab Chip* **8**, 2091–2104 (2008).
39. Ng, A. H. C., Choi, K., Luoma, R. P., Robinson, J. M. & Wheeler, A. R. Digital microfluidic magnetic separation for particle-based immunoassays. *Anal Chem* **84**, 8805–8812 (2012).
40. Abdulwahab, S. *et al.* Towards a personalized approach to aromatase inhibitor therapy: A digital microfluidic platform for rapid analysis of estradiol in core-needle-biopsies. *Lab Chip* **17**, 1594–1602 (2017).
41. Ng, A. H. C. *et al.* A digital microfluidic system for serological immunoassays in remote settings. *Sci Transl Med* **10**, 1–13 (2018).
42. Coudron, L. *et al.* Fully integrated digital microfluidics platform for automated immunoassay; A versatile tool for rapid, specific detection of a wide range of pathogens. *Biosens Bioelectron* **128**, 52–60 (2019).
43. Sista, R. S. *et al.* Digital microfluidic platform to maximize diagnostic tests with low sample volumes from newborns and pediatric patients. *Diagnostics* **10**, 1–18 (2020).
44. Zhou, J. *et al.* Electrowetting-based multi-microfluidics array printing of high resolution tissue construct with embedded cells and growth factors. *Virtual Phys Prototyp* **2**, 217–223 (2007).
45. Barbulovic-Nad, I., Au, S. H. & Wheeler, A. R. A microfluidic platform for complete mammalian cell culture. *Lab Chip* **10**, 1536–1542 (2010).

46. Fiddes, L. K. *et al.* Hydrogel discs for digital microfluidics. *Biomicrofluidics* **6**, 1–11 (2012).
47. Bogojevic, D., Chamberlain, M. D., Barbulovic-Nad, I. & Wheeler, A. R. A digital microfluidic method for multiplexed cell-based apoptosis assays. *Lab Chip* **12**, 627–634 (2012).
48. Barbulovic-nad, I., Yang, H., Park, S. & Wheeler, A. R. Digital microfluidics for cell-based assays. *Lab Chip* **8**, 519–526 (2008).
49. Pollack, M. G., Shenderov, A. D. & Fair, R. B. Electrowetting-based actuation of droplets for integrated microfluidics. *Lab Chip* 96–101 (2002) doi:10.1039/b110474h.
50. Lippmann, G. Relations entre les phénomènes électriques et capillaires. *Annales de Chimie et de Physique* **5**, 494–549 (1875).
51. Beni, G. & Hackwood, S. Electro-wetting displays. *Appl Phys Lett* **38**, 207–209 (1981).
52. Pesant, J., Hareng, M., Mourey, B. & Perbet, J. Electrodes for a device operating by electrically controlled fluid displacement. (1986).
53. Colgate, E. & Matsumoto, H. An investigation of electrowetting-based microactuation. *Journal of Vacuum Science & Technology A: Vacuum, Surfaces, and Films* **8**, 3625–3633 (1990).
54. Berge, B. Électrocapillarité et mouillage de films isolants par l'eau. *Comptes rendus de l'Académie des sciences. Série 2, Mécanique, physique, chimie, sciences de l'univers, sciences de la terre.* **317**, 157–163 (1993).
55. Shamai, R., Andelman, D., Berge, B. & Hayes, R. Water, electricity, and between… On electrowetting and its applications. *Soft Matter* **4**, 38–45 (2008).
56. Quilliet, C. & Berge, B. Electrowetting: A recent outbreak. *Curr Opin Colloid Interface Sci* **6**, 34–39 (2001).
57. Pollack, M. G., Fair, R. B. & Shenderov, A. D. Electrowetting-based actuation of liquid droplets for microfluidic applications. *Appl Phys Lett* **77**, 1725–1726 (2000).
58. Lee, J. & Kim, C. J. Surface-tension-driven microactuation based on continuous electrowetting. *Journal of Microelectromechanical Systems* **9**, 171–180 (2000).
59. Lee, J., Moon, H., Fowler, J., Schoellhammer, T. & Kim, C.-J. Electrowetting and electrowetting-on-dielectric for microscale liquid handling. *Sens Actuators A Phys* **95**, 259–268 (2002).
60. Berthier, J. *Micro-Drops and Digital Microfluidics*. (Elsevier Inc., 2013).
61. Mugele, F. & Baret, J. Electrowetting: from basics to applications. *Journal of Physics: Condensed Matter* **17**, R705–R774 (2005).

62. Shapiro, B., Moon, H., Garrell, R. L. & Kim, C. J. Equilibrium behavior of sessile drops under surface tension, applied external fields, and material variations. *J Appl Phys* **93**, 5794–5811 (2003).
63. Peykov, V., Quinn, A. & Ralston, J. Electrowetting: A model for contact-angle saturation. *Colloid Polym Sci* **278**, 789–793 (2000).
64. Verheijen, H. J. J. & Prins, M. W. J. Reversible electrowetting and trapping of charge: Model and experiments. *Langmuir* **15**, 6616–6620 (1999).
65. Papathanasiou, A. G. & Boudouvis, A. G. Manifestation of the connection between dielectric breakdown strength and contact angle saturation in electrowetting. *Appl Phys Lett* **86**, 1–3 (2005).
66. Klarman, D. & Andelman, D. A model of electrowetting, reversed electrowetting, and contact angle saturation. *Langmuir* **27**, 6031–6041 (2011).
67. Jiang, C., Ma, H., Hasko, D. G. & Nathan, A. Influence of polarization on contact angle saturation during electrowetting. *Appl Phys Lett* **109**, (2016).
68. Mugele, F. Fundamental challenges in electrowetting: From equilibrium shapes to contact angle saturation and drop dynamics. *Soft Matter* **5**, 3377–3384 (2009).
69. Papathanasiou, A. G., Papaioannou, A. T. & Boudouvis, A. G. Illuminating the connection between contact angle saturation and dielectric breakdown in electrowetting through leakage current measurements. *J Appl Phys* **103**, 1–4 (2008).
70. Drygiannakis, A. I., Papathanasiou, A. G. & Boudouvis, A. G. On the Connection between Dielectric Breakdown Strength, Trapping of Charge, and Contact Angle Saturation in Electrowetting. *Langmuir* **25**, 147–152 (2009).
71. Kolodzey, J. *et al.* Electrical conduction and dielectric breakdown in aluminum oxide insulators on silicon. *IEEE Trans Electron Devices* **47**, 121–128 (2000).
72. Moon, H., Cho, S. K., Garrell, R. L., Kim, C.-J. 'Cj' & Garrell, R. L. Low voltage electrowetting-on-dielectric. *J Appl Phys* **92**, 4080–4087 (2002).
73. Specialty Coating Systems. SCS Parylene Properties. High performance conformal coatings. *Parylene Knowledge* Preprint at (2018).
74. Gerratt, A. P. & Bergbreiter, S. Dielectric breakdown of PDMS thin films. *Journal of Micromechanics and Microengineering* **23**, (2013).
75. Massachusetts Institute of Technology. PDMS (polydimethylsiloxane). *Material Property Database* http://www.mit.edu/~6.777/matprops/pdms.htm.
76. EESemi. Properties of SiO2 and Si3N4 at 300K. https://www.eesemi.com/sio2si3n4.htm (2004).

77. Melai, J., Salm, C., Smits, S., Visschers, J. & Schmitz, J. The electrical conduction and dielectric strength of SU-8. *Journal of Micromechanics and Microengineering* **19**, 1–7 (2009).
78. Li, Y. *et al.* Anodic Ta2O5 for CMOS compatible low voltage electrowetting-on-dielectric device fabrication. *Solid State Electron* **52**, 1382–1387 (2008).
79. Tan, M. K., Friend, J. R. & Yeo, L. Y. Microparticle collection and concentration via a miniature surface acoustic wave device. *Lab Chip* **7**, 618–625 (2007).
80. Mark, D., Haeberle, S., Roth, G., von Stetten, F. & Zengerle, R. Microfluidic lab-on-a-chip platforms: Requirements, characteristics and applications. *Chem Soc Rev* **39**, 1153–1182 (2010).
81. Galopin, E. *et al.* SPR biosensing coupled to a digital microfluidic microstreaming system. *Biosens Bioelectron* **23**, 746–750 (2007).
82. Li, Y. *et al.* Test structures for characterizing the integration of EWOD and SAW technologies for microfluidics. *IEEE Transactions on Semiconductor Manufacturing* **25**, 323–330 (2012).
83. Renaudin, A. *et al.* Monitoring SAW-actuated microdroplets in view of biological applications. *Sens Actuators B Chem* **138**, 374–382 (2009).
84. Collignon, S., Friend, J. & Yeo, L. Planar microfluidic drop splitting and merging. *Lab Chip* **15**, 1942–1951 (2015).
85. Shilton, R. J. *et al.* Rapid and controllable digital microfluidic heating by surface acoustic waves. *Adv Funct Mater* **25**, 5895–5901 (2015).
86. Min, X. & Kim, W. S. Beyond high voltage in the digital microfluidic devices for an integrated portable sensing system. *Microfluid Nanofluidics* **23**, 1–14 (2019).
87. Chiou, P. Y., Moon, H., Toshiyoshi, H., Kim, C. J. & Wu, M. C. Light actuation of liquid by optoelectrowetting. *Sens Actuators A Phys* **104**, 222–228 (2003).
88. Chiou, P. Y., Park, S. Y. & Wu, M. C. Continuous optoelectrowetting for picoliter droplet manipulation. *Appl Phys Lett* **93**, 1–4 (2008).
89. Chuang, H. S., Kumar, A. & Wereley, S. T. Open optoelectrowetting droplet actuation. *Appl Phys Lett* **93**, (2008).
90. Park, S.-Y., Teitell, M. & Chiou, E. P. Y. Single-sided continuous optoelectrowetting (SCOEW) for droplet manipulation with light patterns. *Lab Chip* **10**, 1655–1661 (2010).
91. Yu, T. M. *et al.* Integration of organic opto-electrowetting and poly(ethylene) glycol diacrylate (PEGDA) microfluidics for droplets manipulation. *Sens Actuators B Chem* **180**, 35–42 (2013).

92. Tailor, N. K., Aranda, C. A., Saliba, M. & Satapathi, S. Negative Photoconductivity: Bizarre Physics in Semiconductors. *ACS Mater Lett* **4**, 2298–2320 (2022).
93. Jiang, D. & Park, S. Y. Light-driven 3D droplet manipulation on flexible optoelectrowetting devices fabricated by a simple spin-coating method. *Lab Chip* **16**, 1831–1839 (2016).
94. Chiou, P. Y., Chang, Z. & Wu, M. C. Droplet manipulation with light on optoelectrowetting device. *Journal of Microelectromechanical Systems* **17**, 133–138 (2008).
95. Kumar, A., Chuang, H. S. & Wereley, S. T. Dynamic manipulation by light and electric fields: Micrometer particles to microliter droplets. *Langmuir* **26**, 7656–7660 (2010).
96. Valley, J. K., NingPei, S., Jamshidi, A., Hsu, H.-Y. & Wu, M. C. A unified platform for optoelectrowetting and optoelectronic tweezers. *Lab Chip* **11**, 1292–1297 (2011).
97. Lee, S., Thio, S. K., Park, S. Y. & Bae, S. An automated 3D-printed smartphone platform integrated with optoelectrowetting (OEW) microfluidic chip for on-site monitoring of viable algae in water. *Harmful Algae* **88**, 101638 (2019).
98. Thio, S. K., Bae, S. & Park, S. Y. Plasmonic nanoparticle-enhanced optoelectrowetting (OEW) for effective light-driven droplet manipulation. *Sens Actuators B Chem* **308**, 127704 (2020).
99. Jiang, D., Lee, S., Bae, S. W. & Park, S. Y. Smartphone integrated optoelectrowetting (Si-OEW) for on-chip sample processing and microscopic detection of water quality. *Lab Chip* **18**, 532–539 (2018).
100. Lindsay, S. *et al.* Discrete microfluidics with electrochemical detection. *Analyst* **132**, 412–416 (2007).
101. Egatz-Gómez, A. *et al.* Discrete magnetic microfluidics. *Appl Phys Lett* **89**, 1–3 (2006).
102. Schneider, J., Garcia, A. A. & Marquez, M. Automated digital magnetofluidics. *J Phys Conf Ser* **127**, (2008).
103. Koh, W. H., Lok, K. S. & Nguyen, N. T. A digital micro magnetofluidic platform for lab-on-a-chip applications. *Journal of Fluids Engineering, Transactions of the ASME* **135**, 1–6 (2013).
104. Mandal, C., Banerjee, U. & Sen, A. K. Transport of a Sessile Aqueous Droplet over Spikes of Oil Based Ferrofluid in the Presence of a Magnetic Field. *Langmuir* (2019) doi:10.1021/acs.langmuir.9b00631.
105. Egatz-Gómez, A. *et al.* Silicon nanowire and polyethylene superhydrophobic surfaces for discrete magnetic microfluidics. *Appl Surf Sci* **254**, 330–334 (2007).

106. Paul, G., Das, P. K. & Manna, I. Motion, deformation and pearling of ferrofluid droplets due to a tunable moving magnetic field. *Soft Matter* **16**, 1642–1652 (2020).
107. Lyuksyutov, I. F., Naugle, D. G. & Rathnayaka, K. D. D. On-chip manipulation of levitated femtodroplets. *Appl Phys Lett* **85**, 1817–1819 (2004).
108. Khalil, K. S., Mahmoudi, S. R., Abu-Dheir, N. & Varanasi, K. K. Active surfaces: Ferrofluid-impregnated surfaces for active manipulation of droplets. *Appl Phys Lett* **105**, 1–4 (2014).
109. Damodara, S. & Sen, A. K. Magnetic field assisted droplet manipulation on a soot-wax coated superhydrophobic surface of a PDMS-iron particle composite substrate. *Sens Actuators B Chem* **239**, 816–823 (2017).
110. Cui, W., Zhang, M., Zhang, D., Pang, W. & Zhang, H. Island-ground single-plate electrowetting on dielectric device for digital microfluidic systems. *Appl Phys Lett* **105**, 1–5 (2014).
111. Chang, J. H., Kim, D. S. & Pak, J. J. Simplified ground-type single-plate electrowetting device for droplet transport. *Journal of Electrical Engineering and Technology* **6**, 402–407 (2011).
112. Abdelgawad, M., Park, P. & Wheeler, A. R. Optimization of device geometry in single-plate digital microfluidics. *J Appl Phys* **105**, 1–6 (2009).
113. Berthier, J. Principle of droplet motion: quasi-static aspects and departure from equilibrium. in *Micro-Drops and Digital Microfluidics* 233 (Elsevier Inc., 2013).
114. Kumar, A., Pluntke, M., Cross, B., Baret, J. & Mugele, F. Finite conductivity effects and apparent contact angle saturation in AC electrowetting. *Materials Research Society* **899**, 1–8 (2006).
115. García-Sánchez, P., Ramos, A. & Mugele, F. Electrothermally driven flows in ac electrowetting. *Phys Rev E Stat Nonlin Soft Matter Phys* **81**, 1–4 (2010).
116. Chen, L. & Bonaccurso, E. Electrowetting - From statics to dynamics. *Adv Colloid Interface Sci* **210**, 2–12 (2014).
117. Yoon, J. Y. & Garrell, R. L. Preventing biomolecular adsorption in electrowetting-based biofluidic chips. *Anal Chem* **75**, 5097–5102 (2003).
118. Davoust, L., da Cruz, C. A. & Theisen, J. On the use of AC electrowetting for biosensing based on dynamic contact angle. *Sens Actuators B Chem* **236**, 849–857 (2016).
119. Berthier, J. & Peponnet, C. A model for the determination of the dimensions of dents for jagged electrodes in electrowetting on dielectric microsystems. *Biomicrofluidics* **1**, 1–9 (2007).

120. Datta, P. *et al.* A Design of Digital Microfluidic Biochip along with Structural and Behavioural Features in Triangular Electrode Based Array. *Procedia Comput Sci* **93**, 183–190 (2016).
121. Berthier, J. *et al.* Computer aided design of an EWOD microdevice. *Sens Actuators A Phys* **127**, 283–294 (2006).
122. Samad, M. F., Kouzani, A. Z., Rahman, M. M., Magniez, K. & Kaynak, A. Design and Fabrication of an Electrode for Low-actuation-Voltage Electrowetting-on-Dielectric Devices. *Procedia Technology* **20**, 20–25 (2015).
123. Jain, V., Devarasetty, V. & Patrikar, R. Effect of electrode geometry on droplet velocity in open EWOD based device for digital microfluidics applications. *J Electrostat* **87**, 11–18 (2017).
124. Das, D., Das, S. & Biswas, K. Effect of electrode geometry on voltage reduction in EWOD based devices. *International Conference on Systems in Medicine and Biology, ICSMB 2010 - Proceedings* 371–375 (2010) doi:10.1109/ICSMB.2010.5735406.
125. Lienemann, J., Greiner, A. & Korvink, J. G. Electrode shapes for electrowetting arrays. *2003 Nanotechnology Conference and Trade Show - Nanotech 2003* **1**, 94–97 (2003).
126. Su, F., Chakrabarty, K. & Fair, R. B. Microfluidics-based biochips: Technology issues, implementation platforms, and design automation challenges. *Design Automation Methods and Tools for Microfluidics-Based Biochips* **25**, 1–29 (2006).
127. Armani, M., Walker, S. & Shapiro, B. Modeling and control of electrically actuated surface tension driven micro-fluidic systems. *Proceedings of the 20th IEEE International Symposium on Intelligent Control, ISIC '05 and the 13th Mediterranean Conference on Control and Automation, MED '05* **2005**, 131–138 (2005).
128. Lienemann, J., Greiner, A. & Korvink, J. G. Modeling, Simulation, and Optimization of Electrowetting. *IEEE Transactions on Computer-Aided Design of Integrated Circuits and Systems* **25**, 234–247 (2006).
129. Samad, M. F., Kouzani, A. Z., Hossain, M. F., Mohammed, M. I. & Alam, M. N. H. Reducing electrowetting-on-dielectric actuation voltage using a novel electrode shape and a multi-layer dielectric coating. *Microsystem Technologies* **23**, 3005–3013 (2017).
130. Moon, I. & Kim, J. Using EWOD (electrowetting-on-dielectric) actuation in a micro conveyor system. *Sens Actuators A Phys* **130–131**, 537–544 (2006).
131. Monkkonen, L. *et al.* Screen-printed digital microfluidics combined with surface acoustic wave nebulization for hydrogen-deuterium exchange measurements. *J Chromatogr A* **1439**, 161–166 (2016).

132. Ugsornrat, K. *et al.* Screen printed electrochemical detector combine with digital microfluidic microchip. *2016 13th International Conference on Electrical Engineering/Electronics, Computer, Telecommunications and Information Technology (ECTI-CON)* 1–5 (2016) doi:10.1109/ECTICon.2016.7561296.
133. Mohamed, Y., Saurabh, S. & Homayoun, N. Fabrication of digital microfluidic devices on flexible paper-based and rigid substrates via screen printing. *Journal of Micromechanics and Microengineering* **25**, 57001 (2015).
134. Dryden, M. D. M., Rackus, D. D. G., Shamsi, M. H. & Wheeler, A. R. Integrated digital microfluidic platform for voltammetric analysis. *Anal Chem* **85**, 8809–8816 (2013).
135. Dixon, C., Ng, A. H. C., Fobel, R., Miltenburg, M. B. & Wheeler, A. R. An inkjet printed, roll-coated digital microfluidic device for inexpensive, miniaturized diagnostic assays. *Lab Chip* **16**, 4560–4568 (2016).
136. Yamada, K., Henares, T. G., Suzuki, K. & Citterio, D. Paper-based inkjet-printed microfluidic analytical devices. *Angewandte Chemie - International Edition* **54**, 5294–5310 (2015).
137. Chang, Y. H., Lee, G.-B., Huang, F.-C., Chen, Y.-Y. & Lin, J.-L. Integrated polymerase chain reaction chips utilizing digital microfluidics. *Biomed Microdevices* **8**, 215–225 (2006).
138. Luk, V. N., Mo, G. C. & Wheeler, A. R. Pluronic additives: A solution to sticky problems in digital microfluidics. *Langmuir* **24**, 6382–6389 (2008).
139. Wang, Y., Zhao, Y. & Cho, S. K. Efficient in-droplet separation of magnetic particles for digital microfluidics. *Journal of Micromechanics and Microengineering* **17**, 2148–2156 (2007).
140. Karuwan, C. *et al.* Electrochemical detection on electrowetting-on-dielectric digital microfluidic chip. *Talanta* **84**, 1384–1389 (2011).
141. Abualsayed, A., Abouelmagd, S. & Abdelgawad, M. Nanoparticles synthesis using digital microfluidics. in *Proceedings of the 14th Annual IEEE International Conference on Nano/Micro Engineered and Molecular Systems, NEMS 2019* 201–204 (IEEE, 2019). doi:10.1109/NEMS.2019.8915616.
142. Fouillet, Y. *et al.* EWOD digital microfluidics for Lab on a Chip. in *ASME 4th International Conference on Nanochannels, Microchannels and Minichannels* (ed. The American Society of Mechanical Engineers) 1255–1264 (ASME Press, 2006). doi:0-7918-4760-8.
143. Kühnemund, M., Witters, D., Nilsson, M. & Lammertyn, J. Circle-to-circle amplification on a digital microfluidic chip for amplified single molecule detection. *Lab Chip* **14**, 2983–2992 (2014).

144. Han, S. *et al.* A digital microfluidic diluter-based microalgal motion biosensor for marine pollution monitoring. *Biosens Bioelectron* **143**, 111597 (2019).
145. Dubois, P. *et al.* Ionic Liquid Droplet as e-Microreactor devices usually based on continuous-flow in microchan-. *Anal Chem* **78**, 4909–4917 (2006).
146. Abdelgawad, M., Freire, S. L. S., Yang, H. & Wheeler, A. R. All-terrain droplet actuation. *Lab Chip* **8**, 672–677 (2008).
147. Jebrail, M. J. *et al.* A solvent replenishment solution for managing evaporation of biochemical reactions in air-matrix digital microfluidics devices. *Lab Chip* **15**, 151–158 (2014).
148. Lee, M. S. *et al.* Simultaneous detection of two growth factors from human single-embryo culture medium by a bead-based digital microfluidic chip. *Biosens Bioelectron* **150**, (2020).
149. Rival, A. *et al.* An EWOD-based microfluidic chip for single-cell isolation, mRNA purification and subsequent multiplex qPCR. *Lab Chip* **14**, 3739–3749 (2014).
150. Young, H. & Freedman, R. *University Physics with Modern Physics*. (Pearson Education, 2016).
151. Serway, R. & Jewett, J. *Physics for Scientists and Engineers with Modern Physics*. (Brooks/Cole CENGAGE Learning, 2014).
152. Kalsi, S. *et al.* Rapid and sensitive detection of antibiotic resistance on a programmable digital microfluidic platform. *Lab Chip* **15**, 3065–3075 (2015).
153. Schultz, A., Chevalliot, S., Kuiper, S. & Heikenfeld, J. Detailed analysis of defect reduction in electrowetting dielectrics through a two-layer 'barrier' approach. *Thin Solid Films* **534**, 348–355 (2013).
154. Dhindsa, M., Kuiper, S. & Heikenfeld, J. Reliable and low-voltage electrowetting on thin parylene films. *Thin Solid Films* **519**, 3346–3351 (2011).
155. Lin, Y. Y. *et al.* Low voltage electrowetting-on-dielectric platform using multi-layer insulators. *Sens Actuators B Chem* **150**, 465–470 (2010).
156. de Campos, R. P. S. *et al.* 'plug-n-Play' Sensing with Digital Microfluidics. *Anal Chem* **91**, 2506–2515 (2019).
157. Ng, A. H. C., Dean Chamberlain, M., Situ, H., Lee, V. & Wheeler, A. R. Digital microfluidic immunocytochemistry in single cells. *Nat Commun* **6**, (2015).
158. Zou, F. *et al.* Rapid, real-time chemiluminescent detection of DNA mutation based on digital microfluidics and pyrosequencing. *Biosens Bioelectron* **126**, 551–557 (2019).

159. Norian, H. S., Shepard, K., Kymissis, J. & Field, R. An integrated CMOS quantitative-polymerase-chain-reaction lab-on-chip for point-of-care diagnostics. *Lab Chip* **14**, 4076–4084 (2014).
160. Fu, X., Zhang, Y., Yuan, H., Binks, B. P. & Shum, H. C. Controlled Actuation of Liquid Marbles on a Dielectric. *ACS Appl Mater Interfaces* **10**, 34822–34827 (2018).
161. Abdelgawad, M. & Wheeler, A. R. Rapid prototyping in copper substrates for digital microfluidics. *Advanced Materials* **19**, 133–137 (2007).
162. Keng, P. Y. *et al.* Micro-chemical synthesis of molecular probes on an electronic microfluidic device. *Proceedings of the National Academy of Sciences* **109**, 690–695 (2012).
163. Nichols, K. P. & Gardeniers, H. J. G. E. A Digital Microfluidic System for the Investigation of Pre-Steady-State Enzyme Kinetics Using Rapid Quenching with MALDI-TOF Mass Spectrometry. *Anal Chem* **79**, 8699–8704 (2007).
164. Fouillet, Y., Jary, D., Chabrol, C., Claustre, P. & Peponnet, C. Digital microfluidic design and optimization of classic and new fluidic functions for lab on a chip systems. *Microfluid Nanofluidics* **4**, 159–165 (2008).
165. Gong, J., Fan, S. & Kim, C. Portable Digital Microfluidics Platform with Active but Disposable Lab-On-Chip. in *17th IEEE International Conference on Micro Electro Mechanical Systems. Maastricht MEMS 2004 Technical Digest* (ed. IEEE) vol. 3 355–358 (IEEE, 2004).
166. Ugsornrat, K., Afzulpurkar, N. v, Wisitsoraat, A. & Tuantranont, A. Design, Simulation, and Experimental Study of a Droplet-Based PCR by EWOD. *Sensors and Materials* **22**, 271–284 (2010).
167. Mashraei, Y., Sivashankar, S., Buttner, U. & Salama, K. N. Integration of Fractal Biosensor in a Digital Microfluidic Platform. *IEEE Sens J* **16**, 8775–8783 (2016).
168. Hu, J. *et al.* Advances in paper-based point-of-care diagnostics. *Biosens Bioelectron* **54**, 585–597 (2014).
169. Wan, L. *et al.* LampPort: a handheld digital microfluidic device for loop-mediated isothermal amplification (LAMP). *Biomed Microdevices* **21**, (2019).
170. Huang, C. Y. *et al.* AMPFLUID: Aggregation Magnified Post-Assay Fluorescence for Ultrasensitive Immunodetection on Digital Microfluidics. *Proceedings of the IEEE* **103**, 225–235 (2015).
171. Welch, E. R. F., Lin, Y. Y., Madison, A. & Fair, R. B. Picoliter DNA sequencing chemistry on an electrowetting-based digital microfluidic platform. *Biotechnol J* **6**, 165–176 (2011).
172. SCS Coatings. https://scscoatings.com/ (2020).

173. Chang, T. Y. *et al.* Cell and protein compatibility of parylene-C surfaces. *Langmuir* **23**, 11718–11725 (2007).
174. Miller, E. M., Ng, A. H. C., Uddayasankar, U. & Wheeler, A. R. A digital microfluidic approach to heterogeneous immunoassays. *Anal Bioanal Chem* **399**, 337–345 (2011).
175. Min, X., Bao, C. & Kim, W. S. Additively Manufactured Digital Microfluidic Platforms for Ion-Selective Sensing. *ACS Sens* **4**, 918–923 (2019).
176. Abdelgawad, M. & Wheeler, A. R. Low-cost, rapid-prototyping of digital microfluidics devices. *Microfluid Nanofluidics* **4**, 349–355 (2008).
177. Abadian, A. & Jafarabadi-Ashtiani, S. Paper-based digital microfluidics. *Microfluid Nanofluidics* **16**, 989–995 (2014).
178. Zhou, J. *et al.* Superhydrophobic ZnO for EWOD digital microfluidic device for application in micro total analysis system (-TAS). *J Adhes Sci Technol* **26**, 2087–2098 (2012).
179. Verplanck, N. *et al.* Reversible electrowetting on superhydrophobic silicon nanowires. *Nano Lett* **7**, 813–817 (2007).
180. Mats, L., Bramwell, A., Dupont, J., Liu, G. & Oleschuk, R. Electrowetting on superhydrophobic natural (Colocasia) and synthetic surfaces based upon fluorinated silica nanoparticles. *Microelectron Eng* **148**, 91–97 (2015).
181. Khan, A., Sohail, S. & Jacob, C. Adhesion of water droplets by low voltage electrowetting on a superhydrophobic surface of a 3C-SiC nanorod network. *Mater Res Express* **2**, 125004 (2015).
182. Dhindsa, M. S. *et al.* Reversible electrowetting of vertically aligned superhydrophobic carbon nanofibers. *Langmuir* **22**, 9030–9034 (2006).
183. Malic, L., Brassard, D., Veres, T. & Tabrizian, M. Integration and detection of biochemical assays in digital microfluidic LOC devices. *Lab Chip* **10**, 418–431 (2010).
184. Rabe, M., Verdes, D. & Seeger, S. Understanding protein adsorption phenomena at solid surfaces. *Adv Colloid Interface Sci* **162**, 87–106 (2011).
185. Brassard, D., Malic, L., Normandin, F., Tabrizian, M. & Veres, T. Water-oil core-shell droplets for electrowetting-based digital microfluidic devices. *Lab Chip* **8**, 1342–1349 (2008).
186. Li, C.-C., Hsu, Y.-W., Huang, H.-Y. & Fan, S.-K. Dynamic embryo culture on a digital microfluidic chip. in *2012 IEEE 6th International Conference on Nano/Molecular Medicine and Engineering (NANOMED)* 74–77 (2012). doi:10.1109/NANOMED.2012.6509124.
187. Eydelnant, I. A., Uddayasankar, U., Li, B., Liao, W. & Wheeler, A. R. Lab on a Chip Virtual microwells for digital microfluidic reagent dispensing and cell culture. *Lab Chip* 750–757 (2012) doi:10.1039/c2lc21004e.

188. Eydelnant, I. A., Li, B. B. & Wheeler, A. R. Microgels on-demand. *Nat Commun* **5**, 1–9 (2014).
189. Ng, A. H. C. Development of Digital Microfluidic Heterogeneous Immunoassays. (University of Toronto, 2015).
190. Luk, V. N. A Digital Microfluidic Approach to Proteomic Sample Processing. (University of Toronto, 2012).
191. Au, S. H., Kumar, P. & Wheeler, A. R. A New Angle on Pluronic Additives: Advancing Droplets and Understanding in Digital Microfluidics. *Langmuir* **27**, 8586–8594 (2011).
192. Fobel, R., Fobel, C. & Wheeler, A. R. DropBot: An open-source digital microfluidic control system with precise control of electrostatic driving force and instantaneous drop velocity measurement. *Appl Phys Lett* **102**, 1–5 (2013).
193. SciBots. Little Drops. Big Science. https://sci-bots.com/ (2020).
194. SciBots. DropBot DB3-120 kit. https://shop.sci-bots.com/product/dropbot-db3-120-kit/ (2019).
195. GauidiLabs. OpenDrop V3. http://www.gaudi.ch/OpenDrop/?p=389 (2018).
196. Yafia, M., Ahmadi, A., Hoorfar, M. & Najjaran, H. Ultra-portable smartphone controlled integrated digital microfluidic system in a 3D-printed modular assembly. *Micromachines (Basel)* **6**, 1289–1305 (2015).
197. Digi.Bio. https://digi.bio/ (2019).
198. Zeng, Z., Zhang, K., Wang, W., Xu, W. & Zhou, J. Portable Electrowetting Digital Microfluidics Analysis Platform for Chemiluminescence Sensing. *IEEE Sens J* **16**, 4531–4536 (2016).
199. Digifluidic. http://digifluidic.com/home (2020).
200. GenMark DX. https://www.genmarkdx.com/ (2019).
201. GenMark DX. ePlex. https://www.genmarkdx.com/solutions/systems/eplex-system/ (2019).
202. Baebies. https://baebies.com/ (2019).
203. Baebies. SEEKER. https://baebies.com/products/seeker/ (2019).
204. Illumina. https://emea.illumina.com/ (2020).
205. Miroculus. https://miroculus.com/ (2020).
206. Drop Genie. https://www.drop-genie.com/ (2019).
207. Shih, S. C. C. *et al.* A droplet-to-digital (D2D) microfluidic device for single cell assays. *Lab Chip* **15**, 225–236 (2015).

208. Bindiganavale, G. S., Amaya, M. & Moon, H. Demonstration of hotspot cooling using digital microfluidic device. *Journal of Micromechanics and Microengineering* **28**, (2018).
209. Wan, L. *et al.* A digital microfluidic system for loop-mediated isothermal amplification and sequence specific pathogen detection. *Sci Rep* **7**, 1–11 (2017).
210. Fang, X., Chen, H., Yu, S., Jiang, X. & Kong, J. Predicting viruses accurately by a multiplex microfluidic loop-mediated isothermal amplification chip. *Anal Chem* **83**, 690–695 (2011).
211. Sathyanarayanan, G., Haapala, M., Kiiski, I. & Sikanen, T. Digital microfluidic immobilized cytochrome P450 reactors with integrated inkjet-printed microheaters for droplet-based drug metabolism research. *Anal Bioanal Chem* **410**, 6677–6687 (2018).
212. Shen, H. H., Su, T. Y., Chang, H. Y. & Yao, D. J. SNP detection based on temperature-controllable EWOD digital microfluidics system. *2012 IEEE Nanotechnology Materials and Devices Conference, IEEE NMDC 2012* 92–95 (2012) doi:10.1109/NMDC.2012.6527576.
213. Sayad, A. A. *et al.* A microfluidic lab-on-a-disc integrated loop mediated isothermal amplification for foodborne pathogen detection. *Sens Actuators B Chem* **227**, 600–609 (2016).
214. Yang, F., Yang, N., Huo, X. & Xu, S. Thermal sensing in fluid at the micro-nano-scales. *Biomicrofluidics* **12**, (2018).
215. Mullis, K. *et al.* Specific Enzymatic Amplification of DNA In Vitro: The Polymerase Chain Reaction. *Cold Spring Harb Symp Quant Biol* **51**, 263–273 (1986).
216. Promega. Nucleic acid amplification protocols and guidelines. in *Protocols & Applications Guide* 1–27 (Promega Corporation, 2011).
217. Wolcott, M. J. Advances in nucleic acid-based detection methods. *Clin Microbiol Rev* **5**, 370–386 (1992).
218. Barany, F. Genetic disease detection and DNA amplification using cloned thermostable ligase. *Proc Natl Acad Sci U S A* **88**, 189–193 (1991).
219. Zhao, Y., Chen, F., Li, Q., Wang, L. & Fan, C. Isothermal Amplification of Nucleic Acids. *Chem Rev* **115**, 12491–12545 (2015).
220. Zhao, W., Ali, M. M., Brook, M. A. & Li, Y. Rolling circle amplification: Applications in nanotechnology and biodetection with functional nucleic acids. *Angewandte Chemie - International Edition* **47**, 6330–6337 (2008).
221. Jeong, Y. J., Park, K. & Kim, D. E. Isothermal DNA amplification in vitro: the helicase-dependent amplification system. *Cell Mol Life Sci* **66**, 3325–3336 (2009).

222. Craw, P. & Balachandran, W. Isothermal nucleic acid amplification technologies for point-of-care diagnostics: A critical review. *Lab Chip* **12**, 2469–2486 (2012).
223. Khilko, Y. *et al.* DNA assembly with error correction on a droplet digital microfluidics platform. *BMC Biotechnol* **18**, 1–14 (2018).
224. Kalsi, S., Valiadi, M., Turner, C., Sutton, M. & Morgan, H. Sample pre-concentration on a digital microfluidic platform for rapid AMR detection in urine. *Lab Chip* **19**, 168–177 (2019).
225. Kalsi, S., Sellars, S. L., Turner, C., Sutton, J. M. & Morgan, H. A programmable digital microfluidic assay for the simultaneous detection of multiple anti-microbial resistance genes. *Micromachines (Basel)* **8**, (2017).
226. Foo, P. C. *et al.* Loop-mediated isothermal amplification (LAMP) reaction as viable PCR substitute for diagnostic applications: a comparative analysis study of LAMP, conventional PCR, nested PCR (nPCR) and real-time PCR (qPCR) based on Entamoeba histolytica DNA derived from faecal sample. *BMC Biotechnol* **20**, 34 (2020).
227. Moeini-Zanjani, A. *et al.* Comparison of loop-mediated isothermal amplification and conventional PCR tests for diagnosis of common Brucella species. *BMC Res Notes* **13**, 533 (2020).
228. New England Biolabs Inc. Loop-mediated isothermal amplification. https://international.neb.com/applications/dna-amplification-pcr-and-qpcr/isothermal-amplification/loop-mediated-isothermal-amplification-lamp (2020).
229. Mordente, A., Meucci, E., Martorana, G. E. & Silvestrini, A. Cancer Biomarkers Discovery and Validation: State of the Art, Problems and Future Perspectives. in *Advances in Cancer Biomarkers: From biochemistry to clinic for a critical revision* (ed. Scatena, R.) 9–26 (Springer Netherlands, 2015). doi:10.1007/978-94-017-7215-0_2.
230. Kumar, R. R., Kumar, A., Chuang, C.-H. & Shaikh, M. O. Recent Advances and Emerging Trends in Cancer Biomarker Detection Technologies. *Ind Eng Chem Res* **62**, 5691–5713 (2023).
231. Smith, D. R., Myint, T. & Goh, H. S. Over-expression of the c-myc proto-oncogene in colorectal carcinoma. *Br J Cancer* **68**, 407–413 (1993).
232. Deming, S. L., Nass, S. J., Dickson, R. B. & Trock, B. J. C-myc amplification in breast cancer: a meta-analysis of its occurrence and prognostic relevance. *Br J Cancer* **83**, 1688–1695 (2000).
233. Prochownik, E. V. c-Myc as a therapeutic target in cancer. *Expert Rev Anticancer Ther* **4**, 289–302 (2004).

234. Pajic, A. *et al.* Cell cycle activation by c-myc in a Burkitt lymphoma model cell line. *Int J Cancer* **87**, 787–793 (2000).
235. Lombardi, L., Newcomb, E. W. & Dalla-Favera, R. Pathogenesis of Burkitt lymphoma: Expression of an activated c-myc oncogene causes the tumorigenic conversion of EBV-infected human B lymphoblasts. *Cell* **49**, 161–170 (1987).
236. ThermoFisher Scientific. Real-Time vs. Digital PCR vs. Traditional PCR. *Real-Time PCR Basics* https://www.thermofisher.com/pt/en/home/life-science/pcr/real-time-pcr/real-time-pcr-learning-center/real-time-pcr-basics/real-time-vs-digital-vs-traditional-pcr.html#top (2020).
237. Kaltenboeck, B. & Wang, C. Advances in Real-Time PCR: Application to Clinical Laboratory Diagnostics. *Adv Clin Chem* **40**, 219–259 (2005).
238. S.A. Deepak *et al.* Real-Time PCR: Revolutionizing Detection and Expression Analysis of Genes. *Curr Genomics* **8**, 234–251 (2007).
239. Zhang, X., Lowe, S. B. & Gooding, J. J. Brief review of monitoring methods for loop-mediated isothermal amplification (LAMP). *Biosens Bioelectron* **61**, 491–499 (2014).
240. Mori, Y., Nagamine, K., Tomita, N. & Notomi, T. Detection of Loop-Mediated Isothermal Amplification Reaction by Turbidity Derived from Magnesium Pyrophosphate Formation. *Biochem Biophys Res Commun* **289**, 150–154 (2001).
241. Huang, G. *et al.* Detection and application of microfluidic isothermal amplification on chip. *J Innov Opt Health Sci* **1**, 257–265 (2008).
242. Zhang, H. *et al.* LAMP-on-a-chip: Revising microfluidic platforms for loop-mediated DNA amplification. *TrAC - Trends in Analytical Chemistry* **113**, 44–53 (2019).
243. Zhu, Q. *et al.* Self-priming compartmentalization digital LAMP for point-of-care. *Lab Chip* **12**, 4755–4763 (2012).
244. Gansen, A., Herrick, A. M., Dimov, I. K., Lee, L. P. & Chiu, D. T. Digital LAMP in a sample self-digitization (SD) chip. *Lab Chip* **12**, 2247–2254 (2012).
245. Xie, M. *et al.* Multiplex detection of foodborne pathogens by real-time loop-mediated isothermal amplification on a digital microfluidic chip. *Food Control* **136**, 108824 (2022).
246. Park, B. H. *et al.* An integrated rotary microfluidic system with DNA extraction, loop-mediated isothermal amplification, and lateral flow strip based detection for point-of-care pathogen diagnostics. *Biosens Bioelectron* **91**, 334–340 (2017).
247. Tomlinson, J. A., Dickinson, M. J. & Boonham, N. Rapid detection of phytophthora ramorum and P. kernoviae by two-minute DNA extraction followed by isothermal

amplification and amplicon detection by generic lateral flow device. *Phytopathology* **100**, 143–149 (2010).

248. Kiatpathomchai, W., Jaroenram, W., Arunrut, N., Jitrapakdee, S. & Flegel, T. W. Shrimp Taura syndrome virus detection by reverse transcription loop-mediated isothermal amplification combined with a lateral flow dipstick. *J Virol Methods* **153**, 214–217 (2008).
249. Ravan, H. & Yazdanparast, R. Development and evaluation of a loop-mediated isothermal amplification method in conjunction with an enzyme-linked immunosorbent assay for specific detection of Salmonella serogroup D. *Anal Chim Acta* **733**, 64–70 (2012).
250. Belizario, V. Y. *et al.* Evaluation of loop-mediated isothermal amplification assay and enzyme-linked immunosorbent assay in detecting Schistosoma japonicum in Siargao Island, Surigao del Norte, the Philippines. *Acta Trop* **228**, (2022).
251. Ravan, H. & Yazdanparast, R. Loop region-specific oligonucleotide probes for loop-mediated isothermal amplification-enzyme-linked immunosorbent assay truly minimize the instrument needed for detection process. *Anal Biochem* **439**, 102–108 (2013).
252. Urrutia-Cabrera, D. *et al.* Comparative analysis of loop-mediated isothermal amplification (LAMP)-based assays for rapid detection of SARS-CoV-2 genes. *Sci Rep* **11**, (2021).
253. Jomoui, W., Srivorakun, H., Chansai, S. & Fucharoen, S. Loop-mediated isothermal amplification (LAMP) colorimetric phenol red assay for rapid identification of α0-thalassemia: Application to population screening and prenatal diagnosis. *PLoS One* **17**, (2022).
254. Tanner, N. A., Zhang, Y. & Evans, T. C. Visual detection of isothermal nucleic acid amplification using pH-sensitive dyes. *Biotechniques* **58**, 59–68 (2015).
255. Suebsing, R. *et al.* Evaluation of colorimetric loop-mediated isothermal amplification assay for visual detection of Streptococcus agalactiae and Streptococcus iniae in tilapia. *Lett Appl Microbiol* **57**, 317–324 (2013).
256. Kim, J. H., Yoo, I. S., An, J. H. & Kim, S. A novel paper-plastic hybrid device for the simultaneous loop-mediated isothermal amplification and detection of DNA. *Mater Lett* **214**, 243–246 (2018).
257. Goto, M. *et al.* Rapid detection of Pseudomonas aeruginosa in mouse feces by colorimetric loop-mediated isothermal amplification. *J Microbiol Methods* **81**, 247–252 (2010).
258. Veigas, B., Pedrosa, P., Couto, I., Viveiros, M. & Baptista, P. v. *Isothermal DNA amplification coupled to Au-nanoprobes for detection of mutations associated to Rifampicin resistance in Mycobacterium tuberculosis*. http://www.jnanobiotechnology.com/content/11/1/38 (2013).

259. Garrido-Maestu, A. *et al.* Combination of microfluidic loop-mediated isothermal amplification with gold nanoparticles for rapid detection of Salmonella spp. in food samples. *Front Microbiol* **8**, (2017).
260. Olabarria, G. *et al.* Highly sensitive and fast Legionella spp. in situ detection based on a loop mediated isothermal amplification technique combined to an electrochemical transduction system. *Talanta* **217**, (2020).
261. Safavieh, M., Ahmed, M. U., Tolba, M. & Zourob, M. Microfluidic electrochemical assay for rapid detection and quantification of Escherichia coli. *Biosens Bioelectron* **31**, 523–528 (2012).
262. Ahmed, M. U., Hasan, Q., Mosharraf Hossain, M., Saito, M. & Tamiya, E. Meat species identification based on the loop mediated isothermal amplification and electrochemical DNA sensor. *Food Control* **21**, 599–605 (2010).
263. Quyen, T. L., Ngo, T. A., Bang, D. D., Madsen, M. & Wolff, A. Classification of Multiple DNA Dyes Based on Inhibition Effects on Real-Time Loop-Mediated Isothermal Amplification (LAMP): Prospect for Point of Care Setting. *Front Microbiol* **10**, 2234 (2019).
264. Sun, Y. *et al.* A lab-on-a-chip system with integrated sample preparation and loop-mediated isothermal amplification for rapid and quantitative detection of Salmonella spp. in food samples. *Lab Chip* **15**, 1898–1904 (2015).
265. Coelho, B. J. *et al.* Digital Microfluidics-Powered Real-Time Monitoring of Isothermal DNA Amplification of Cancer Biomarker. *Biosensors (Basel)* **12**, 201 (2022).
266. Ahmed, M. U. *et al.* Electrochemical genosensor for the rapid detection of GMO using loop-mediated isothermal amplification. *Analyst* **134**, 966–972 (2009).
267. Hsieh, K., Patterson, A. S., Ferguson, B. S., Plaxco, K. W. & Soh, H. T. Rapid, sensitive, and quantitative detection of pathogenic DNA at the point of care through microfluidic electrochemical quantitative loop-mediated isothermal amplification. *Angewandte Chemie - International Edition* **51**, 4896–4900 (2012).
268. Ramírez-Chavarría, R. G. *et al.* Loop-mediated isothermal amplification-based electrochemical sensor for detecting SARS-CoV-2 in wastewater samples. *J Environ Chem Eng* **10**, (2022).
269. Ganguli, A. *et al.* High Sensitivity Graphene Field Effect Transistor-Based Detection of DNA Amplification. *Adv Funct Mater* **30**, (2020).
270. Wachiralurpan, S. *et al.* A one-step rapid screening test of Listeria monocytogenes in food samples using a real-time loop-mediated isothermal amplification turbidity assay. *Analytical Methods* **9**, 6403–6410 (2017).

271. Wang, S., Liu, N., Zheng, L., Cai, G. & Lin, J. A lab-on-chip device for the sample-in-result-out detection of viable Salmonella using loop-mediated isothermal amplification and real-time turbidity monitoring. *Lab Chip* **20**, 2296–2305 (2020).
272. Bello, I. *Vacuum and Ultravacuum: Physics and Technology*. (CRC Press, 2018).
273. Mwema, F. M., Jen, T.-C. & Zhu, L. *Thin Film Coatings*. (CRC Press, 2022). doi:10.1201/9781003202615.
274. Lin, Y. *Advanced Nano Deposition Methods*. (Wiley-VCH, 2016).
275. Gorham, W. F. A New, General Synthetic Method for the Preparation of Linear Poly-p-xylylenes. *J Polym Sci A1* **4**, 3027–3039 (1966).
276. Specialty Coating Systems. *SCS Parylene Properties*. https://scscoatings.com/technical-library/ (2018).
277. Gao, J. *et al.* Adhesion promoter for a multi-dielectric-layer on a digital microfluidic chip. *RSC Adv* **5**, 48626–48630 (2015).
278. Charmet, J. *et al.* Optimizing Parylene C Adhesion for MEMS Processes: Potassium Hydroxide Wet Etching. *Journal of Microelectromechanical Systems* **22**, 855–864 (2013).
279. Mack, C. *Fundamental Principles of Optical Lithography*. (Wiley-VCH, 2008).
280. Makhlouf, A. S. H. *Nanocoatings and Ultra-Thin Films: Technologies and Applications*. (Elsevier, 2011).
281. Nguyen, N.-T. *Micromixers: Fundamentals, Design and Fabrication*. (Elsevier, 2011). doi:10.1016/C2011-0-69734-0.
282. Seshan, K. & Schepis, D. *Handbook of Thin Film Deposition*. (Elsevier, 2018).
283. Gudmundsson, J. T. Physics and technology of magnetron sputtering discharges. *Plasma Sources Sci Technol* **29**, 113001 (2020).
284. Rossnagel, S. M. Thin film deposition with physical vapor deposition and related technologies. *Journal of Vacuum Science & Technology A: Vacuum, Surfaces, and Films* **21**, S74–S87 (2003).
285. Branquinho, R. Label-free detection of biomolecules with Ta2O5-based field effect devices. (NOVA School of Science and Technology, 2012).
286. Magar, H. S., Hassan, R. Y. A. & Mulchandani, A. Electrochemical Impedance Spectroscopy (EIS): Principles, Construction, and Biosensing Applications. *Sensors* **21**, 6578 (2021).
287. Lvovich, V. *Impedance Spectroscopy: Applications to Electrochemical and Dielectric Phenomena*. (Wiley, 2012).

288. Tribollet, B. & Orazem, M. *Electrochemical Impedance Spectroscopy*. (John Wiley & Sons, 2008).
289. Keysight Technologies. *B1500A Semiconductor Device Analyzer. Technical Overview*. https://www.keysight.com/br/pt/assets/7018-03960/technical-overviews/5991-2443.pdf (2020).
290. Cullity, B. *Elements of X-ray Diffraction*. (Addison-Wesley Publishing Company Inc., 2014).
291. Jameson, D. M. *Introduction to Fluorescence*. (CRC Press, 2014). doi:10.1201/b16502.
292. Demchenko, A. P. *Introduction to Fluorescence Sensing*. *Introduction to Fluorescence Sensing* (Springer International Publishing, 2015). doi:10.1007/978-3-319-20780-3.
293. Zurich Instruments. *Principles of lock-in detection and the state of the art*. https://www.zhinst.com/europe/en/resources/principles-of-lock-in-detection.
294. Libbrecht, K. G., Black, E. D. & Hirata, C. M. A basic lock-in amplifier experiment for the undergraduate laboratory. *Am J Phys* **71**, 1208–1213 (2003).
295. Stachowiak, G. & Batchelor, A. *Experimental Methods in Tribology*. (Elsevier B.V, 2004).
296. Kruss Scientific. Contact angle. https://www.kruss-scientific.com/en/know-how/glossary/contact-angle (2022).
297. Laurén, S. *Contact angle: what is it and how do you measure it?* (2022).
298. Kruss Scientific. Drop shape analysis. (2022).
299. Lee, P. Y., Costumbrado, J., Hsu, C.-Y. & Kim, Y. H. Agarose Gel Electrophoresis for the Separation of DNA Fragments. *Journal of Visualized Experiments* (2012) doi:10.3791/3923.
300. Martin, R. *Gel Electrophoresis: Nucleic Acids*. (Garland Science, 2020). doi:10.1201/9781003076988.
301. Cunha, I. *et al.* Healable Cellulose Iontronic Hydrogel Stickers for Sustainable Electronics on Paper. *Adv Electron Mater* **7**, 1–10 (2021).
302. Cunha, I. *et al.* Reusable Cellulose-Based Hydrogel Sticker Film Applied as Gate Dielectric in Paper Electrolyte-Gated Transistors. *Adv Funct Mater* **27**, (2017).
303. Teng, H. Overview of the development of the fluoropolymer industry. *Applied Sciences (Switzerland)* **2**, 496–512 (2012).
304. Gardiner, J. Fluoropolymers: Origin, Production, and Industrial and Commercial Applications. *Aust J Chem* **68**, 13–22 (2015).
305. Ratner, B., Hoffman, A., Schoen, F. & Lemons, J. *Biomaterials Science: An Introduction to Materials in Medicine*. (Academic Press, 2013).

306. Zaky, A. A., Megahed, I. Y. & Yehia, S. A. The direct breakdown voltage of silicone oil under uniform fields. *IEEE Transactions on Electrical Insulation* **EI-20**, 333–337 (1985).
307. Kuffel, E., Zaengl, W. S. & Kuffel, J. *High Voltage Engineering*. *Springer Handbooks* (Butterworth-Heinemann, 2000). doi:10.1007/978-981-32-9938-2_3.
308. Suwarno, Widyanugraha, T., Hs, P. D. & Suharto. Dielectric properties of silicone oil, natural ester, and mineral oil under accelerated thermal aging. *Proceedings of 2012 IEEE International Conference on Condition Monitoring and Diagnosis, CMD 2012* 1139–1142 (2012) doi:10.1109/CMD.2012.6416360.
309. Yang, C. S., Chen, K. H., Hsu, W. M. & Li, Y. S. Cytotoxicity of silicone oil on cultivated human corneal endothelium. *Eye* **22**, 282–288 (2008).
310. Malchiodi-Albedi, F. *et al.* Biocompatibility assessment of silicone oil and perfluorocarbon liquids used in retinal reattachment surgery in rat retinal cultures. *J Biomed Mater Res* **60**, 548–555 (2002).
311. Merck. Silicone oil - Product Comparison Guide. https://www.sigmaaldrich.com/PT/en/substance/siliconeoil1234563148629?context=product (2021).
312. Zhang, S., Bi, S. & Song, X. *Nucleic acid amplification strategies for biosensing, bioimaging and biomedicine*. (Springer Nature Singapore, 2019). doi:10.1007/978-981-13-7044-1.
313. Santos, E. A., Ichinose, R. M. & Almeida, R. T. The effectiveness of temperature control of thermocyclers in PCR optimization. *Biotechniques* **67**, 271–275 (2019).
314. New England Biolabs Inc. FAQ: Can Bst DNA Polymerase be used at temperatures other than 65°C? *Frequently Asked Questions* https://international.neb.com/faqs/2011/12/17/can-bst-dna-polymerase-be-used-at-temperatures-other-than-65-176-c (2021).
315. Shin-Etsu Silicone. Silicone Fluid. Preprint at https://www.shinetsusilicone-global.com/catalog/pdf/fluid_us.pdf (2021).
316. Dincer, I. & Zamfirescu, C. Thermophysical Properties of Water. in *Drying Phenomena: Theory and Applications* (John Wiley & Sons, 2016). doi:10.1002/9781118534892.
317. Karazi, S. M., Ahad, I. U. & Benyounis, K. Y. Laser Micromachining for Transparent Materials. in *Elsevier Reference Collection in Materials Science and Materials Engineering* 1–22 (Elsevier Science, 2017). doi:10.1016/B978-0-12-803581-8.04149-7.
318. SubsTech Substances & Technologies. Thermoplastic Acrylonitrile-Butadiene-Styrene (ABS). https://www.substech.com/dokuwiki/doku.php?id=thermoplastic_acrylonitrile-butadiene-styrene_abs (2021).

319. DM Dielectric Manufacturing. ABS (Acrylonitrile-Butadlene-Styrene). https://dielectric-mfg.com/knowledge-base/abs/ (2021).
320. Samiei, E., Tabrizian, M. & Hoorfar, M. A review of digital microfluidics as portable platforms for lab-on a-chip applications. *Lab Chip* **16**, 2376–2396 (2016).
321. Hassler, C., von Metzen, R. P., Ruther, P. & Stieglitz, T. Characterization of parylene C as an encapsulation material for implanted neural prostheses. *J Biomed Mater Res B Appl Biomater* **93B**, 266–274 (2010).
322. Hsu, J.-M., Rieth, L., Kammer, S., Orthner, M. & Solzbacher, F. Effect of thermal and deposition processes on surface morphology, crystallinity, and adhesion of Parylene-C. *Sensors and Materials* **20**, 87–102 (2008).
323. Jakabovič, J. *et al.* Preparation and properties of thin parylene layers as the gate dielectrics for organic field effect transistors. *Microelectronics J* **40**, 595–597 (2009).
324. Senkevich, J. J. & Desu, S. B. Morphology of poly(chloro-p-xylylene) CVD thin films. *Polymer (Guildf)* **40**, 5751–5759 (1999).
325. Surendran, G., Gazicki, M., James, W. J. & Yasuda, H. Polymerization of para-xylylene derivatives. V. Effects of the sublimation rate of di-p-xylylene on the crystallinity of parylene C deposited at different temperatures. *J Polym Sci A Polym Chem* **25**, 2089–2106 (1987).
326. Rao, V. K. P. & Sagar, T. Numerical evaluation of the influence of AC and DC electric field on the response of the droplet. *3Rd International Conference on Condensed Matter and Applied Physics (Icc-2019)* **2220**, 130006 (2020).
327. Fair, R. B. Digital microfluidics: Is a true lab-on-a-chip possible? *Microfluid Nanofluidics* **3**, 245–281 (2007).
328. Nelson, W. C. & Kim, C.-J. 'Cj'. Droplet Actuation by Electrowetting-on-Dielectric (EWOD): A Review. *J Adhes Sci Technol* **26**, 1747–1771 (2012).
329. Chemorus. *Teflon™ AF Amorphous Fluoroplastic Resins - Product Information*. https://www.teflon.com/en/-/media/files/teflon/teflon-af-product-info.pdf (2016).
330. 3M Science. *3M™ Fluorinert™ Electronic Liquid FC-40 Product description*. https://multimedia.3m.com/mws/media/64888O/3m-fluorinert-electronic-liquid-fc40.pdf (2019).
331. Kaneko, H., Kawana, T., Fukushima, E. & Suzutani, T. Tolerance of loop-mediated isothermal amplification to a culture medium and biological substances. *J Biochem Biophys Methods* **70**, 499–501 (2007).
332. Francois, P. *et al.* Robustness of a loop-mediated isothermal amplification reaction for diagnostic applications. *FEMS Immunol Med Microbiol* **62**, 41–48 (2011).

333. Higuchi, R., Fockler, C., Dollinger, G. & Watson, R. Kinetic PCR analysis: Real-time monitoring of DNA amplification reactions. *Bio/Technology* **11**, 1026–1030 (1993).
334. Bio-Rad. Real-Time PCR Detection Systems. https://www.bio-rad.com/en-pt/category/real-time-pcr-detection-systems?ID=059db09c-88a4-44ad-99f8-78635d8d54db (2020).
335. Applied Biosystems. Applied Biosystems Real-Time PCR Instruments. https://www.thermofisher.com/pt/en/home/life-science/pcr/real-time-pcr/real-time-pcr-instruments.html (2020).
336. Qiagen. Rotor-Gene Q. https://www.qiagen.com/us/products/discovery-and-translational-research/epigenetics/dna-methylation/methylation-specific-pcr/rotor-gene-q/?clear=true#orderinginformation (2020).
337. Roche. High-Performance real-time PCR with LightCycler(R) Systems. https://lifescience.roche.com/en_pt/brands/realtime-pcr-overview.html#overview (2020).
338. Biotium. PCR & DNA Amplification. https://biotium.com/technology/pcr-dna-amplification/ (2020).
339. Paik, P., Pamula, V. K., Pollack, M. G. & Fair, R. B. Electrowetting-based droplet mixers for microfluidic systems. *Lab Chip* **3**, 28–33 (2003).
340. Paik, P., Pamula, V. K. & Fair, R. B. Rapid droplet mixers for digital microfluidic systems. *Lab Chip* **3**, 253–259 (2003).
341. Mugele, F., Baret, J. C. & Steinhauser, D. Microfluidic mixing through electrowetting-induced droplet oscillations. *Appl Phys Lett* **88**, 1–4 (2006).
342. Li, M. *et al.* Hydrodynamic-flow-enhanced rapid mixer for isothermal DNA hybridization kinetics analysis on digital microfluidics platform. *Sens Actuators B Chem* **287**, 390–397 (2019).
343. Samiei, E., de Leon Derby, M. D., den Berg, A. van & Hoorfar, M. An electrohydrodynamic technique for rapid mixing in stationary droplets on digital microfluidic platforms. *Lab Chip* **17**, 227–234 (2017).
344. Bansal, S. & Sen, P. Mixing enhancement by degenerate modes in electrically actuated sessile droplets. *Sens Actuators B Chem* **232**, 318–326 (2016).
345. Mugele, F., Staicu, A., Bakker, R. & van den Ende, D. Capillary Stokes drift: A new driving mechanism for mixing in AC-electrowetting. *Lab Chip* **11**, 2011–2016 (2011).
346. Fowler, J., Moon, H. & Kim, C. J. Enhancement of mixing by droplet-based microfluidics. in *Technical Digest. MEMS 2002 IEEE International Conference. Fifteenth IEEE*

International Conference on Micro Electro Mechanical Systems 97–100 (IEEE, 2002). doi:10.1109/memsys.2002.984099.

347. Shapiro, S. S. & Wilk, M. B. An Analysis of Variance Test for Normality (Complete Samples). *Biometrika* **52**, 591 (1965).
348. Brown, M. B. & Forsythe, A. B. Robust Tests for the Equality of Variances. *J Am Stat Assoc* **69**, 364 (1974).
349. Mao, F., Leung, W. Y. & Xin, X. Characterization of EvaGreen and the implication of its physicochemical properties for qPCR applications. *BMC Biotechnol* **7**, 1–16 (2007).
350. Kremers, T., Thelen, S., Bosbach, N. & Schnakenberg, U. PortaDrop: A portable digital microfluidic platform providing versatile opportunities for Lab-On-A-Chip applications. *PLoS One* **15**, 1–26 (2020).
351. Sci-Bots. DropBot DB3-120 kit. https://shop.sci-bots.com/product/dropbot-db3-120-kit/ (2022).
352. Chapman, J. R. & Waldenström, J. With Reference to Reference Genes: A Systematic Review of Endogenous Controls in Gene Expression Studies. *PLoS One* **10**, e0141853 (2015).
353. Chervoneva, I. *et al.* Selection of optimal reference genes for normalization in quantitative RT-PCR. *BMC Bioinformatics* **11**, 1–15 (2010).
354. Suzuki, T., Higgins, P. J. & Crawford, D. R. Control Selection for RNA Quantitation. *https://doi.org/10.2144/00292rv02* **29**, 332–337 (2018).
355. Mac, M., Uchacz, T., Wróbel, T., Danel, A. & Kulig, E. New Fluorescent Sensors Based on 1H-pyrazolo[3,4-b]quinoline Skeleton. *J Fluoresc* **20**, 525–532 (2010).
356. Tomin, V. I. & Ushakou, D. v. Effect of salt ions on the proton-transfer rate in 3-hydroxyflavone. *J Appl Spectrosc* **82**, 193–199 (2015).
357. Ward, K. & Fan, Z. H. Mixing in microfluidic devices and enhancement methods. *Journal of Micromechanics and Microengineering* **25**, 94001 (2015).
358. Lee, C.-Y., Wang, W.-T., Liu, C.-C. & Fu, L.-M. Passive mixers in microfluidic systems: A review. *Chemical Engineering Journal* **288**, 146–160 (2016).
359. Heaviside, O. *Electrical papers*. (MacMillan and Co., 1894).
360. Zrinzo, L. Brain Mapping Techniques Used to Guide Deep Brain Stimulation Surgery. *Brain Mapping: An Encyclopedic Reference* **3**, 721–730 (2015).
361. Randviir, E. P. & Banks, C. E. Electrochemical impedance spectroscopy: an overview of bioanalytical applications. *Anal. Methods* 1098–1115 (2013) doi:10.1039/C3AY26476A.

362. Katz, E. & Willner, I. Probing biomolecular interactions at conductive and semiconductive surfaces by impedance spectroscopy: Routes to impedimetric immunosensors, DNA-sensors, and enzyme biosensors. *Electroanalysis* **15**, 913–947 (2003).
363. Menon, S., Mathew, M. R., Sam, S., Keerthi, K. & Kumar, K. G. Recent advances and challenges in electrochemical biosensors for emerging and re-emerging infectious diseases. *Journal of Electroanalytical Chemistry* **878**, 1–14 (2020).
364. Lisdat, F. & Schäfer, D. The use of electrochemical impedance spectroscopy for biosensing. *Anal Bioanal Chem* **391**, 1555–1567 (2008).
365. Bahadir, E. B. & Sezgintürk, M. K. A review on impedimetric biosensors. *Artif Cells Nanomed Biotechnol* **44**, 248–262 (2016).
366. Reddy, B., Salm, E. & Bashir, R. Electrical Chips for Biological Point-of-Care Detection. *Annu Rev Biomed Eng* **18**, 329–355 (2016).
367. Derkus, B., Emregul, E., Yucesan, C. & Cebesoy Emregul, K. Myelin basic protein immunosensor for multiple sclerosis detection based upon label-free electrochemical impedance spectroscopy. *Biosens Bioelectron* **46**, 53–60 (2013).
368. Bryan, T., Luo, X., Bueno, P. R. & Davis, J. J. An optimised electrochemical biosensor for the label-free detection of C-reactive protein in blood. *Biosens Bioelectron* **39**, 94–98 (2013).
369. Rezaei, B., Askarpour, N. & Ensafi, A. A. A novel sensitive doxorubicin impedimetric immunosensor based on a specific monoclonal antibody-gold nanoaprticle-sol-gel modified electrode. *Talanta* **119**, 164–169 (2014).
370. Ito, Y. *et al.* Third generation impedimetric sensor employing direct electron transfer type glucose dehydrogenase. *Biosens Bioelectron* **129**, 189–197 (2019).
371. Naderi Asrami, P., Mozaffari, S. A., Saber Tehrani, M. & Aberoomand Azar, P. A novel impedimetric glucose biosensor based on immobilized glucose oxidase on a CuO-Chitosan nanobiocomposite modified FTO electrode. *Int J Biol Macromol* **118**, 649–660 (2018).
372. Mozaffari, S. A., Rahmanian, R., Abedi, M. & Amoli, H. S. Urea impedimetric biosensor based on reactive RF magnetron sputtered zinc oxide nanoporous transducer. *Electrochim Acta* **146**, 538–547 (2014).
373. Rahmanian, R., Mozaffari, S. A., Amoli, H. S. & Abedi, M. Development of sensitive impedimetric urea biosensor using DC sputtered Nano-ZnO on TiO2 thin film as a novel hierarchical nanostructure transducer. *Sens Actuators B Chem* **256**, 760–774 (2018).

374. Furst, A. L. & Francis, M. B. Impedance-Based Detection of Bacteria. *Chem Rev* **119**, 700–726 (2019).
375. Pellitero, M. A., Shaver, A. & Arroyo-Currás, N. Critical Review—Approaches for the Electrochemical Interrogation of DNA-Based Sensors: A Critical Review. *J Electrochem Soc* **167**, 037529 (2020).
376. Scott-Murrell, E., Lanza, D. & Schertzer, M. J. Dimensionless model for impedimetric sensing of particle laden droplets in digital microfluidic devices. *Microsystem Technologies* **23**, 3131–3139 (2017).
377. Li, C. *et al.* Feedback control system for large scale 2D digital microfluidic platforms. *Sens Actuators B Chem* **255**, 3616–3622 (2018).
378. Zhang, C. *et al.* An Impedance Sensing Platform for Monitoring Heterogeneous Connectivity and Diagnostics in Lab-on-a-Chip Systems. *ACS Appl Mater Interfaces* **5**, 5098–5104 (2020).
379. Hu, X., Mibus, M., Knospe, C. R., Zangari, G. & Reed, M. L. Impedance spectroscopy and electrical modeling of electrowetting on dielectric devices. *Journal of Micromechanics and Microengineering* **25**, 1–8 (2015).
380. Shih, S. C. C., Barbulovic-Nad, I., Yang, X., Fobel, R. & Wheeler, A. R. Digital microfluidics with impedance sensing for integrated cell culture and analysis. *Biosens Bioelectron* **42**, 314–320 (2013).
381. Li, Y. J. & Cahill, B. P. Frequency Dependence of Low-Voltage Electrowetting Investigated by Impedance Spectroscopy. *Langmuir* **33**, 13139–13147 (2017).
382. Dak, P., Ebrahimi, A. & Alam, M. A. Non-faradaic impedance characterization of an evaporating droplet for microfluidic and biosensing applications. *Lab Chip* 2469–2479 (2014) doi:10.1039/c4lc00193a.
383. Sadeghi, S. *et al.* On chip droplet characterization: A practical, high-sensitivity measurement of droplet impedance in digital microfluidics. *Anal Chem* **84**, 1915–1923 (2012).
384. Hadwen, B. *et al.* Programmable large area digital microfluidic array with integrated droplet sensing for bioassays. *Lab Chip* **12**, 3305–3313 (2012).
385. Hu, X., Mibus, M., Zangari, G., Knospe, C. & Reed, M. L. Interrogation of Droplet Configuration During Electrowetting via Impedance Spectroscopy. *Journal of Microelectromechanical Systems* **24**, 2092–2100 (2015).
386. Lederer, T., Clara, S., Jakoby, B. & Hilber, W. Integration of impedance spectroscopy sensors in a digital microfluidic platform. *Microsystem Technologies* **18**, 1163–1180 (2012).

387. Liu, Y., Banerjee, A. & Papautsky, I. Precise droplet volume measurement and electrode-based volume metering in digital microfluidics. *Microfluid Nanofluidics* **17**, 295–303 (2014).
388. Shih, S. C. C., Fobel, R., Kumar, P. & Wheeler, A. R. A feedback control system for high-fidelity digital microfluidics. *Lab Chip* **11**, 535–540 (2011).
389. Shih, S. C. C. *et al.* Dried blood spot analysis by digital microfluidics coupled to nanoelectrospray ionization mass spectrometry. *Anal Chem* **84**, 3731–3738 (2012).
390. Ng, A. H. C., Li, B. B., Chamberlain, M. D. & Wheeler, A. R. Digital Microfluidic Cell Culture. *Annu Rev Biomed Eng* **17**, 91–112 (2015).
391. Rudnitskaya, A. Calibration update and drift correction for electronic noses and tongues. *Front Chem* **6**, (2018).
392. Holmberg, M. *et al.* Drift counteraction in odour recognition applications: Lifelong calibration method. *Sens Actuators B Chem* **42**, 185–194 (1997).
393. Pei, S. N., Wang, Y., Lin, C. & Wu, M. C. Isothermal real-time polymerase chain reaction detection of herpes simplex virus type 1 on a light-actuated digital microfluidics platform. in *2013 Transducers & Eurosensors XXVII: The 17th International Conference on Solid-State Sensors, Actuators and Microsystems (TRANSDUCERS & EUROSENSORS XXVII)* 2791–2794 (IEEE, 2013). doi:10.1109/Transducers.2013.6627385.
394. Seale, B. *et al.* Digital Microfluidics for Immunoprecipitation. *Anal Chem* **88**, 10223–10230 (2016).
395. Zhang, X. *et al.* Monitoring the progression of loop-mediated isothermal amplification using conductivity. *Anal Biochem* **466**, 16–18 (2014).
396. Cao, Y. *et al.* Development of a real-time fluorescence loop-mediated isothermal amplification assay for rapid and quantitative detection of Ustilago maydis. *Scientific Reports 2017 7:1* **7**, 1–12 (2017).
397. Ghasemi, A. & Zahediasl, S. Normality Tests for Statistical Analysis: A Guide for Non-Statisticians. *International Journal of Endocrinology and Metabolism 2012 10:2* **10**, 486–489 (2012).
398. Nernst, W. Methode zur Bestimmung von Dielektrizitätskonstanten. *Zeitschrijt für Elektrochemie* **14**, 622–663 (1894).
399. Ramírez Barat, B. & Cano, E. In Situ Electrochemical Impedance Spectroscopy Measurements and their Interpretation for the Diagnostic of Metallic Cultural Heritage: A Review. *ChemElectroChem* **5**, 2698–2716 (2018).

400. Middlemiss, L. A., Rennie, A. J. R., Sayers, R. & West, A. R. Characterisation of batteries by electrochemical impedance spectroscopy. *Energy Reports* **6**, 232–241 (2020).
401. Tang, Z. *et al.* Recent progress in the use of electrochemical impedance spectroscopy for the measurement, monitoring, diagnosis and optimization of proton exchange membrane fuel cell performance. *J Power Sources* **468**, (2020).
402. Bahadir, E. B. & Sezgintürk, M. K. A review on impedimetric biosensors. *Artif Cells Nanomed Biotechnol* **44**, 248–262 (2016).
403. Guiseppi-Elie, A. & Lingerfelt, L. Impedimetric detection of DNA hybridization: Towards near-patient DNA diagnostics. in *Immobilisation of DNA on Chips I. Topics in Current Chemistry* (ed. Wittmann, C.) vol. 260 161–186 (Springer Berlin Heidelberg, 2005).
404. Sadighbayan, D., Sadighbayan, K., Khosroushahi, A. Y. & Hasanzadeh, M. Recent advances on the DNA-based electrochemical biosensing of cancer biomarkers: Analytical approach. *TrAC - Trends in Analytical Chemistry* **119**, 115609 (2019).
405. Du, Y. & Dong, S. Nucleic acid biosensors: Recent advances and perspectives. *Anal Chem* **89**, 189–215 (2017).
406. Wu, Q., Zhang, Y., Yang, Q., Yuan, N. & Zhang, W. Review of electrochemical DNA biosensors for detecting food borne pathogens. *Sensors (Switzerland)* **19**, (2019).
407. Veigas, B., Fortunato, E. & Baptista, P. Field Effect Sensors for Nucleic Acid Detection: Recent Advances and Future Perspectives. *Sensors* **15**, 10380–10398 (2015).
408. Branquinho, R. *et al.* Real-time monitoring of PCR amplification of proto-oncogene c-MYC using a Ta2O5 electrolyte-insulator-semiconductor sensor. *Biosens Bioelectron* **28**, 44–49 (2011).
409. Jeong, S., Lim, J., Kim, J., Kim, M. Y. & Lee, J. H. Label-free electrochemical impedance spectroscopy using a micro interdigitated electrode inside a PCR chip for real-time monitoring. *Microsystem Technologies* **25**, 3503–3510 (2019).
410. Lim, J., Kim, J., Lee, E., Park, H. & Lee, J. H. An analysis method to detect the presence of DNA using electrochemical impedance spectroscopy (EIS) for real-time PCR. *Microsystem Technologies* **27**, 3211–3217 (2020).
411. Gamry Instruments. Mott Schottky EIS. *Electrochemical Impedance Spectroscopy Software* https://www.gamry.com/assets/Uploads/EIS300-Product-Brochure.pdf (2021).
412. Barquinha, P. Transparent oxide thin-film transistors: production, characterization and integration. (NOVA School of Science and Technology, 2010).
413. Veigas, B. Development of field effect sensors for gene expression analysis: Application to cancer diagnosis. (NOVA School of Science and Technology, 2016).

414. Park, S. *et al.* The Effect of Annealing Ambient on the Characteristics of an Indium-Gallium-Zinc Oxide Thin Film Transistor. *J Nanosci Nanotechnol* **11**, 6029–6033 (2011).
415. Sung, S. Y. *et al.* Effects of Post-Annealing Treatments on the Transfer Characteristics of Amorphous Indium-Gallium-Zinc Oxide Thin Film Transistors. *Journal of Nanoelectronics and Optoelectronics* **6**, 310–314 (2011).
416. Salm, E. *et al.* Electrical detection of nucleic acid amplification using an on-chip quasi-reference electrode and a PVC REFET. *Anal Chem* **86**, 6968–6975 (2014).
417. Charoenpanich, P., Mungkung, A. & Seeviset, N. A pH sensitive, loop-mediated isothermal amplification assay for detection of Salmonella in food. *Science, Engineering and Health Studies* **2020**, 160–168 (2020).
418. WarmStart Colorimetric LAMP 2X Master Mix (DNA & RNA) | NEB. https://international.neb.com/products/m1800-warmstart-colorimetric-lamp-2x-master-mix-dna-rna#Product%20Information.
419. Bst 2.0 WarmStart DNA Polymerase NEB. https://international.neb.com/products/m0538-bst-20-warmstart-dna-polymerase#Product%20Information_Properties%20&%20Usage.
420. Pattanayak, P. *et al.* Microfluidic chips: recent advances, critical strategies in design, applications and future perspectives. *Microfluid Nanofluidics* **25**, 99 (2021).
421. Sohrabi, S., kassir, N. & Keshavarz Moraveji, M. Droplet microfluidics: fundamentals and its advanced applications. *RSC Adv* **10**, 27560–27574 (2020).
422. Zhou, W., Dou, M., Timilsina, S. S., Xu, F. & Li, X. Recent innovations in cost-effective polymer and paper hybrid microfluidic devices. *Lab Chip* **21**, 2658–2683 (2021).
423. Komatsu, T., Tokeshi, M. & Fan, S.-K. Determination of blood lithium-ion concentration using digital microfluidic whole-blood separation and preloaded paper sensors. *Biosens Bioelectron* **195**, 113631 (2022).
424. Dou, M., Dominguez, D. C., Li, X., Sanchez, J. & Scott, G. A Versatile PDMS/Paper Hybrid Microfluidic Platform for Sensitive Infectious Disease Diagnosis. *Anal Chem* **86**, 7978–7986 (2014).
425. Shih, S. C. C. *et al.* A Versatile Microfluidic Device for Automating Synthetic Biology. *ACS Synth Biol* **4**, 1151–1164 (2015).
426. Abdelgawad, M., Watson, M. W. L. & Wheeler, A. R. Hybrid microfluidics: a digital-to-channel interface for in-line sample processing and chemical separations. *Lab Chip* **9**, 1046–51 (2009).

427. Watson, M. W. L., Jebrail, M. J. & Wheeler, A. R. Multilayer Hybrid Microfluidics: A Digital-to-Channel Interface for Sample Processing and Separations. *Anal Chem* **82**, 6680–6686 (2010).
428. Samlali, K., Ahmadi, F., Quach, A. B. v, Soffer, G. & Shih, S. C. C. One Cell, One Drop, One Click: Hybrid Microfluidics for Mammalian Single Cell Isolation. *Small* **16**, 2002400 (2020).
429. Ahmadi, F., Samlali, K., Vo, P. Q. N. & Shih, S. C. C. An integrated droplet-digital microfluidic system for on-demand droplet creation, mixing, incubation, and sorting. *Lab Chip* **19**, 524–535 (2019).
430. Olmedillas-López, S., Olivera-Salazar, R., García-Arranz, M. & García-Olmo, D. Current and Emerging Applications of Droplet Digital PCR in Oncology: An Updated Review. *Mol Diagn Ther* **26**, 61–87 (2022).
431. Kojabad, A. A. *et al.* Droplet digital PCR of viral DNA/RNA, current progress, challenges, and future perspectives. *J Med Virol* **93**, 4182–4197 (2021).
432. Hindson, B. J. *et al.* High-Throughput Droplet Digital PCR System for Absolute Quantitation of DNA Copy Number. *Anal Chem* **83**, 8604–8610 (2011).
433. Datta, P. *et al.* Enhancement of mixing operation through new movement strategies in digital microfluidic biochips. *Proceedings of 2nd International Conference on 2017 Devices for Integrated Circuit, DevIC 2017* 611–614 (2017) doi:10.1109/DEVIC.2017.8074023.
434. Collins, D. J., Neild, A., deMello, A., Liu, A. Q. & Ai, Y. The Poisson distribution and beyond: methods for microfluidic droplet production and single cell encapsulation. *Lab Chip* **15**, 3439–3459 (2015).
435. Zhu, P. & Wang, L. Passive and active droplet generation with microfluidics: a review. *Lab Chip* **17**, 34–75 (2017).
436. Amirifar, L. *et al.* Droplet-based microfluidics in biomedical applications. *Biofabrication* **14**, 022001 (2022).
437. Christopher, G. F. & Anna, S. L. Microfluidic methods for generating continuous droplet streams. *Journal of Physics D: Applied Physics* vol. 40 Preprint at https://doi.org/10.1088/0022-3727/40/19/R01 (2007).
438. Teo, A. J. T. *et al.* Negative Pressure Induced Droplet Generation in a Microfluidic Flow-Focusing Device. *Anal Chem* **89**, 4387–4391 (2017).
439. Filatov, N. A., Evstrapov, A. A. & Bukatin, A. S. Negative Pressure Provides Simple and Stable Droplet Generation in a Flow-Focusing Microfluidic Device. *Micromachines (Basel)* **12**, 662 (2021).

440. Lashkaripour, A., Rodriguez, C., Ortiz, L. & Densmore, D. Performance tuning of microfluidic flow-focusing droplet generators. *Lab Chip* **19**, 1041–1053 (2019).
441. Lashkaripour, A. *et al.* Machine learning enables design automation of microfluidic flow-focusing droplet generation. *Nat Commun* **12**, (2021).
442. Teo, A. J. T. *et al.* Negative Pressure Induced Droplet Generation in a Microfluidic Flow-Focusing Device. *Anal Chem* **89**, 4387–4391 (2017).
443. Crawford, D. F., Smith, C. A. & Whyte, G. Image-based closed-loop feedback for highly mono-dispersed microdroplet production. *Sci Rep* **7**, 10545 (2017).
444. Wilcox, R. R. *Basic statistics: understanding conventional methods and modern insights*. (Oxford University Press, 2009).
445. Teh, S.-Y., Lin, R., Hung, L.-H. & Lee, A. P. Droplet microfluidics. *Lab Chip* **8**, 198 (2008).
446. Yobas, L., Martens, S., Ong, W.-L. & Ranganathan, N. High-performance flow-focusing geometry for spontaneous generation of monodispersed droplets. *Lab Chip* **6**, 1073 (2006).
447. Ibrahim, A. M., Padovani, J. I., Howe, R. T. & Anis, Y. H. Modeling of Droplet Generation in a Microfluidic Flow-Focusing Junction for Droplet Size Control. *Micromachines (Basel)* **12**, 590 (2021).
448. Oliveira, B. *et al.* Fast Prototyping Microfluidics: Integrating Droplet Digital Lamp for Absolute Quantification of Cancer Biomarkers. *Sensors* **20**, 1624 (2020).
449. Tanaka, H. *et al.* Hands-Off Preparation of Monodisperse Emulsion Droplets Using a Poly(dimethylsiloxane) Microfluidic Chip for Droplet Digital PCR. *Anal Chem* **87**, 4134–4143 (2015).
450. Park, J. *et al.* Pushbutton-activated microfluidic dropenser for droplet digital PCR. *Biosens Bioelectron* **181**, 113159 (2021).
451. Aharoni, D. & Hoogland, T. M. Circuit investigations with open-source miniaturized microscopes: Past, present and future. *Front Cell Neurosci* **13**, 141 (2019).
452. Bonsai Foundation. Bonsai. https://bonsai-rx.org/ (2022).
453. Lopes, G. *et al.* Bonsai: an event-based framework for processing and controlling data streams. *Front Neuroinform* **9**, (2015).
454. Biotium. EvaGreen® Dye, 20X in Water - Product description. https://biotium.com/product/evagreen-dye-20x-in-water/ (2020).

APPENDICES

A | Capacitance of the MIM structures

Appendix Figure 1 illustrates the capacitance (*C*) and capacitance per unit area (*C/A*) at 5 kHz measured for MIM structures produced with Parylene C and PTFE as the dielectric layer, prior to any stimulus.

a) Capacitance (*C*) for single-layered Parylene C

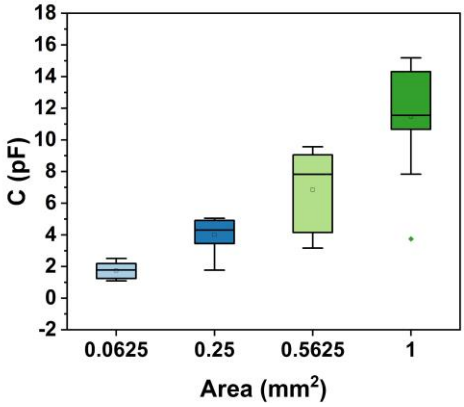

b) Capacitance (*C*) for double-layered Parylene C

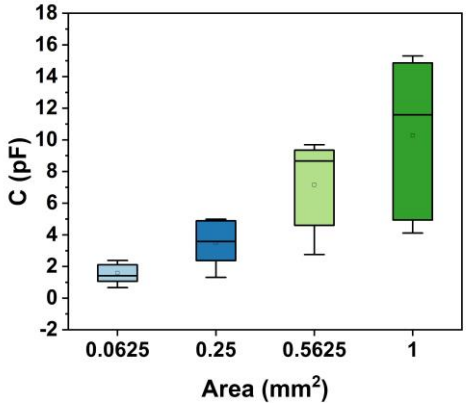

c) Capacitance per unit area (*C/A*) for single-layered Parylene C

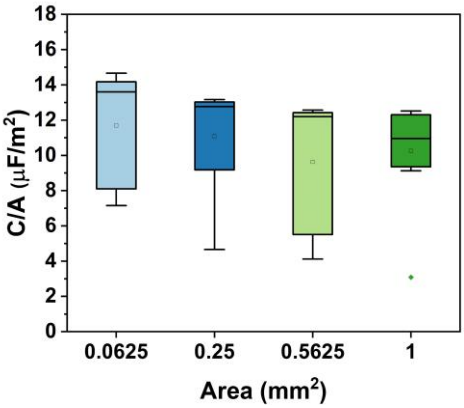

d) Capacitance per unit area (*C/A*) for double-layered Parylene C

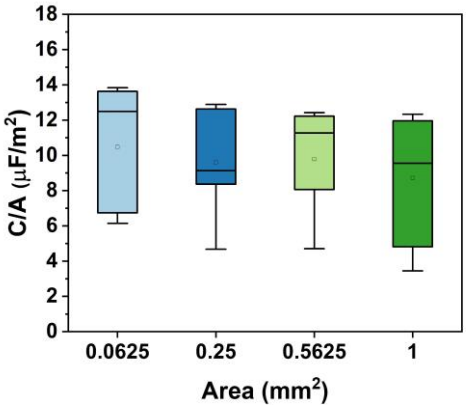

Appendix Figure 1: Capacitance measured for the MIM structures used in this work, prior to any stimulus. a) Capacitance measured for devices with single-layered Parylene C; b) Capacitance measured for devices with double-layered Parylene C; c) Capacitance per unit area measured for devices with single-layered Parylene C; d) Capacitance per unit area measured for devices with double-layered Parylene C. Please note that physical quantities have not been italicized for ease of visualization.

As can be observed in Appendix Figure 1, for both single- (a) and double-layered (b) Parylene C, the absolute capacitance increases with the MIM area, as expected. There is, however, a slightly greater dispersion of the capacitance values for double-layered Parylene C, which could be due to interfacial phenomena between the two layers. As for the capacitance per unit area for single-layered Parylene C, some abnormal values are present, as may be inferred from the greater distances between maximum and minimum value points in the box charts. Nevertheless, for all the areas studied, the median value is quite stable, ranging from 11.0 μF/m^2 to 13.6 μF/m^2. Regarding double-layered Parylene C, abnormal values are also

present, however the median value remains fairly stable across MIM areas, despite presenting a moderately higher dispersion (9.1 μF/m^2 to 12.5 μF/m^2). Once again, this moderate dispersion could be due to interfacial phenomena between the two layers, not accounted for with the normalization per area.

B | Relative permittivity of the MIM structures

Similarly to the capacitance (see Appendix A), the relative permittivity (ε_R) was determined for the MIM structures at 5 kHz, prior to any stimulus being applied.

a) Relative permittivity (ε_R) for single-layered Parylene C

b) Relative permittivity (ε_R) for double-layered Parylene C

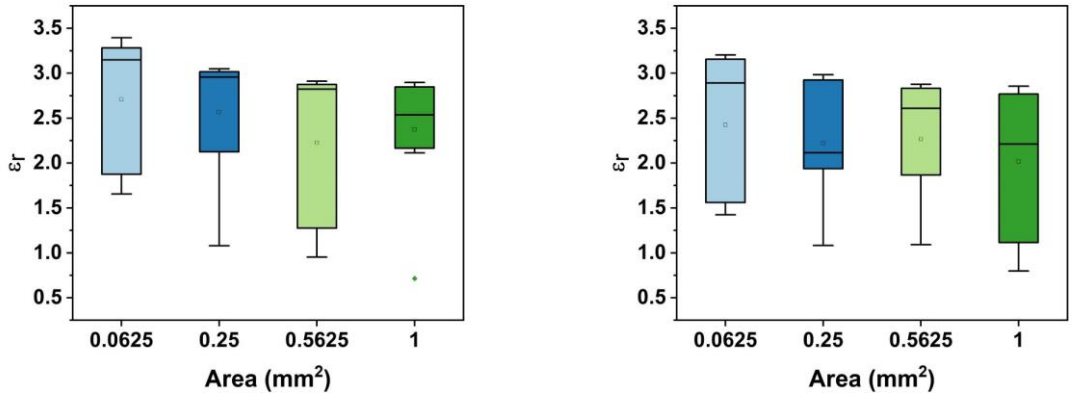

Appendix Figure 2: Relative permittivity for MIM structures produced with PTFE and Parylene C deposited in single (a) or double layer (b). Please note that the relative permittivity has not been italicized in the graphics for ease of visualization.

As can be seen on Appendix Figure 2 a), the median relative permittivity of single-layered Parylene C MIM structures is approximately 3.0, which is consistent with the ε_R reported for Parylene C only (see Appendix Table 1). This also illustrates the reduced influence that the PTFE-based layer has on the overall dielectric layer, which would be expected considering the small thickness of this layer (50 nm) as compared to the Parylene C thickness (2 µm). Nevertheless, for double-layered Parylene C, a greater variation in the permittivity results is observed, which may be attributed to the interface between the two Parylene C layers.

Appendix Table 1: Relative permittivity measured for Parylene C, according to different suppliers.

Relative Permittivity	Frequency	Reference
2.65	1 kHz	[1]
3.10	1 kHz	[2]
3.10	1 kHz	[3] (material used in this study)

B.1 References for Appendix B

1. VSI Parylene. Parylene Properties. https://vsiparylene.com/parylene-properties/ (2022).

2. Advanced Coatings. Parylene C Specifications. https://www.advancedcoating.com/typical-specification-parylene-c (2022).

3. Specialty Coating Systems. SCS Parylene Properties. https://scscoatings.com/technical-library/ (2018).

C | Loss tangent of the MIM structures

Appendix Figure 3 illustrates the loss tangent for the MIM structures assembled within the scope of this work.

a) Loss tangent for single-layered Parylene C

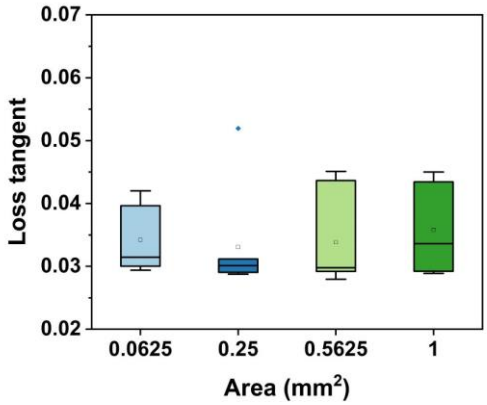

b) Loss tangent for double-layered Parylene C

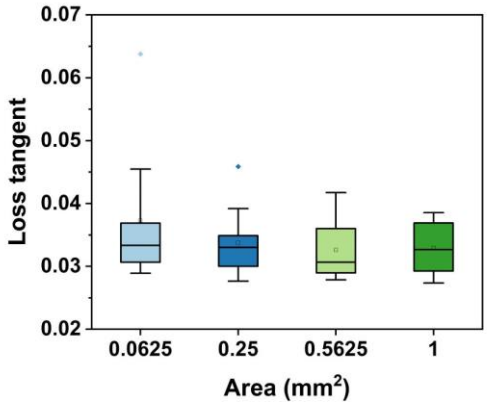

Appendix Figure 3: Loss tangent for the MIM structures, composed of either single- (a) or double-layered (b) Parylene C, measured at 5 kHz.

As can be seen from Appendix Figure 3, the median loss tangent for both single- and double-layered Parylene C is quite low, indicating that the dielectric layer composed of PTFE and Parylene C presents low energy dissipation.

D | Cross sections of the bottom plate of a digital microfluidic device

Appendix Figure 4 illustrates several images of the bottom plate of a DMF device, acquired by SEM, evidencing all the layers composing this plate. DMF devices were frozen in liquid nitrogen and broken afterwards, so that all layers were visible. Cutting the substrates without the liquid nitrogen treatment would lead to a complete cover of the chromium layer by Parylene C.

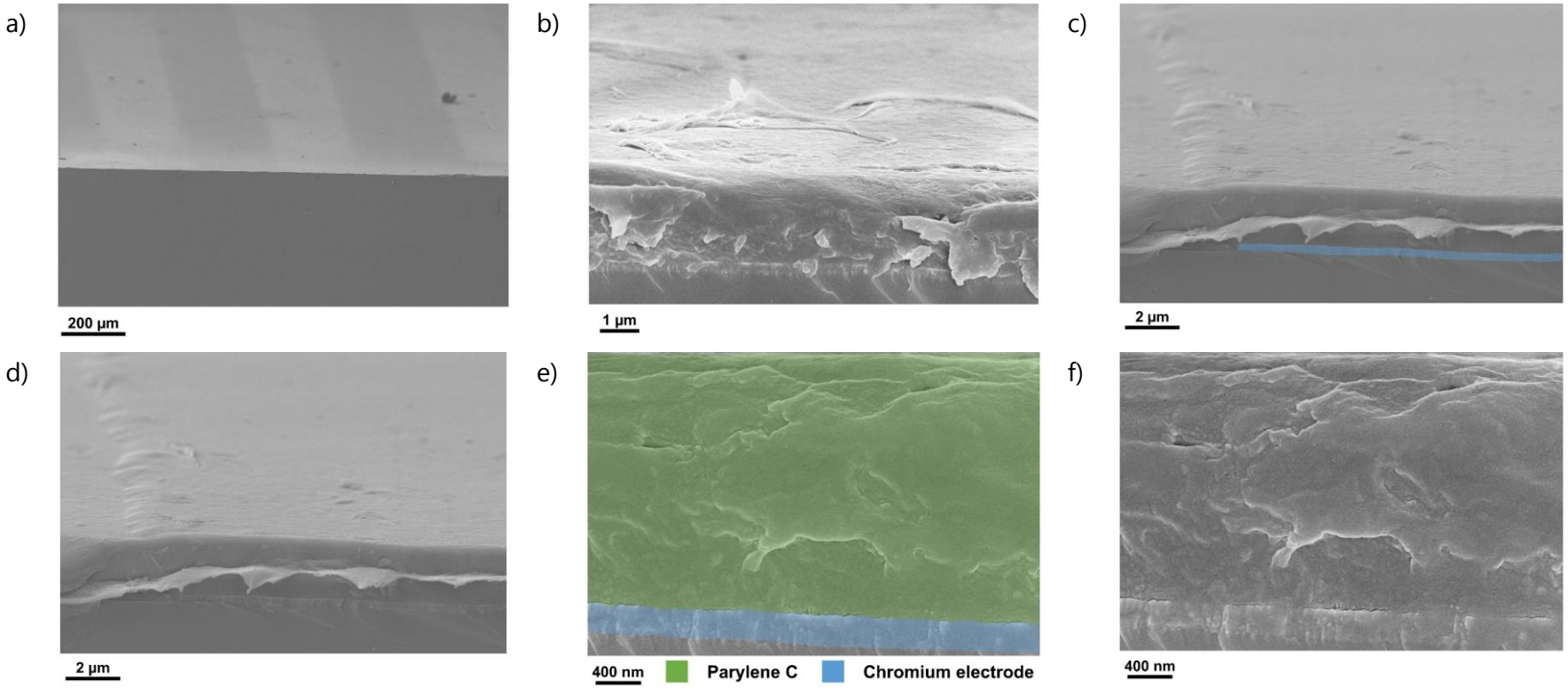

Appendix Figure 4: SEM-acquired cross-sectional views of the bottom plate of a DMF device, evidencing all the composing layers. a) Top view of the DMF bottom plate, where chromium connector lines are visible below the Parylene C and PTFE layers, in a light gray color. b) Surface of the DMF bottom plate, where the PTFE layer is visible as two small wrinkles bending over the Parylene C layer. c) Detail of the cross section of a chromium connector line, with chromium highlighted in blue. It is also visible that the layers on top of the chromium suffer an increase in height, which follows the length of the connector line. d) Representation of Appendix Figure 4 c) without the blue filter for the chromium connector line, where the interface between chromium and the glass substrate, as well as the interface between chromium and Parylene C, are clearly visible. e) Detail of the interface between Parylene C (on top) and chromium (at the bottom). f) Representation of Appendix Figure 4 e) without the blue filter for the chromium connector line and the green filter for Parylene C.

E | PHOTOBLEACHING

Photobleaching refers to the degradation of a fluorophore, such that the ability of said fluorophore to emit fluorescence is eliminated[292]. In this work, initial assays for monitoring LAMP reactions in DMF devices revealed severe photobleaching, as demonstrated in the figure below.

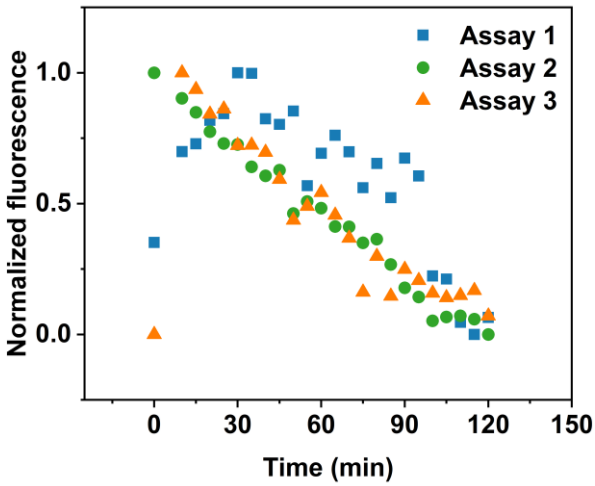

Appendix Figure 5: Normalized fluorescence (0 to 1) for three random assays performed at the initial experimentation of LAMP reaction monitoring on DMF devices by fluorescence measurements.

As demonstrated on Appendix Figure 5, fluorescence continually decreases during LAMP reactions, contrarily to what would be expected. Ideally, during a LAMP reaction, new strands of DNA are produced and fluorophore binding agents such as EvaGreen® intercalate with the strands and emit fluorescence[349,454]. As more strands are produced, more fluorescence is emitted. This was clearly not the case for the initial LAMP reactions represented in Appendix Figure 5, where a decreasing linear tendency is visible for assays 2 and 3. Assay 1 does not exactly follow a decreasing linear tendency, yet the decrease in fluorescence during the LAMP reaction is certainly present.

This photobleaching phenomenon may be attributed to the fluorescence detection mechanism. Due to the sub-optimal detection capability of the microscope used, the samples

had to be irradiated with the maximum power of the excitation light source (approximately 46 mW) for the maximum acquisition time allowed (1.73 s). Irradiating the same droplet with such conditions and a small interval between measurements (5 min, or even 10 min in other attempts) lead to over-exposure of the EvaGreen® fluorophore and consequently, photobleaching. Nevertheless, a successful strategy for preventing photobleaching was developed, as properly explained in section 6.2. This strategy proves that amplification monitoring of LAMP reactions is possible via fluorescence measurements, even for low-resource laboratories, considering that it is not necessary to acquire expensive fluorimeters or fluorescence microscopes, as conventional optical microscopes equipped with a fluorescence adaptor are enough. Such adaptors are significantly less expensive than the previous equipment.

F | DMF PROTOCOL FOR OFF-CHIP REAGENT MIXING

In this case, positive and negative controls were prepared as described in section 6.2 of the main text and reagents were mixed through vortex mixing. Subsequently, positive and negative LAMP control samples were inserted onto the chip via access orifices on the top plate (Appendix Figure 6 a)) and moved towards the reaction region via digital processes. Three smaller droplets were then split from the positive and negative control droplets (Appendix Figure 6 b)). After correct positioning of both smaller and larger droplets, the DMF platform (chip and support system) was placed under a microscope and heated for a 59.5 °C setpoint measured at the top plate, for 90 min. During the LAMP reaction, every 10 min, one small droplet from each control is irradiated (Appendix Figure 6 c)) and the emission is captured by the microscope detector. Irradiation conditions are similar to those referred in the main text, as well as droplet actuation parameters. Finally, the endpoint LAMP products (i.e. all droplets from each reaction) were pulled together by DMF (Appendix Figure 6 d)), removed from the device and submitted to agarose gel electrophoresis analysis.

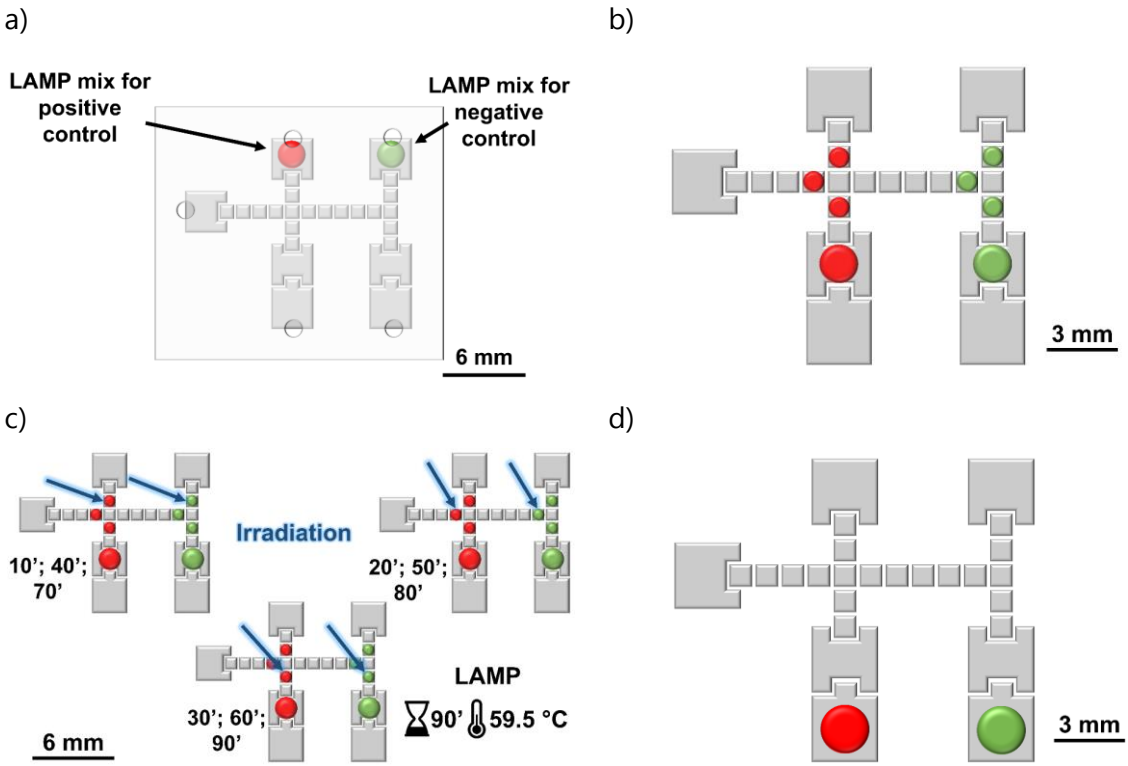

Appendix Figure 6: Steps required for on-device LAMP amplification of sample DNA, with off-chip reagent mixing. Firstly, droplets containing the positive and negative controls are loaded onto the DMF chip (a) and moved towards the reaction areas. Secondly, three small droplets are withdrawn from each control and placed along the electrode paths (b). The DMF chip is then heated with 59.5 °C measured at the top plate, for 90 min and the smaller droplets are sequentially irradiated (c). Finally, the smaller droplets are merged with the original ones, as to be removed from the device (d). Note that the top plate has been removed on b), c) and d) for better visualization.

G | PRIMER DIMERS

For on-chip LAMP reactions, background noise in the form of negative control fluorescence was detected by the proposed DMF system. Considering that the working mechanism of the EvaGreen® fluorophore consists of binding to double-stranded DNA, fluorescence for the negative control could be due to the formation of primer dimers, which may be identified by agarose gel electrophoresis as low-sized strands (Appendix Figure 7).

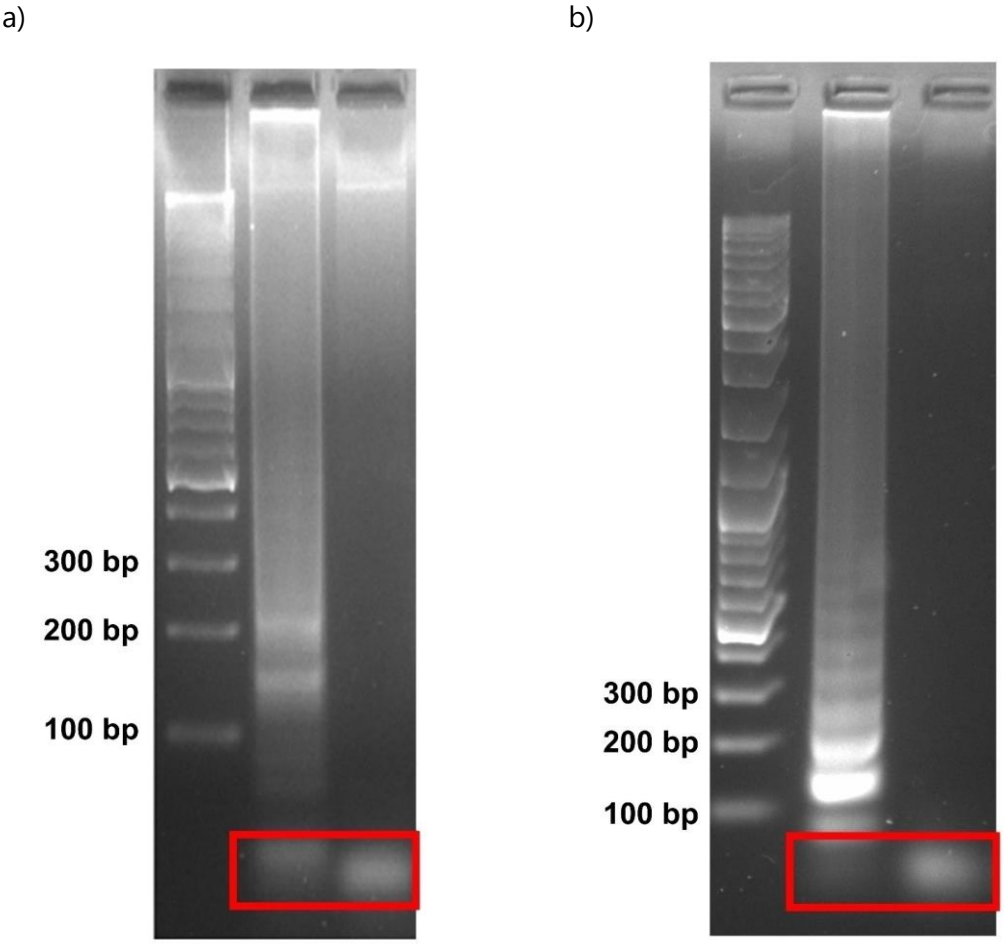

Appendix Figure 7: Examples of gel electrophoresis conducted for two distinct on-chip LAMP experiments, where primer dimers are visible (highlighted in red). For both trials (a and b), the lane order, from left to right, is as follows: DNA ladder | positive control | negative control.

H | Relative fluorescence for on- and off-chip reagent mixing

Appendix Figure 8 illustrates the relative fluorescence achieved with both on-chip and off-chip mixing of the LAMP master mix with the DNA sample.

a) b)

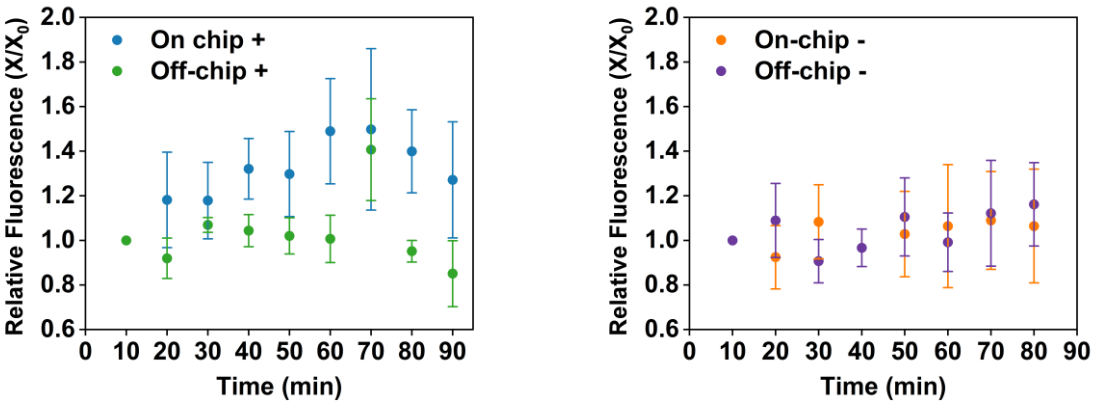

Appendix Figure 8: Relative fluorescence (normalized to the initial measurement at 10 min - X_0) in LAMP reactions, for both amplifying "+" (a) and non-amplifying "-" (b) samples, where reagents were mixed either on-chip or off-chip. Error bars correspond to the 90% confidence interval of a minimum 4 experiments for each time frame.

Regarding amplifying samples, similarly to the information withdrawn from Z scores at the main text, analysis of the relative fluorescence reveals that target DNA amplification is detected from 40 min onwards with on-chip mixing, whereas for off-chip mixing, amplification is only detectable from 60 min to 70 min. Moreover, for non-amplifying samples (mixed either on- or off-chip), fluorescence does not significantly increase during the reaction time, as expected. However, a slight increment in fluorescence is visible at 80 min and 90 min, which is attributed to background noise generated by the formation of primer dimers (see Appendix G), to which the fluorophore can bind.

I | Typical EISm working principle and turnarounds used in this work

Let us consider the EISm structure developed in this work, which relies on an IGZO semiconductor layer and a dual insulating layer comprised of Parylene C and Ta_2O_5. The capacitance of the insulating layers is expected to be constant for a voltage sweep at a constant frequency. However, the capacitance of the semiconductor layer is expected to vary, as the semiconductor changes its behavior from an insulator to a conductor or vice-versa (according to the direction of the voltage sweep). For n-type IGZO (used in this case), the expected *C-V* curve is as follows:

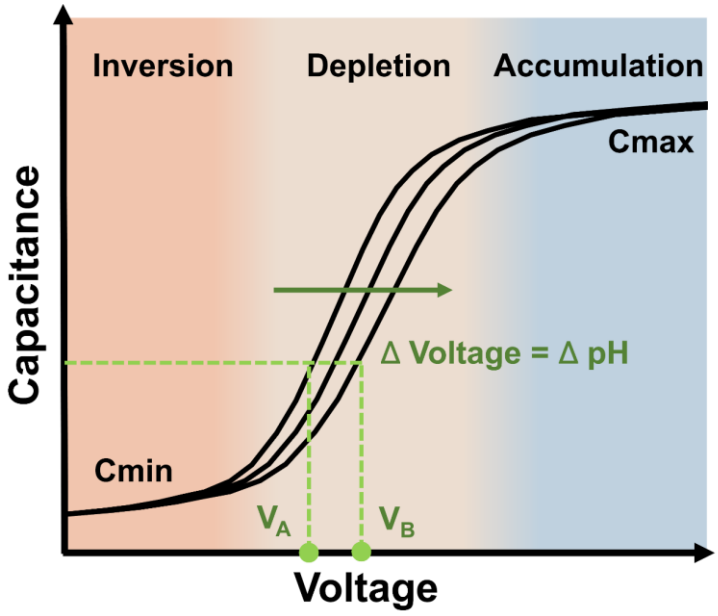

Appendix Figure 9: Typical capacitance-voltage (*C-V*) curves for EISm devices, evidencing all the working modes (inversion, depletion and accumulation) as well as the voltage variation accompanying pH variation. Image based on reference[1], with permission from the author.

When positive voltage is applied, negative carriers in the semiconductor (the majority of carriers, since it is an n-type material) will accumulate at the interface between the

semiconductor and the insulator, and the capacitance of the EISm structure will be at its maximum (accumulation mode). As the applied voltage is reduced, negative carriers will abandon the interface and the capacitance of the EISm structure will gradually decrease (depletion mode). If the applied voltage is low enough, the number of positive carriers at the semiconductor-insulator interface will be higher than the number of negative carriers (inversion mode) and the EISm capacitance reaches its minimum value.

Applied to pH sensing, the higher or lower presence of hydrogen ions in a solution will promote protonation or deprotonation of the Ta_2O_5 at the interface with the liquid, which in turn will lead to a shift in voltage for a fixed capacitance[2]. The interface between Ta_2O_5 and aqueous solutions is governed by the equations below:

$$TaOH_2^+ \leftrightharpoons TaOH + H^+ \quad \text{(I1)}$$

$$TaOH \leftrightharpoons TaO^- + H^+ \quad \text{(I2)}$$

In acidic medium, particularly below the point of zero charge (p_{zc}) of Ta_2O_5, excess hydrogen ions will promote positive charging of the interface. Reversely, in basic medium, decrease in hydrogen ions will promote negative charging of the interface[2,3]. This variation in the surface charge is the mechanism behind the shift in voltage for C-V curves. However, the behavior of the devices produced deviates from what was expected, as can be verified in the figure below, where C-V curves achieved for two distinct devices (randomly selected) are depicted.

a) *C-V* curve for device 1

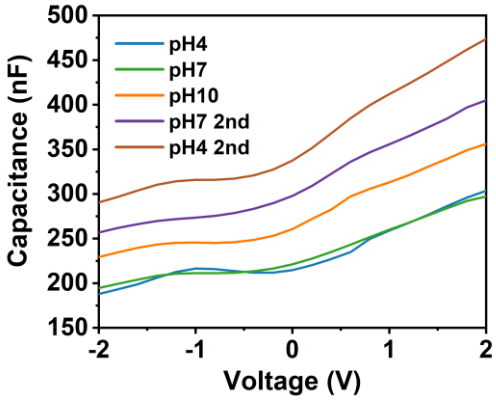

b) Normalized *C-V* curve for device 1

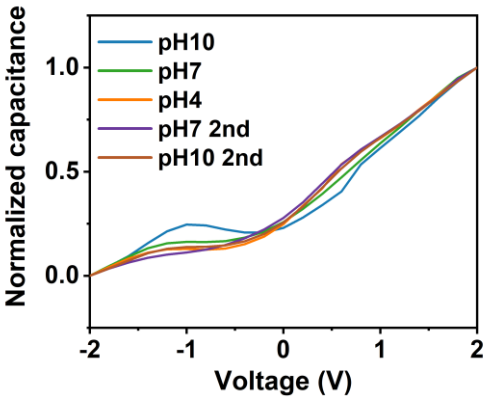

c) *C-V* curve for device 2

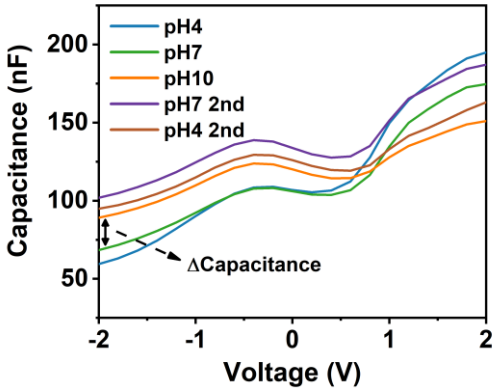

d) Normalized *C-V* curve for device 2

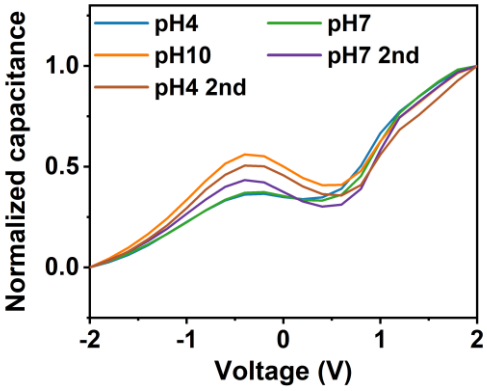

Appendix Figure 10: Examples of *C-V* curves for two randomly selected EISm devices. a) and c) are *C-V* curves presenting the absolute capacitance values, whereas b) and d) present normalized capacitance values, from 0 to 1.

The expected voltage shift is not well defined in any of the curves, however, it is quite clear that the measured capacitance (absolute value) varies according to different pH solutions. Thus, capacitance was isolated for three voltages (-2 V, 0 V and +2 V) and the difference in capacitance between successive pH solutions was determined, as exemplified in Appendix Figure 10 c).

I.1 A note on the point of zero charge of tantalum pentoxide

The p_{zc} of Ta_2O_5 is not mentioned within this work, considering the dispersion of values in the literature. Nevertheless, this value was not necessary, neither for the pH measurements herein nor for other pH sensors based on this oxide, produced within the Department of

Materials Science. The table below includes a comprehensive list of p_{zc} values reported for Ta_2O_5 in the literature.

Appendix Table 2: Point of zero charge determined for Ta_2O_5 from several references in the literature.

Point of zero charge determined	Reference
2.8	[4]
3.0	[5]
2.9	[6]

I.2 References for Appendix I

1. Branquinho, R. Label-free detection of biomolecules with Ta2O5-based field effect devices. (NOVA School of Science and Technology, 2012).

2. Chen, M., Jin, Y., Qu, X., Jin, Q. & Zhao, J. Electrochemical impedance spectroscopy study of Ta2O5 based EIOS pH sensors in acid environment. *Sens Actuators B Chem* **192**, 399–405 (2014).

3. Poghossian, A. & Schöning, M. J. Capacitive field-effect eis chemical sensors and biosensors: A status report. *Sensors (Switzerland)* vol. 20 1–32 Preprint at https://doi.org/10.3390/s20195639 (2020).

4. Poghossian, A. A. *Determination of the pH pzc of insulators surface from capacitance-voltage characteristics of MIS and EIS structures*. *Sensors and Actuators B* vol. 44 (1997).

5. Bousse, L. *et al. Zeta Potential Measurements of Ta2Os and SiO2 Thin Films*. (1991).

6. Butler, M. A. & Ginley, D. S. Prediction of Flatband Potentials at Semiconductor-Electrolyte Interfaces from Atomic Electronegativities. *J Electrochem Soc* **125**, 228–232 (1978).

J | Results of ANOVA tests for pH-shift capacitance

Appendix Tables 3 through 6 summarize the results obtained for ANOVA tests performed to evaluate statistical relevance between pH shifts measured by the devices produced for capacitance measurements on liquid solutions.

Appendix Table 3: Statistical evaluation of the capacitance variation for all pH shift combinations, for 100 Hz and decreasing pH condition. "Yes" and "No" indicate statistically relevant and not statistically relevant differences in capacitance, respectively.

Applied voltage	pH shift	ANOVA result	Tukey test result
-2 V	pH10 to pH7 vs pH7 to pH4	No	No
	pH10 to pH7 vs pH4 to pH7		No
	pH4 to pH7 vs pH7 to pH4		No
	pH7 to pH10 vs pH10 to pH7		No
	pH7 to pH10 vs pH7 to pH4		No
	pH7 to pH10 vs pH4 to pH7		No
0 V	pH10 to pH7 vs pH7 to pH4	No	No
	pH10 to pH7 vs pH4 to pH7		No
	pH4 to pH7 vs pH7 to pH4		No
	pH7 to pH10 vs pH10 to pH7		No
	pH7 to pH10 vs pH7 to pH4		No
	pH7 to pH10 vs pH4 to pH7		No
+2 V	pH10 to pH7 vs pH7 to pH4	No	No
	pH10 to pH7 vs pH4 to pH7		No
	pH4 to pH7 vs pH7 to pH4		No
	pH7 to pH10 vs pH10 to pH7		No
	pH7 to pH10 vs pH7 to pH4		No
	pH7 to pH10 vs pH4 to pH7		No

Appendix Table 4: Statistical evaluation of the capacitance variation for all pH shift combinations, for 100 Hz and increasing pH condition. "Yes" and "No" indicate statistically relevant and not statistically relevant differences in capacitance, respectively.

Applied voltage	pH shift	ANOVA result	Tukey test result
-2 V	pH4 to pH7 vs pH7 to pH4	No	Yes (p = 0.0960)
	pH7 to pH10 vs pH10 to pH7		No
	pH7 to pH10 vs pH7 to pH4		No
	pH7 to pH10 vs pH4 to pH7		No
	pH10 to pH7 vs pH7 to pH4		No
	pH10 to pH7 vs pH4 to pH7		No
0 V	pH4 to pH7 vs pH7 to pH4	No	No
	pH7 to pH10 vs pH10 to pH7		No
	pH7 to pH10 vs pH7 to pH4		No
	pH7 to pH10 vs pH4 to pH7		No
	pH10 to pH7 vs pH7 to pH4		No
	pH10 to pH7 vs pH4 to pH7		No
+2 V	pH4 to pH7 vs pH7 to pH4	Yes	Yes (p = 0.0883)
	pH7 to pH10 vs pH10 to pH7		No
	pH7 to pH10 vs pH7 to pH4		Yes (p = 0.0619)
	pH7 to pH10 vs pH4 to pH7		No
	pH10 to pH7 vs pH7 to pH4		No
	pH10 to pH7 vs pH4 to pH7		No

Appendix Table 5: Statistical evaluation of the capacitance variation for all pH shift combinations, for 500 Hz and decreasing pH condition. "Yes" and "No" indicate statistically relevant and not statistically relevant differences in capacitance, respectively.

Applied voltage	pH shift	ANOVA result	Tukey test result
-2 V	pH10 to pH7 vs pH7 to pH4	No	No
	pH10 to pH7 vs pH4 to pH7		No
	pH4 to pH7 vs pH7 to pH4		No
	pH7 to pH10 vs pH10 to pH7		No
	pH7 to pH10 vs pH7 to pH4		No
	pH7 to pH10 vs pH4 to pH7		No
0 V	pH10 to pH7 vs pH7 to pH4	No	No
	pH10 to pH7 vs pH4 to pH7		No
	pH4 to pH7 vs pH7 to pH4		No
	pH7 to pH10 vs pH10 to pH7		No
	pH7 to pH10 vs pH7 to pH4		No
	pH7 to pH10 vs pH4 to pH7		No
+2 V	pH10 to pH7 vs pH7 to pH4	No	No
	pH10 to pH7 vs pH4 to pH7		No
	pH4 to pH7 vs pH7 to pH4		No
	pH7 to pH10 vs pH10 to pH7		No
	pH7 to pH10 vs pH7 to pH4		No
	pH7 to pH10 vs pH4 to pH7		No

Appendix Table 6: Statistical evaluation of the capacitance variation for all pH shift combinations, for 500 Hz and increasing pH condition. "Yes" and "No" indicate statistically relevant and not statistically relevant differences in capacitance, respectively.

Applied voltage	pH shift	ANOVA result	Tukey test result
-2 V	pH4 to pH7 vs pH7 to pH4	Yes	No
	pH7 to pH10 vs pH10 to pH7		No
	pH7 to pH10 vs pH7 to pH4		Yes (p = 0.0785)
	pH7 to pH10 vs pH4 to pH7		No
	pH10 to pH7 vs pH7 to pH4		Yes (p = 0.0565)
	pH10 to pH7 vs pH4 to pH7		No
0 V	pH4 to pH7 vs pH7 to pH4	Yes	No
	pH7 to pH10 vs pH10 to pH7		No
	pH7 to pH10 vs pH7 to pH4		Yes (p = 0.0987)
	pH7 to pH10 vs pH4 to pH7		No
	pH10 to pH7 vs pH7 to pH4		Yes (p = 0.0960)
	pH10 to pH7 vs pH4 to pH7		No
+2 V	pH4 to pH7 vs pH7 to pH4	Yes	No
	pH7 to pH10 vs pH10 to pH7		No
	pH7 to pH10 vs pH7 to pH4		Yes (p = 0.0718)
	pH7 to pH10 vs pH4 to pH7		No
	pH10 to pH7 vs pH7 to pH4		Yes (p = 0.0975)
	pH10 to pH7 vs pH4 to pH7		No

K | Large print of the DrMF standalone devices

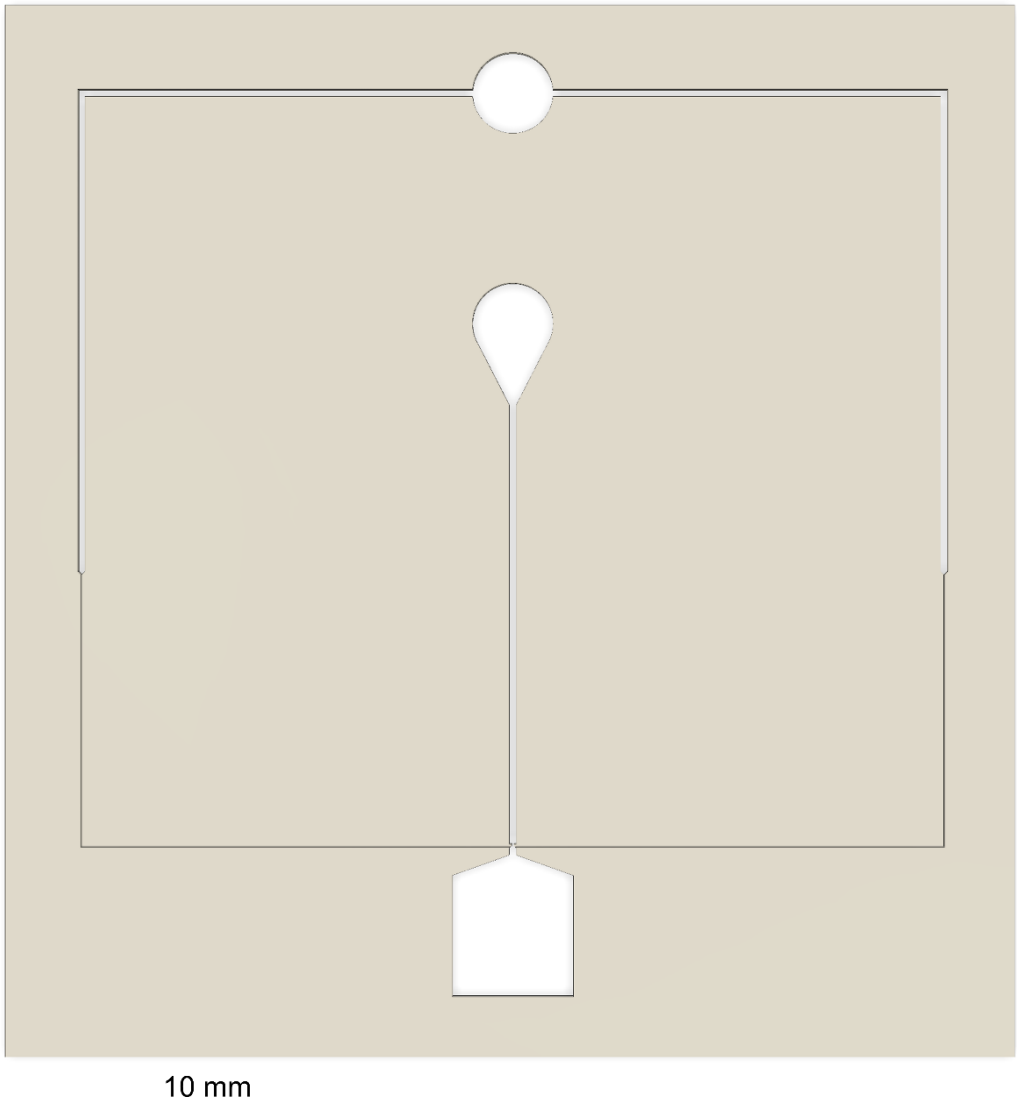

Appendix Figure 11: Larger print of a standalone DrMF device, for better visualization of smaller features in the design.

L | Channel width variation after deposition of Parylene C and PTFE

As stated in section 9.3.1, the production of DMF-DrMF hybrid devices requires the deposition of a dielectric layer (Parylene C) and a hydrophobic layer (PTFE-based), necessary to the DMF section of the devices. To avoid any possible disruption at the interface between moieties, which leads to electrolysis of the LAMP buffer solution (results not shown), both layers were deposited after sealing the DrMF section to the glass substrate containing the DMF electrodes. Moreover, the entrance to the DrMF microfluidic channel was not covered, also to avoid any disruption at the interface between both moieties. Thus, the deposition of the dielectric and hydrophobic layers led to a decrease in the diameter of the entrance of the microfluidic channel at the DrMF section (see Figure 9.4 b) and c)). Appendix Figure 12 illustrates the width variation of the entrance of the microfluidic channel after deposition of the fore-mentioned layers at the flow focusing region, according to the equations below:

$$\Delta\ channel\ width\ after\ Parylene\ C\ = \\ = Initial\ channel\ width\ -\ channel\ width\ after\ Parylene\ C\ deposition \tag{L1}$$

$$\Delta\ channel\ width\ after\ PTFE\ = \\ Initial\ channel\ width\ -\ channel\ width\ after\ PTFE\ deposition \tag{L2}$$

a) b)

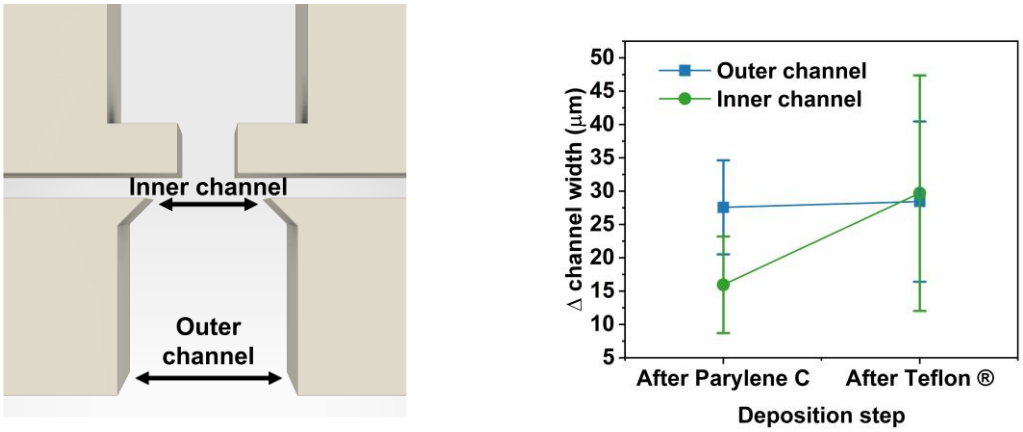

Appendix Figure 12: a) Schematic representation of the channel widths in DMF-DrMF devices defined for this study, i.e., the entrance of the DrMF microfluidic channel (outer channel) and the entrance to the flow focusing region (inner channel). b) Graphical representation of the variation of the channel widths, after deposition of the Parylene C layer and the PTFE-based layer. Error bars correspond to the standard variation.

As shown in Appendix Figure 12 b), both Parylene C and PTFE depositions lead to subsequent decreases in the width of the inner and outer channels of the DrMF section in hybrid devices. The inner channel is less affected by the Parylene C deposition, which in turn leads to a larger width variation of the outer channel. The PTFE layer is deposited by spin-coating, directionally perpendicular to the microfluidic channel, which could promote a greater penetration of the PTFE solution, down to the inner channel. Nevertheless, regarding the Parylene C deposition, both inner and outer channel width variations are greater than expected, since the deposition process is highly conformable[1] and deposition parameters were optimized to ensure a 2 μm thickness. Appendix Figure 13 illustrates one of the DMF-DrMF devices used to study the variation of channel widths, from the initial clean state to the final state, after Parylene C and PTFE depositions. The depositions were performed exactly as described previously, and in the same order: Parylene C was firstly deposited with the Labcoater® PDS 2010 system, after which the PTFE layer was deposited by spin-coating. All images were acquired with a Leica M80 stereo microscope (Leica Microsystems, Wetzlar, Germany). Please note that all images are mirrored on their left side as a result of reflection from the metallic interfacial electrode. The mirrored portion of images was not cropped since the author considered this an interesting aspect of the produced devices.

a) Outer channel before depositions

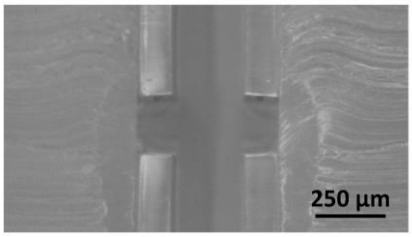

b) Inner channel before depositions

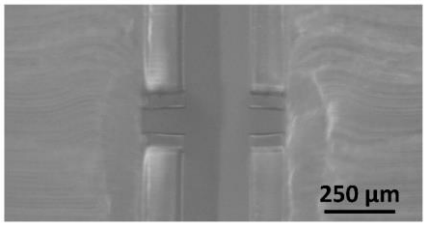

c) Outer channel after Parylene C deposition

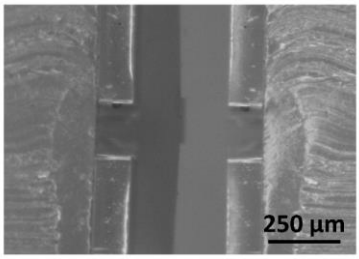

d) Inner channel after Parylene C deposition

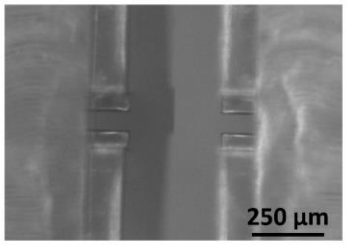

e) Outer channel after PTFE deposition

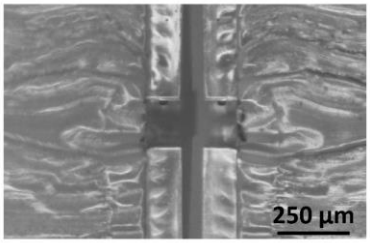

f) Inner channel after PTFE deposition

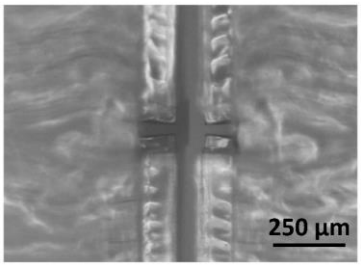

Appendix Figure 13: Cross section images of a DMF-DrMF hybrid device, evidencing the outer (left) and inner (right) channels before any deposition (a) and b) respectively), after the Parylene C deposition (c) and d) respectively), and after PTFE deposition (e) and f) respectively).

As can be seen on Appendix Figure 13, the deposition of Parylene C leads to a considerable reduction in the width of both outer (a) to c)) and inner (b) to d)) DrMF microfluidic channels. However, visually it seems that there was channel shrinkage rather than Parylene C deposition on the channel walls. Considering that the Parylene C is deposited in vacuum and the PDMS is porous[2,3], the PDMS channel could have suffered shrinkage, thus decreasing both inner and outer channels. Moreover, the silane adhesion promoter used in the Parylene C deposition could have induced a greater adhesion of the PDMS to the glass, further decreasing the width of microfluidic channels. After Parylene C deposition, the PTFE hydrophobic layer was deposited by spin-coating. By spin-coating, the PTFE solution is spread through the glass substrate containing both DMF and DrMF moieties (see Figure 9.4 a)), perpendicularly to the

entrance of the DrMF microfluidic channel. An accumulation of the solution is therefore likely to occur in this area, and even though the curing process will then eliminate a considerable part of the solution solvent, the overall material accumulation should be greater at this region than for the remainder of the DMF section. Thus, the deposition of the dielectric and hydrophobic layers on the hybrid devices will lead to a decrease in the inner and outer channel widths, which will contribute to variations in droplet characteristics of the DMF-DrMF hybrid devices, as opposed to standalone DrMF devices.

L.1 References for Appendix L

1. Specialty Coating Systems, *SCS Parylene Properties*, 2018.
2. A. Lamberti, S. L. Marasso and M. Cocuzza, *RSC Adv.*, 2014, **4**, 61415–61419.
3. G. Firpo, E. Angeli, L. Repetto and U. Valbusa, *J Memb Sci*, 2015, **481**, 1–8.

M | CONTACT ANGLE FOR MATERIALS PRESENT AT DMF-DRMF HYBRID DEVICES

Appendix Table 7 indicates the contact angles for all materials present at the interface between the DMF and the DrMF moieties of the hybrid devices, as measured in-house. Each measurement represents the average contact angle between the left and right contact angles measured for a minimum 3 substrates.

Appendix Table 7: Contact angle measurements for multiple materials used in standalone DrMF and DMF-DrMF hybrid devices.

Material	Present in:	Contact angle (º)
PDMS (polydimethylsiloxane, Sylgard 184® from Dow Corning)	Standalone DrMF devices and DMF-DrMF devices	109.2 ∓ 1.3
Parylene C	DMF-DrMF devices	100.2 ∓ 1.0
PTFE solution used in this study	DMF-DrMF devices	122.6 ∓ 0.5

2023

BEATRIZ JORGE COELHO

DIGITAL MICROFLUIDICS FOR ISOTHERMAL NUCLEIC ACID AMPLIFICATION